Development of an advanced high speed flywheel energy storage system

Document Version:
Publisher's PDF, also known as Version of Record (includes final page, issue and volume numbers)

Please check the document version of this publication:

• A submitted manuscript is the version of the article upon submission and before peer-review. There can be important differences between the submitted version and the official published version of record. People interested in the research are advised to contact the author for the final version of the publication, or visit the DOI to the publisher's website.
• The final author version and the galley proof are versions of the publication after peer review.
• The final published version features the final layout of the paper including the volume, issue and page numbers.

[Link to publication](#)

DEVELOPMENT
OF AN ADVANCED HIGH SPEED
FLYWHEEL
ENERGY STORAGE SYSTEM

F.J.M. THOOLEN

DEVELOPMENT

of an advanced high speed

FLYWHEEL

ENERGY STORAGE SYSTEM

F.J.M. THOOLEN

DEVELOPMENT

of an advanced high speed

FLYWHEEL

ENERGY STORAGE SYSTEM

PROEFSCHRIFT

ter verkrijging van de graad van doctor aan de
Technische Universiteit Eindhoven, op gezag van
de Rector Magnificus, prof. dr. J.H. van Lint,
voor een commissie aangewezen door het College
van Dekanen in het openbaar te verdedigen op
dinsdag 7 december 1993 om 16.00 uur

door

FRANCISCUS JOHAN MARIE THOOLEN

geboren te Echt (L)

Dit proefschrift is goedgekeurd door

de promotoren   :   prof.dr.ir. M.J.W. Schouten (T.U.E., Nederland)
en
prof. A.A. Frank (University of California, U.S.A.)

en de co-promotor :   dr. H.K. Asper (Consultant energiesystemen,
voorheen ETH Zürich, Zwitserland)

Aan Anneke,
Jean-Pierre, François, Lilian
en aan mijn ouders

Summary

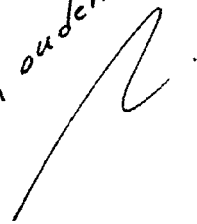This thesis presents the results of a study concerning a regenerative energy storage system for mobile applications. The main objectives are the reduction of the fossil energy consumption and the related environmental pollution. The study comprises three parts which succeed each other, starting with a general reflection and ending with a flywheel energy storage system, which has been elaborated on in detail.

Part I gives a rough inventory of regenerative energy storage systems. First of all, their potential for energy and emission reduction is considered. It appears that energy storage for mobile applications will become very important for future environmentally benign vehicles. Many investigations show a considerable potential for energy and emission reduction for vehicular applications in urban areas. This is made possible by brake energy recovery and conversion improvement of the prime mover.
The realized regenerative energy storage systems for vehicular applications show, as yet, too limited energy storage and power capacity in respect of volume and weight to enable successful application. On the other hand, it appears that a flywheel energy storage system offers the best prospects for mobile applications. A further optimization of such a system is required, however, to enable large scale application.

Part II deals with the optimization of a flywheel energy storage system starting with the performance demands, as required for mobile applications in city buses and commuter trains. For that purpose several alternatives for the flywheel component as well as the transmission subsystem have been considered.
It appears that metal disc as well as composite rim flywheels are the most favourable options. As a transmission subsystem, a continuously variable transmission (CVT) is required. The investigation into CVT alternatives leads to the purely electrical CVT, which is based on a permanent magnet machine in conjunction with an electronic converter, as the most favourable CVT.
The combination of the flywheel with the electrical transmission system in a flywheel motor/generator unit as a compact component with a high versatility is then possible in several ways. From a comparison between several concepts, it follows that the optimal flywheel energy storage system consists of a thick rim composite flywheel integrated with a permanent magnet motor/generator.
This concept has been designated as EMAFER: Electro Mechanical Accumulator For Energy Reuse, an energy and power density optimized flywheel energy storage system for a great number of load cycles with high power demands.

Part III comprises the mechanical aspects of the development of the EMAFER high speed flywheel system. The concept and final design are described with the help of the main parts as they have been worked out as a result of the investigations into several aspects. The investigations focus on flywheel development and vibration research.

The flywheel development deals with two construction alternatives for the thick rim flywheel as used in the EMAFER concept. These alternatives apply to the woven ribbon process flywheel, which consists of a tape wound under pretension and the layered flywheel, which is composed of concentric annular elements of different materials.

Both alternatives have been investigated theoretically, with the help of simulation models, as well as practically, with the aid of test wheels. A kind of integration of the techniques used in the two principles leads to an optimal result for the EMAFER concept.

As far as the vibration research is concerned, the problems related to the high speed operation of the EMAFER system have been dealt with extensively. Using simulation models, supported by practical tests, the effects of design measures are predicted. A construction with rigid main assemblies, that are weakly coupled via proper stiffness and damping elements, appears to be the main condition in achieving good vibration behaviour.

The testing of the prototype, in which all the above investigation results were implemented, has showed that the required speed specifications could be met without showing any sign of failure. The vibration behaviour appeared to be excellent with no critical speeds in the operating speed range and with very acceptable vibration levels. Thus the technical feasibility of the EMAFER concept has been demonstrated.

Samenvatting

Dit proefschrift beschrijft de resultaten van een studie naar een regeneratief energie-opslagsysteem voor mobiele toepassingen. De hoofddoelstellingen zijn het terugdringen van het fossiele energiegebruik en de daarmee samenhangende milieuvervuiling. De studie omvat drie gedeelten die elkaar opvolgen, te beginnen met een algemene beschouwing en eindigend met een vliegwielsysteem voor energie-opslag dat tot in detail is uitgewerkt.

Deel I geeft een globale inventarisatie van regeneratieve energie-opslagsystemen. Allereerst worden hiervan de mogelijkheden met betrekking tot het terugdringen van het energiegebruik en de milieubelasting beschouwd. Het blijkt dat energie-opslag voor mobiele toepassingen zeer belangrijk zal worden voor toekomstige, milieuvriendelijke voertuigen. Allerlei onderzoeken tonen een aanzienlijk potentieel aan voor terugdringing van het energiegebruik en de milieubelasting bij toepassing in voertuigen voor stedelijk verkeer. Dit is mogelijk door de recuperatie van remenergie en het verbeteren van het conversierendement van de krachtbron.
De regeneratieve energie-opslagsystemen zoals gerealiseerd voor voertuigtoepassingen hebben vooralsnog een te beperkte energie- en vermogenscapaciteit met betrekking tot het volume en het gewicht om een succesvolle toepassing mogelijk te maken. Anderzijds blijkt een vliegwielsysteem de beste perspectieven te bieden voor mobiele toepassingen. Er is echter een verdergaande optimalisering van een dergelijk systeem nodig om tot grootschalige toepassing te komen.

Deel II beschrijft de optimalisering van een vliegwielsysteem voor energie-opslag op basis van prestatie-eisen zoals vereist voor mobiele toepassing in stadsbussen en forenzentreinen. Daartoe zijn verschillende alternatieven beschouwd voor zowel de vliegwielcomponent als het transmissiesubsysteem.
Het blijkt dat zowel metalen schijfwielen als uit composietmateriaal bestaande velgwielen de meest aantrekkelijke opties voor een vliegwiel zijn. Als transmissiesubsysteem is een continu variabele transmissie (CVT) vereist. Het onderzoek naar CVT-alternatieven resulteert in de zuiver elektrische CVT, op basis van een permanentmagneetmachine met een elektronische omzetter, als de meest gunstige CVT.
De combinatie van het vliegwiel met de elektrische transmissie tot een vliegwiel-motor/generator-eenheid als een compacte component met een grote veelzijdigheid is dan op verschillende manieren mogelijk. Uit een vergelijking tussen verschillende concepten volgt dat het optimale vliegwielsysteem voor energie-opslag bestaat uit een dikwandig vliegwiel van composietmateriaal, geïntegreerd gebouwd met een permanentmagneetmachine. Dit concept wordt aangeduid met EMAFER: Electro Mechanical Accumulator For Energy Reuse, een vliegwielsysteem voor energie-opslag dat geoptimaliseerd is naar energie- en vermogensdichtheid en geschikt is voor een groot aantal belastingcycli met hoge vermogenseisen.

Deel III omvat de mechanische aspecten van de ontwikkeling van het hoogtoerige vliegwielsysteem EMAFER. Het concept en definitieve ontwerp worden beschreven aan de hand van de hoofdonderdelen zoals deze zijn uitgewerkt als resultaat van de onderzoeken naar diverse aspecten.

De onderzoeken concentreren zich op de vliegwielontwikkeling en het trillingsonderzoek. De vliegwielontwikkeling heeft betrekking op twee constructie-alternatieven voor het dikwandige vliegwiel zoals toegepast in het EMAFER-concept. Deze alternatieven betreffen het bandwikkelproces waarbij een band onder voorspanning tot een vliegwiel wordt gewikkeld en het gelaagde vliegwiel dat is samengesteld uit concentrische ringelementen van verschillende materialen.

Beide alternatieven zijn zowel theoretisch onderzocht, met behulp van simulatiemodellen, als praktisch door middel van testwielen. Een bepaalde mate van integratie van de technieken, zoals toegepast in beide principes, leidt tot het optimale resultaat voor het EMAFER-concept.

Wat betreft het trillingsonderzoek, wordt uitgebreid ingegaan op de problemen met betrekking tot het hoogtoerige bedrijf van het EMAFER-systeem. Met behulp van simulatiemodellen, ondersteund door praktijktesten, worden de effecten van ontwerpmaatregelen voorspeld. Een constructie met starre hoofdsamenstellingen, slap gekoppeld via geschikte stijfheids- en dempelementen, blijkt de hoofdvoorwaarde te zijn om een goed trillingsgedrag te bewerkstelligen.

Het testen van het prototype waarin alle bovengenoemde onderzoeksresultaten zijn geïmplementeerd, heeft aangetoond dat aan de vereiste toerenspecificaties kon worden voldaan zonder enig teken van faalgedrag. Het trillingsgedrag bleek voortreffelijk, zonder kritische toerentallen in het werkgebied en met zeer aanvaardbare trillingsniveaus. Aldus is de technische haalbaarheid van het EMAFER-concept aangetoond.

Contents

Appendices

Appendix I: Specifications for a future gyrobus

Introduction

For the past fifty years, since World War II, the industrialized nations mainly experienced an unprecedented growth of the standard of living and material wealth. These developments were possible because of strong human dedication and immensely advancing technology, science, education, etc. Unfortunately, this was also at the expense of the exhaustible fossil energy resources and at the expense of the environment.

Over the past two decades, the efficient use of energy resources has become a major topic. Starting with the first energy crisis of 1973, mankind realized the finiteness of the fossil energy resources. Since then another aspect has been added to the public awareness of the large scale fossil energy use: the environmental pollution.

Because of the World's present energy demands, which are still increasing, the fossil energy resources will be exhausted in the foreseeable future. In addition, because of the large scale of energy use, the environmental pollution assumes large proportions. The related damaging effects to human health, animals and plants could be immense and may have an enormous impact. The public awareness of this has led to extensive research into energy management related areas, creating new or renewed attention to subjects like:
- Energy saving and energy reuse.
  The conventional energy sources are not used efficiently. The overall utilization efficiency is clearly lower than 40 percent.
  The utilization efficiency can in general be raised considerably by improving the energy conversion processes and by recovering used energy. During the last few years, some important energy conversion improvements have been made possible for domestic, industrial and transport applications by means of the use of electronic control systems. Heat insulation is an example of a simple and equally effective measure for the improvement of the utilization efficiency in heating processes.
- Substitution of fossil energy resources by renewables such as solar and wind energy.
  This substitution is still difficult as conventional energies, e.g. oil, can be stored conveniently for extended periods prior to utilization, while renewable energies have a variable availability, must be converted first and then stored adequately. Electricity as an intermediate power means could become very important in this respect.
- Control and reduction of environmental pollution associated with energy reuse.
  Better control strategies and control systems for energy conversion processes in connection with measures for treating emissions will make significant reductions of the environmental pollution possible.

Regenerative energy storage may be an important means of contributing to the solution of the dual problems of fossil energy shortage and environmental pollution, since it has the potential to greatly enable the implementation of the possibilities mentioned above.

This particularly applies to energy storage for mobile applications with strongly alternating power demands, i.e. urban vehicles, excavators, payloaders, lifting and hoisting devices. Here, energy storage enables energy conversion improvement, energy recovery and emission reduction.

This study describes the role and the development of an energy storage system for mobile applications where low weight, high power and a long service life with an acceptable energy storage capacity are required. As follows from the preparatory study into regenerative energy storage, a flywheel energy storage system based on fibre composite technology with electromechanical power transmission offers the best prospects for these purposes.

The system developed is designated as EMAFER: Electro Mechanical Accumulator For Energy Reuse. The objective of the development of this system is a versatile flywheel energy storage system. As a pilot application, a system for the use in large vehicles, such as a commuter train and a city bus, has been chosen.

INVENTORY OF REGENERATIVE

ENERGY STORAGE SYSTEMS

IN PARTICULAR FOR MOBILE APPLICATIONS

Chapter 1[*]

Importance of regenerative energy storage systems

1.1. Introduction

At the moment mankind faces the problems of threatening fossil energy shortage and environmental pollution. The World's energy consumption is almost totally supplied by fossil energy resources with a low energy utilization efficiency whereas the substitution of these resources is difficult.

The energy storage considered next is regenerative in the way that taking up and returning of energy are possible in a reversible way. By this characteristic energy storage systems can reduce the fossil energy demand and the related environmental pollution.

1.2. Energy and pollution considerations

a) Energy supply

At the moment the World's energy demand is mainly supplied by fossil energy resources. With the world's present energy demand the fossil energy resources will be exhausted within the foreseeable future. This can be illustrated by the Reserve/Production (R/P) ratio of fossil fuels. If the reserves remaining at the end of any year are divided by the production in that year, the result is the length of time that those remaining reserves would last if production were to continue at the then current level. The reserves concern the proved reserves, which can be recovered in the future from known reservoirs under existing economic and operating conditions. Fig. 1.1. illustrates the fossil fuel R/P ratios at the end of 1992.

It can be seen that the World's reserves of oil and natural gas will run out in near future. The World's reserves of coal will last considerably longer than those of oil and natural gas, but are certainly not unlimited.

Nuclear energy is also limited. Energy supply by nuclear fission depends on the success of the enrichment technology for uranium 238 since uranium 235 is as scarce as oil and gas. Moreover nuclear fission has as disadvantage that it causes radio active waste. Nuclear fusion seems still to be behind the horizon and it may also cause radio active waste, albeit less and with shorter half life times than in case of fission.

* Modified version of [1.1].
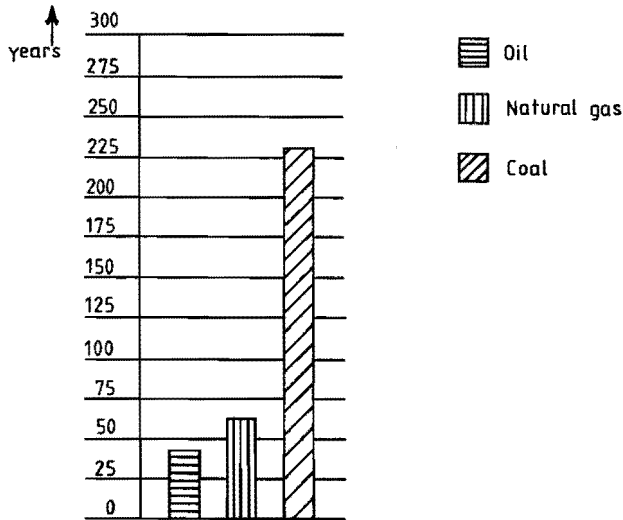
Fig. 1.1. World's fossil fuel R/P ratios at the end of 1992 [1.2].

b) Environmental pollution

The consequence of large scale energy use is that the environment is polluted in the way of emissions (solid, liquid and gaseous) and physical influences (noise, heat and radiation). Most of the solid emissions can be controlled in practical ways before they have come into the environment. Fluid and gaseous emissions and similarly physical influences can only be controlled by tackling them at the source, e.g. by energy saving and substitution, process changes and removal at the source.

The traditional reason for the reduction of pollution by harmful substance is the protection of human health. Today, in addition to the damaging effects on human health, the damage to the environment (plants, animals and materials) is also taken into account. One of the reasons is the growing awareness that some effects can be on a great scale and can have such enormous consequences, that urgent measures are necessary. Recently it has been established that in order to prevent the most serious damage through photochemical pollution and acidification, the emissions of nitrogen oxide (NO_x), sulphur dioxide (SO_2), ammonia (NH_3) and hydrocarbons (C_xH_y) will have to be reduced by 60% to 90% by the year 2000, as compared to the 1990 level [1.3]. After the turn of the century even further reductions will be necessary.

1.3. Social interest of energy storage

The World's energy demand can be distinguisted into four demand categories.

- Heating : Low temperature heat for buildings and high temperature heat for industrial processes.
- Power/Lighting : Stationary propulsion systems and all lighting systems.
- Traction : Vehicles (cars, trains, buses), vessels and aircraft.
- Feedstock : Raw material (oil, natural gas) for petrochemical industry and chemical manure.

Almost all demand categories are directly supplied by fossil fuels. Only the power/lighting demand category is supplied by electricity as an intermediate power means. The traction energy demand category is only for a small part supplied by electricity.
The first three demand categories represent energy purposes and in these categories energy storage has the potential for the reduction of the fossil energy consumption and the related evironmental pollution. This is made possible by:
a) A more efficient energy utilization of the remaining fossil resources, by the recovering of energy and the peak shaving of the energy demand. Peak shaving allows the prime movers to operate more efficiently.
b) Enabling substitution of energy resources. Although renewable energy resources have many advantages (inexhaustable, no pollution), a restriction is the variable character. Energy storage can take away this restriction.

1.4. Classification of energy storage systems

The known energy storage systems can be classified depending on the kind of energy that is stored. In this way, the following classifications can be distinguished. Depending on the kind of stored energy, the systems are applicable in the different energy demand categories as mentioned in section 1.3.

a) Thermal energy storage
Thermal energy can be accumulated by heating the medium with respect to the surrounding temperature or by changing the medium phase, e.g. melting of salts. The first alternative is called sensible energy accumulation, the second one latent energy accumulation. Sensible energy accumulation is used for low temperature (up to 100°C) heat. Water is the most proper storage means because of its high heat capacity and its good heat transport capability. For short period (weeks, days) storage, water in insulated tanks is used, for long period (seasonal, months) storage, water in aquifers (shallow water transporting ground layers) is used. Most of this low temperature heat is used for the heating of buildings. Industry needs high temperature heat. For this application latent energy accumulation can be considered.

b) Electrical energy storage
Electrical energy can be stored in the electrical field between capacitor plates. Capacitors for energy accumulation are only used for very short period (minutes) storage of small energy quantities or for high current shocks, e.g. rail and coil guns. Because of the very low storage capacity most applications concern the control of the dynamic behaviour in electrical circuits of several devices.

c) Magnetic energy storage
Energy can also be stored in the magnetic field of an electrical coil. The major disadvantage is the need of an electrical current during energy conservation. This causes extra losses which can be avoided by super conduction. These systems are voluminous with respect to the energy storage capacity. Applications are energy storage with short period high power demands, e.g. in uninterruptable power supply systems.

d) Chemical energy storage
An electrochemical battery stores the energy as chemical energy. By a reversible chemical reaction the stored energy is taken up or returned as electrical energy. Storage capacity and charging and discharging power are small with respect to volume and weight and the number of load cycles is restricted. Applications are decentral storage of small energy quantities with small power demands, e.g. start batteries for vehicles.

Chemical energy stored in fossil fuels can not be used in a reversible way and is therefore not considered as regenerative energy storage. However, very attractive for the future is chemical storage by hydrogen, because of its pollution free combustion (only water) and its high storage capacity with respect to volume and weight. It can be produced pollution free by electrolytical fusion of water with solar electricity. Moreover, in combination with a fuel cell, it can be directly converted, with a high efficiency (60%) at low temperature, into electricity [1.4].

e) Potential energy storage
Potential energy can be stored in masses in the gravitation field, and as compression energy of gases or elastic bodies.

For accumulation of large quantities of energy, e.g. in the electricity production, water reservoirs on different heights and air compression in underground cavities are used. These potential energy storage systems are voluminous systems, meant for stationary applications where large amounts of energy have to be stored for mid long (hours, days) periods.

For storage of smaller energy quantities, hydraulic accumulators are used. They store the energy as compression energy: a gas, usually nitrogen, is compressed by a liquid in a steel container. Applications are short (minutes) or mid long period (hours, days) storage of relatively small energy quantities with relatively small power demands, e.g. in some vehicles.

For storage of still smaller energy quantities, compression energy of elastic bodies is used, e.g. springs. Accumulators of this type are used to take up and return small energy quantities in short times, e.g. for control of dynamic behaviour of parts and for mechanical positioning systems.

f) Kinetic energy storage
Kinetic energy can be stored as rotational energy in a flywheel. The storage capacity, with respect to volume and weight, was relatively small. However, with the development of strong and light materials (composites), the storage capacity has been increased. Advantages are the possibility of high load and unload torques of the flywheel and the long life time. Applications are short period (seconds, minutes) storage of small energy quantities.

The utilization of new technologies and materials in kinetic energy flywheels can result in improved energy storage elements, applicable for storing larger quantities of energy with high power demands and for longer periods.

1.5. Quantitative potential of energy storage

To get an insight in the maximum achievable potential of energy storage a rough analysis has been made in which the fossil energy reduction for each concerning energy demand category by appropriate energy storage systems has been considered. This has been done for the situation in The Netherlands, which is representative for developed western countries. The energy demand for 1990 without and with energy storage has been considered.

1.5.1. Energy demand without energy storage

Fig. 1.2. illustrates the net and gross energy demand without energy storage for The Netherlands in 1990 with a population of 15 million. The net energy demand is divided over the different demand categories and is the energy demand measured "at the door of the consumer". It includes thus the conversion losses of the consumer. The gross energy demand is divided over the different energy resources and is the primary energy "at the well", required to supply the net energy demand. It includes thus the winning, conversion and transport losses to bring the energy in a suitable form at the door of the consumer. For fossil fuels as energy carrier, the net/gross ratio is about 0.95 [1.5]. In this respect electricity as an intermediate power means is not energy efficient due to the relatively low efficiency of the fossil energy/electricity conversion. At the 1990 level this efficiency is about 40%, however is expected to be raised above 50% in future when electricity is produced with the help of combined steam/gas turbines.

Net energy demand
2125 PJ.*

a (56%)   high temp. (26%)   b (11%)   low temp. (30%)   c (20%)   d (13%)

Gross energy demand
2600 PJ.*

B (14%)   C (35%)   D (2%)   E (1%)   A (48%)

		low temp. 645 PJ.
a. Heating	: 1190 PJ.	high temp. 545 PJ.
b. Power/lighting	: 234 PJ.	
c. Traction	: 425 PJ.	
d. Feedstock	: 276 PJ.	

A. Natural gas	: 1248 PJ.
B. Coal.	: 364 PJ.
C. Oil	: 910 PJ.
D. Nuclear	: 52 PJ.
E. Renewable	: 26 PJ.

*1 PJ ≙ 278·10^6 kWh ≙ 23,800 ton oil equivalent
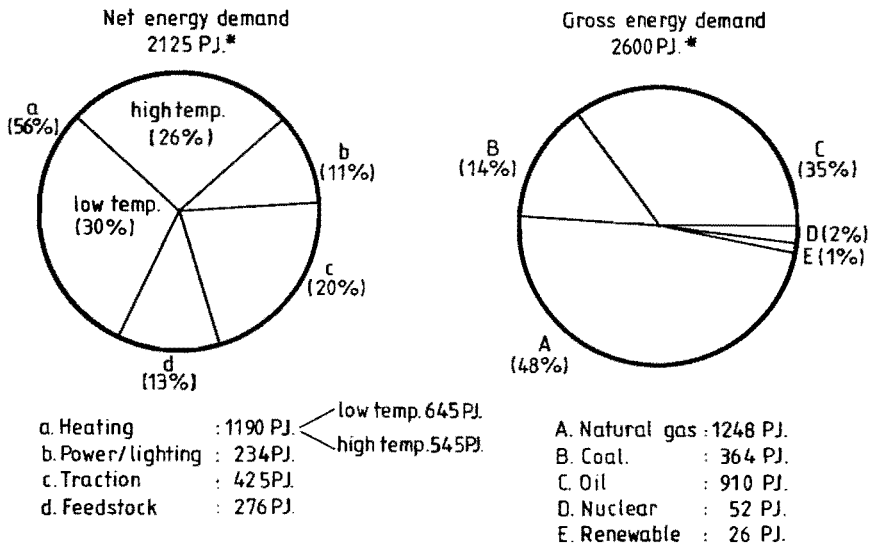
Fig. 1.2. Net and gross energy demand divided over respectively demand categories and energy resources. Reference, The Netherlands 1990 [1.5].

It can be seen from this figure that the heat demand category is the major demand category and that the total energy demand is almost totally supplied by fossil energy resources.

1.5.2. Energy demand with energy storage

The energy demand categories to be considered for fossil energy reduction by energy storage are heating, power/lighting and traction, see also section 1.3.

a) Heat demand category

In this category only thermal energy storage is applicable, see section 1.4. This storage concerns mainly sensible heat accumulation for heating of buildings as latent heat accumulation (high temperature heat for industrial processes) is still in the experimental stage. High temperature heat has still to be generated directly with fossil fuels, nuclear energy or electricity. Sensible heat accumulation makes a better energy utilization and substitution possible by means of heat insulation, heat recovery, heat pumps and seasonal heat storage of solar energy. Following the considerations in [1.5], an energy reduction of 10% should be possible by the mentioned measures.

Further savings are possible by ultilization of the waste heat of the electricity production. At the moment the major part (60%) of the primary energy is here, because of the Carnot or Rankine cycle, converted into low temperature heat which could be stored, e.g. in aquifers, and be supplied to the heat demand category.

At the 1990 level 12% of the net energy demand (=0.12x2125PJ=255 PJ) is supplied via electricity [1.5]. With a fossil energy/electricity conversion efficiency of about 40%, the waste heat amounts then 0.6/0.4 x 255PJ = 382.5 PJ. Assuming an "in/out" efficiency of the storage system of 80%, the energy reduction potential of waste heat utilization is 0.8 x 382.5 = 306 PJ which is about 25% of the total heat demand.

The total fossil energy reduction potential of energy storage for the heat demand category can amount thus about 10+25=35% and is restricted to the low temperature heat demand.

b) Power/Lighting demand category

This demand category is almost completely supplied by electricity. Fossil energy reduction is possible by introducing large scale utilization of renewable energies (sun, wind, tidal energy) for the electricity production. Energy storage enables this option by compensating the variable character of renewable energies. Relatively large amounts of energy have to be stored then for mid long periods (hours, over night). As appears from the classification of energy storage systems, three kind of energy storage have to be considered for this application: magnetic (e.g. electrical coil with super conduction), chemical (batteries) and potential (e.g. hydro and compressed air) energy storage.

The Netherlands receive yearly about 130,000 PJ solar energy and 15,000 PJ wind energy (up to 100 m height). In total about 55 times more than the total yearly gross demand (2630 PJ in 1990) [1.5]. However, the conversion techniques are still restricted. Because of the low conversion efficiencies of solar cells and wind generators (respectively 10 and 40%), the supply of solar and wind energy is calculated on maximum 150 PJ of electrical energy [1.5]. It is also calculated that about 10 PJ can be fed directly into the public electrical grid without energy storage [1.6]. This gives the energy storage an energy subsitution potential of 140 PJ. This means in turn a fossil energy reduction potential of energy storage for the power/lighting demand category of about 60%.

c) Traction demand category

In this category many propulsion systems have to deal with strongly alternating power demands, e.g. urban vehicles, excavators, payloaders, lifting and hoisting devices. Incorporation of practical energy storage elements in these systems has a large fossil energy reduction potential.

The fossil energy reduction potential is made possible by recovering the kinetic and/or potential energy of the vehicle and by improving the efficiency of the prime mover, which is in turn possible by peak shaving the power demand.

For mobile application, storage elements with relatively high energy and power density are needed. From the classification in section 1.4. it can be seen that only chemical (battery), potential (hydraulic accumulator) and kinetic (flywheel) storage elements have to be considered for this application.

From literature [1.7] to [1.9], investigations are known where the above energy reduction has been considered, assuming loss free systems. Urban vehicles can save minimum 30% of the traction energy by recuperation of braking energy [1.7] and [1.8]. Peak shaving of the actual power demand of these vehicles enables the prime mover to supply the required mean power with an optimal efficiency. A reduction in specific fuel consumption of minimum 25% is possible then [1.9]. Assuming an "in/out" efficiency of the storage system of 80%, the total energy saving in urban transport is minimum $0.8 \times 30\%$ + $0.8 \times 0.25 \, (100\% - 0.8 \times 30\%) \approx 40\%$.

Urban transport represents to a great extent the traction energy demand, e.g. in The Netherlands for 37.5% [1.10]. The theoretical fossil energy reduction potential of energy storage for the traction demand category is then minimum $0.375 \times 40\% = 15\%$.

If all storage systems are used in combination, the fossil energy reduction for the heat demand category will be considerably smaller then calculated before. Due to 150 PJ electricity production by renewable energies, the recoverable waste heat in the electricity production will amount to $0.6/0.4 \, (255-150) = 157.5$ PJ. This is about 13% of the total heat demand. The total fossil energy reduction potential of energy storage for the heat demand category is then about 23% instead of the 35% derived earlier.

The total reduction in the gross fossil energy demand by optimum use of energy storage has been calculated for a net/gross energy ratio of 0.95 for the heat and traction demand category and $0.95 \times 0.4 = 0.38$ for the power/lighting demand category, see also section 1.5.1. Fig. 1.3. illustrates the thus determined quantitative potential of energy storage. It can be seen from this figure that yearly 723 PJ primary fossil energy can be saved. This is a reduction of about 28% of the yearly total gross fossil energy demand.

About half of this reduction is due to substitution by renewable energies for the electricity production. In the heat demand category the better energy utilization is responsible for an important fossil energy reduction. Energy storage in the traction demand category has the smallest fossil energy reduction potential. It is, however, very important with respect to its emission reduction potential in urban areas where the reduction of noise, heat and hazardous smog conditions is of vital interest. The emission reduction will be directly related to the fossil energy reduction if no emission improvements of the energy conversion process by energy storage are supposed.

Total fossil energy reduction 723 PJ.
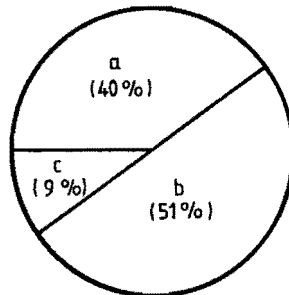
a. Heating   : 288 PJ.
b. Power/lighting : 368 PJ.
c. Traction   : 67 PJ.

Fig. 1.3. Fossil energy reduction by energy storage. Reference, The Netherlands 1990.

1.5.3. Marginal notes

Some marginal notes have to be made to the computed potentials as these cannot be realized in practice.

- The energy and pollution needed for realizing and installing the storage system reduce the potential of energy storage systems. Very important in the "net energy analysis" [1.11], is the service life of the system. This should in any case be longer than the time to amortize the energy and pollution for realizing and installing the system. This time can be indicated as "energy pay back time".
- Economical considerations.
  From an economical point of view investments are done if in any way there is an acceptable "pay back time". This condition is always met as soon as the preceding condition, service life longer than energy pay back time is met. In this frame work it would be better if the producer and the consumer of goods would pay the same unit price for energy.
- Restrictions in availability of suitable storing facilities, e.g. aquifers, water reservoirs and compressed air reservoirs. It is thinkable that, for instance in the heat and electricity demand category, the required storage capacity would be impractically large.

1.6. Conclusions

The preceding considerations can be summarized in the following conclusions:
- Energy storage can reduce the fossil energy demands and the related evironmental pollution. A theoretical fossil energy reduction potential of 28% is possible.
- In the respect of fossil energy reduction, large scale systems for stationary applications (heat, electricity) and based on thermal, electrical, magnetic, chemical and potential energy storage are the most attractive options.
- Energy storage in the traction demand category has a relatively small fossil energy reduction potential. It is especially important with respect to its emission reduction potential in urban areas. It can enable pollution free vehicles while retaining free mobility.

The energy storage for mobile applications will be further subject of study in this thesis as it is still in the development stage and as it will become very important for future, environmentally benign vehicles.
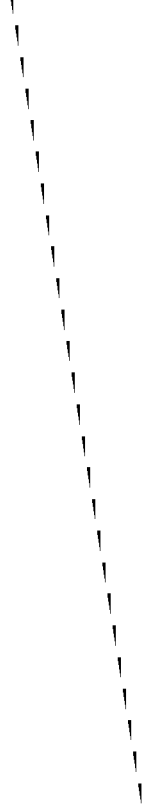
Chapter 2

Literature research to regenerative energy storage for mobile applications

2.1. Introduction

The public awareness of the threatening fossil energy shortage and air pollution has provided impetus for finding new vehicle propulsion alternatives. As such, regenerative energy storage systems for mobile applications have been a subject of study, especially during the last two decades.

2.2. Prospects

Regenerative energy storage, with the goal to reduce the fossil energy demand and related air pollution, is only effective in applications with strongly alternating power demands. For mobile applications this applies to propulsion systems in:
- vehicles for urban transport: city buses, metros, street cars, dustbin lorries, delivery vans, commuter trains [2.1] to [2.3].
- hoisting and lifting devices: cranes, forklift trucks [2.4].
- earth moving equipment: draglines, excavators, payloaders etc. [2.5].

In these applications regenerative energy storage can offer important and considerable energy and emission reductions by recuperating the braking energy and improving the conversion efficiency of the prime mover. See also section 1.5.2.
The other potential of regenerative storage systems in the traction demand category is the substitution of energy resources. Energy storage systems enable the use of an intermediate power means like electrical power without being dependent on overhead wire and/or rail systems. Electricity can be generated from several energy resources, among others renewables.

2.2.1. Brake energy recovery

This is a technique of recovering kinetic and/or potential energy which is conventionally converted into heat by braking systems. Studies have been made for cases where brake energy recovery can be applied effectively with regard to vehicle parameters and driving characteristics [1.7] and [2.1] to [2.4]. The vehicle parameters concern mass, air drag and rolling resistance. Only the energy related with the mass, kinetic and/or potential, can be recovered. The driving characteristics concern start-stop distance, acceleration, deceleration and maximum speed and can be expressed by means of the driving cycle. The driving cycle determines to what extent the energy related to the vehicle mass can be recovered.

The effectiveness of the regenerative brake is expressed by the ratio of recovered to delivered energy at the driving wheels of the vehicle. This ratio is indicated as the recuperation factor. In most of the studies the recuperation factor is calculated without considering transmission and storage losses.

In [1.7] and [2.1] in particular the influence of the vehicle parameters on the recuperation factor has been investigated. Therefore an ideal driving cycle is considered. The ideal driving cycle can be derived from a real one as illustrated in Fig. 2.1.
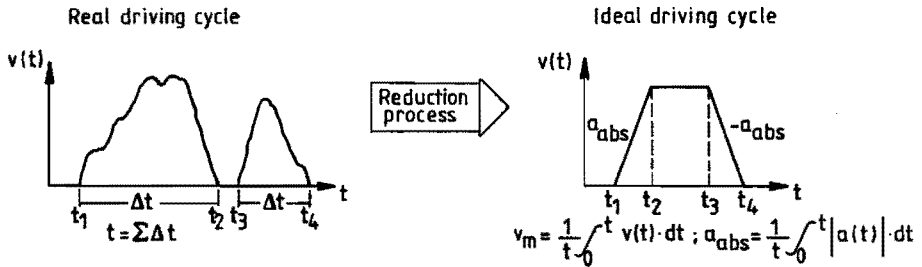
Fig. 2.1. Presentation of driving cycle [1.7].

In [1.7] the recuperation factor has been investigated for two different types of vehicles, the passenger car and the city bus. It appears that for the considered range of driving characteristics, the absolute mean value of acceleration as defined in Fig. 2.1., has the major influence on the recuperation factor. Fig. 2.2. shows the recuperation factor as a function of the absolute mean value of acceleration. The influence of the other driving characteristics is expressed by the scattering range of the recuperation factor.
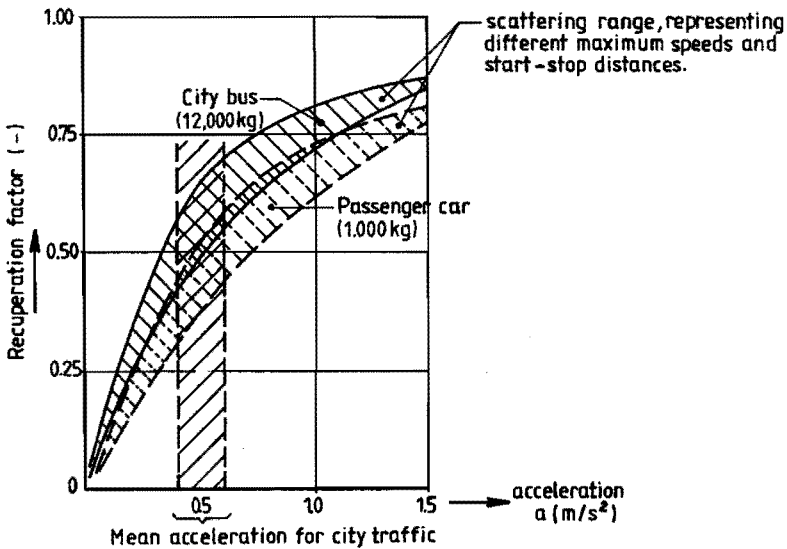
Fig. 2.2. Recuperation factor for a passenger car and a city bus [1.7].

It can be seen from this figure that substantial energy savings are possible with the considered loss free recuperation systems. In urban traffic these savings range from 30 to 65%, depending on vehicle type and driving cycle. It follows also that the effectiveness of regenerative braking is higher for a city bus than for a passenger car, in urban traffic about 30% higher.

In [2.1] and [2.2] similar calculations have been done to investigate the recoverable part of the traction energy of large vehicles. Fig. 2.3. represents the simulation results of [2.1]. The recuperation factor is plotted here against the distance between stops for a city bus and an urban rail vehicle. The influence of different accelerations and maximum speeds is represented here via the scattering range of the recuperation factor. Transmission and storage losses are not considered in this figure.

It follows from this figure that brake energy recuperation is considerably more effective in an urban rail vehicle than in a city bus. For situations with relatively short distances between stops, for a train 3500 m and for a city bus 500 m, 50% of the traction energy can be saved when loss free recuperation systems are considered. For refuse collection trucks this percentage ranges even to more than 60% [2.2].
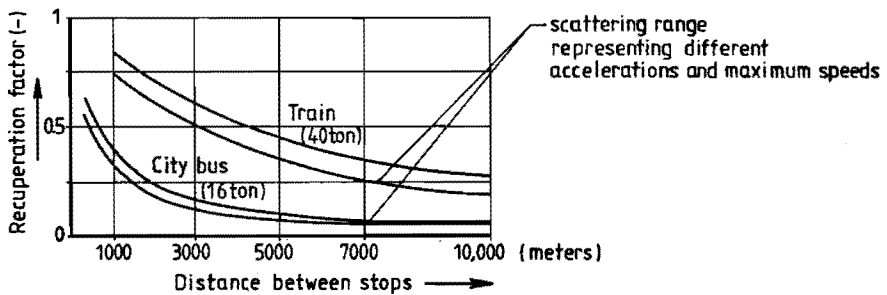
Fig. 2.3. Recuperation factor for a city bus and an urban rail vehicle [2.1].

The influence of different driving cycles on the recuperation factor can be demonstrated with the help of some practical considerations, which have been done for passenger cars [2.3] and [1.8].

In [2.3] the required power, propulsion energy and brake energy have been calculated for the European ECE 15 city cycle as well as for the American EPA city cycle. The last one differs from the first one by more aggressive accelerations and a higher top speed. The calculations have been performed for a 1000 kg passenger car without considering drive line losses. It appears that the energy recovery efficiency is about the same for both cycles namely 21% for the ECE 15 cycle and 26% for the EPA city cycle. The difference with the results presentated in Fig. 2.2., recuperation factor minimum 30%, is probably due to differences in the considered driving cycles.

In [1.8] the recuperation factor has been calculated for several American driving cycles, also without considering drive line losses. The considered driving cycles are the:

- FUDC (Federal Urban Driving cycle) representing typical urban driving in metropolitan area with an average speed of 31.5 km/h and a large number of accelerations, decelerations and periods of idling.

- EPA Highway Cycle representing turnpike driving with a fairly constant speed averaging 77.6 km/h.
- EPA Congested Freeway Cycle with an average speed of 56 km/h and a considerable amount of acceleration and deceleration.
- NYCC (New York City Cycle), a low-speed cycle with many starts and stops and a significant amount of idling, with an average speed of 11.4 km/h.
- LDC (Low Duty Cycle) with an average speed of 23.8 km/h and no hard accelerations.

The results are summarized in Fig. 2.4. from which it can be concluded that the type of driving cycle strongly influences the recuperation factor as this ranges from 0.1 to 0.7.
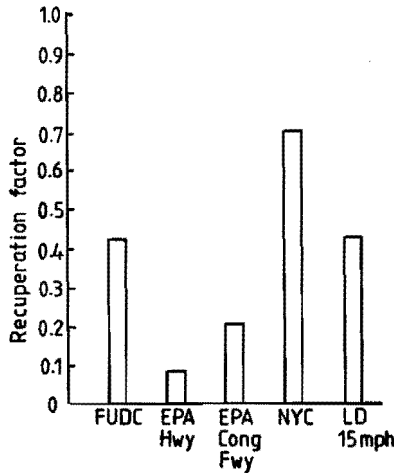
Fig. 2.4. Recuperation factor for a 1360 kg passenger car for several American driving cycles [1.8].

It follows from the above investigations that brake energy recovery can be very effective in urban traffic and is more favourable for larger than for smaller vehicles. According to Fig. 2.2., 2.3. and 2.4., an energy saving of at least 30% is possible in this way, preconceived that there are no transmission and storage losses. Assuming an "in/out" efficiency of the storage system of 80%, brake energy recovery enables a net energy saving of 0.8 x 30% = 24%.

2.2.2. Conversion improvement of prime mover

The installed prime mover power in road vehicles is determined by load demands, e.g. acceleration, high speed operation and hill climbing, that are obviously higher than the mean load demand for urban traffic. Therefore the time average power demand in urban traffic is below the level at which good fuel economy of the prime mover is possible. This can be illustrated with the help of the efficiency curves of some internal combustion engines as used in vehicles.

Fig. 2.5. shows such a graph for a city bus diesel engine. From this figure, it can be seen that the optimal specific fuel consumption (200 gr/kWh) is achieved at high engine torque and at a demand of about half of the maximum power capacity.

The power demand of a city bus is highly variable which results in a low time average power demand. During a practical test cycle of a city bus the measured time average specific fuel consumption during this test was, including automatic gear box about 350 gr/kWh. Assuming a drive line efficiency of 80% [2.7], the time average specific fuel consumption without transmission losses is 0.8 x 350 = 270 gr/kWh. By running the engine at optimal specific fuel consumption, a reduction from 270 gr/kWh to 200 gr/kWh is still possible. This corresponds to an improvement in conversion efficiency of about 25%.
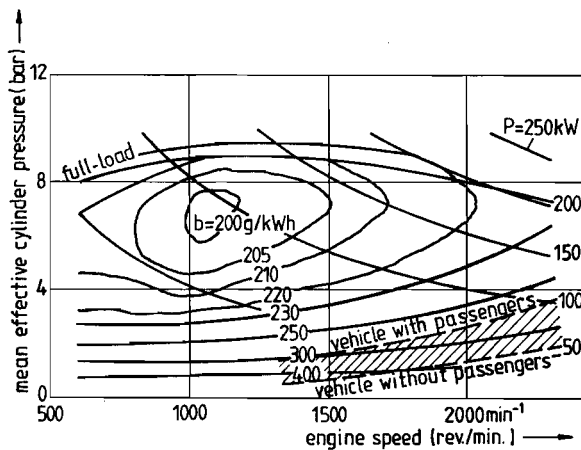
Fig. 2.5. Stationary load and fuel consumption characteristics of a city bus diesel engine [1.9].

For a passenger car with a gasoline internal combustion engine the load characteristics for different gear drives (horizontal plane, no appreciable head winds) and the specific fuel consumptions are illustrated in Fig. 2.6.

From this figure it can be seen that only in the E-drive, corresponding with high torque and high speed, the engine can be run near its area of optimum specific fuel consumption of 280 gr/kWh. In urban traffic, mainly corresponding with the 2nd and 3rd gear, the specific fuel consumption is at least 500 gr/kWh, including drive line losses. Taking into account a drive line efficiency of 90% for a manual gear box [2.7], the time average specific fuel consumption without transmission losses is 0.9 x 500 = 450 gr/kWh. With an optimal specific fuel consumption of 280 gr/kWh, an improvement in conversion efficiency of even 38% is possible then.

The above improvement of 38% for passenger cars will, however, in general not be achieved. In a city bus the engine can be rated for a constant supply of the average road load requirement for an urban cycle. However, a passenger car with energy storage equipment and intended for general purposes, needs an installed prime mover power which is higher than the average road load requirement for an urban cycle.

The engine size has to be 10-12 times higher than the average urban cycle power demand in order to have satisfactory hill climbing and high speed driving capacity [1.8].
The optimal specific fuel economy is achieved at high torques at 1/3 to 1/2 of the maximum power capability. Therefore the time average power demand for urban cycle operation has to be supplied by an on-off mode of the engine with sufficient high power to operate the engine with or near optimal specific fuel consumption. For practical reasons, (less on/off switching of the engine) the supply may be chosen at lower speed levels. This will result in a lower conversion improvement than the 38% derived earlier.
It is further assumed that the improvement in the conversion efficiency of prime movers for city buses and passenger cars is for both 25% and that all energy supplied by the prime mover goes via the storage system to the driving wheels with an "in/out" efficiency of the storage system of 80%. The energy saving by conversion improvement is then 0.8 x 25% = 20%.
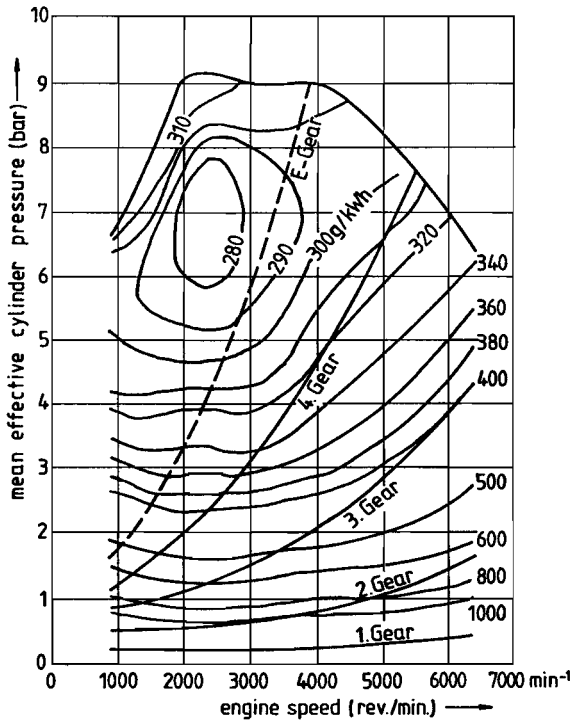
Fig. 2.6. Stationary load and specific fuel consumptions of a passenger car with gasoline engine and manual 4+E gear box [1.9].

Energy storage enables thus by combined brake energy recovery and conversion improvement, a total energy saving of 24% + 0.2 (100-24)% ≈ 40%.

2.3. Comparison of principles for regenerative energy storage systems

A complete energy storage system consists of a subsystem for energy storage and a subsystem for energy transmission. In mobile applications the recoverable energy concerns mechanical energy. From an efficiency point of view a minimum number of conversions is preferable. It would therefore be obvious to store and to transmit the energy in a mechanical way. But also other practical criteria covering the demands for mobile applications have to be considered such as weight and volume limitations, efficiency, durability, convenient component location, costs etc. Therefore several alternatives, for the storage subsystem as well as transmission subsystem, have been compared roughly with the help of former studies to these subjects [2.3] and [2.8].

2.3.1. Storage subsystem

In mobile applications the energy and power density, representing the energy and power with respect to weight and volume, need to be high. Therefore only chemical (batteries), potential (hydraulic accumulator) and kinetic (flywheel) storage elements are suitable, see also section 1.4. Main characteristic data of these storage elements for a rough comparative evaluation are shown in Table 2.1. [2.3].

Table 2.1. Comparison of energy accumulators for mobile applications [2.3].

Storage device / Criterion	Flywheel	Hydropneumatic accumulator	Electrochemical battery
Energy density (Wh/kg)	4 - 50	.6 - 4	20 - 100
(Wh/l)	10 - 50	1.0 - 4	40 - 150
Power density	++	++	-
Storage efficiency			
.short term	+	+	++
.long term	--	+	o
Efficiency of energy conversion	+	-	-
Cycle life	++	++	--
Overload capacity	+	+	--
Reliability	+	+	-
Maintenance free	+	+	--
Noise level (+:low)	+	+	++
Capital cost (+:low)	+	-	--

++ excellent
+ good
o moderate
- bad
-- very bad

From this comparison it appears that the flywheel characteristics meet the demands for mobile application in a most favourable way. The hydro-pneumatic accumulator follows being much heavier and much more voluminous. The electrochemical battery has the best energy density. However this characteristic is, for the mobile applications, being overshadowed by two main disadvantages, a poor power density and a limited service life. In another study [2.8] a theoretical comparison of the above three storage principles has been made for a complete energy storage system including transmission. The system is rated for 5 kWh energy storage capacity and 300 kW power capacity and is meant for train application. The different systems have been compared with respect to mass and investment costs. The results of this investigation are presented in Fig. 2.7.

Assuming the most optimal transmission for each storage system it can be concluded that again the flywheel is the most favourable energy storage means for mobile applications.

STORAGE CAPACITY 5kW/h ; MAXIMUM POWER 300kW ; ☐ SCATTERING RANGE
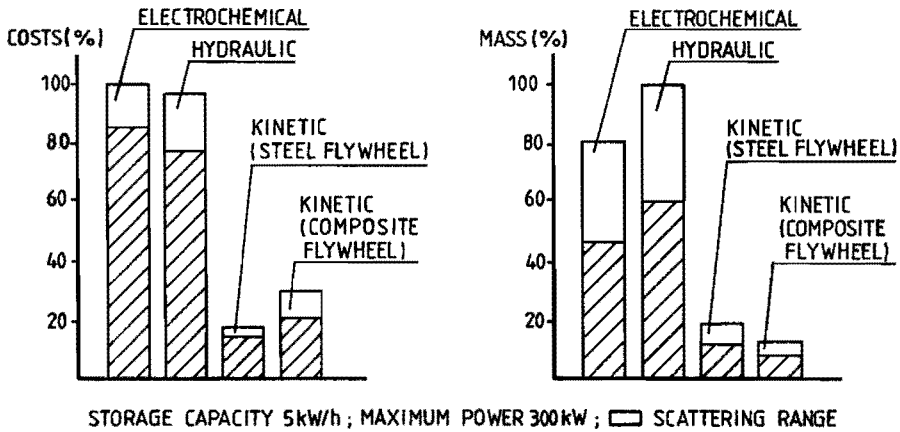
Fig. 2.7. Comparison of different energy storage systems, including transmission [2.8].

With the general conclusions of these orienting studies, still many flywheel variants are possible. These variants concern shape (e.g. disc, cylinder) and materials (metals, composites). This will be investigated further for the specific applications as considered later in this thesis.

2.3.2. Transmission subsystem

The transmission subsystem, which exchanges the energy between the storage subsystem and the rest of the propulsion system, has to be necessarily a continuously variable transmission (CVT) to match the different speeds of all involved components under all operating conditions. The flywheel shows a good adaptability to the mechanical, hydrostatic, electrical and power-split CVT as will be seen.

In [2.3] the mechanical, hydrostatic and electrical CVT have been compared and evaluated roughly in view of a set of practical criteria as shown in Table 2.2.

Table 2.2. Comparison of continuously variable transmissions [2.3].

Transmission type Criterion	Mechanical CVT	Hydrostatic pump/motor	Electric generator/motor
Power density (W/kg)	200-2000	1000-3000	50-200
Efficiency	.6 - .9	.2 - .8	.4 - .8
Durability	o	+	++
Overload capacity	-	o	++
Maintenance free	o	o	+
Control ratio	o	+	++
Controllability	-	+	++
Noise level (+: low)	+	-	++
Capital cost (+: low)	+	-	-

++ excellent
+ good
o moderate
- bad
-- very bad

The mechanical CVT considered in this comparison is a traction drive CVT (power transmission via friction), consisting of a metal V-belt (MVB) running over variable diameter V-pulleys. The MVB is a belt of thin trapezoidal transverse elements kept together by a number of thin endless steel bands which are embodied in the plate elements, see Fig. 2.8. As appears from a numerical evaluation [2.9], the MVB-CVT has, compared to other mechanical CVT types, the best compactness for higher torque and power ratings.
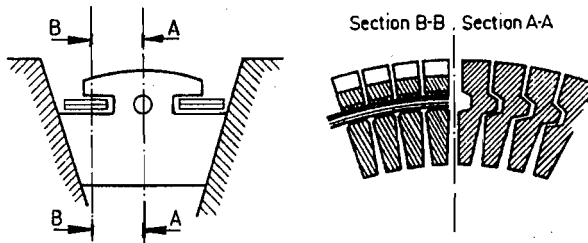
Fig. 2.8. Metal V-belt construction [2.9].

According to Table 2.2., the electrical CVT is the most advantageous one. However, power density, price and efficiency are not competitive with these of the MVB-CVT. It is noted that it is possible to obtain higher power densities and better efficiences for electrical CVT's as mentioned in Table 2.2. By the application of high speed synchronous machines with permanent magnet excitation in conjunction with a power electronic converter, electrical CVT's with power densities of 500-1000 W/kg and efficiencies of easily 0.8-0.9 are possible [2.10] and [2.11].
The hydrostatic transmission has an excellent power density but is according to this table not competitive, mainly because of the efficiency and noise production.

Another type of CVT which has not been considered in the above study is the power-split CVT. This type of CVT transmits mechanical power by the power-split principle. Most of the mechanical power is transmitted through a straight mechanical path with fixed ratio whereas only part of the power is sent through the variable ratio bypass. By reducing the power transmitted by the less efficient variable ratio path, the overall efficiency is improved. Splitting and adding of power flows is taken care of by a planetary drive. In this way the power-split CVT consists of a gear drive for the main power flow and a continuously variable bypass for the remaining power flow. The continuously variable bypass can be of the mechanical, hydrostatic or electrical type, see Fig. 2.9.

Besides an improved efficiency, other advantages of this concept could include a smaller CVT; extented ratio; one set of gears for forward and reverse operation; higher torque and power rating. The power-split principle enables in this way a modification of the characteristics of the pure CVT. This can make this principle very favourable as transmission subsystem for a flywheel.

\# Power flow reversible
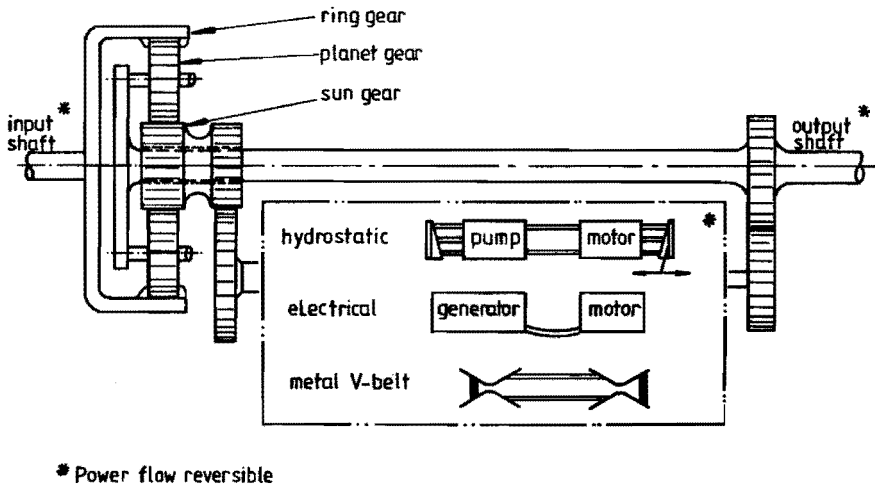
Fig. 2.9. Power-split CVT.

From the above rough consideration it can be concluded that the flywheel shows a good adaptability to all the discussed CVT types. It may be obvious that the specific application of the energy storage system needs also to be considered for making an unequivocal choice for the transmission subsystem. For instance in case of a vehicle with hybrid propulsion system the energy storage system has to be integrated in the main propulsion of the vehicle. When the main propulsion is of the mechanical type, the choice of an electrical CVT is less likely and vice versa.

The CVT evaluation will be worked out further on the basis of the specific applications as considered later in this thesis.

2.4. Realized regenerative energy storage systems

Regenerative energy storage systems for mobile applications, with the goal of energy and pollution reduction, are the subject of study already for a long time. As such, many systems have been evaluated theoretically but only a few have been built.

It is interesting to note that the realized concepts include all three kinds of storage principles (kinetic, hydropneumatic and electrochemical), which are in most cases combined with a commercially available hydrostatic or electrical transmission. In this section an overview of the most important systems is given. A more comprehensive description is given in [2.12].

2.4.1. Systems with kinetic energy storage

Flywheels have the ability to store kinetic energy and have, as such, been used in many vehicular and non-vehicular applications during the past 6000 years. They range from the ancient potter's wheel via the steam engine and punch press to the modern reciprocating combustion engine, all for smooth running. Also they range from small machinery such as flywheel driven toys, razors, drills and starters to very large installations. An example of the last one is the JET-project: Joint European Torus. Here the flywheel serves for pulsed power supply of a fusion reactor.

A historical overview of the most important regenerative flywheel systems for vehicular applications is given in Table 2.3. In most of these systems much attention has been paid for optimizing the flywheel with respect to energy density, whereas the transmission is an electrical, hydrostatic or power-split CVT, consisting of commercially available components.

Most of the older, before the 1980's, systems, e.g. the Oerlikon system and the Garret system for the New York subway, are based on conventional technology and proved to be technically successful but did not become a decisive economic success. The main objections were the energy and power density as well as the efficiency of the CVT subsystem which were too low for mobile applications. The later, after the 1980's, systems, e.g. the integrated flywheel-motor/generator units of Garret AiResearch and Magnet Motor, are based on advanced technology and show an improved energy and power density. However, until now they are not commercially available.

Table 2.3. Flywheel energy storage systems for vehicular applications.

Period	Producer	Application (HP1,HP2 or FFP)[1]	System principle	Main system data			
				flywheel mass (kg)	storage capacity (kWh)	power capacity (kW)	Ref.
Late 1880's	Commander Howell U.S. Navy	Torpedo missiles (FFP + stabilizing)	Steel flywheel with fixed ratio gear drive	160			[2.13]
Early 1910's	Italy U.S.R.R.	Mountain railway (HP1) Mine Locomative (FFP)	Steel flywheel Steel flywheel with hydrostatic transmission	44000 1650	34		[2.13]
Mid 1940's to end 1960's	Oerlikon, Switzerland	Mine Locomatives and city buses (FFP)	Steel flywheel directly coupled with squirrel cage M/G [2]	1500 (3000)[3]	6.4	140	[2.14]
Early 1970's	Garret AiResearch U.S.A.	New York R32 subway cars (HP1)	Steel flywheel coupled via planetary drive with M/G [2]	(2300)[3]	1.6	650	[2.15]
Mid 1970's Mid 1970's Mid 1970's	Volvo, Sweden Techn. University Aachen, Germany University of Wisconsin-Madison, U.S.A.	City bus (HP1) Minibus (HP2) Passenger car (HP1)	Steel flywheel with hydrostatic CVT Steel flywheel with power-split CVT (electrical bypass) Steel flywheel with power-split CVT (hydrostatic bypass)	330 100	1.75 0.13 0.5	225	[2.16] [2.17] [2.18]
Late 1970's Late 1970's Late 1970's Late 1970's	Daimly Benz, Germany M.A.N., Germany General Electric, U.S.A. Garret AiResearch, U.S.A.	Minibus (HP1) City bus (HP1) City bus (FFP) Passenger car (HP2) Postal vehicle (HP2)	Steel flywheel with power-split CVT (electrical bypass) Steel flywheel with power-split CVT (hydrostatic bypass) Steel flywheel, directly coupled with induction M/G [2] Composite flywheel with power-split CVT (electrical bypass)	105 1360 25	0.75 2.8 0.75	150 112 60	[2.19] [2.20] [2.21] [2.22 2.23]
Early 1980's Early 1980's Early 1980's	Garret AiResearch, U.S.A. British Petroleum, England University of Queensland, Australia	City bus (FFP) (UMTA bus) Self contained unit Passenger car (HP2)	Composite flywheel directly coupled with homopolar M/G [2] Composite flywheel with fixed ratio gear box Steel flywheel with power-split CVT (electrical bypass)	210 28(160)[3] 38	7.2 0.3 0.06	290 160 44.5	[2.31] [2.24] [2.25]
Late 1980's	Magnetmotor, Germany	City bus (HP1)	Composite flywheel integrated with permanent magnet M/G [2]	110 (460)[3]	1.8	160	[2.26 2.27]

[1] HP1 = Hybrid propulsion with flywheel and prime mover (or electrical supply).
HP2 = Hybrid propulsion with flywheel, electrochemical battery and prime mover.
FFP = Fully flywheel propulsion.

[2] M/G = electrical motor/generator.
[3] Total mass flywheel storage unit.

2.4.2. Systems with hydropneumatic energy storage

A regenerative energy storage system consisting of a hydropneumatic accumulator in combination with a hydrostatic transmission can be composed of commercially available components. As seen in section 2.3., the system will be heavier, more voluminous and less efficient than a kinetic energy storage system. In practice only larger vehicles can adopt the relatively large component weight and volume.

It may be for the above reasons that only two realized hydropneumatic energy storage systems are known. Both concern a storage system which is used in parallel with a diesel engine as regenerative propulsion system for a city bus. These systems are listed in Table 2.4. Prototype systems are being tested in practice. Fuel reduction, noise and maintenance requirements are, as yet, at unacceptable levels.

Table 2.4. Hydropneumatic energy storage systems for vehicular applications

Period	Producer	Application	System principle	Main system data			
				system mass (kg)	storage capacity (kWh)	power capacity (kW)	Ref.
Late 1970's	M.A.N., Germany	City bus (HP)[1]	High and low pressure accumulator, coupled via hydrostatic path of power-split CVT	800 [2]	0.200	220	[2.20 + 2.28]
Early 1980's	Volvo, Sweden	City bus (HP)[1]	High and low pressure accumulator, coupled via hydraulic motor/pomp	750	0.265	125	[2.29]

[1] HP = Hybrid Propulsion = Diesel engine and hydropneumatic system.
[2] Including 470 kg for main transmission.

2.4.3. Systems with electrochemical energy storage

Since the electrochemical batteries have limited power capacity and service life, their use is in general restricted to passenger cars and forklift trucks. Although many developments have been done on "pure" battery cars, it is not a decisive success. The main reason is that the power and energy storage capacity of the batteries are too limited to provide sufficient power and range of action needed for a general purpose car which should be suitable for highway operation, hill climbing etc.

The hybrid propulsion, consisting of an internal combustion engine with batteries, could offer a solution. Until now only three European manufacturers and an American University are known that have built hybrid propulsion systems in order to enable pollution free city cycle and congested traffic operation. See also Table 2.5.

From practical tests it was concluded that small improvements in fuel economy could be obtained while good improvements in emissions were possible. However the performance was reduced by the added weight, mainly due to battery weight. This as well as increased investment costs hinder, as yet, a sucessful introduction.

Table 2.5. Electrochemical energy storage systems for vehicular applications.

Period	Producer	Application (HP or FBP)[1]	System principle	Main system data			
				system mass (kg)	storage capacity (kWh)	power[2] capacity (kW)	Ref.
Early 1970's	Daimler Benz, Germany	Vans (FBP)	FBP: electrical motor/generator with battery.				[2.19]
		City bus (HP)	HP : diesel engine with battery, coupled via power-split CVT (electrical bypass)				
Early 1970's	University of Wisconsin-Madison, U.S.A.	Passenger car (HP)	Battery with electrical motor/ generator switchably coupled via planetary drive with i.c. engine and wheels	225 (battery mass)			[2.32]
Early 1980's	Alfa Romeo, Italy	Passenger car (HP)	Battery with electrical motor/ generator switchably coupled with conventional propulsion system	130		11	[2.30]
Mid 1980's	Volkswagen, Germany	Passenger car (HP)	Battery with electrical motor/ generator switchably coupled with conventional propulsion system	29 (excl. battery mass)		6	[2.31]

[1] FBP = Fully Battery Propulsion.
 HP = Hybrid Propulsion = I.C. engine and battery/electrical motor system.
[2] Electrical propulsion only for low power operation.

2.5. Conclusions

From the above literature research regarding regenerative energy storage systems for mobile applications, the following conclusions can be drawn:
- Regenerative energy storage has an important energy and emission reduction potential for urban traffic.
- The flywheel is the most favourable regenerative energy storage element.
- All CVT types are possible in conjunction with the flywheel. The most favourable CVT type depends upon the application of the flywheel energy storage system.
- Realized energy storage systems for vehicular applications are mostly composed of an energy density optimized flywheel component and a CVT consisting of commercially available electrical or hydrostatic components.
- An energy storage system as integrated flywheel/transmission system is a new approach in the development of these systems.

Summarizing it can be said that the development of a flywheel energy storage system with integrated and system optimized flywheel and CVT component, is a challenge to enable large scale application of these systems.

PART II

OPTIMIZATION

OF A

FLYWHEEL ENERGY STORAGE SYSTEM

FOR

MOBILE APPLICATIONS

Chapter 3

Starting points for the flywheel energy storage system

3.1. Introduction

From the literature research as presented in chapter 2, it appears that a flywheel energy storage system can meet the general demands made upon energy storage systems for mobile applications in the most favourable way, compared to other alternatives. In order to attain an optimized pilot system, the application as well as the quantitative demands made upon the energy storage system, have to be defined. These aspects are considered in this chapter.

3.2. Applications

The envisioned flywheel energy storage system should be a complete, self contained system, suitable for all kinds of mobile applications with strongly alternating power demands such as urban vehicles, hoisting and lifting devices and earthmoving equipment. Such a system is also suitable for stationary applications with high power demands such as uninterruptable power supply systems (U.P.S.) and load leveling systems in electric power systems. By these power regulation functions, this application is expected to become an economically attractive option for electric utilities [3.1].

As pilot applications for the envisioned flywheel energy storage system, city buses and commuter trains have been chosen:

- This investigation focuses mainly on the flywheel energy storage system itself. Passenger cars are general purpose vehicles. This implies more demands and complexity to the propulsion system than in case of pure urban vehicles. See also passenger car propulsions with energy storage systems as developed by Alfa Romeo, Volkswagen, Garret AiResearch and University of Wisconsin, section 2.4. The application in a pure urban vehicle is therefore more obvious.
- Urban vehicles such as city buses and commuter trains are the most effective vehicles for implementation of energy storage systems, see also section 2.2., and therefore also the best option to evaluate the practical effectiveness of energy storage systems in vehicles. However, for the quantitative energy and emission reduction, passenger cars are the most attractive candidates as they represent the major part of the energy demand for urban transport [1.10].
- An energy storage system for city bus and commuter train application has to be rated at such high specifications, e.g. energy and power capacity, that it is suitable in all large vehicles and by scaling down for smaller vehicles e.g. passenger cars.

3.2.1. City bus

The city bus application concerns a fully flywheel driven city bus in which the flywheel is charged by brake energy recovery and by the electrical supply at the bus stops. See also Photo 3.1. The flywheel supplies in turn the total propulsion energy for the bus. This enables for urban areas fully emission free public transport vehicles with the flexibility of the current diesel buses. Moreover the public urban transport can thus be made oil independent.

Photo 3.1. Charging of a fully flywheel driven city bus at the bus stop.

The performance of the fully flywheel driven city bus is determined as such that this bus can participate as a full value vehicle in the present and future city traffic and is in every way competitive with current city buses (both, diesel and trolley).
This leads to the following starting points for the bus [3.2]:
- City bus for maximum 80 passengers with a total mass, including passengers, of 17.5 tons.
- Maximum speed 70 km/h.
- Acceleration, fully loaded, on horizontal plane:
  0 - 18 km/h: constant acceleration (1.2 m/s^2);
  18 - 50 km/h: constant acceleration power (120 kW);
  50 - 70 km/h: decreasing acceleration power (inversely proportional with velocity).
- Deceleration, fully loaded, on horizontal plane:
  electrical brake: 70-50 km/h constant braking power (273 kW);
            50- 5 km/h constant deceleration (1.3 m/s^2).
  friction brake : up to 4.5 m/s^2.
- Rolling resistance 1.5% of total weight.
- Airdrag at 70 km/h: 1400 N.
- Recharging facilities: electrical (750V DC), by means of overhead contacts at the bus stops, see Photo 3.1.
- Bus stops: every 300 m to 600 m; on horizontal plane; stop time 15 to 20 s.

3.2.2. Commuter train

In the Netherlands the major part of the commuter trains uses electrical energy for propulsion and is supplied by overhead wire. See also Photo 3.2. The flywheel energy storage system is then used for on board brake energy recovery. Acceleration energy is supplied by the overhead wire as well as by the flywheel energy storage system. The flywheel energy storage system enables in this way energy and emission reduction, a less heavy loaded overhead wire system and reduction of brake wear and maintenance. Of course the flywheel energy storage system is also possible for energy management of a train with a diesel generator set for electricity supply instead of an overhead wire.
It is noted that in case of the electrical train, brake energy recovery via the overhead wire is technically a more simple option. However, this option will make stronger demands upon the overhead wire and power regulation system. Moreover the effectiveness will be strongly dependent on the train density.
The main specifications of the commuter train are [3.3]:
- Train (Netherlands Railways) with a total mass of 139 tons, including passengers.
- Maximum speed 120 km/h.
- Deceleration, fully loaded, on horizontal plane: electrical brake 0.7 m/s^2 and friction brake up to 4.5 m/s^2.
- Rolling resistance and airdrag:
 $3475 + 6x$ (train velocity [m/s] $+ 5)^2$ [N].
- Energy supply: electrical (1500 V DC by overhead wire).
- Start-stop distance: minimum 900 m; maximum 7400 m; on horizontal plane.
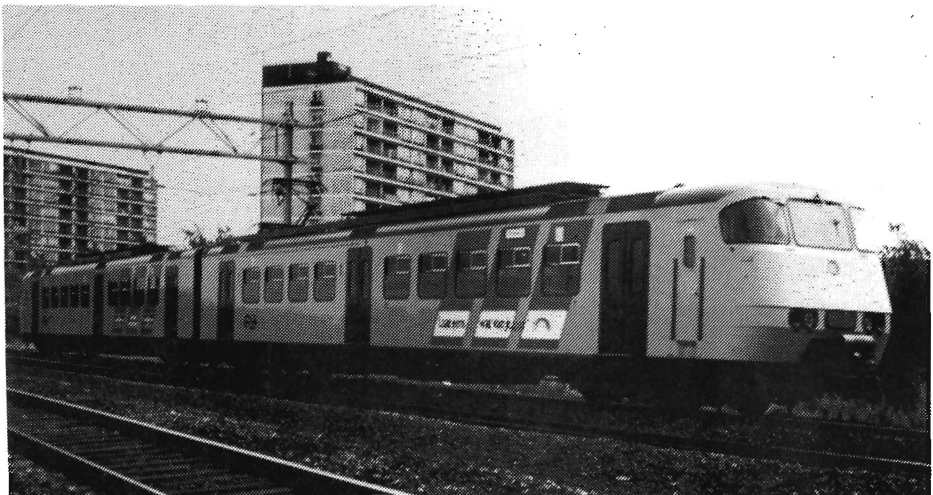
Photo 3.2. Commuter train of Netherlands Railways.

For practical reasons, costs and test facilities, the fully flywheel driven city bus has been chosen as first application. More data of this city bus, indicated as gyrobus, are given in appendix I: Specifications for a future gyrobus.

3.3. Quantitative demands

The quantitative demands, made upon the flywheel energy storage system for these applications, have been determined in such a way that one system unit can provide the gyrobus performance whereas four system units can provide the train performance. The quantitative demands are then [3.4]:
- Power capacity 300 kW continuous (determined by charging and recuperation demands).
- Energy storage capacity: 4 kWh effective (for gyrobus recharging after four 300 m or two 600 m driving cycles is possible; for train full brake energy recovery possible down from 100 km/h).
- Total system mass: 1000 kg (determined by mass of current diesel propulsion system).
- Dimensions: maximum system height 800 mm; diameter limited to 1000 mm.
- Overall system efficiency for charging or discharging: minimum 90%.
  At least 80% of the recoverable energy should be utilized to have acceptable energy and pollution reduction potentials, see also section 1.5.
- Service life: 10^7 load cycles needed to have an acceptable life time (at least 15 years) in a public transport vehicle.
- Electrical energy supply at 750 V DC.

3.4. Conclusions

The mobile application of a flywheel energy storage system is concerned with a short period storage of energy, a great number of load cycles, high power demands and moreover with weight and volume limitations. This makes strong technical demands upon these systems such as: high energy and power density which is the energy, respectively power capacity with respect to weight and volume; high conversion efficiency and a high service life. Optimization of a flywheel energy storage system with respect to these combined characteristics ought to make it possible to meet the quantitative demands mentioned above.

Flywheel energy storage systems for other vehicular applications than a train and a city bus have lower demands concerning energy and power capacity and can be derived by down scaling the pilot system.

Chapter 4

The flywheel component

4.1. Introduction

As was shown in section 2.3.1., the flywheel is most advantageous for regenerative energy storage systems with high and frequent power demands. Flywheel geometry as well as flywheel material offer many alternatives for the design and construction of the flywheel.

4.2. Flywheel geometries

The large variety of flywheel geometries can be categorized into a few basic types [4.1] and [4.2]. This allows the kinetic energy stored in a flywheel to be expressed as:

$$E_k = K.V.\sigma \qquad (4.1)$$

where
E_k = kinetic energy stored in flywheel
K = shape factor
V = material volume of flywheel
σ = maximum stress in flywheel

The above expression, which defines the K-factor, is valid if the conditions of axial symmetry and of plane stress can be assumed. The condition of axial symmetry applies for nearly all flywheel geometries. The condition of plane stress is quite adequate if the axial height of the disc is small compared with the diameter and if the height gradient along the radius is not too high.

The maximum energy stored per unit volume can now be written as:

$$e_v = K.\sigma_a \qquad (4.2)$$

and the maximum energy stored per unit mass as:

$$e_m = K.\frac{\sigma_a}{\rho} \qquad (4.3)$$
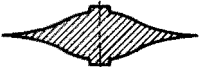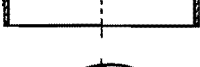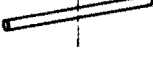
In these expressions
e_v, e_m = energy per unit volume, respectively mass
K = shape factor
σ_a = allowable material stress
ρ = mass density (assumed constant over flywheel volume)

Thus the K-factor can be described as a measure of utilization efficiency of the flywheel material and is also indicated as shape factor.

In Table 4.1. the main basic types of flywheel geometries are given with their K-factors as they apply for homogeneous isotropic materials with a Poisson's ratio v of 0.3.

The highest value of the K-factor, $K=1$, is achieved by the so-called "constant stress disc" or "Laval disc". This shape was developed by the Swedish engineer Carl de Laval for turbine discs. All the material is uniformly biaxially stressed such that the radial and tangential stress components remain at equal levels up to an outer radius of infinity.

Table 4.1. Overview of main flywheel geometries and their K-factors (for homogeneous isotropic materials) [4.2].

Flywheel Geometry	Cross-Section or Pictorial View	Shape Factor K	
Constant-Stress Disc (OD -> ∞)		1.000	
Modified Constant-Stress Disc (Typical)		.931	Suitable for
			Homogeneous
Truncated Conical Disc (Typical)		.806	Materials Only
Flat Unpierced Disc		.606	
Thin Rim (ID/OD -> 1.0)		.500	
Shaped Bar (OD -> ∞)		.500	Suitable for
			Homogeneous
Rim with Web (Typical)		.400	or Filamentary
			Materials
Single Filament Bar		.333	
Flat Pierced Disc		.305	

Also indicated in this table are the flywheel geometries that are suitable for composite (filamentary) materials. A derivation of the K-factor for these wheels has been made in [4.1].

When loaded by an uni-directional stress field (tangential or radial), the derivation and the K-factor are similar to those of flywheels of isotropic materials. This applies for the thin rim wheel (tangential stresses) and the shaped bar as well as for the single filament bar wheel (radial stresses). The thin rim wheel and shaped bar wheel are very good candidates for uni-directional composite material application as they exploit the high uni-directional strength of the fibres in an optimal way. This means that the K-factor of composite flywheels has a maximum value of 0.5, see Table 4.1.

All other configurations are loaded by a bi-directional stress field (tangential and radial stresses). In these configurations the strengths in the fibre directions are usually not a factor for failure, because of the poor strength capabilities perpendicular to the fibre directions. The K-factor, defined with respect to the longitudinal material strength, can then be derived taking into account Poisson's ratio and especially the amount of anisotropy given by the ratio between Young's moduli in tangential and radial direction. The K-factors derived in this way [4.1] are always smaller than those for flywheels of isotropic material and moreover also smaller than 0.5. This can be illustrated with the help of the derivation of the K-factor for a thick rim flywheel.

From the stress distribution and a failure criterium, the K-factor has been calculated as a function of the ratio inner to outer radius (r_i/r_o) and the material properties. The failure criterium concerns the radial or tangential strength depending on the ratio of inner to outer radius. The material properties concern Poisson's ratio ν_{tr}, the amount of anisotropy given by the ratio of Young's moduli in tangential and radial direction $\mu^2 = E_t/E_r$ and the ratio between tangential and radial ultimate strength $S = \sigma_{ut}/\sigma_{ur}$. The results are shown in Fig. 4.1.
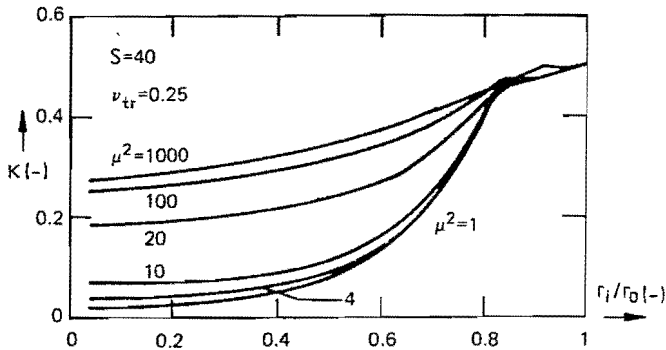
Fig. 4.1. K-factor for a composite thick rim flywheel [4.1].

From the above considerations it can be concluded that flywheels fabricated from isotropic materials (e.g. metals or cast glass; $K_{max} = 1$) have the potential for twice the specific mass energy density compared to flywheels made of filamentary composites ($K_{max} = 0.5$), assuming the same specific strength (σ_u/ρ) for both materials. However this specific strength is strongly determined by the choice of the flywheel material. At this point the composite materials are much more advantageous than metals as will be seen in the next section.

4.3. Flywheel materials

For high energy density flywheels, strong materials (enable high volume energy density), by preference with a low mass density (enable high mass energy density), are needed. Two basically different groups of materials are considered, isotropic and anisotropic materials.

a) Isotropic materials

Isotropic materials, e.g. steel, have been used extensively for the construction of flywheels and are still used for most common flywheel applications. Their specific strength (σ_u/ρ) is usually not very high due to their high mass density. However they are suitable for all basic flywheel geometries and allow with this K-factors up to 1, see Table 4.1.

In Table 4.2. some isotropic materials, suited for flywheel applications are listed. In this table also the fatigue strengths for 10^7 load cycles are given. The energy density of reliable rotors for long-term use has to be calculated with the time-dependent allowable stress which is the fatigue or creep strength. In this case the allowable stress concerns the fatigue strength for a cycle life of 10^7 cycles. The energy densities are calculated with these fatigue strengths for the maximum obtainable K-factor ($K = 1$).

Table 4.2. Relevant data for some isotropic flywheel materials (data gathered from [4.3], [4.4] and [4.5]).

Material data / Materials	Mass density (kg/m³)	Young's modulus (GPa)	Tensile strength (MPa)	Fatigue strength (10^7 cycles) (MPa)	Energy density (K=1)	
					volume (Wh/1)	mass (Wh/kg)
Ferro 360	7800	210	360	120	33.3	4.3
Maraging steel 18 Ni-400	8000	189.6	2337	765	212.5	26.5
Wrought steel 26 NiCrMoV 14 5	7800	210	950	550	152.8	19.6
Titanium 6AL-6V	4500	115	1186	662	183.9	40.8
Aluminium 7075-T6	2800	71.8	529	173	48	17.2

Since isotropic materials enable K-factors up to 1, it can be concluded from Table 4.2. that, in case of maraging steel, a maximum volume energy density of 212 Wh/1 is obtainable whereas in case of titanium a maximum mass energy density of 40 Wh/kg is obtainable.

b) Anisotropic materials

In respect of mass energy density, modern high strength composite materials are very attractive as flywheel material. These materials however have highly anisotropic properties, particularly if uni-directional composites are used. This anisotropy limits the choice in flywheel geometries and limits moreover the K-factor to a maximum value of 0.5 as explained in section 4.2.

The more usual choices for composite flywheel materials are epoxy materials reinforced with glass, aramid or carbon fibres. As is obvious, definition of the time-dependent allowable stresses of the composites is essential for developing reliable rotors for long-term use.

For this purpose fibre controlled designs, e.g. tangentially wound thin rim flywheels, and matrix controlled designs, e.g. tangentially wound thick rim flywheels, are distinguished. In fibre controlled designs the longitudinal fatigue data, respectively for the matrix con- trolled designs the transverse creep-strain (stress-rupture) data of the composite material are representative for the service life of the flywheel [4.6] and [4.7]. In general the precise data for this purpose have not yet been generated. However, it is possible to make a good estimate by adjusting longitudinal and transverse ultimate strength with a fatigue, respectively creep reduction factor (<1) to reflect the effects of the mentioned time dependency.
In Table 4.3. some characteristic data of uni-directional composites with different, most common applied, reinforcement fibres are given. The material data of these fibres, in particular the carbon fibres, are continuously being improved. This is shown in Table 4.3. for the tensile strength data of the carbon composites. A new type of fibre (Dyneema SK60, [4.8]), with as key properties high tensile strength, high modulus and low weight, has not been included in the table. The long term properties (creep-strain) of this fibre make it unsuitable for flywheel application. In the future even stronger materials may be considered like whiskers, extremely fine single crystal fibres with a superbly high strength (20,000 MPa). However, commercial applications of whiskers as a plastics reinforcement are not known yet.
The maximum energy density is obtained for K=0.5 and is, as this concerns a fibre controlled design, based on the fatigue strengths.

Table 4.3. Relevant data for some anisotropic flywheel materials.

Material data[a] Uni-directional composites (60% fibre vol.)	Mass density (kg/m³)	Young's modulus (GPa)		Tensile strength (MPa)		Allowable stress[3] (MPa)		Energy Density (//;K=0.5)	
		//[2]	⊥[2]	//	⊥	//	⊥	volume (Wh/l)	mass (Wh/kg)
E-glass	2000	45	10	1100	35	220	10	30	15
High modulus aramid	1400	75	5.5	1400	27	700	8	97	69
High strength carbon	1550	130	10	1400 2000[1b]	50	1100 1600	15	222	143
High modulus carbon	1650	220	6	1100 1728[1b]	40	850 1380	12	192	116

[1a] According to Nijhof (1983), [4.9]; [1b] According to Courtaulds (1989), [4.10].
[2] // = longitudinal; ⊥ = tranverse.
[3] Calculated from tensile strength: // using fatigue reduction factor for 10^7 cycles according to [4.11];
        ⊥ using creep reduction factor (0.3), according to [4.6] and [4.7].

From Table 4.3. it can be seen that high strength carbon composite enables the highest energy density with respect to the volume as well as the mass of the flywheel material, respectively 222 Wh/l and 143 Wh/kg. Further it can be concluded, by comparing Tables 4.2. and 4.3., that flywheels of E-glass composite are not competitive, neither in weight nor in volume, with strong metal flywheels.

4.4. Evaluation

The choices of flywheel geometry and material are closely associated with each other and have important design consequences. The optimal isotropic and anisotropic flywheel geometries, as they appeared from the preceding sections, have been evaluated on design consequences with starting points as given in chapter 3.

a) Weight and volume

The effective stored energy of a flywheel (E_{keff}) used within a speed range from ω_{min} (minimum angular velocity) to ω_{max} (maximum angular velocity) is given by:

$$E_{keff} = \frac{1}{2}.I_p.(\omega_{max}^2 - \omega_{min}^2) = \frac{1}{2}.I_p.\omega_{max}^2.\left[1 - \frac{\omega_{min}^2}{\omega_{max}^2}\right] \tag{4.4}$$

in which I_p is the polar moment of inertia.

The ratio $\omega_{min}/\omega_{max}$ is determined by the type of transmission. A very low ratio of $\omega_{min}/\omega_{max}$ puts serious demands to the transmission whereas the increase of effective energy is rather small. A reasonable compromise offers $\omega_{min}/\omega_{max} = 0.5$. For this ratio, as follows from eq. (4.4), 75% of the total stored energy can be extracted from the flywheel. According to the demands in chapter 3, the effective energy is rated at 4 kWh. With $\omega_{min}/\omega_{max} = 0.5$, this is 75% of the total storage capacity which is consequently 5.33 kWh. For this energy storage capacity the flywheel weight and volume are determined, for the optimal isotropic and anisotropic flywheel geometries, with the help of the data of Tables 4.2. and 4.3. The results are shown in the upper part of Table 4.4. In this screening the shaped bar geometry is not further considered because of practical limitations. These concern the large outside diameter dimension and the low energy density with respect to the swept volume.

From the first part of Table 4.4. it can be concluded that:
- Composite flywheels (of aramid or carbon epoxy) can be 2 to 5 times lighter in weight than metal flywheels for the same energy storage capacity.
- Composite flywheels (aramid or carbon epoxy) are equal or more voluminous than metal flywheels for the same energy storage capacity.

b) Speed

The circumferential speed v_c is directly determined by the choice of the flywheel geometry and material and can be calculated from the stress distribution. In case of the constant stress disc wheel (with a finite outer radius), the tangential as well as radial stress at any place in the flywheel is given by [4.1]:

$$\sigma = \frac{\rho.v_c^2}{2.\ln(h_c/h_o)} \tag{4.5}$$

Assuming $h_c = 4.5 \, h_o$ (height at centre about 4.5 times height at outer radius)
gives:

$$\sigma = \frac{1}{3} . \rho . v_c^2 \qquad (4.6)$$

In case of the thin rim wheel, the tangential stress is given by [4.1]:

$$\sigma = \rho . v_c^2 \qquad (4.7)$$

Together with equation (4.3), it follows that the circumferential speed is a measure for
the mass energy density for a given shape faktor K.

With the equations (4.6) and (4.7) and the mass densities and fatigue strengths as given
in Tables 4.2. and 4.3., the circumferential speeds as well as the angular speeds,
assuming an outside diameter of 0.8 m, have been calculated. The results are shown in
the middle part of Table 4.4.

From these calculations it can be concluded that:

- The circumferential speeds are high. As a consequence the flywheel has to operate in
  a vacuum environment in order to avoid high aerodynamic drag losses. Therefore the
  containment structure for providing personal safety, has to provide a vacuum
  environment as well.
- For optimized flywheels the composite ones, excluded glass epoxy, have about 1.5
  times higher circumferential speeds than the metal ones. This means larger diameter
  and/or higher angular speeds for composite flywheels than for metal ones.

c) **Dimensions**

Because of constraints on size for mobile applications also the height dimensions have
been calculated (outer diameter 0.8m assumed). In case of the constant stress disc (with
finite outer radius) this can be done with [4.1]:

$$m = 2.\pi.h_c.\frac{C}{\omega^2}.\left[1 - e^{\frac{-\rho.\omega^2.r_o^2}{2C}} \right] \qquad (4.8)$$

where
$\quad m \quad$ = flywheel mass
$\quad \rho \quad$ = mass density
$\quad h_c \quad$ = flywheel height at centre
$\quad r_o \quad$ = outer radius
$\quad C \quad$ = maximum (constant) stress
$\quad \omega \quad$ = angular speed

In case of the thin rim wheel:

$$m = \rho.\pi.h.r_o^2.\left[1 - \left[\frac{r_i}{r_o} \right]^2 \right] \qquad (4.9)$$

where
$\quad r_i/r_o \quad$ = ratio of inner to outer radius
$\quad h \quad$ = axial rim height

In these calculations the ratio of inner to outer radius is rated at 0.85. For lower ratios the material utilization is no longer optimal by which the K-factor decreases well below 0.5, see section 4.2. With the equations (4.8) and (4.9) and the mass densities and fatigue strengths as given in Tables 4.2. and 4.3., the heights of the flywheels have been calculated. See lower part of Table 4.4.

From this dimension calculation it can be concluded:
- A composite flywheel of glass epoxy is, because of its large dimensions, not possible for a flywheel energy storage system as specified in chapter 3.
- Metal flywheels occupy the swept volume (= volume of the rotating flywheel) by a factor 2.5 to 5 better than composite flywheels do. This means larger containment structures for composite than for metal flywheels, which reduces the weight advantage of composite flywheels related to metal flywheels. On the other hand, the containment weight is strongly influenced by the failure behaviour of the flywheel. Here the composite flywheel is much more advantageous than the metal flywheel, see also section e) next.

Table 4.4. Design parameters for some optimized flywheels of 0.8 m diameter and 5.33 kWh energy storage.

Flywheel 5.33 kWh; 0.8m diameter / Design parameters	Isotropic			Anisotropic		
	Disc wheel (constant stress, K=1)			Rim wheel (thin rim, K=0.5)		
	Metals			Uni-directional composites		
	Maraging steel	Wrought steel	Titanium	E-glass	aramid	HS carbon
Mass (kg)	201	272	131	355	77	54
Volume (l)	25	35	29	177	55	35
Speed Circumferential (m/s)	535	460	664	331	717	842
Angular (rpm)	13,000	11,000	16,000	8,000	17,000	20,000
Dimensions (outer diameter = 0.8 m) Disc height (mm)						
- at centre	84	114	100			
- at outer radius	18.5	25	22			
Rim height (mm) (inner to outer radius = 0.85)				1272	394	250

d) Flywheel attachment and dynamic problems

Isotropic materials, especially steel, have in comparison with anisotropic materials, a higher Young's modulus by which they exhibit smaller displacements due to centrifugal load, thus reducing the dynamic problems originated by asymmetrical deformations and simplifying some problems related to the flywheel attachment.

This difference in displacements is moreover enlarged by the difference in circumferential speed. The flywheel attachment for thin rim wheels is the more difficult since the only possible practical connection elements to a shaft are spokes or discs which all have a certain amount of flexibility and/or a hysteresis (friction in the material and in the connection areas). Considering rotor dynamics, hysteresis in high speed rotor constructions can cause instability at high rotational speeds, unless adequate measures concerning bearing damping systems are taken. For this reason a rigid rotor construction is preferred [4.12]. This is only possible with a thick rim construction. But as explained before, these geometries utilize the material in a more inefficient way ($K < 0.5$) which causes higher flywheel weights. On the other hand, a more efficient utilization of the swept volume is possible and by this smaller and lighter containment structures.

e) Failure behaviour

The failure behaviour is also closely related to the flywheel material. Isotropic materials show for all flywheel geometries a harmful failure mode in the way of fragmentation and "missile behaviour". This can be prevented by weight costing measures: safe design stresses and/or application of safety containment structures. The weight of the cylindrical shell for preventing perforation is at least equal to twice the flywheel weight [4.13]. The energy density of metal flywheels is of course further lowered by these measures.

Composite materials enable a relatively benign failure behaviour in the way of desintegration. This failure behaviour enables smaller safety factors and/or lighter containment structures than in case of metal flywheels. In [4.14] and [4.15] is shown that containment rings, able to prevent any fragment penetration of about half the flywheel weight, are possible. However, the above mentioned containment weights will be further raised by other requirements set to the containment structure, e.g. torque transfer during a flywheel failure, vacuum support and safe response to vehicle collision.

4.5. Conclusions

From the preceding considerations the following conclusions can be drawn:
- The advantages of the composite flywheels compared to the metal flywheels are the light weight construction (except glass expoxy) and the benign failure behaviour, whereas disadvantages are the more complex design consequences: bearing construction, flywheel attachment and rotor dynamic behaviour.
- Flywheels, not optimized with respect to energy density (fail safe stresses for metal flywheels and thick rim wheels for composite flywheels), can also be advantageous with respect to the consequently smaller containment weight and volume. This is made possible by the less strong safety function, respectively by a better utilization of the swept volume.

In this stage a choice is not made. Low as well as high stress metal disc wheels and thin as well as thick rim composite flywheels will be considered in the system optimization.

Chapter 5

The transmission subsystem

5.1. Introduction

The transmission subsystem is a critical part of the total flywheel energy storage system as it has to meet several stringent performance demands. The viability of the flywheel system depends strongly upon its characteristics.
From the rough comparison of several continuously variable transmission (CVT) alternatives (mechanical, hydrostatic, electrical and power-split) in section 2.3.2., it appears that all are possible in conjunction with the flywheel. For an unequivocal choice the specific application has to be taken into account. This is done in the next survey.

5.2. Performance demands

The most stringent performance demands made upon the transmission subsystem are in case of mobile application of the flywheel energy storage system. The following qualitative demands are required for this application.
- Continuously variable transmission (CVT) to match the different speeds of all involved components under all operating conditions.
- Large overall speed ratio range. As long as the ratio of flywheel and vehicle speed is within the overall speed ratio range, slip losses can be avoided.
- Bi-directional transmission of power to enable energy recovery.
- High transmission efficiency to enable a good energy utilization.
- Bi-directional torque control to enable a well controllable drive performance.
- High power density: the power capacity with respect to weight and volume has to be high to enable "on board" energy recovery.
- Convenient component location to increase the system versatility.
- Good durability and compatibility to enable a substantial energy and pollution reduction potential.
- Reasonable costs to enable large scale-application.

For stationary applications the weight and volume restrictions can be less stringent. The quantitative demands for the mobile applications in question are listed in section 3.3.

5.3. CVT types and drive system concepts

The mobile applications in question, city buses and commuter trains, concern electrical flywheel drive systems. Fig. 5.1. shows a schematic diagram of the basic concept of this drive system. In this configuration the flywheel can be charged, depending on the state (on/off) of the clutches, by the electrical motor and/or by regenerative braking. The wheels can be driven by the electrical motor and/or the flywheel.
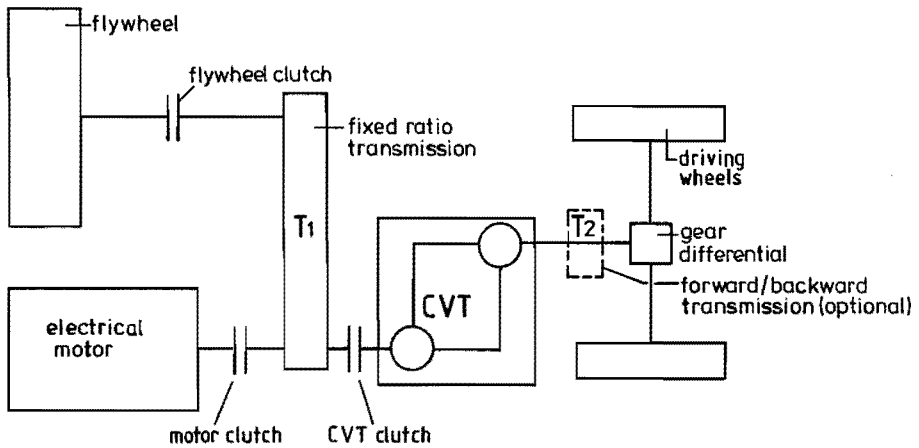
Fig. 5.1. Basic concept electrical/flywheel drive system.

Depending on the CVT type a number of constructive variations, mainly with respect to the packaging of the components, to this basic concept is possible. The extent to which the required characteristics, see also section 5.2., can be satisfied, depends strongly on the CVT type. This is considered next for the mechanical, hydrostatic, electrical and power-split CVT.

a) Mechanical CVT

The considered mechanical CVT concerns a traction drive CVT (power transmission via friction). The most favourable traction drive CVT concerns the variable ratio Metal V-Belt transmission (MVB - CVT) as explained in section 2.3.2. The MVB-CVT has recently become commercially available for passenger cars and is reasonable in terms of size, weight, ease of control and costs in production [5.1]. However, MVB-CVT's for the envisioned applications (300 kW, bi-directionally) are not available at the moment. The drive line lay out of the electrical/flywheel drive system based on the MVB-CVT, is according to Fig. 5.1. All components, flywheel, transmission and electrical motor are separately packaged and mechanically connected via shafts and couplings. The resulting non-flexible drive line lay-out is a serious disadvantage of this mechanical CVT concept. Another disadvantage is the speed ratio range of the MVB-CVT wich is limited with respect to the flywheel application. This means that, besides the usual transmission losses (micro slip and torque losses), additional slip losses will be generated as soon as flywheel speed and vehicle speed are out of the speed ratio range of the transmission.

These losses can be minimized by using a "pre-transmission" for shifting the CVT ratio range.

A wide ratio range can also be obtained by traversing the CVT ratio range twice. The drive train is shifted kinematically: what was the CVT output becomes the input thereby enabling the CVT ratio range to be traversed a second time. Shifting of the drive train is done by the use of couplings and requires complex functional requirements, e.g. an asynchronous shift.

A different approach for a mechanical CVT is the matching of speeds through a slipping clutch as proposed in [5.2]. This CVT consists of a 5-speed gear box in series with a two speed reduction unit that includes one or more clutches designed for continuous slip, see Fig. 5.2. By proper design such a CVT can have comparable characteristics as the more sophisticated MVB-CVT. A disadvantage of the concept is, however, the high frequency of gear shifting.
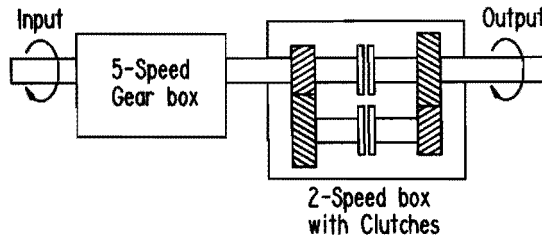
Fig. 5.2. CVT consisting of a 10-speed gear transmission with slipping clutches [5.2].

Coming back to the drive system concept, it is obvious that all mechanical transmissions inherently have a non-flexible drive line lay out. This restricts the versatility of the flywheel energy storage system.

b) **Hydrostatic CVT**

A straight hydrostatic CVT (pump/motor) will have certain distinct advantages such as: a good power density, a good versatility in packaging and hardware commercially available for the envisioned applications.

In case of the electrical/flywheel drive system, the hydrostatic CVT can be implemented in the drive line lay out as illustrated in Fig. 5.1., but offers also the possibility for a more flexible drive line lay out. The electrical motor, flywheel and one pump/motor can be combined in one package. This package can be located arbitrarily from the driving wheels. By using one hydraulic motor/pump for each driving wheel, the final drive differential can be eliminated.

Disadvantages are the additional mechanical/hydraulic energy conversions in the drive line, wich will negatively influence the total transmission efficiency and the inherently high noise production of this CVT type.

c) **Electrical CVT**

An electrical/flywheel drive system based on a purely electrical CVT consists basically of a motor/generator, directly coupled (for efficiency reasons) to the flywheel package, and a motor/generator coupled to the drive shaft. The flywheel machine and the traction machine are electrically coupled by a power electronic control circuit.

This concept offers a good versatility in packaging. It is possible to place one electrical machine in a hermetically sealed flywheel package that requires no rotating shaft seals, thus minimizing aerodynamic and seal losses. This configuration is illustrated in Fig. 5.3. Also a direct wheel drive via a wheel hub motor/generator is possible, thus offering a very large flexibility in drive line lay-out and convenient component location.
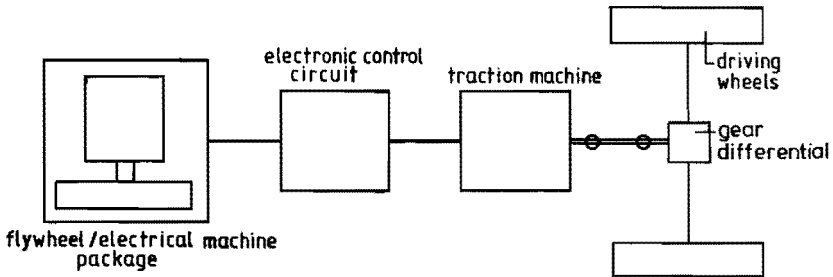
Fig. 5.3. Electrical/flywheel drive system based on a purely electrical CVT.

The inherently low power density of electrical machines can be increased by carefully choosing the right type and design of electrical machines. As mentioned in section 2.3.2., an advanced electrical CVT consisting of synchronous machines with permanent magnet excitation, has a raised power density and efficiency compared to a conventional electrical CVT. It is the high speed which is obtainable with this machine type that allows for these features. Also other favourable features with respect to speed ratio range, controllability, overload capacity, durability and convenient component location, make the electrical CVT very attractive for flywheel vehicles.

However, hardware for this CVT type with the required power range is commercially, until now, not yet available. A serious disavantage will certainly be the high production costs as some relatively expensive materials are required.

d) **Power-split CVT**
The power-split CVT transmits mechanical power, partially by a fixed ratio path and partially by a continuously variable ratio bypass (mechanical, hydrostatic, electrical). See also section 2.3.2. and Fig. 2.9. Compared to a pure CVT in which all the power is transmitted via a variable ratio path, advantages of the power-split CVT can include: improved efficiency, higher torque and power rating, smaller weight, less volume and extented speed ratio range. For a comprehensive description, see [5.3] where backgrounds and possible constructive designs of the power-split CVT with hydrostatic bypass are given.

The drive line lay-out of the electrical/flywheel drive system will depend on the type of bypass (mechanical, hydrostatic or electrical) in the power-split CVT. In case of a power-split CVT with a MVB-CVT or a hydrostatic CVT as bypass, the drive line lay-out will be according to Fig. 5.1. In case of the electrical CVT as bypass, the electrical motor for recharging the flywheel can be part of the bypass, if the power rating of the electrical machine in question is sufficient. Integrating the power-split CVT with the flywheel in a sealed package, as is the case with the purely electrical CVT, is however not possible.

Fig. 5.4. shows the scheme of this configuration. An additional gear reduction O_1 is necessary to couple the high speed CVT with the driving wheels. The disadvantage of non-flexible drive line lay out is also inherent to the power-split CVT.
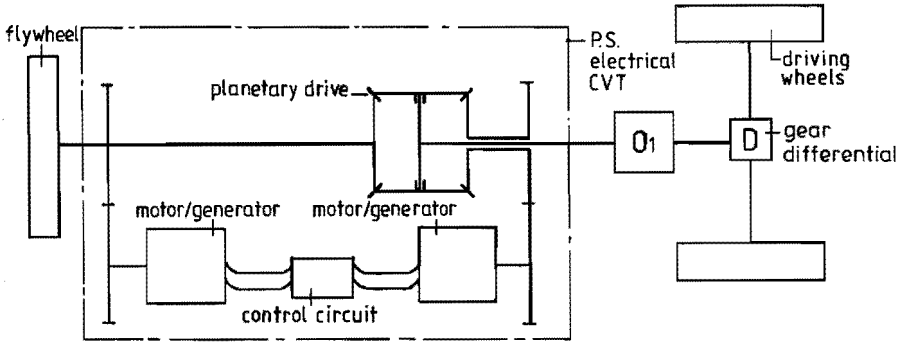
Fig. 5.4. Electrical/flywheel drive system based on a power-split electrical CVT.

Besides the considered power-split principle with the help of a planetary drive that takes care of splitting and adding of power, an electrical as well as a hydrostatic CVT offer another, relatively simple power splitting principle which does not involve the use of gears. Fig. 5.5. illustrates this principle, for the mechanical/electrical CVT. One of the electrical machines has a stator that is allowed to rotate. Both machines are mechanically directly coupled, either the rotor of the one with the rotating "stator" of the other (see Fig. 5.5.A), or the rotor of the one with the rotor of the other (see Fig. 5.5.B). In both cases the rotating "stator" is electrically coupled with the other electrical machine over slip rings. Thus the power can be transmitted mechanically and/or electrically. This mechanical/electrical CVT can be implemented as a relatively simple mechanical construction offering many advantages with respect to speed ratio range, controllability, durability and efficiency [5.4].
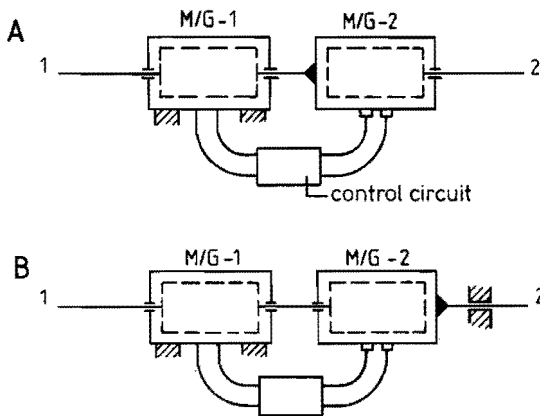
Fig. 5.5. PS-electrical CVT without gear drive.

The last power-split principle can be implemented hydraulically by connecting pump and motor together is one housing and allowing this to rotate [5.5]. There is some commercially available hardware of the mechanical/hydrostatic CVT type.
The drive line lay out for the power-split CVT without gears will be similar as shown in Figs. 5.1. and 5.4. for respectively the mechanical/hydrostatic and the mechanical/electrical CVT. This means that the main disadvantage of non-flexible drive line lay out remains as well with these power-split CVT types.

As follows from the above considerations, the major influence of the CVT type on the drive system concept for the electrical/flywheel drive system is the packaging and coupling of the components. This strongly influences the flexibility in drive line layout as well as the versatility of the energy storage system. For the envisioned electrical/flywheel drive system, the hydrostatic and electrical CVT are the most attractive options in this respect. The electrical CVT is the more attractive as it enables a flywheel/electrical machine package as an "electromechanical battery". Due to its favourable characteristics including an excellent controllability, overload capacity, durability and silent operation, such "battery" will have a high versatility in many mobile as well as stationary applications.
It is for this reason as well as for the newness aspects that the advanced electrical CVT is the most favourable transmission for the envisioned flywheel energy storage system. This choice is of course under condition of good energy prospects.

5.4. Energy evaluation

Besides vehicle and driving parameters, see section 2.2., also the CVT type will influence the energy prospects of a flywheel drive system. The energy influence of the CVT type and associated flywheel drive systems as considered above, has been evaluated for the envisioned city bus application.

5.4.1. CVT efficiency and speed ratio range

In case of the fully flywheel driven city bus, the energy reduction is realized with brake energy recovery. The influence of the CVT efficiency and speed ratio range has been evaluated using the energy reduction factor of the flywheel drive system. The energy reduction factor is the ratio of required propulsion energy with and without brake energy recovery.
The calculation of the energy reduction factor can be illustrated with the help of Fig. 5.6. This figure shows schematically the power profile associated with a 300 m and a 600 m city bus driving cycle. The power is given at the driving wheels (without transmission losses) and at the flywheel (with transmission losses).
As can be seen, the flywheel system for a city bus has to deal continuously with peak power demands. This puts stringent demands to the drive system, but is advantagous for the energy prospects of the flywheel drive system.
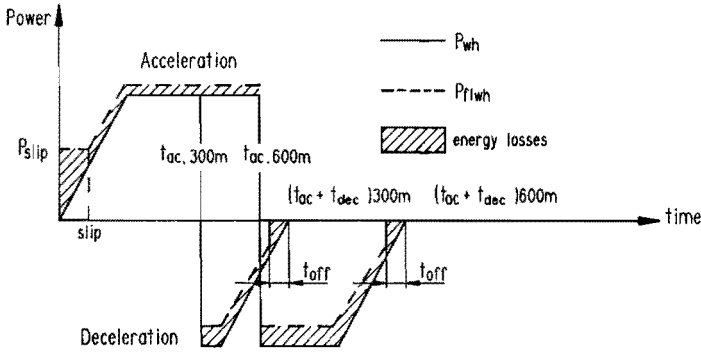
Fig. 5.6. Schematic power profile for 300 m and 600 m city bus driving cycles.

The required energy for a driving cycle to be supplied to the flywheel can be calculated with:

$$E_{flwh} = P_{slip} \cdot t_{slip} + \int_{t_{slip}}^{t_{ac}} \frac{P_{wh,ac}}{\eta_{tr,ac}} \cdot dt - \int_{0}^{t_{dec}-t_{off}} \eta_{tr,dec} \cdot P_{wh,dec} \cdot dt \qquad (5.1)$$

whereas the required energy for a driving cycle to be supplied to the driving wheels can be calculated with:

$$E_{wh} = \int_{0}^{t_{ac}} P_{wh,ac} \cdot dt \qquad (5.2)$$

In the above formula's, the following symbols are used:

E_{flwh} and E_{wh} = energy for a driving cycle, required at the flywheel (with recovery), respectively required at the driving wheels (without recovery)

P_{slip} = power related to slip losses in the transmission

$P_{wh,ac}$ and $P_{wh,dec}$ = acceleration, respectively deceleration power at the driving wheels

t_{ac} and t_{dec} = acceleration, respectively deceleration time in driving cycle

t_{slip} and t_{off} = time during which ratio of rotational speeds of flywheel and driving wheels is out of speed ratio range, respectively during acceleration and deceleration

$\eta_{tr,ac}$ and $\eta_{tr,dec}$ = overall efficiency of total transmission between flywheel and driving wheels, respectively for + and - torques; is dominated by CVT efficiency

It is further assumed that directly charging of the flywheel or directly driving the wheels is done by the same primary source of power and with the same transmission efficiency. The Energy Reduction Factor (ERF) of the drive system is then expressed by:

$$ERF = \frac{E_{flwh}}{E_{wh}} \qquad (5.3)$$

For an exact calculation of the energy reduction factor, the efficiencies have to be known at each operating point. In other words, the efficiency curves for + and - torques of the complete transmission have to be known. However, there is a lack of reliable component (especially CVT's) data concerning efficiencies and losses over the full range of operating conditions as occur in a flywheel drive system. In the further considerations the overall efficiency is for simplicity reasons assumed to be a constant load average efficiency being the same for bidirectional power flows.

The energy reduction factor can thus be presented as a function of the load average transmission efficiency with the speed ratio range as a parameter. This has been done for the city bus application with starting points as given in section 3.2.1. and appendix I. The influence of the speed ratio has been considered for a mean flywheel speed of 11,000 rpm. The results are presented in Figs 5.7 A. and 5.7 B. for respectively the 300 m and 600 m driving cycle.
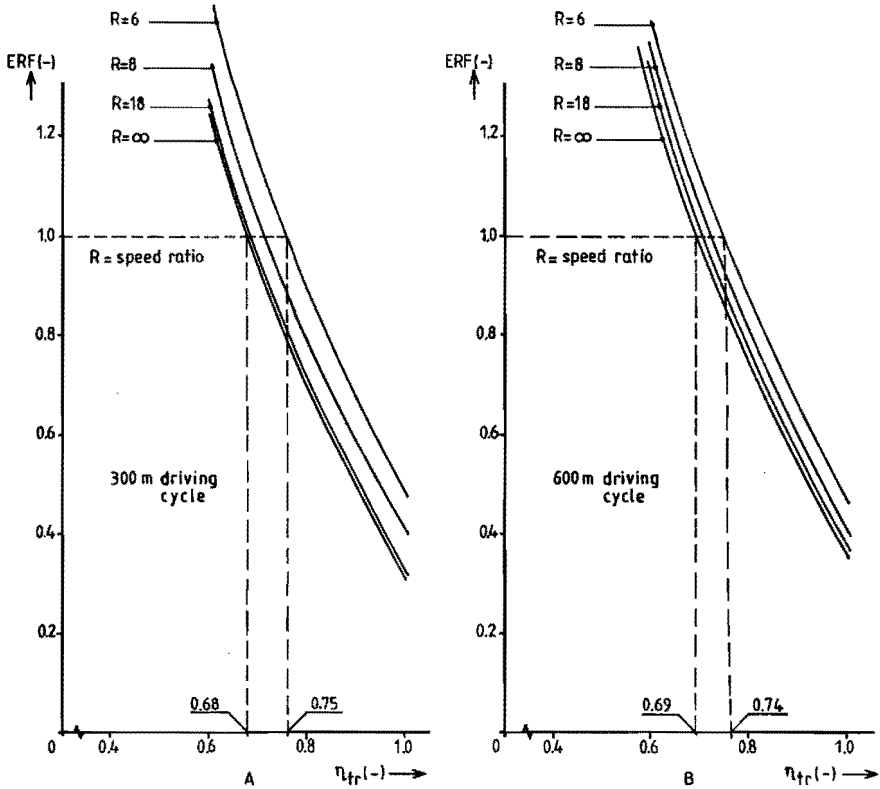
Fig. 5.7. Energy reduction factor for fully flywheel driven city bus as a function of the load average transmission efficiency.

From these figures it follows that:
- The energy reduction potentials for the 300 m and 600 m driving cycle hardly differ from each other.
- The energy reduction factor hinges on the load average transmission efficiency. The load average transmission efficiency has to be minimum 70 to 75% depending on the speed ratio range, to enable an effective brake energy recovery. This emphasizes the necessity of using CVT designs which are optimized with respect to efficiency.
- The speed ratio range does not influence strongly the energy reduction factor. Enlarging of the speed ratio range above 18 hardly improves the energy reduction.

5.4.2. Energy comparison of CVT types

With the help of Fig. 5.7. the energy prospects of the several CVT types have been evaluated on the basis of load average efficiency and speed ratio range of the total transmission between flywheel and driving wheels. In this way the CVT influence on the drive system concept is also taken into account.

Referring to the general drive system concept of Fig. 5.1., the overall transmission efficiency is calculated from:

$$\eta_{tr} = \eta_{flwh} \cdot \eta_{T1} \cdot \eta_{CVT} \cdot \eta_{diff} \tag{5.4}$$

where:
η_{tr} = overall transmission efficiency
η_{flwh} = transmission efficiency flywheel package
η_{T1} = transmission efficiency gear drive
η_{CVT} = transmission efficiency CVT
η_{diff} = transmission efficiency gear differential

The following data, which are uniform for all considered drive system concepts, have been used in this evaluation:
- Average cycle power : 125 kW.
- Flywheel package : operational speed range 7,500 to 15,000 rpm (for dimension reasons, see Table 4.4.); load average efficiency 0.98 (due to aerodynamic and bearing losses, derived from [5.6]).
- Gear drives : fixed ratio gear drives; load average efficiency 0.98 (adapted from [2.7] and [2.9]).
- CVT : characterized by a load average efficiency and a speed ratio range. The load average efficiency has a scattering range to evaluate its sensivity on the energy reduction factor.

a) **Mechanical CVT**
The mechanical CVT, based on the MVB-CVT is not currently available for the required power rating. Judging from the current state of development of this CVT type, the following assumptions for the energy evaluation may be done [5.7].
- Load average efficiency 0.85 - 0.95.
- Speed ratio range R = 8, symmetrical.
The load average efficiency of the total transmission is in case of the MVB-CVT calculated will the help of eq. (5.4). For an enlarged speed ratio range, e.g. 18, an additional gear drive is required, which lowers the overall transmission efficiency.

The alternative where the speed ratio range is enlarged by using twice the speed ratio range of the CVT, enables a considerable enlargement of the speed ratio range without lowering the overall efficiency. The resulting transmission efficiencies and energy reduction factors of these alternatives are represented in Table 5.1.

b) Hydrostatic CVT

A hydrostatic CVT for the required power rating is state of the art. The efficiency of a proper designed hydrostatic CVT can approximate the efficiency of the mechanical CVT [5.8]. However, for partial loads, under 30% of the maximum load, the efficiency will be considerably lower than the maximum efficiency [2.6]. In this consideration a properly designed hydrostatic CVT is assumed with:
- a load average efficiency ranging from 0.70 to 0.90.
- a speed ratio range of infinity.
The drive system does not necessarily have a gear differential, see also section 5.3. The overall transmission efficiency is then derived from eq. (5.4) but without considering a gear differential. The resulting overall transmission efficiency as well as the associated energy reduction factors are represented in Table 5.1.

c) Electrical CVT

The most favourable electrical CVT for a flywheel vehicle is based on synchronous machines with permanent magnet excitation. See also section 5.3. The electrical machines have to be independently coupled. This is done via a DC interconnection and two electronic converters for varying the electrical frequencies of each machine. The electrical machines [2.10] as well as the electronic converter [2.11] and [5.9] have high load average efficiencies, ranging from 0.90 to 0.95, respectively from 0.95 to 0.98. The electrical CVT is supposed to have the following characteristics.
- load average transmission efficiency varying from 0.75 to 0.85.
- speed ratio range infinity.
The drive system concept has, as explained in section 5.3., no gear drives. The overall efficiency is then the CVT efficiency influenced by the efficiency of the flywheel package. The resulting overall efficiencies and energy reduction factors are listed in Table 5.1.

d) Power-split CVT

The power-split principle enables modifying of the efficiency and speed ratio range of the pure CVT. The consequences of this CVT type for the energy effectiveness of the flywheel drive system have been considered for the PS-mechanical, PS-electrical and PS-hydrostatic CVT with the help of the derivations for efficiency and speed ratio range as given in Appendix II: A synopsis on PS-CVT's.

- PS-mechanical CVT
The considered PS-CVT is on the basis of a MVB-CVT with a planetary drive. The MVB-CVT has a load average efficiency of 0.85 to 0.95 and a speed ratio range $R=8$. Three modified speed ratio ranges have been considered $R=6,18$ and ∞. The conditions for the gear ratios for increasing or decreasing the speed ratio range of the MVB-CVT can be found with the help of Fig. II.3, respectively Fig. II.4 in appendix II. The gear ratios derived in this way are listed next.

Transmission ratio	Decreased speed ratio range, configuration C*	Increased speed ratio range, configuration B*	
	R=6	R=18	R=∞
i_o* planetary gear drive	-1	-3	-3
i_t* coupling gears	0,14	0,8319	1,4142

* See appendix II, Fig. II.2.

The resulting efficiencies of the PS-CVT's have been calculated with the help of the following formula, see also eq. (II.8) in appendix II.

$$\eta_{ps-cvt} = \frac{1}{1 + (1 - \eta_{MVB})(\frac{P_{MVB}}{P_{out}})} \qquad (5.5)$$

in which
η_{ps-cvt} = transmission efficiency PS-CVT
η_{MVB} = transmission efficiency MVB
P_{MVB} = power transmitted via MVB
P_{out} = power transmitted via output shaft of PS-CVT

The ratio (P_{MVB}/P_{out}) can be calculated with the help of the formulas given in Fig. II.2 of appendix II. In this way the PS-CVT efficiencies can be calculated as a function of the PS-CVT transmission ratio. For the considered driving cycles the load average power ratio $(P_{MVB}/P_{out}) = 0.8$, 1.5 and 2, respectively for a speed ratio range R = 6, 18 and ∞.

The associated drive system concept is according to Fig. 5.1. The overall transmission efficiency is derived from eq. (5.4.). The resulting overall transmission efficiency and associated energy reduction factors are represented in Table 5.1.

- PS-electrical and PS-hydrostatic CVT
From an energy point of view, the interesting option of these CVT types is improvement of the transmission efficiency of the pure CVT. The consequently reduction in speed ratio range is less significant because of the wider speed range capability of the pure CVT.
The most advantagous type in energy respect is the PS-CVT without gear drives. This PS-CVT type has negligable mechanical losses. See also section II.3. in appendix II.
The efficiency of the PS-electrical or PS-hydrostatic CVT without gear drive can be calculated from, see also Appendix II, section II.3.:

$$\eta_{ps-cvt} = \eta_{cvt} + i_{ps-cvt}(\eta_m - \eta_{cvt}) \qquad (5.6)$$

in which
η_{ps-cvt} = transmission efficiency PS-CVT
η_{cvt} = transmission efficiency pure CVT
η_m = transmission efficiency mechanical path
i_{ps-cvt} = transmission ratio PS-CVT

The further considered load average efficiency is based on an average transmission ratio of 0.4 as can be assumed for the considered driving cycles. The efficiencies of the mechanical path is assumed 0.98 as there will be some mechanical losses due to slip rings and bearings, see also Fig. 5.5.

The drive line layout can be according to Fig. 5.4. The resulting overall transmission is calculated then with the help of eq. (5.4). The resulting efficiencies and energy reduction factors are listed in Table 5.1.

Table 5.1. Energy evaluation of several CVT types for a fully flywheel driven city bus.

CVT-type	Load average efficiency	Speed ratio range	Overall transmission efficiency	Energy Reduction Factor	
				range	average
MVB	0.85-0.95	8	0.80-0.90	0.80-0.60	0.70
		18	0.78-0.88	0.76-0.56	0.66
		64	0.80-0.90	0.73-0.53	0.63
Hydrostatic	0.70-0.90	∞	0.68-0.86	1.0-0.58	0.79
Electrical	0.75-0.85	∞	0.73-0.83	0.85-0.65	0.75
Power-split MVB (with gear drive)	0.89-0.96	6	0.83-0.90	0.83-0.70	0.76
	0.81-0.93	18	0.76-0.87	0.82-0.58	0.70
	0.77-0.91	∞	0.72-0.85	0.87-0.59	0.73
Power-split (without gears) electrical	0.84-0.90	∞	0.79-0.84	0.70-0.60	0.65
hydrostatic	0.81-0.93	∞	0.76-0.87	0.80-0.58	0.69

From this table, it follows that from an energy point of view, the MVB-CVT and the power-split CVT without gear drive are most favourable. The other CVT alternatives have acceptable energy prospects, which are much the same.

It can further be seen that the allowable scattering range in load average CVT efficiency is relatively small in order to enable a reasonable energy reduction.

It is noted that in case of a hybrid propulsion, the energy reduction will be higher than calculated for a fully flywheel driven city bus. This is because of the conversion improvement of the prime mover. In case of a city bus with a hybrid propulsion, consisting of an internal combustion engine with a flywheel energy storage system based on a purely electrical CVT as considered above, the total energy reduction will amount more than 40% compared to a city bus with a conventional diesel propulsion [5.10].

5.5. Conclusions

From the preceding considerations, it follows that none of the considered CVT types combines all features as desired for a flywheel system. The purely electrical CVT is most favourable with respect to versatility, durability, speed ratio range, controllability and overload capacity. The PS-electrical (without gear drive) and mechanical CVT are most favourable concerning energy prospects.

In the case at issue a high system versatility of the flywheel system is required. It has to be suitable for vehicular and uninterruptable power supply applications. Only the purely electrical CVT allows for this system versatility while combining it with other excellent system features as controllability, overload capacity and durability. When using an electrical CVT, which is based on a synchronous permanent magnet machine, it is also possible to achieve a high power density and good energy prospects.

Chapter 6

Design alternatives for a flywheel motor/generator unit

6.1. Introduction

From chapters 4 and 5 it can be concluded that the combination of a flywheel and a synchronous permanent magnet machine enables a regenerative energy storage system with favourable characteristics concerning versatility, durability, controllability, overload capacity, packaging and energy prospects. By combining flywheel and electrical machine into one package, a general purpose electromechanical battery can be obtained.

Several design alternatives are possible to combine the flywheel and the electrical machine into a flywheel motor/generator unit. Design alternatives with metal disc wheels as well as composite rim wheels in conjunction with a permanent magnet machine have been considered.

6.2. Metal disc flywheel motor/generator unit

This concept consists of a metal disc wheel of the Laval type (see Table 4.1.), for reasons of efficiency and compactness directly coupled with a permanent magnet motor/generator. This machine type enables several lay-outs: radial field machines with cylindrical rotor as well as an axial field machine with a disc rotor [2.10].

The most compact flywheel motor/generator unit with a disc flywheel can be obtained by combining the disc wheel with a disc rotor machine. A prototype of this machine type has been realized by Weh [2.11]. This machine is constructed with two glass fibre reinforced plastic disc rotors with permanent magnets. It is rated at 280 kW power at a maximum speed of 7,200 rpm. The envisioned flywheel motor/generator unit has been based on this machine. The electrical machine determines the maximum speed of the unit and by this, for a given design stress, the diameter and height dimensions of the flywheel. The flywheel dimensions in the considered concept apply for 7,200 rpm and will therefore differ from those in Table 4.4., which apply for 8,000 rpm.

The flywheel and electrical machine are enclosed by a vacuum containment for reduction of the windage losses. This design requires no rotating shaft seals. The containment also has to provide personal safety and its weight will strongly depend on the adopted safety philosophy with respect to flywheel failure. Two alternatives have been considered: (1) a flywheel with high design stresses and therefore requiring a high containment weight and (2) a flywheel with low design stresses resulting in a minimum containment weight. The high design stresses are rated at 550 MPa (fatigue stresses for wrought steel). Higher design stresses for titanium and maraging steel result in unacceptable diameter dimensions with respect to vehicular applications. The low design stresses are rated at 300 MPa, which results in an infinite "life safe behaviour" of the flywheel and moreover in acceptable diameter dimensions.

These alternatives have been worked out in concept designs as illustrated in Figs. 6.1A. (high stress flywheel) and 6.1B. (low stress flywheel). The two disc rotor electrical machine can be constructed symmetrically with respect to the flywheel (Fig.6.1A.) or at one side of the flywheel (Fig.6.1B.)
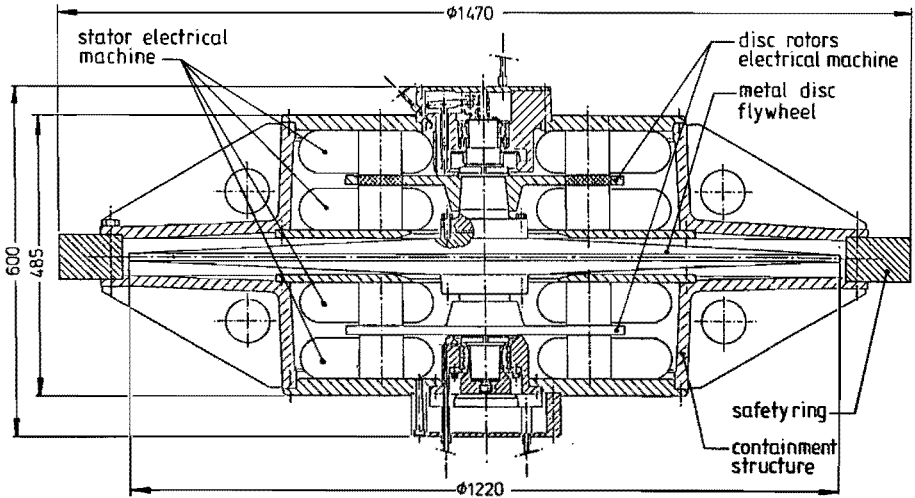
A. Unit with high stress flywheel
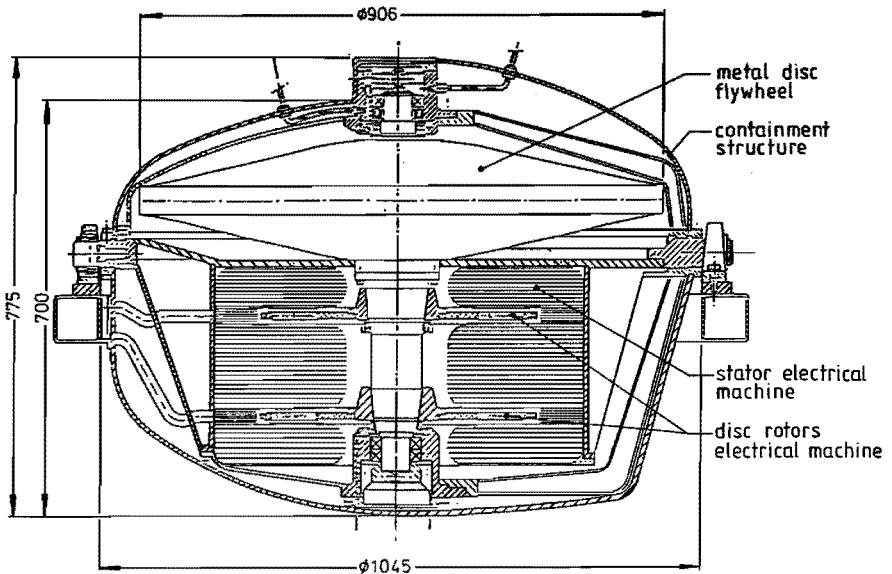
B. Unit with low stress flywheel

Fig.6.1. Design alternatives for metal disc flywheel motor/generator unit.

With the help of these designs the volumes and masses have been determined [6.1]. As containment material, steel and composite material (aramid), have been considered. The mass of the safety containment structure has been determined from former investigations into this subject [4.13]. An overview of the dimensions and the total masses of the various metal disc flywheel motor/generator units is given in Table 6.1.

Table 6.1. Dimensions and masses of various metal disc flywheel motor/generator units with 4 kWh net storage capacity and 300 kW power capacity.

Design alternative Main data	High stress flywheel (550 MPa)	Low stress flywheel (300 MPa)
Operating speed range (rpm) Dimensions (mm) Volume (m³) Mass (kg)	3,600 - 7,200 ø 1470 * 600 1.00 1486[1] 1236[2]	3,600 - 7,200 ø 1000 * 700 0.55 1270[1] 1205[2]

[1] steel containment; [2] composite containment

It can be concluded that for the considered metal disc flywheel motor/generator units:
- A low stress flywheel is more favourable concerning the total mass and volume of the unit, than a high stress flywheel.
- In conjunction with the electrical machine type, material stresses of more than 300 MPa result in diameter dimensions, which are unacceptable for vehicular applications. The only reasons for application of high strength metals like titanium and maraging steel as flywheel material for mobile application would be to win additional safety.

6.3. Composite rim flywheel motor/generator unit

This concept is an integrated flywheel system consisting of a high speed cylindrical flywheel, made of tangentially wound fibre composite with an electrical machine integrated in the hub of the flywheel. The electrical machine is of the exterior type (the rotor is outside of the stator), which enables very high rotational speeds. The considered design is based on a prototype, built by Canders [6.2]. This prototype was designed for a power of 100 kW at a maximum speed of 18,000 rpm. This machine type meets thus the speed demands for compact composite flywheels, see also Table 4.4. The flywheel, with integrated electrical machine is enclosed by a vacuum containment, which can be a light weight structure since the tangentially wound fibre rim wheels have a benign failure behaviour [4.14].
The flywheel machine attachment is one of the major construction problems as explained in section 4.4. It can be solved, depending on the rim geometry (thin or thick), in two basically different ways: spokes or disc elements when using a thin rim flywheel and direct mounting when using a thick rim flywheel. Both alternatives have been worked out in concept designs as illustrated in Figs. 6.2A. (thin rim flywheel) and 6.2B. (thick rim flywheel).
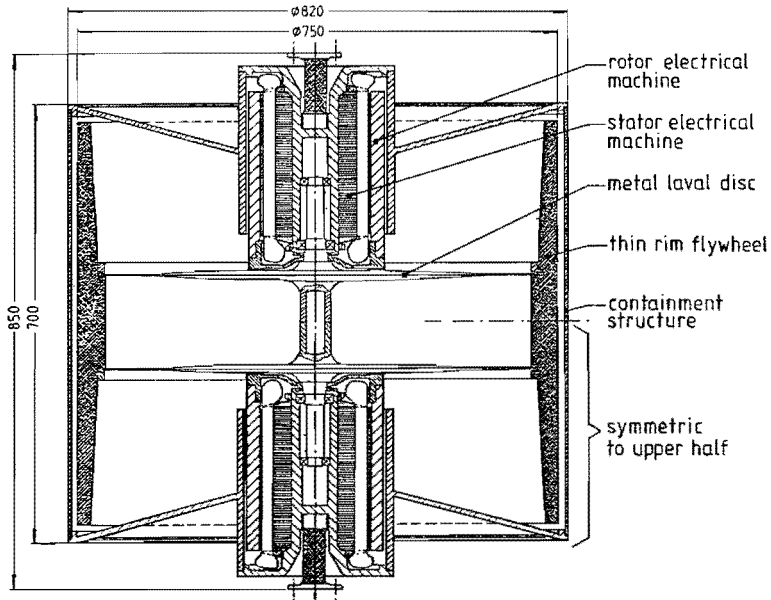
A. Unit with thin rim flywheel
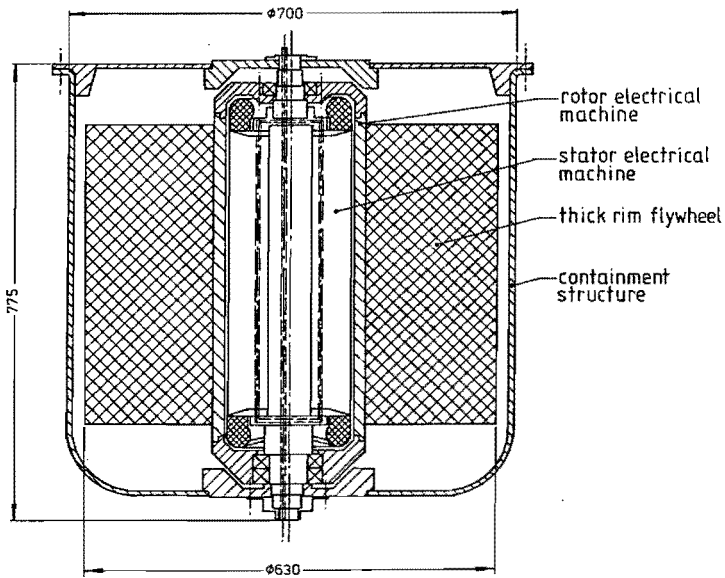
B. Unit with thick rim flywheel

Fig.6.2. Design alternatives for composite rim flywheel motor/generator unit.

The maximum rotational flywheel speed, determined by the electrical machine, is in both alternatives 18,000 rpm and is based on the prototype design of Canders. This means that, for this speed and a limited outside diameter of 0.8m, aramid is the best material choice concerning optimum material utilization, see also Table 4.4.

The thin rim flywheel can be attached to the machine rotor in a practical way, via two metal Laval discs which enable large outside diameters. By the difference in specific Young's modulus (Young's modulus with respect to mass density) between steel and composite material, there will be a difference in elongation caused by the centrifugal load, at the place of attachment of disc and cylinder. An elastic coupling or sliding joint has to compensate for this difference. As a consequence, the inherent damping or friction can cause instability for the higher speeds, unless adequate measures concerning bearing damping systems are provided, see also section 4.4.

Since the Laval discs cannot be pierced, it is not possible to situate the electrical machines between the discs. Therefore the discs have been situated close to the middle of the cylinder and are connected each with an electrical machine of 150 kW, see Fig.6.2A.

The other alternative, as illustrated in Fig.6.2B., is based on a rigid rotor construction which is preferable from a rotordynamics point of view, see also section 4.4. The flywheel is directly attached to the rotor of the inversely built electrical machine. In this way the swept volume is completely occupied by material. However as a consequence, the flywheel is a thick rim wheel and is thus subjected to tangential stresses as well as radial stresses. Special attention has to be paid to these radial stresses as well as the stresses in the flywheel/rotor attachment. There are possibilities to optimize the radial and tangential stress distribution in the flywheel, see also chapter 8.

With the help of these designs the volumes and masses have been determined [6.1]. The material of the containment is supposed to be aluminimum or composite material (aramid). An overview of the overall dimensions and total masses of the various composite rim flywheel motor/generator units is given in Table 6.2.

Table 6.2. Dimensions and masses of various composite rim flywheel motor/generator units with 4 kWh net storage capacity and 300 kW power capacity.

Design alternative / Main data	Thin rim flywheel (700 MPa)	Thick rim flywheel (radial stress determining)
Operating speed range (rpm)	9,000 - 18,000	9,000 - 18,000
Dimensions (mm)	ø 820 * 850	ø 700 * 775
Volume (m³)	0.45	0.30
Mass (kg)	550[1]	590[1]
	490[2]	545[2]

[1] aluminium containment; [2] composite containment

From this table it can be concluded that, for the considered composite rim flywheel motor/generator units, the unit with thick rim flywheel has a better compactness, caused by a better utilization of the swept volume, than the unit with thin rim flywheel.

This is however at cost, be it to a less extent, of the mass.
From a design point of view, the unit with thick rim flywheel is preferable because of rotordynamic behaviour (see section 4.4.) and failure behaviour. The thick rim flywheel encloses the rotating steel parts of the unit fully whereas the thin rim wheel will not be able to contain the rotating metal parts in case of a failure.

6.4. Evaluation

Several energy storage units have been compared concerning energy and power density and number of load cycles. Two of these units concern realized systems (see also section 2.4.1.): the Oerlikon flywheel accumlulator unit and the Garret flywheel accumulator unit for the New York subway. The others are the most advantageous of those considered above: the flywheel motor/generator units with low stress metal disc flywheel and with composite thick rim flywheel. All these energy storage units concern electromechanical accumulators. For comparison reasons the electrochemical accumulator (battery) is also considered in this evaluation. The results are summarized in Table 6.3. in which the absolute as well as, with respect to the Oerlikon accumulator, the relative figures are given.

Table 6.3.   Comparison of several electromechanical and electrochemical accumulators.

Characteristic data / Energy storage device	Energy density[1] (effective)		Power density[1]		Load cycles
	(Wh/kg)	(kWh/m³)	(W/kg)	(kW/m³)	
Electromechanical accumulators					
Oerlikon (section 2.4.)	2.1 (1.0)	5.1 (1.0)	47 (1.0)	112 (1.0)	10^7
Garret, New York Subway (section 2.4.)	0.7 (0.3)	2.0 (0.4)	283 (6.0)	812 (7.2)	10^7
Low stress metal disc wheel (Fig.6.1B.)	3.3 (1.6)	7.3 (1.4)	249 (5.3)	545 (4.9)	10^7
Composite thick rim wheel (Fig.6.2B.)	7.3 (3.5)	13.3 (2.6)	550 (11.7)	1000 (8.9)	10^7
Electrochemical accumulators[2]					
Lead acid	30 (14.3)	80 (15.7)	100 (2.1)	270 (2.4)	2.10^3
Natrium sulphur	100 (47.6)	270 (52.9)	150 (3.2)	400 (3.6)	10^3

[1] Electronic converter not included.
[2] Data derived from [6.3] and [6.4].
( ) Between parentheses relative values (base Oerlikon)

6.5. Conclusions

The results of the preceding considerations are summarized in Table 6.3. from which can be concluded that:
- The electrochemical accumulator has considerably better energy density than all other alternatives. However the power density and in particular the number of load cycles are not competitive with the electromechanical accumulators.
- The electromechanical accumulator with composite thick rim flywheel and integrated permanent magnet motor/generator has the best power density combined with a considerable number of load cycles. Moreover, the energy density of this alternative is far better than of the other electromechanical accumulators. This combination of characteristics makes it very attractive for short period storage with high and frequent power demands, e.g. in mobile propulsion systems of urban vehicles.
- Advanced technology is needed to meet the requirements for mobile applications.

This concept has further been designated as EMAFER:
Electro Mechanical Accumulator For Energy Reuse, an energy and power density optimized flywheel energy storage system for a great number of load cycles with high power demands.

MECHANICAL DEVELOPMENT

OF

ELECTROMECHANICAL ACCUMULATOR

FOR ENERGY REUSE

(EMAFER)

Chapter 7

Mechanical EMAFER design

7.1. Introduction

The preceding optimization of a flywheel energy storage system for mobile applications has led to the EMAFER concept: Electro Mechanical Accumulator For Energy Reuse. This concept includes a flywheel motor/generator unit controlled by an electronic power converter. Advanced technologies are used for the flywheel (composite material), the motor/generator (synchronous permanent magnet machine) and the converter (high frequency Gate Turn Off thyristors).
The mechanical design of the flywheel motor/generator unit is presented in the following sections.

7.2. Overall design

The concept of the flywheel motor/generator unit of the EMAFER system is illustrated in Fig.7.1. and is characterized by:
- Integrated construction of flywheel and electrical machine.
- A high speed thick rim flywheel, made of tangentially wound fibre composite. Modularity of energy capacity as well as improved failure behaviour are achieved by the application of disc modules.
- A high speed permanent magnet electrical machine for the transmission of power, integrated in the hub of the flywheel. The electrical machine is of the exterior type: the rotor is outside the stator.
- The flywheel is mounted directly on the rotor of the electrical machine. Special measures are necessary for the reduction of the radial stresses in the thick rim flywheel (see also section 7.3.) and the prevention of high speed rotor instability (see also section 7.5.).
- The rotor of the electrical machine has permanent magnets and allows, because of its simple construction with no material means for supply or drain of energy, for very high rotational speeds. The stator is the central part of the construction and forms a closed system to or from which electrical energy, cooling liquid and lubrication oil are transported. This is done via the hollow journals at the stator ends, see also section 7.4.
- The bearing system is based on high speed ball bearings, see also section 7.6.
- The total flywheel/electrical machine combination, including the bearing system, is enclosed by a vacuum containment for both safety reasons and minimizing of the windage losses, see also section 7.7.
- The unit is mounted in a cardanic suspension for preventing the bearing loads due to gyroscopic effects.
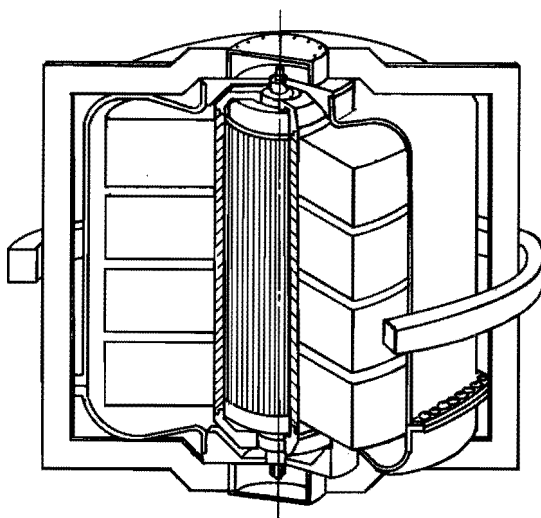
Fig.7.1. EMAFER flywheel motor/generator concept.

7.3. Thick rim composite flywheel

In the EMAFER concept the inertia is formed by a set of tangentially wound thick rim flywheels (disc modules), directly mounted on the steel rotor of the electrical machine. The thick rim composite flywheel offers: a fairly high energy density with respect to mass and volume, combined with a relatively simple and effective rim-hub attachment. As the flywheel material is not at equal distance from the axis of rotation, each subsequent annular element tends to stretch more than the previous one. For this reason this type of flywheel is subjected to radial tensile stresses which, although much smaller than the tangential ones, can cause failure of the rotor due to the very low radial tensile strength of the material.

From the literature there are three principally different ways known to reduce the radial stresses in the wheel. These are in a nutshell:

a) Varying the material properties with the flywheel radius.

The principle of this method is reduction of the radial stretching of the flywheel material and its variation along the flywheel radius by raising the specific Young's modulus (Young's modulus with respect to mass density) with increasing flywheel radius. This principle can be executed in several ways.

- Varying the mass density and/or the fibre content of the composite material and/or the winding angle of the fibre with the tangential direction, all as a function of the flywheel radius.

- Dividing the rim in concentric annular elements of different materials.

b) Applying prestress effects.

The principle of prestressing the material is to reduce the radial tensile stresses due to centrifugal load with the amount of applied radial compression stress in the flywheel.

This principle can be executed in several ways:

- Shrink-fit prestressing.

- Variation of winding tension as a function of the radius.

c) Avoiding radial stress transfer.
This can be realized by composing the ring of concentric annular elements separated by elastic layers.

All the above principles and methods have been considered further in chapter 8, see section 8.4. From these considerations the following two methods have been investigated further for the EMAFER concept: the variation of winding tension as a function of the flywheel radius and varying of the specific stiffness by using different materials. The other alternatives have not been considered further because of their tendency to reduce the energy content of the flywheel and problems related with the rim-hub attachment.

7.4. Synchronous permanent magnet motor/generator

The most promising machine type for driving a high speed flywheel is the synchronous permanent magnet machine of the exterior rotor type, see chapter 5. The design of this machine has been extensively reported in [7.1] and has been outlined here.
A section of the projected permanent magnet machine is shown in Fig. 7.2.
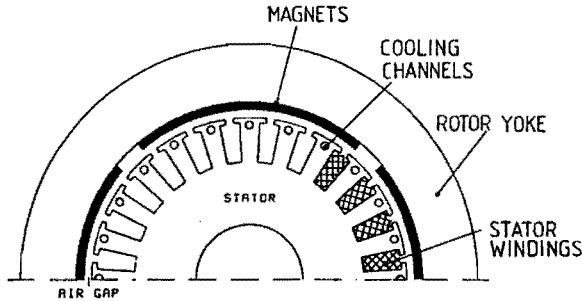
Fig.7.2. Section of electrical machine [7.1].

The rotor consists of a steel cylinder, on the inner surface lined with permanent magnets. There are no material means needed for supply or drain of energy to or from the rotor, thus enabling very high rotor speeds and high power density.
High grade permanent magnets like Samarium-Cobalt or Neodymium-Iron-Boron magnets, in a radial orientation, enable a high air gap induction with only a few mm magnet height. The iron for the magnetic circuit in the rotor is taken primarily for its mechanical strength. The chosen rotor material (26NiCrMoV145), a kind of wrought steel, shows both good mechanical and magnetic qualities.
Concerning the magnets, the number of poles is very important since the switching frequency of the converter is directly connected to this number. A 2 pole machine would be ideal from this point of view. However, the rotor yoke height in a 2 pole machine has to be about twice the yoke height in a comparable 4 pole machine and the resulting rotor weight will not be acceptable. A 4 pole machine is still feasible within the allowable rotor weight and available dimensions.

The higher switching frequency for the machine, twice the frequency as compared to a 2 pole machine, is possible with modern power electronic devices (GTO's). A description of the converter that has been developed for the flywheel drive is given in [7.2].

Since the machine has to operate at high speed in an evacuated environment, practically all conventional methods to cool the rotor are eliminated. Special attention has been paid to reduce any rotor losses, surface loss in the permanent magnets and eddy current loss in the solid rotor iron, to a minimum.

With motion of the magnets relative to the stator slots, the induction variations cause eddy currents in the magnets. This surface loss has been reduced by a kind of "lamination" of the rotor poles. The other source of rotor losses, the eddy currents in the solid iron of the rotor yoke, is caused by the non-sinusoidal nature of the feeding current which is unavoidable with the type of converter used. These losses have been reduced by lining the magnets with an electrically conducting material (copper sheet). With the measures taken, the total rotor losses can be reduced to less then 0.2% of the transmitted power [7.1]. This loss has to be removed via radiation and some convection to the stator and containment surfaces, see also section 7.7.1.

The stator consists of a conventional iron lamination stack with slots for a three phase winding. The laminated iron forms the magnetic circuit in the stator and the material is chosen for minimum core losses. The iron core is enclosed by a composite sheeting and thus forms a closed system to or from which electrical energy, cooling liquid and lubrication oil are transported. This is done via the hollow journals at the stator ends.

The major part of stator loss is the iron core loss. The motion of the magnets relative to the stator slots will cause eddy currents in the stator iron surface. The core loss will mainly depend on the rotational frequency of the machine. The only way to minimize this loss is a sufficiently fine laminated core of the right material. In this way the core loss is expected to be about 5 kW at maximum speed [7.1].

The other source of loss is the resistance of the stator winding. In those parts of the winding embedded in the stator iron, skin effect and proximity effect can become very large at high rotational frequencies in a poorly constructed winding. An elegant solution against the skin effect has been found by subdividing the winding into a great number of small wires. Experiments have shown that with the right construction of the winding, the skin effect can be practically eliminated [7.1].

Nevertheless a cooling system is required to remove the stator loss which is the major electrical loss in the machine. This loss has been minimized to achieve a high machine efficiency and to reduce the necessary cooling capacity. This capacity is provided via a closed liquid cooling system which limits the temperature of the stator surface below 50°C in order to prevent heating of the rotor from the stator. Therefore the cooling channels in the stator iron are positioned in the stator teeth, see Fig. 7.2. Choice of the right channel dimensions allows for sufficient cooling capacity while not disturbing the magnetic circuit too much.

This machine type thus enables a compact high speed machine with a high electrical efficiency of about 98% at maximum power capacity. However, the main disadvantage is the non-controllability of the field. The varying frequency of the machine implies varying voltages thereby making extra demands on the converter.

Also because the field cannot be switched off, there will always be losses in the iron of the stator when the machine is running. Thus, the permanent magnet machine is mostly suited for driving a flywheel used in an energy storage system with relatively short cycles.

7.5. Flywheel-electrical machine attachment

The attachment of a composite rim flywheel to a steel shaft or any other inner element (at issue is the rotor of the electrical machine) for suspension and driving is a major problem in a flywheel construction with respect to:
- Radial elongation differences at the connection interface of flywheel and inner element.
- Dynamic stability of the flywheel.

Radial elongation differences
In general the radial displacement due to centrifugal load at a cylindrical connection interface, provided that nowhere in the material radial stresses are present, is given by:

$$U_i = \rho_i \omega^2 r^3 / E_i \tag{7.1.}$$

in which: i = indicates the material ; ω = angular speed;
         U = radial displacement   ;   r = radius of connection interface;
         ρ = mass density   ; E = Young's modulus.

A composite rim flywheel will show higher radial displacement at the connection interface than the metal inner element. In case of a thin rim flywheel this is due to the smaller radius of the inner element. In case of a thick rim flywheel this is due to the ρ/E-ratio, which is for the inner material of the composite rim generally higher than for the metal inner element. The high ρ/E-ratio of the inner material of the rim is required to prevent high radial tensile stresses in the rim, see also section 7.3.
A variety of solutions has been proposed for the rim-shaft coupling which accomodate this difference [4.1]. For the thin rim the coupling is implemented via a disc or a spoke system, for the thick rim via an elastomeric layer. All these elements must accomodate this difference of radial displacement without exerting strong radial stresses which implies elastic coupling elements or sliding joints. As a consequence, the low radial stiffness of the flywheel can cause undesirable natural frequencies. Moreover material damping or friction in these coupling elements can cause rotor instability, see next paragraph.
The other solution for matching the radial elongation differences is with the help of a press fit at the connection interface. Depending on the extent of the press fit this coupling is able to accomodate the elongation difference at the connection interface up to a certain speed. The radial compressive stresses that attend this press fit can in addition be exploited to reduce the dangerous radial tensile stresses in a thick rim flywheel. The radial compressive stresses in the connection interface affect the cycle life of the flywheel positively.
With an increasing flywheel speed the hoop stresses caused by the press fit will decrease whereas the hoop stresses caused by the centrifugal load will increase with as a result, that the hoop stress amplitude will show little variation with flywheel speed.

Dynamic stability of the flywheel
The dynamic stability of a flywheel rotor depends highly on the ratio that the material damping bears to the inner damping of a system [7.3]. The inner damping can be caused by friction in rotating sliding joints or by rotating material damping. The material damping is also called structural damping of the rotor.

Several damping mechanisms can be responsible for the material damping, such as damping of the rotating shaft material, damping of rotating elastic coupling between shaft and rotor, or the air gap between rotor and casing. The damping in the non rotating parts of a system is responsible for the outer damping.

The two types of damping have different effects on the rotating system. The influence of the outer damping is well known: it always reduces the resonance amplitude of the oscillating system and has a stabilizing effect. Rotating material damping on the contrary can have a destabilizing effect [7.3] and [4.12].

This effect can be illustrated with the help of a "Laval Rotor" with inner damping (δ_m) and outer damping (δ_o), see Fig.7.3. (Section 9.5. gives an extensive consideration on this subject).
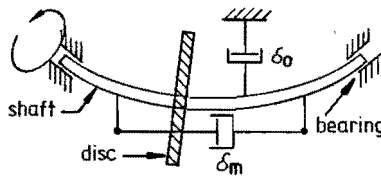
Fig.7.3. Dynamic model of a Laval rotor [4.12].

The stability characteristics of this rotor can be presented on a stability map, see Fig.7.4.
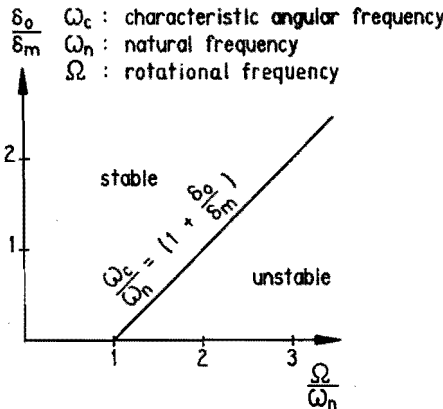
Fig.7.4. Stability map of Laval rotor [4.12].

In this map a characteristic angular frequency

$$\omega_c = (1 + \delta_o/\delta_m) * \omega_n \qquad (7.2)$$

is defined.

This characteristic angular frequency divides the area of the possible working orders of the rotor into a stable and an unstable region. In this way the shaft coupling of a flywheel may, depending on the stiffness and damping characteristics of the coupling and of the surroundings, move the flywheel operating area into the unstable region of the stability map and thus lead to the destruction of the system.

For this reason sliding joints and relatively weak coupling elements consisting of spokes, discs or an elastomeric intermediate layer, which are all favourable elements for compensation of elongation differences, are inadequate from a dynamic stability point of view. A rigid flywheel coupling with minimized damping characteristics is preferred. A press fit as attachment method for a composite rim flywheel is in this way favourable for both matching of elongation differences as well as preventing of dynamic instability.

Press fitting for a thick rim flywheel is possible by shrink fitting, conical interfaces and by pretension winding techniques. For a thin rim flywheel a modified press fit can be realized by fitting on a spoked hub, slightly oversized, so that it assumes a subcircular shape of the rim [7.4]. In the EMAFER concept the press fitting is provided by pretension winding techniques and by conical interfaces, see chapter 8, sections 8.5.1. and 8.6.1.

The above flywheel attachment problems apply also for the rotor cylinder/bearing attachment in the electrical machine. In the EMAFER concept this attachment is therefore provided via an S-shaped flange construction, see Fig.7.5. The S-shape separates more or less inner and outer bore with respect to centrifugal expansion while providing sufficiently large radial stiffness.
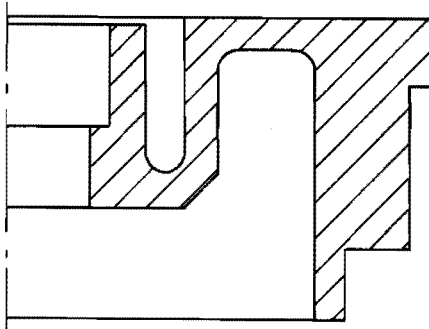
Fig.7.5. S-shaped flange construction.

7.6. Bearing system

The bearing system of flywheel rotors, especially for mobile applications, has to meet a combination of severe demands. These consist of high loads, due to rotor weight and dynamic loads, high speeds, minimized drag torque and acceptable service life.

Bearing selection

Many solutions have been proposed in the literature to overcome the difficult demands made upon flywheel bearing systems. Most applications use rolling element bearings, but hydrostatic and hydrodynamic bearings have been used too.

Magnetic bearings as active bearings are not considered because of their complexity, costs and low force density, which are all unfavourable characteristics for mobile applications. On the other hand they have very favourable features such as: no need of lubrication, very low drag torque, absence of wear, high maximum speeds and the possibility of controlling the stiffness and damping characteristics. These characteristics make them attractive to be used in special applications (e.g. in space where lubricants are undesirable) to improve the performance of the system. As a passive bearing, magnet bearings are attractive in combination with rolling element bearings for load reduction of the last ones. The recent development of autostable magnetic bearings with superconducting materials may be interesting for the future as these bearings are self centering without requiring an active control system [7.5].

Air bearings would only be possible in combination with fluid seals since in the majority of cases the bearings of a flywheel system have to operate under vacuum conditions. This alternative leans to a sophisticated fluid film bearing.

With these considerations the bearings for flywheel applications are restricted to either rolling element bearings or to fluid film bearings, which can be hydrostatic or the more simple (design, lubrication, costs) hydrodynamic (journal) bearings. With the help of the literature [7.6] and in consultation with bearing experts [7.7] these bearing types have been evaluated. It followed that from these types the rolling element bearings are preferred above the journal bearings because of the superior properties in the areas of:

a) Stability : the limit of stability of journal bearings due to half speed whirl would be a design consideration.

b) Lubrication/ : a relatively complicated lubrication system is required for journal
   safety   bearings; rolling element bearings have better emergency running characteristics in case of lubrication failure than journal bearings.

c) Misalignment : journal bearings would tolerate less misalignment than rolling element bearings.

d) Loading : journal bearings, for the same size as rolling element bearings, would have lower radial and dynamic load capacities.

e) Accuracy : journal bearings provide much less accurate location than rolling element bearings.

High precision angular contact ball bearings with axial preloading have been found perfectly suited for the EMAFER design. They can be loaded both axially and radially and are in general the most common approach for high speed machinery. Preloading, which is necessary for enabling radial loads, must be reduced to a practical minimum in order to minimize the frictional loss and to enlarge the speed limit and bearing life. The preloading controls also the bearing stiffness, which can be relatively large.

The demands made upon the ball bearings in the EMAFER design are enlarged by the inverse construction of the electrical machine, which has as consequences:

- Large bore diameters of the bearings. The transport of electrical energy and cooling liquid to and from the stator is, with the projected stator diameter and length, only possible via hollow, large diameter journals at the stator ends.

- Enlarged circumferential speed conditons of the bearings.

The straigth forward solution is a construction with a rotating outer race and a static innerrace. However, a rotating outerrace results, compared to a rotating innerrace, in higher ball speeds and thus higher internal centrifugal loading of the bearing. Compared to a rotating innerrace, the allowable speed limit is reduced to 60% for a rotating outerrace due to the resulting higher ball speeds [7.8].

A rotating innerrace and static outerrace needs in the case at issue, a more sophisticated construction with consequently larger bore diameters than the alternative with rotating outerrace. The advantage of higher speed limit will be partly annulled then.

Another solution for meeting the high speed condition of the rolling element bearing is a cascaded rolling element bearing: two bearings in series, one running inside the other. However, this solution goes at cost of other constructive complications such as bad misalignment, accuracy, heat removal and undefined speed conditions.

Lubrication

The lubrication conditions determine strongly the speed limit, bearing losses and bearing temperature. The speed limit is in turn strongly related to bearing losses and bearing temperature. The bearing losses of rolling element bearings are due to friction between moving parts, the viscous drag in the lubricating fluid and, to a lesser extent to hysteresis of the material. In highly loaded bearings the first cause dominates whereas at lower load, high speed applications, the second cause dominates.

The relationship between oil quantity, frictional loss and bearing temperature is shown in Fig.7.6. (optimized lubrication conditions assumed; bearing losses are indicated here as frictional loss). Five regions for the oil quantity can be distinguished:

region A: insufficient oil for complete separation of rolling elements and raceways.
region B: forming of a cohesive load carrying oil film.
region C: increase of hydrodynamic losses and by this of the temperature.
region D: equilibrium between heat generation and heat loss.
region E: the cooling effect of the oil predominates.
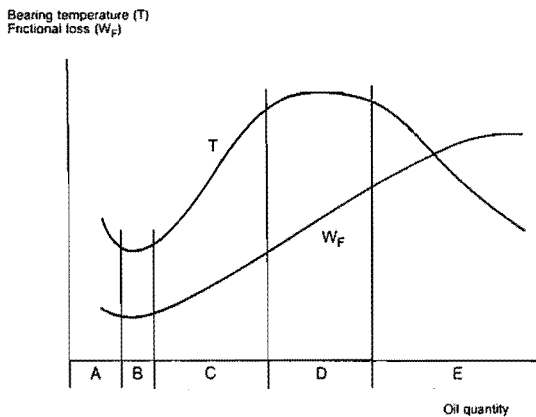
Fig.7.6. Bearing temperature and bearing loss as a function of oil quantity [7.9].

The optimal lubrication method is the oil spot method (region B in Fig.7.6.), in which very small, accurately metered quantities of oil are as a continuous flow directed at the bearing. This minimum quantity minimizes losses and enables bearings to operate at lower temperatures or at higher speeds than with any other method of lubrication.

Besides the oil quantity also the vacuum operation has to be taken into account. This is not a problem in itself, as most lubricant oils have a suitably low vapour pressure for medium vacuum ($1-10^{-3}$ mbar). For high vacuum ($< 10^{-3}$ mbar) it may be necessary to resort to special vacuum lubricants.

In the EMAFER concept the oil spot lubrication method with a kind of (low vapour pressure) aircraft turbine oil has been applied.

Bearing support

Special attention has to be paid to the bearing support construction as a consequence of dynamic loads to which composite flywheels can be subjected especially. The dynamic loads may be caused by the flywheel itself (e.g. imbalance loads) or by the motion of the housing. The last ones can be minimized by adequate construction measures, e.g. cardanic suspension and "weak" attachment to the surroundings.

Composite flywheels however, are expected to suffer from variation in imbalance due to a possible displacement of an initial imbalance during spinning and can cause high dynamic loads by this [7.10]. The only way to avoid these bearing loads is supercritical operation with the help of a "self-centering" bearing system. Since rolling element bearings have considerably high stiffness and bad damping characteristics, a support structure with defined stiffness and damping characteristics is needed. The damping is needed in order to ensure a quiet and safe running in the supercritical range. See also sections 7.5. and 9.5.

The most common type of bearing support with these characteristics is a squirrel cage, as defined stiffness element, with a squeeze film damper as used in aircraft turbines. It is basically a journal bearing in which the journal is restrained from rotating and connected to the housing by a spring system, see Fig.7.7. The oil which is supplied to the space between the journal and the housing is "squeezed" when the journal orbits, thereby providing the damping. The rolling element bearing is mounted on the journal and provides the rotation.

All these aspects, dealing with the vibration behaviour of the system, are rather complicated and are dealt with extensively in chapter 9.
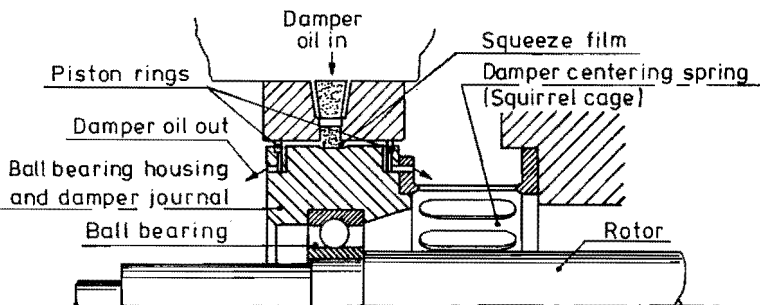
Fig.7.7. Bearing support with squirrel cage and squeeze film damper [7.3.].

7.7. Flywheel containment

In all (terrestrial) applications of a flywheel energy storage system, a flywheel containment is functionally needed for providing the vacuum environment and personal safety. Vacuum operation of high energy density flywheels is necessary to reduce the windage losses. Too high windage losses cause an unacceptable system efficiency and an overheating of the flywheel. The personal safety concerns safety from contact of rotating parts and in case of rotor failure a reliable protection against injury.

7.7.1. Vacuum function

The windage loss and flywheel temperature can be controlled by the vacuum level in the containment. Both will be unacceptably high if the vacuum level is not deep enough. This can be illustrated by a parametric study to this subject [7.11].
In this study a calculation model has been assembled to predict the power dissipated in fluid friction and the steady state temperature of a circle cylindrical flywheel. By varying the parameters which describe the flywheel system (energy density, diameter/height ratio, storage capacity and vacuum pressure), important trends in the scaling of the windage loss and the flywheel temperature were discerned:
- Windage loss and flywheel temperature increase substantially with pressure.
- Windage loss and flywheel temperature increase with energy density, but decrease with mass density. This behaviour strongly penalizes high energy density, composite flywheels in comparison to steel flywheels. Composite flywheels are the more critical so as their high temperature behaviour is poor.
- For equal energy per mass, the temperature of aramid and steel flywheels are about equal; the losses with aramid flywheels are approximately twice those with steel flywheels.
- If the temperature of a composite flywheel is within acceptable limits, the windage loss is also acceptable.
- The windage loss shows a modest dependance on flywheel diameter/height ratio, for which reasons flywheels may be designed for bearing and packaging constraints without incurring a large penalty loss.

In general it can be concluded from this parametric study that medium energy density flywheels (<40 Wh/kg) should be constructed instead of high energy density flywheels in order to have acceptable windage losses and flywheel temperatures at medium vacuum levels ($1-10^{-3}$ mbar).
Also other investigators [7.12] and [7.13] studied the effect of the vacuum level on windage losses and flywheel temperature:
Genta [7.12] reports that it is generally considered that modern flywheels should operate at a vacuum level between 1 and 10^{-3} mbar. The higher values of the pressure being for large diameter, low energy density flywheels with mechanical power coupling through a rotary seal. Concerning flywheel temperatures, Genta reports that at 10^{-3} mbar no heating problem is present.

Coppa [7.13] concludes that the moderate vacuum (of the order of 1 mbar) is a good choice since further pumping will have little effect on windage losses until the regime of free molecular flow is reached (of the order 10^{-2} mbar). Even with these higher pressure levels Coppa claims that moderate rotor temperatures can be maintained. Radiant heat transfer between the rotor and the housing is the dominant mechanism for maintaining rotor temperature. Surface emissivities required for adequate heat transfer are obtainable in anticipated rotor and housing materials.

Windage losses
The windage losses are related to dimensionless drag coefficients. These are in turn related to the dimensionless, well known peripheral Reynolds number (Re) of the flywheel, in a way depending on the flow type in the boundary layer around the flywheel.
Four flow types are distinguished: turbulent flow, laminar boundary layer flow, Couette flow and free molecular flow. The transition between laminar and turbulent conditions, in both momentum and thermal boundary layers, is determined by the Reynolds number. The Couette flow is a kind of special laminar flow type (linear velocity profile) occurring for small gaps between flywheel and containment, i.e. smaller than the boundary layer thickness.
The flow is a free molecular flow when the viscosity depends on the pressure as well as the temperature. The continuum approximation of the fluid behaviour is no longer valid then and the fluid begins to behave in a manner predicted by kinetic theory. The two last flow types are distinguished by the dimensionless Knudsen number (Kn) being the ratio between the mean free path of the molecules and a dimension of the object under consideration, i.e. the flywheel radius. In practice, according to Genta [7.12], the flow around a flywheel is turbulent at higher containment pressures and laminar until the medium vacuum region (< 1 mbar). Only for very low values of the pressure, the high vacuum region (< 10^{-3} mbar), a certain free molecular effect becomes important.
The power loss as a function of the containment pressure for the EMAFER design has been calculated using the models of [7.11], [7.12] and [7.14]. The results are shown in Fig.7.8. The flow regimes are also shown, the wavy lines indicating that the transitions are not very sharply defined. It can be seen that the calculations according to Genta are the most conservative approach. Further it is obvious that the containment pressure has to be in any way smaller than 1 mbar in order to have acceptable losses.
The absolute level of the pressure is further determined by the aerodynamic heating process and resulting flywheel temperature.

Flywheel temperature
The steady state flywheel temperature is determined by the windage losses and the heat transfer in the vacuum environment.
The primary components of heat transfer from the wheel to the surroundings are convection and radiation. Heat transfer by convection depends on the average heat transfer coefficient, which may be normalized through the use of the dimensionless Nusselt number (Nu). In this way the amount of heat transferred by convection from the wheel surface to the fluid is related to the Nusselt number by the thermal conductivity of the fluid, the flywheel radius, the surface area and the flywheel and containment temperatures. The Nusselt number in turn is strongly related to the Reynolds number.

For pressures lower than 10^{-1} mbar the heat transfer by convection can be neglected, mainly due to the strong decrease of the Reynolds number. The radiant heat transfer is, as known, independent of medium, and the transfer per unit area is related to the flywheel and containment temperatures by the Stefan Boltzman constant and the radiant interchange factor. This last one is a function of the surface emissivities of flywheel and containment (black or "gray").

The total heat transfer has been calculated for the EMAFER design, assuming steady state temperatures of the flywheel of 80°C and of the containment of 40°C. The results are shown in Fig.7.8. From this figure it can be concluded that:

- For pressures lower than 10^{-1} mbar, the radiant heat transfer becomes dominant.
- The vacuum region between 1 and 10^{-2} mbar would be sufficient for maintaining adequate flywheel temperatures, on condition that the surface emissivities meet the "black surface" conditions.
- Vacuum levels lower than 10^{-2} mbar ensure in any way no overheating problems of the flywheel.

The definite choice of the vacuum level will depend on the total power needed for the vacuum system and the windage losses. The sealing of the containment will influence this strongly and special attention has to be paid for minimizing leakage losses.
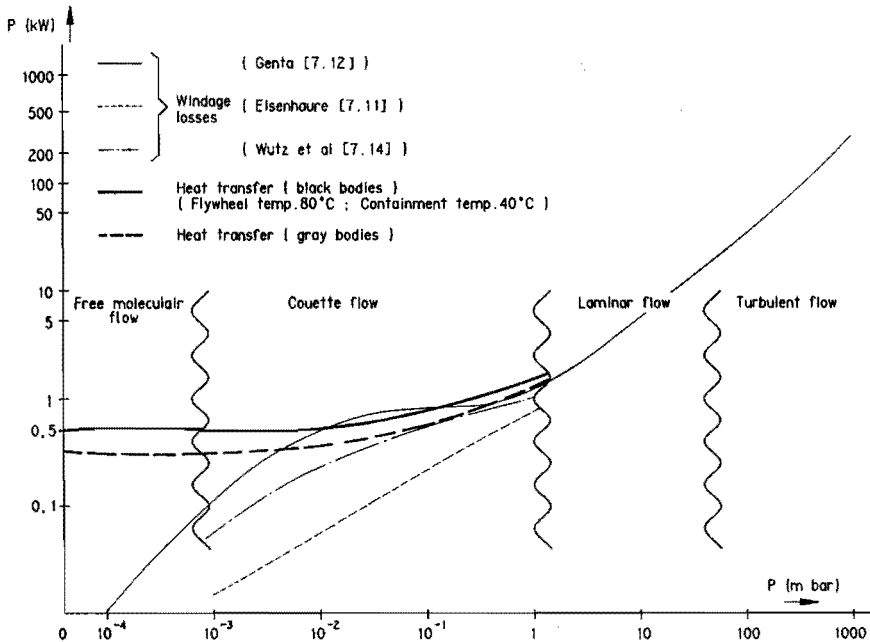
Fig.7.8. Windage loss and heat transfer as a function of the containment pressure.

7.7.2. Safety function

High speed rotating machinery, such as a flywheel system, is always a potential source of danger. A flywheel burst containment must be able to:
a. prevent any fragment penetration;
b. predictably limit the torque and forces transferred to the surroundings during a containment event;
c. take care of the debris management;
d. offer a safe response to vehicle collision.

Fragment penetration
Fragment penetration depends above all on the size of the rotor fragments. If the fragments are very large, the limiting case being a single fragment extended for 360°, the fragment energy is high, but rotational. As the fragments become smaller, the energy approaches 100 % translational and appears to the containment as an explosion. The energy of a rim fragment is given as a function of its angular width in Fig.7.9. From this figure, it can be seen that the translational energy is maximum for fragments extended for 90°-150°, which usually happens in the failure of monolithic metal rotors.
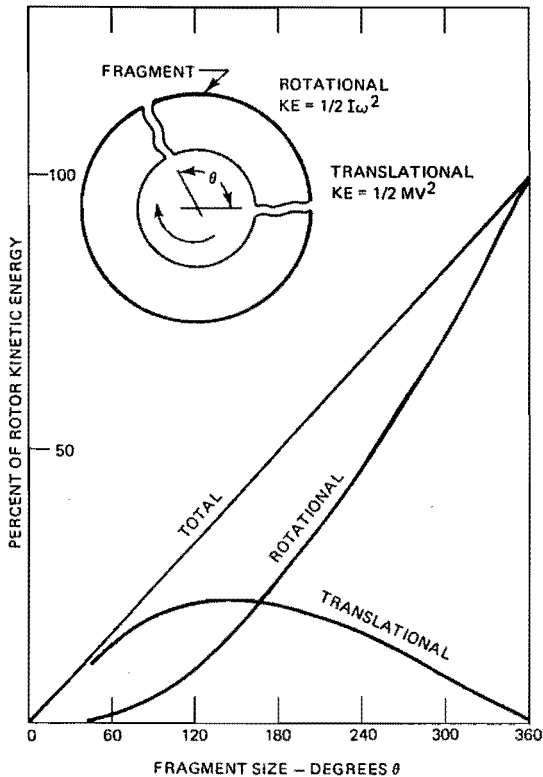
Fig.7.9. Rim fragment energy [7.15].

An analysis into containment processes that involve a relatively small number of rigid rotor fragments is described in [4.13]. This method has been shown to give realistic estimates of containment requirements for metallic rotor bursts which induce a large amount out-of-round as well as stretching deformations of the containing ring.

For composite rotors, which release a relatively large number of well distributed fragments, this method is too conservative due to the fact that large out-of-round bending displacements of the ring are not produced [4.14] and [7.13]. Composite, circumferentially wound thick rim rotors, as the EMAFER flywheel is, have been found to fail by delamination into fragments which are initially circumferentially, extending 360° or more, and radially thin. As can be seen from Fig.7.9. these fragments will have very little translational energy.

In [4.14] a two phase failure process is considered, based on the description of initial fragmentation of composite wheels. Phase 1 involves a transfer of radial impuls momentum from the fragments to the containment structure and the latter is required to absorb the associated radial kinetic energy by undergoing a uniform stretching process. The radial momentum is due principally to the initial rotor clearance which should be minimized for this reason. Phase 2 follows sequentially and involves the tangential motion of the fragments along the circular contour of the containment liner. The containment ring has to withstand then the centrifugal pressure exerted by the fragments as a result of this motion.

It is very important that the circularity of the containment structure is preserved during the burst process. If circularity is not preserved, then additional radial momentum will have to be absorbed by the containment. In addition, the tangential sliding motion of the fragments will be inhibited by higher curvature and will generate larger centrifugal pressures in these regions. These effects will in turn produce greater non-circularity.

It may be obvious that the above method results in substantially lower containment requirements than the previous method for metal flywheel containment. However, with the assumption that the initial fragmentation remains intact during the whole failure process, this method is still very conservative. Post-test debris of aramid/epoxy rotors has been found in a loose, fluffy consistency and that of glass/epoxy rotors is highly delaminated and fragmented [7.13].

Friction at the rubbing surface, in the presence of high centrifugal pressures, loads such planes shear and introduces high heat fluxes into the composite near the rubbing interface. Such effects induce rapid break up of fragments into small-scale debris. This mechanism reduces thus significantly the containment requirements concerning fragment penetration.

The EMAFER design is in itself advantageous with respect to fragment penetration, due to the modular flywheel construction (smaller fragment sizes). Special attention has been paid to prevent fragment penetration with a light weight containment structure, see Fig.7.10. The structure has a minimal radial clearance space to the flywheel and consists of a metallic liner overwound with a bare high performance fibre. The liner provides, besides vacuum structure and circumferential rigidity by ribs on the outer surface, load distribution of the fragments onto the overwrap. The overwrap provides a substantial addition of strength and strain capability.

Both, the increased circumferential rigidity and the overwrap, have moreover a noise surpressing effect. A light weight circular structure can be an effective radiator of sound.

However, the overwrap influences the heat transport to the surroundings negatively. For this reason a liquid cooled liner is required, e.g. by means of a heat exchanger or a double skinned liner.
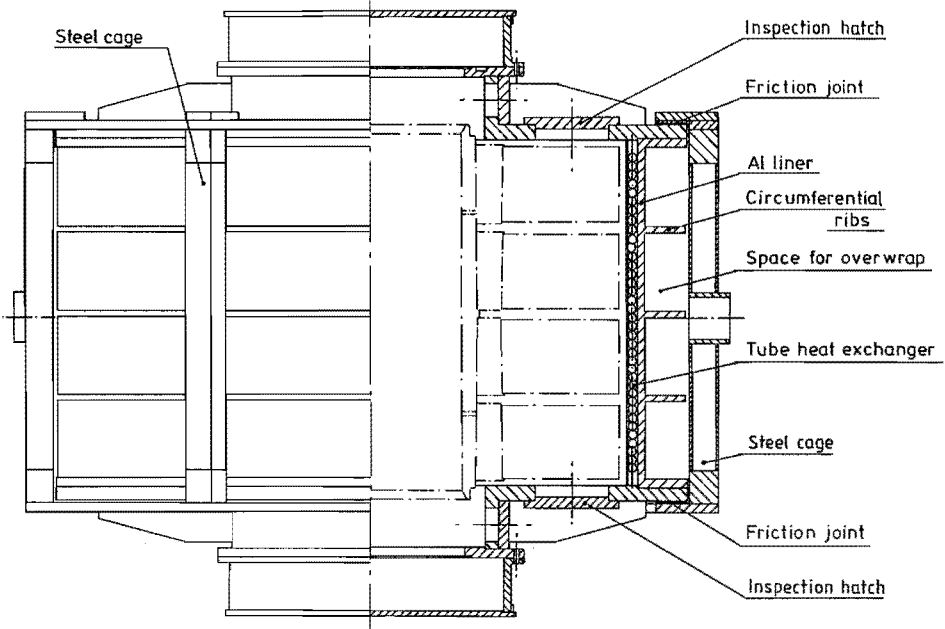
Fig.7.10. Light weight containment structure.

In the safety analysis of the above containment [7.16] a worst case analysis has been followed in which flywheel delamination at the metallic hub/composite rim interface is supposed. The initial fragment expands the full size composite rim and is moreover supposed to remain intact during the containment process. Penetration of the containment is prevented by minimizing the initial rotor clearance to 10 mm in combination with an aluminium (7075-T6) liner thickness of 10 mm and a bare fibre (Dyneema) overwrap thickness of 40 mm.

Limitation of reactions
Concerning the limitations of the reaction forces and torques transferred to the surroundings during a containment event, two critical situations can be distinguished: the tangential kinetic energy dissipation and loose rotor control.
The tangential kinetic energy dissipation can be critical when the rotor is locked by the rotor debris or by large circumferential bending deflections. The tangential momentum which is transferred to the surroundings will be extremely high then. The tangential reactions can be limited by enabling a defined, torque limited, rotation of the whole containment structure.

The loose rotor control involves the break away of an essentially intact rotor from its shaft and subsequent interactions with the housing. This problem has been analysed in [7.13]. It is shown that the radial clearance has a strong effect on force and torque reactions. However, the reactions can be limited to reasonable levels for typical running clearances (1-2 % of rotor outside diameter). It is also shown in the analyses that both, the force and torque reactions can be significantly decreased if rotation of the containment structure is permitted. Hence containment rotation obtains benefits relative to both the primary burst event and the loose rotor control.

In the EMAFER design, the containment is supported, via friction joints on circular rails, in a steel structure (cage), see Fig.7.10. The friction joints limit the tangential reactions to the surroundings as it enables a defined, torque limited, rotation of the whole containment.

In the safety analysis [7.16], rotor break-away of the complete, intact rotor (cylinder plus flywheel discs) has been supposed. This failure mode appears not to be representative for the stresses in the containment.

The final speed that the containment will obtain after such a failure, depends strongly on the magnitude of the fixation momentum of the containment as well as the coefficient of friction between rotor and containment. For coefficients of friction below 1, a fixation torque of about 10 times maximum operational momentum will prevent rotation of the containment. The containment will start rotating when locking of the rotor occurs. This has to be prevented in any way with respect to the final speed of the containment which can then become intolerably high (about 2,000 rpm). A high circumferential rigidity of the containment is therefore very important.

Debris management
The rotor debris that is generated in the containment process can cause considerably high pressures and tangential momentum in containment structures. Hence a proper handling of the debris is desirable for instance by providing space for the debris to move into.

In the EMAFER design, the modular flywheel construction provides axial space around the flywheel discs into which sideward movement of rotor debris is possible, see also Fig.7.10.

Safe response to vehicle collision
Concerning the vehicle collision response function the containment and its attachment to the vehicle must be sufficiently rugged to resist its own inertia loading relative to a 10g load factor due to collision and tolerate a possible loose rotor running condition.

In the EMAFER design, the structural ruggedness of all parts, containment, cage and cardanic suspension, gives a built-in stability to resist the own inertia loading due to collision.

7.8. Emafer preprototype and prototype

The EMAFER preprototype, as predecessor of the prototype, has been realized on the basis of the results of the optimization study (part II) and the preliminary results of the flywheel development (chapter 8) and the vibration research (chapter 9). The objective was the gathering of practical information and experience concerning fabrication as well as system operation, already in a relatively early stage of the investigations. With the help of this practical information and the theoretical simulation models, which are evaluated and adjusted in this way, the optimal design for the prototype system has been made subsequently.

a. Preprototype

The EMAFER preprototype concerns a scale 1:1 test model of the prototype system with restricted storage capacity (1 flywheel disc; effective energy storage capacity max 0.8 kWh instead of 4 kWh), and restricted power capacity (30 kW instead of 300 kW). The storage and power capacity are restricted for practical (production and test facilities) and cost reasons (composite materials, magnets, power thyristors).
The design has been worked out in three composition drawings [7.17]. The most important special features of the main components flywheel, electrical machine, bearing system and containment are described next.

Flywheel.
The flywheel is a tangentially wound composite thick rim wheel with dimensions
ϕ 260 mm* ϕ 600 mm * 100 mm. Two construction principles have been followed (see also section 7.3.): the Woven Ribbon Winding Process (WRWP) with uni-directional fibre weft (see Photo 8.1. in chapter 8) and the layered flywheel with specific stiffer materials from inner to outer radius (e.g. glass, aramid and carbon epoxy, see Photo 8.2.). The maximum projected operating speed (based on radial fatigue stresses) is, due to the materials used, for the WRWP flywheel 12,000 rpm and for the layered flywheel 15,000 rpm which results in respective effective energy storage capacities of 0.4 and 0.6 kWh. Ultimately a speed of 17,000 rpm is possible, corresponding with an effective energy storage capacity of 0.8 kWh. The flywheel attachment is done with a press fit and is realized via a conical clamping sleeve with an oil pressure method for mounting and dismounting, see also section 7.5.

Electrical machine
The electrical machine is mechanically identical to the 300 kW version, see section 7.4., and has been designed for the maximum projected speed of the system of 17,000 rpm. The power capacity is limited because of the restricted line voltage of the machine as obtained by limiting the height of the Samarium-Cobalt magnets.
The rotor losses, eddy currents in the magnets and solid iron, have been minimized by a kind of "lamination" of the rotor poles and by lining the magnets at the inner surface with a copper sheeting, see also section 7.4.
The stator core lamination has been done with standard material (as used in 50 Hz machines) which gives relatively high stator losses. In combination with the low power capacity of 30 kW, the stator losses are thus for the preprototype of the same magnitude as for the prototype system which enables testing of the cooling system in an adequate way.

Bearing system

The bearing system is based on high precision angular contact ball bearings for reasons mentioned in section 7.6.

For simplicity reasons and as best option for starting the evaluation of the theoretical vibration behaviour, see section 9.4.1., the bearings are directly mounted on the stator journals, with the innerrace static and the outerrace rotating. The lower bearing is fixed on the stator journal whereas the upper bearing is mounted on a sliding sleeve which is supported via O-rings on the stator journal. This sliding sleeve is hydraulically pressed for preloading the bearings and provides compensation of elongation differences due to thermal expansion and centrifugal load.

In the above bearing construction there are no vibration dampers at the bearings. Vibrations have to be damped via rubber coupling elements between stator and containment and surroundings.

The rotational speed is a problem due to the relatively large bearing diameter, determined by the hollow stator journals, needed for transport of energy and cooling liquid to and from the stator. The high speed of 17,000 rpm is only obtainable under optimal lubrication conditions. For this reason the lubrication is done with minimum quantities according to the oil spot method, see also section 7.6.

Containment

The containment structure has been designed to provide the vacuum operation of the flywheel motor/generator unit. It has no safety function and needs therefore no cooling system. Thus it enables a good accessibility to the flywheel, for inspecting and balancing, via two large hatches in the cylindrical containment surface. The safety during testing is provided by operating the complete system in a test pit.

Complete system

The tested preprototype system has been assembled with one flywheel disc, according to the layered principle and has main data as listed below:
- Maximum speed   : 15,000 rpm (ultimately 17,000 rpm)
- Energy capacity : 0.6 kWh (speed range 7,500 - 15,000 rpm)
- Power capacity   : 30 kW
- Main dimensions : ϕ 800 mm * 800 mm
- Total mass   : 400 kg

A total view of the preprototype system is given in Photo 7.1.
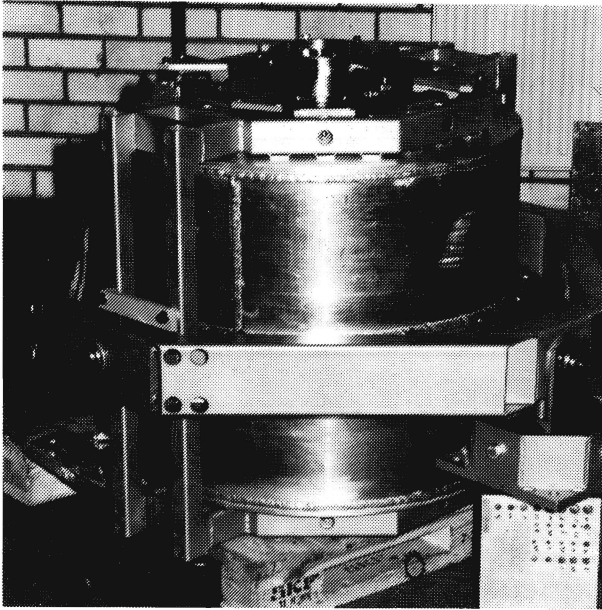
Photo 7.1. EMAFER preprototype system.

b. Prototype

The conclusions of all further theoretical investigations and experiments with the preprototype have been implemented in the prototype.
The prototype mainly differs from the preprototype concerning:
- flywheel and containment construction with respect to the safety behaviour;
- the coupling constructions (flexible steel coupling elements with oil dampers) of the main parts (rotor, stator, containment) with respect to the vibration behaviour;
- operating speed range: 8,000 - 15,000 rpm.

For further details is referred to chapter 10, section 10.2., which gives an extensive description of the prototype.

Chapter 8

Flywheel development

8.1. Introduction

In the EMAFER concept a set of thick rim flywheels is used, see also section 7.2. The thick rim flywheel, fabricated by tangentially winding with a continuous fibre composite, has considerable advantages compared to other flywheel types, as it can offer: a fairly high weight and volume energy density; a relatively simple and effective rim-hub attachment and a predictable and benign failure behaviour by delamination. However, one of the major problems of this type of flywheel is that of premature delamination, as it can only support very low radial tensile stresses. This strongly limits the flywheel speeds and with this the achievable energy density.

Fortunately there are several methods of reducing the radial tensile stresses, due to centrifugal load, in a thick rim flywheel. In this chapter the development of such a type of flywheel is described.

8.2. Rotor stress analysis

A flywheel is in general subjected to various load conditions due to:
- rotation, causing centrifugal forces;
- angular accelerations, caused by gyroscopic moments and power input and output;
- transversal accelerations, e.g. for flywheels used in mobile applications;
- thermal effects, e.g. for composite flywheels caused by cooling from curing temperature or by operating temperatures differing from curing temperature;
- prestressing, e.g. caused by press fitting during assembly;
- forces due to imbalance.

The load conditions due to angular and transversal accelerations as well as imbalance are negligible for high energy density flywheels compared to the other load conditions mentioned above [8.1]. These have been considered in this analysis.

The general three dimensional stress state can be simplified for the considered axisymmetrical disc wheels to a plane stress state [8.1]. This statement has been verified in [8.2] by numerical calculations with a three dimensional finite element method. For a flywheel of comparable dimensions as the EMAFER flywheel, the stress component in axial direction appears to be negligible compared to the stress components in tangential and radial directions.

In case of a plane stress state the stress field is a function of one parameter only, namely the flywheel radius r. The following equations can be derived then [8.1].

In case the mass forces are only centrifugal, the equilibrium equation is:

$$\frac{d}{dr}\left(\sigma_r r h\right) - \sigma_t h + \rho \omega^2 r^2 h = 0 \qquad (8.1)$$

As strain compatability equation is valid:

$$\epsilon_r = \frac{d}{dr}(\epsilon_t r)$$

(8.2)

The uni-directional (U.D.) composite material of the flywheel is an orthotropic material which shows a good linear elastic behaviour. With the tangential and radial directions as principal directions, the constitutive equations of the material can be written as:

$$\epsilon_t = \frac{1}{E_t}(\sigma_t - \nu_{tr}\sigma_r) + \alpha_t \Theta$$

(8.3)

$$\epsilon_r = \frac{1}{E_r}(\sigma_r - \nu_{rt}\sigma_t) + \alpha_r \Theta$$

(8.4)

$$\frac{\nu_{tr}}{E_t} = \frac{\nu_{rt}}{E_r} \quad \text{(Maxwell relation)}$$

(8.5)

In these equations:

σ_r = radial stress ; ϵ_r = radial strain;
σ_t = tangential stress ; ϵ_t = tangential strain;
r = local flywheel radius ; h = local flywheel height;
ω = angular speed ; ρ = mass density;
ν_{tr}, ν_{rt} = Poisson's ratio for respectively tangential and radial orthotropic directions;
E_t, E_r = Young's modulus for respectively tangential and radial orthotropic directions;
α_t, α_r = thermal expansion coefficient for respectively tangential and radial orthotropic directions;
Θ = difference between uniform flywheel operating temperature and curing temperature.

Assuming constant material properties over the radius, the equations (8.1) to (8.5) can be combined to the following second order differential equation in the radial stress:

$$\frac{d^2\sigma_r}{dr^2} + \frac{d\sigma_r}{dr}\left[\frac{3}{r} + \frac{1}{h}\frac{dh}{dr}\right] + \sigma_r\left[\frac{1}{r^2}(1-\mu^2) + \frac{1}{r}(2+\nu_{tr})\frac{1}{h}\frac{dh}{dr} + \frac{d}{dr}\left[\frac{1}{h}\frac{dh}{dr}\right]\right]$$

$$+\rho\omega^2(3+\nu_{tr}) + E_t\alpha_t\left[\frac{\Theta}{r^2}(1-\delta) + \frac{1}{r}\frac{d\Theta}{dr}\right] = 0$$

(8.6)

$$\mu^2 = \frac{E_t}{E_r}; \qquad \delta = \frac{\alpha_r}{\alpha_t}$$

With the appropriate boundary conditions, this equation can be used to solve the stress distribution over the flywheel radius.

Assuming linear elastic material, it is possible to study separately the effects of different load conditions, e.g. centrifugal load, prestressing and thermal effects, and to superimpose the thus obtained solutions for the combined load situation.

8.3. Delamination problem

The thick rim flywheel is favourable for both increasing of the volume energy density and reducing of the rim-hub attachment problem. However, one of the major problems of this type of flywheel is that of the delamination failure due to the very low radial tensile strength of the material. This can be illustrated with the help of the stress distribution for the centrifugal load situation in these flywheels.

The stress distribution in a constant thickness rim with constant material properties can be found from equation (8.6) with dh/dr=0 and as boundary conditions $\sigma_r=0$ at the inner and outer radii (no prestressing effects) and with $\Theta=0$ (no thermal effects). This gives as solution:

$$\sigma_t = \rho\omega^2 r_0^2 \frac{3+\nu_{tr}}{9-\mu^2}\left[\mu\ell\chi^{\mu-1}+\mu(\ell-1)\chi^{-\mu-1}-\frac{\mu^2+3\nu_{tr}}{3+\nu_{tr}}\chi^2\right] \qquad (8.7)$$

$$\sigma_r = \rho\omega^2 r_0^2 \frac{3+\nu_{tr}}{9-\mu^2}\left[\ell\chi^{\mu-1}-(\ell-1)\chi^{-\mu-1}-\chi^2\right] \qquad (8.8)$$

with: $\qquad \mu = \sqrt{\frac{E_t}{E_r}}$; $\quad \chi = \frac{r}{r_0}$; $\quad \ell = \frac{\beta^{-\mu-1}-\beta^2}{\beta^{-\mu-1}-\beta^{\mu-1}}$; $\quad \beta = \frac{r_i}{r_0}$.

r_i, r_0 = respective inner and outer radius of flywheel;
for other symbols, see page 84 or list of symbols.

From eq. (8.8) it can be derived that the radial stresses vanish for thin rims ($\beta \rightarrow 1$), whereas they increase for decreasing ratio between inner and outer radii and thus can cause delamination failure in thick rim flywheels. This is shown in Fig.8.1., in which the ratio between the maximum values of the radial and of the tangential stresses $\sigma_{r,max}/ \sigma_{t,max}$ is given, for several ratios of inner and outer rim radius, as a function of the anisotropy of the material, i.e. the ratio between the tangential and radial Young's moduli. As also the ratios of radial to tangential ultimate strengths and Young's moduli of several composite materials are indicated in Fig. 8.1., it can be seen that tangentially wound rim flywheels of these materials, which rotate with such a speed that their tangential strength is reached, will fail by delamination as soon as the ratio between inner and outer rim radius will be smaller than about 0.8, unless special methods for reducing the radial tensile stresses are used.
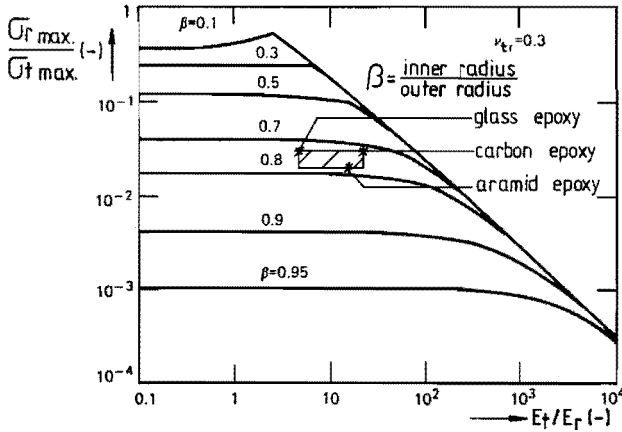
Fig. 8.1. Ratio of maximum radial and tangential stresses in rim flywheels as a function of the elastic anisotropy of the material (derived from [8.1]).

Besides the radial stresses due to centrifugal load, also radial stresses due to thermal effects may cause delamination in thick rim composite flywheels. Radial tensile stresses will be produced when the rim is cooled from curing temperature if the radial expansion coefficent (α_r) is larger than the tangential one (α_t), as is the case for tangentially wound composites. This can directly be derived from eq. (8.6), when a uniform temperature is supposed.

This effect is very important in the case of materials with high α_r/α_t ratio or even with a negative value of α_t and moreover a higher Young's modulus. Therefore aramid expoxy with $\alpha_r/\alpha_t = -14$ or carbon expoxy with $\alpha_r/\alpha_t = -100$ and both with relatively high Young's modulus, are more dangerous with respect to curing stresses than glass epoxy with $\alpha_r/\alpha_t = 6$ and relatively low Young's modulus. As the thermal stresses are added to those produced by centrifugal load, the curing temperature should by preference be below the operating temperature. Then the thermal effect will cause radial compression stresses, which are favourable for reduction of the delamination problem.

8.4. Methods for reduction of the delamination problem

Several methods for reduction of the delamination problem are possible ([8.1] and [8.3] to [8.9]). These methods can be distinguished into next principally different categories:
- Varying the material properties with the flywheel radius.
- Applying prestress effects.
- Avoiding radial stress transfer.

8.4.1. Varying the material properties with the flywheel radius

Since not all the material in a thick rim flywheel is at an equal distance from the axis of rotation, each subsequent annular outer element tends to stretch more than the previous inner one, thus causing the dangerous radial tensile stresses. The methods for reduction of these stresses by variation of the material properties all have in common that they reduce this radial stretching, either by increasing the radial centrifugal growth of the inner material or by decreasing the radial growth of the outer material.
It should however be realized that increasing of the radial growth of the inner material will seriously enlarge the rim-hub attachment problem, see also section 7.5.
Without radial stresses, the radial displacement due to centrifugal load is given by

$$U = \frac{\rho \omega^2 r^3}{E_t} \qquad (8.9)$$

with: U = radial displacement;
for other symbols, see page 84 or list of symbols.

The radial stretching of the material can then be reduced by raising the specific Young's modulus (E_t/ρ), according to the increase of the flywheel radius. This principle can be executed in several ways:

a) Varying the mass density of the composite material as a function of the radius [8.1] and [8.3].
By distributing additional mass in the inner rings of the flywheel (e.g. by blending the resin with lead powder), the radial growth of the inner material will be enlarged. Theoretically it is possible to eliminate the radial stresses completely, but at cost of very high tangential stresses. As a consequence the maximum achievable energy density is strongly reduced.
By loading the inner material according to $\rho \sim 1/r^2$, radial stresses are avoided, while having constant tangential stresses over the flywheel radius [8.1]. Assuming no influence of the ballast on the Young's modulus and Poisson's ratio of the material, it has been derived in [8.3] that the mass energy density of a thick rim flywheel with $\rho \sim 1/r^2$ will be a factor 2 smaller than that of a thick rim flywheel with constant mass density in which the maximum radial stress is 0.1 of the maximum tangential stress.

b) Varying the fibre content as a function of the radius [8.1].
If the rim is built by filament winding, it is possible to vary the fibre content with the radius, namely by varying the winding tension of the fibre with the radius. By this principle the Young's modulus of the material in tangential direction can be increased from the inside to the outside of the rim. The varying of the fibre content is how-ever, for practical reasons, limited so that only quite thin rims can be built in this way. From theoretical analysis in [8.1] it follows that the fibre content of rims built with this technique sharply decreases to the inner radius, e.g. a fibre content of 0.2 at the inner radius is required for a radial stress free flywheel with an inner to outer radius ratio of 0.8.

c) **Varying the winding angle of the fibres with the tangential direction as a function of the radius [8.1]**

By cross winding the flywheel (layers composed of plies with reinforcement fibres at equal and opposite winding angle), decreasing of the crossply angle with the radius will result in an increase of the Young's modulus of the material in tangential direction from the inside to the outside of the rim. This will in turn result in reduced radial tensile stresses due to the decreased radial stretching of the material compared to the situation with constant material properties.

The main disadvantage of this method is, however, that the tensile strength of the material in tangential direction is reduced due to the off-axis loading of the fibres. This causes additional stresses perpendicular to the fibres together with shear stresses in the plane of the plies. This ultimately lowers the maximum achievable energy density.

d) **Dividing the rim in concentric annular elements of different material [8.1], [8.4] and [8.5]**

By using different materials from inner to outer radius, e.g. respectively glass, aramid, high strength carbon and high modulus carbon, the specific stiffness (E_t/ρ) increases with the radius. Very low values of the radial tensile stresses, or even negative ones, can thus be obtained. This method allows a fairly high energy density as the ratio strength to mass density of the inner material is not lowered as is the case in the previous methods a),b) and c). Disadvantages are, however, the use of relatively expensive high modulus fibres for the outer layers and the sensivity for thermal stresses. Due to the different expansion coëfficients of the several materials, e.g. carbon epoxy has a negative longitudinal expansion coëfficient, thermal stresses will be produced for other temperatures than the curing temperature. In conjunction with centrifugal load stresses this can be disadvantageous.

8.4.2. Applying prestress effects

The principle of prestressing the material is to enlarge the allowable radial tensile stresses or strains with the amount of applied radial compression stress or strain distribution in the flywheel. Any stress state, which can cause compression of the inner material and tension of the outer material, both in tangential direction, will therefore be favourable for reduction of the delamination problem. Limits to this practice are the maximum value of the compressive stress state which can be applied to the inner material (hub and inner layers) and the maximum value of the tensile stress state, which can be applied to the outer material. High tangential compressive stresses in the inner layers can cause fibre instability, particularly if low modulus matrices are used. High tangential tensile stresses in the outer material can cause hoop failure or creep. From a safety standpoint the design is preferably adjusted to fail by delamination at a suitable margin prior to hoop failure. Creep of the material will lead to stress relaxation and thus to reduction of the prestress effects.

It may be obvious that, within its limits, prestressing will in any way affect the energy density positively. The principle can be realized in several ways:

a) **Shrink fit prestressing [8.1] and [8.5]**
A multi-layer rim can be built by shrink fitting the rims on to each other, using a difference of temperature during the assembly. Unfortunately, the low thermal expansion coefficient, together with the low Young's modulus, particularly in the case of glass epoxy, forces the use of very high temperature differences. To obtain a significant improvement of the delamination problem, impractical temperatures are needed.

b) **Variation of winding tension [8.6] to [8.8]**
The most direct control on prestress in fibre composites is through variation of winding tension. It is possible to wind the rim under strong tension but in the normal filament winding process, the winding tension is controlled by the required fibre content. Worse, a too high fibre content dramatically lowers the transversal tensile strength. Moreover other variables such as resin shrinkage and thermal stresses usually dominate the generation of residual stresses. As furthermore a significant portion of the winding tension is relaxed almost immediately upon application to the winding surface, due to resin flow, partial curing of thin layers during winding is required. This method for residual stress control by programmed winding has been analysed in [8.6]. As this method requires partial curing, it is a very time costing and expensive method which is seldom considered.
The Woven Ribbon Winding Process (WRWP) for flywheel manufacturing is also based on the prestressing principle by programmed winding tension, but meets the disadvantages of the preceding method. This process has been orginated by ETH-Zürich [8.7] and [8.8] and is based on a low cost philosophy. In this process, the fibre material is as an uni-directional woven ribbon (tape), wound under pretension between auxiliary side plates to a flywheel. Thanks to the pretension, radial compression stresses will arise in the flywheel. The stress distribution in radial and tangential direction is optimized by varying the pretension of the ribbon during winding. The pretension is varied continuously to avoid abrupt stress changes within the composite.
As all fibres to cover the width of the flywheel are wound at one go per layer (disc type flywheels) and the resin flow is restricted by side plates, partial curing is not required. It is obvious that the WRWP process offers a remarkable reduction in manufacturing time, compared to the normal filament winding process with partial curing.

8.4.3. Avoiding radial stress transfer

In this method the rim is composed of concentric annular elements separated by elastic layers [8.9]. The elastic layers have to accomodate the differences in radial growth between the several elements without exerting strong tensile stresses on the rings. This is only possible by using relatively weak elastic layers. This can in turn cause rotordynamic instability due to material hysteresis of the elastic layers, see also section 7.5.

In the EMAFER concept two of the above described methods were investigated further: the WRWP-process and varying the specific material stiffness by using different materials. The other alternatives were not considered further because of their inherent reduction in energy density and difficult rim-hub attachment problem due to the enlarged centrifugal growth of the inner material.

8.5. Development of the woven ribbon wound process (WRWP) flywheel

The principle of this flywheel type has been orginated by ETH-Zürich for small flywheels meant for passenger car application [8.7] and [8.8], see also section 8.4.2. The principle has been scaled up and investigated further for the EMAFER application.

8.5.1. Construction and fabrication of the WRWP flywheel

In the WRWP flywheel, the prestressing is done by winding the fibres, as an uni-directional weft, under relatively large pretension on the flywheel hub. Thanks to the pretension, a pressure between the layers will arise. The stress distribution in radial and tangential direction is optimized by varying the pretension of the ribbon during winding, see Fig. 8.2.
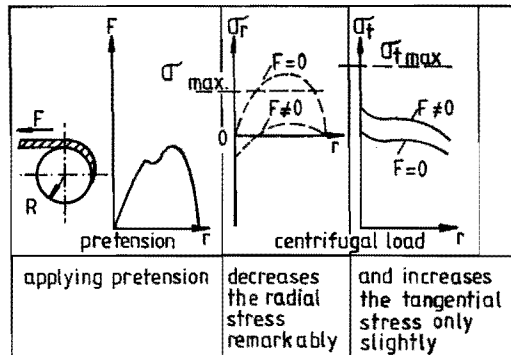
Fig 8.2. Effect of applying pretension [8.8].

In the original concept the pretensioning was meant for both: radial tensile stress reduction and provision of a rigid flywheel attachment to the steel hub. As the pretensioning appeared not sufficient, see section 8.5.3., a conical clamping sleeve between composite flywheel and steel hub, to provide press fitting, was introduced, see Fig. 8.3. The conical clamping sleeve enables moreover, in conjunction with an oil pressure method, relatively easy assembling and disassembling of flywheel and hub.
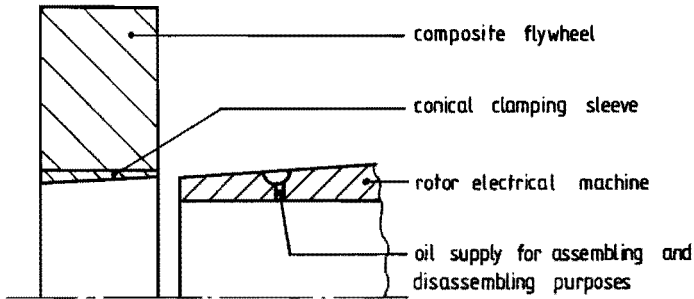
Fig. 8.3.   Composite flywheel with conical clamping sleeve for press fitted flywheel attachment.

The fabrication of the WRWP flywheel is done as illustrated in Fig. 8.4. The fibre (roving) is fed from the bobbin cradle to the weaving machine. The woven ribbon, an uni-directional weft, is taken from the roll and guided through a tensioner to an impregnation bath. From there it is wound, between auxiliary side plates, directly on the clamping sleeve or any type of flywheel hub. After winding it is cured.
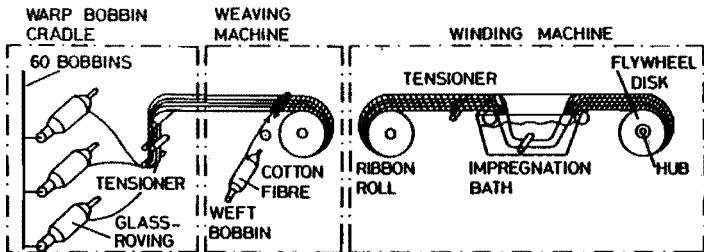
Fig. 8.4. Fabrication of WRWP flywheel [8.7].

The first flywheels manufactured by ETH-Zürich with this technique were meant for passenger car application and had an energy content of 100 Wh. As the EMAFER concept involves modular flywheel discs of about 1 kWh energy content, the technique had to be scaled up. For this scaling up a purpose made flywheel winding machine was designed and built. This flywheel winding machine is based on a relatively large lathe enabling flywheel diameters up to 0.8 m. The supply and pretension of the woven ribbon (tape) is provided by a feeding structure with guiding, tensioning and resin impregnation rolls.
The considered disc width (100 mm) could be fabricated in a reasonable way by stacking two flywheel discs of 50 mm each. The flywheels can be wound prestressed next to each other before they are cured. The woven ribbon is the same as used by ETH-Zürich, see also section 8.5.3. On Photo 8.1. the glass fibre WRWP flywheel with conical clamping sleeve, suited for the EMAFER preprototype, is shown (flywheel disc dimensions ϕ 255 x ϕ 600 x 100 mm).
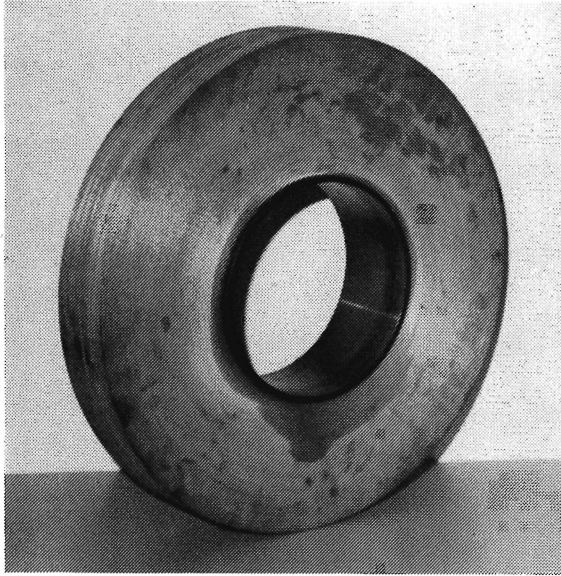
Photo 8.1. Glass fibre WRWP flywheel for EMAFER preprototype.

8.5.2. Stress analysis of the WRWP flywheel

The stresses in the WRWP flywheel can be composed of stresses due to centrifugal load, pretensioning, press fitting and thermal effects. Assuming a plane stress state, a quite adequate assumption for disc type flywheels, and constant material properties over the flywheel radius, the stress analysis can be done with the help of differential equation (8.6) with $dh/dr = 0$, see section 8.2.

As the composite material is supported by a steel hub, which contributes also to the stress distribution, the flywheel is considered as a construction consisting of different material layers (isotropic metal rotor and clamping sleeve and anisotropic composite rim). Each layer has its own differential equation (8.6). For each load situation the associated stress distribution can be calculated using the appropriate boundary conditions.

- Centrifugal load:
  The boundary conditions are radial stress = 0 at the inner and outer radii and radial stress and displacement are continuous at the material interfaces. No thermal effects ($\Theta=0$) are considered.

- Pretensioning:
  By successively calculating and adding the stress distributions due to an applied winding tension of each new winding layer (= radial and tangential stress boundary condition at varying outer radius) up to the outer radius, the resulting stress distribution due to pretensioning can be found. No rotation ($\omega=0$) or thermal effects ($\Theta=0$) are considered.

  It is noted that in these calculations for simplicity, the material properties of the cured composite are used. In reality, when curing after winding, the material properties are those of the uncured material.

- Press fitting:
    The total flywheel assembly is again considered as a multi-layer construction. The boundary conditions are at the inner radius, the interface radii and the outer radius of the flywheel assembly. At the inner and outer radius the radial stress = 0 whereas at the press fit radius the boundary conditions (radial compressive stress and displacement) are dictated by the press fit. Any other interface radius has radial stress and displacement continuity. Again $\omega=0$ and $\Theta=0$.
- Thermal effects:
    Boundary conditions radial stress = 0 at both, inner and outer radius, radial stress and displacement are continuous at the material interfaces. For simplicity reasons a uniformly steady state temperature $(d\Theta/dr =0)$ is assumed. No rotation is considered.

The stress distribution resulting from the combined load situation can be found by superimposing the solutions of the different load situations as linear elastic material is assumed.
The first orientating calculations were done by ETH-Zürich [8.10]. Their computer model took into account the centrifugal load and pretensioning as described above. Press fitting and thermal effects were not considered. As during testing also press fitting appeared to be necessary, see section 8.5.3., a calculation model was set up that, in addition to the model of ETH-Zürich, takes into account press fitting and thermal effects as well [8.11]. All load situations are calculated as described above thus having restrictions for the pretensioning situation due to the assumption of cured material properties.

8.5.3. Theoretical and experimental investigations of the WRWP flywheel

a) Material selection
To build test flywheels for investigating the WRWP principle, the choice of E-glass fibres seems recommandable from a cost point of view. As also the longitudinal as well as the transversal tensile strengths of glass epoxy are of the same order as those of aramid and carbon epoxy, see chapter 4, Table 4.3., the experiences with the WRWP technology have been gathered with the help of flywheels made of E-glass roving ribbon as used by ETH-Zürich, see Fig. 8.5. It has a glass mass of about 8.5 gr/dm² and consists of 49 rovings of 900 Tex (1 Tex = 1 gr/1000 m) each, giving a width of about 50 mm.
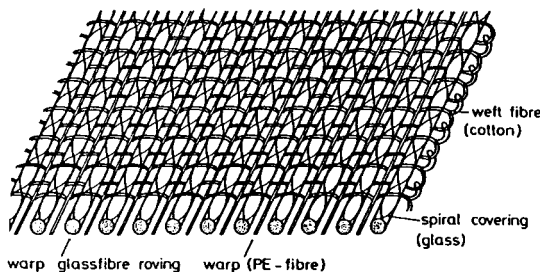
Fig. 8.5. Uni-directional weft [8.8].

As matrix, epoxy resin was used. This is a warm curing resin which was used because of its good impregnation characteristics, however at cost of thermal stresses after curing.

The material data as used for the WRWP investigations are the data as also used by ETH-Zürich and are listed in Table 8.1. Fatigue stresses are not considered here as these are in first instance of less importance for investigating the WRWP principle.

The WRWP wheel is supported by a steel hub, in the case at issue the rotor of the electrical machine. As this hub contributes to the stress distribution, the data of the used rotor steel are also included.

Table 8.1. Material data (at room temperature) for WRWP test flywheels.

E-glass epoxy	fibre content	60	vol.%
	mass density (ρ)	1960	kg/m^3
	longitudinal Young's modulus (E$_l$)	45	GPa
	transversal Young's modulus (E$_r$)	12.5	GPa
	Poisson's ratio (ν_{lr})	0.29	
	longitudinal tensile strength	800	MPa
	longitudinal compressive strength	400	MPa
	transversal tensile strength	40	MPa
	transversal compressive strength	120	MPa
	expansion coefficient longitudinal (α_l)	7.9	10^{-6}K^{-1}
	transversal (α_r)	50	10^{-6}K^{-1}
Wrought steel	mass density	7800	kg/m^3
(26 NiCrMoV 14 5)	Young's modulus	210	GPa
	Poisson's ratio	0.30	
	tensile and compressive strength	950	MPa

b) Calculations

The calculations for investigating the WRWP principle were done with the help of the computer program mentioned in section 8.5.2. [8.11]. This program calculates the radial and tangential stresses and presents these via plots as a function of the flywheel radius.

The considered flywheels are E-glass epoxy flywheels with the material data of Table 8.1. The manufacturing data and operational conditions are listed in the lower side of each stress plot. Several load conditions have been considered.

- Centrifugal load.

First the flywheel was calculated for the centrifugal load condition when directly wound, without applying pretension and/or press fitting, onto the steel rotor of the electrical machine. The dimensions considered concern the preprototype: steel rotor electrical machine ⌀208 x ⌀255 x 500mm and composite disc wheel ⌀255 x ⌀600 x 100 mm. The axial dimensions are not further considered as the calculations are based on the plane stress assumption. The results are shown in Fig. 8.6., page 96, which includes also the explanation of the manufacturing data (design temperature and press fits) and operating conditions (rotational speed and operating temperature).

It can be seen that relatively high radial stresses at the interface radius of composite and steel are needed to ensure the flywheel attachment.

As the radial strength of the composite/steel bonding force is an uncertain factor, the flywheel may lose contact with the steel rotor, which will lead to rotor instability, already at relatively low speeds.

Apart from the flywheel attachment problem, the radial stresses in the composite material will exceed the radial tensile strength (40 MPa) for speeds higher than 10,000 rpm, leading to the delamination problem of thick rim flywheels as mentioned in section 8.3. It is noted that the tangential stress at this speed is considerably lower than the tangential tensile strength (100, respectively 800 MPa).

- Pretensioning

The pretensioning effect on these phenomena has been studied by calculating the resulting stress distribution due to centrifugal load and pretensioning. Taking into account the maximum winding tension from a fabrication point of view (fibre instability at the inner radii), the course of the winding tension with the winding radius has been determined as such, that the radial and tangential stresses of the composite are within the material strength limits at standstill as well as at maximum speed (17,000 rpm). The resulting stresses are illustrated in Fig. 8.7., page 97 and are based on the winding tension as given in Fig. 8.8., page 98. From Fig. 8.7. it can be seen that the pretensioning effects take care of a press fit between flywheel and steel rotor by which the rigidity of the flywheel attachment is ensured for the total speed range. Also delamination will not occur as the radial tensile stresses due to centrifugal load are sufficiently reduced by radial compressive stresses due to the pretensioning.

- Thermal stresses

As a warm curing epoxy resin is used, the flywheel will be subjected to thermal stresses for temperatures others than the curing temperature. Temperatures below curing temperature will cause the unfavourable radial tensile stresses. This is shown for the test wheels in Fig. 8.9., page 98, for operating temperatures of -25˚C, 20˚C and 80˚C, which are all below the used curing temperature of 120˚C. Centrifugal load and pretensioning have not been considered in these calculations. It can be concluded from this figure that, with respect to delamination, the thermal sensitivity cannot be neglected. For other composites than glass epoxy, this effect will still be worse due to the larger difference in orthogonal elongation coefficients of these materials, see also section 8.3.

- Spin testing

For spin testing the flywheel separate from the electrical machine, a massive steel test spindle with dimensions ϕ 255 x 120 mm is used, see also test results on page 100. The stresses for this situation, assuming the same winding tension as before (Fig. 8.8.) and without considering thermal effects, are presented in Fig. 8.10., page 99.

By comparing Figs. 8.7. and 8.10., it can be seen that the massive hub influences the stress distribution in the flywheel less favourably than in case of the hollow rotor of the electrical machine. This is due to the "less flexible" centrifugal growth character of the massive hub compared to the hollow rotor so that the radial displacements at the inner radius of the composite rim will be "less well followed". Thus the test conditions will be less favourable than the operating conditions in the flywheel motor/generator unit.
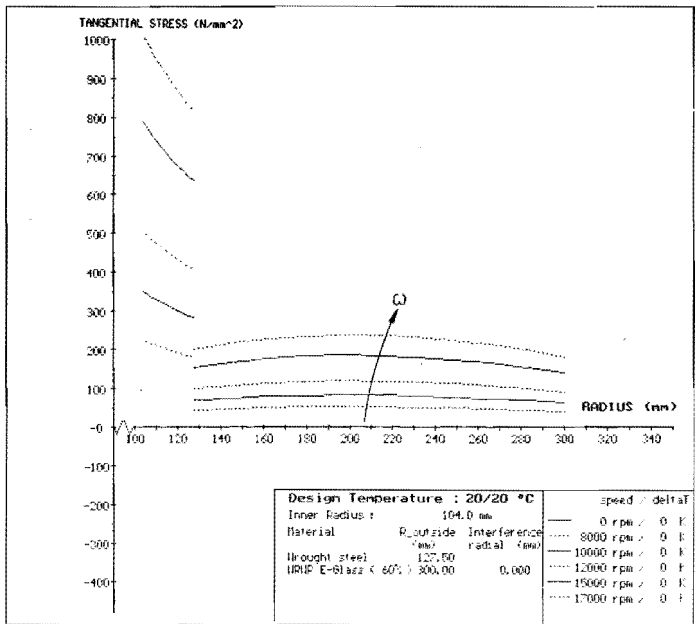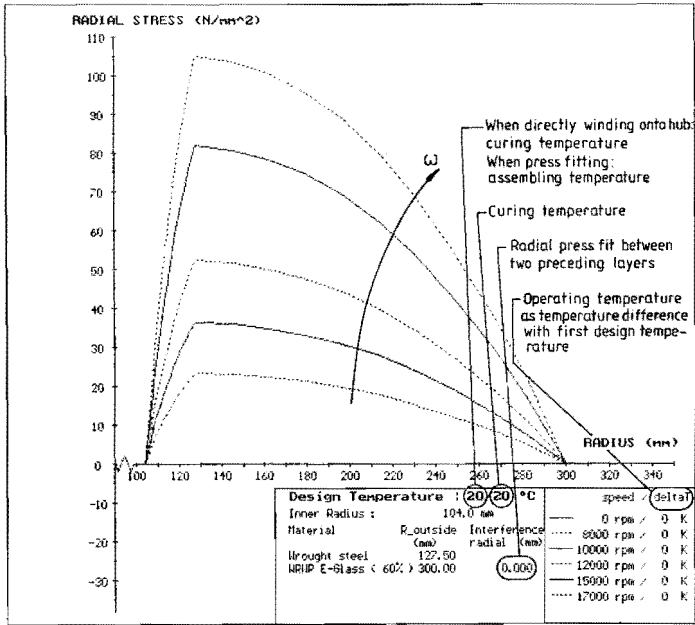
Fig. 8.6. Calulated stress distribution in E-glass epoxy WRWP flywheel on rotor of electrical machine without applying pretension and/or press fitting.
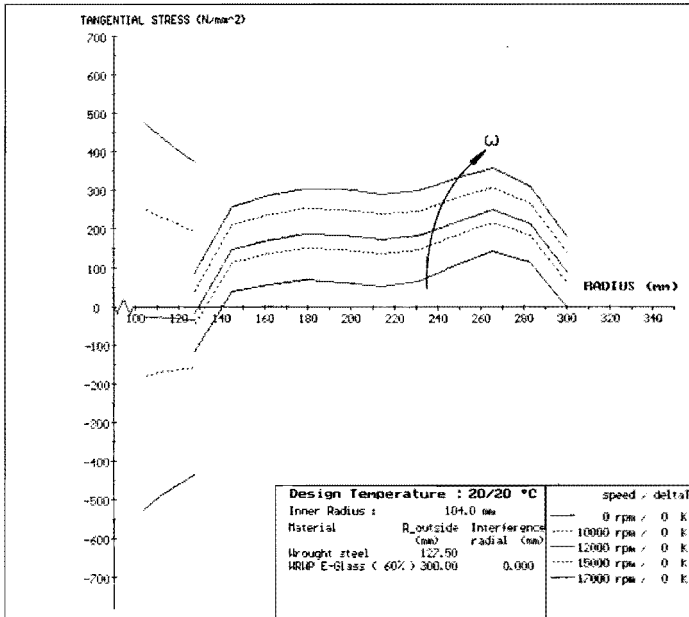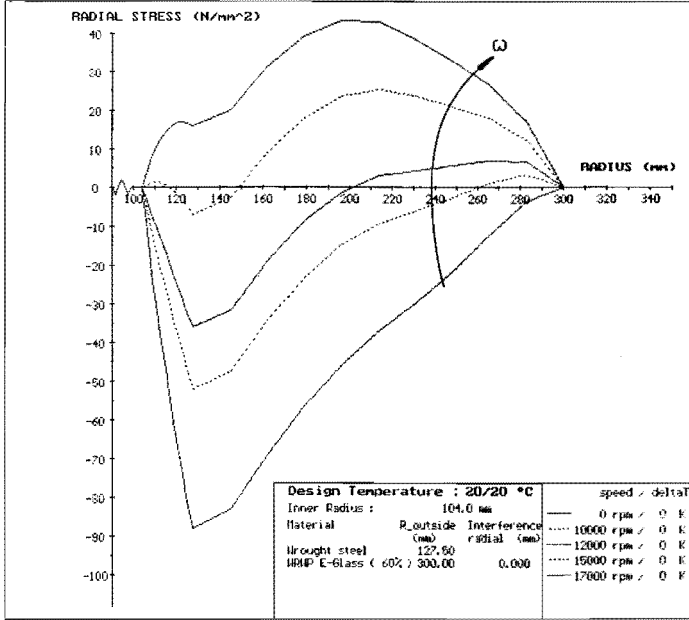
Fig. 8.7. Calculated stress distribution in E-glass epoxy WRWP flywheel on rotor of electrical machine when applying pretension (according to Fig. 8.8.).
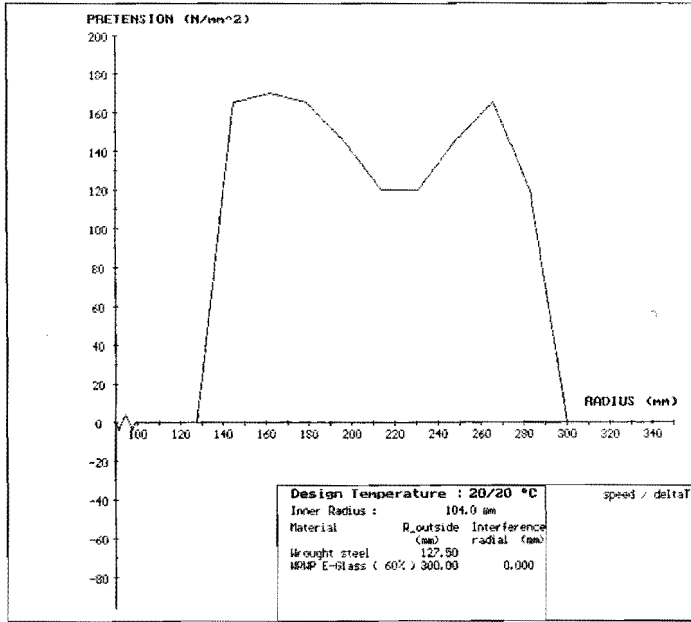
Fig. 8.8. Winding tension of WRWP flywheel.
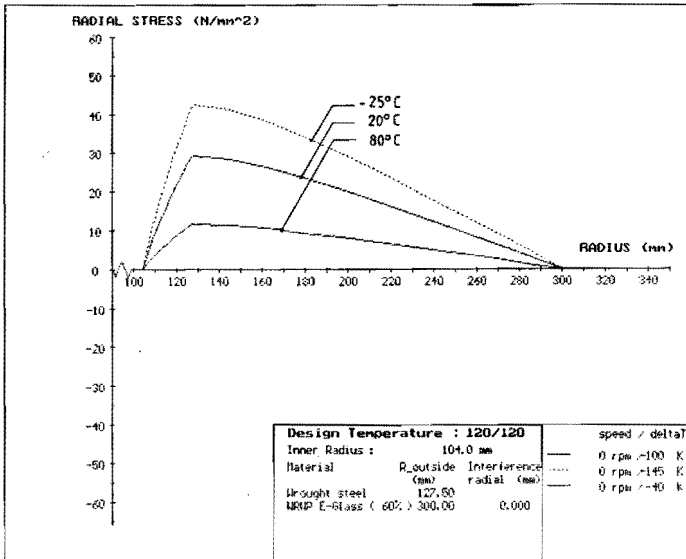
Fig. 8.9. Calculated radial stresses due to thermal effects in E-glass epoxy WRWP flywheel.
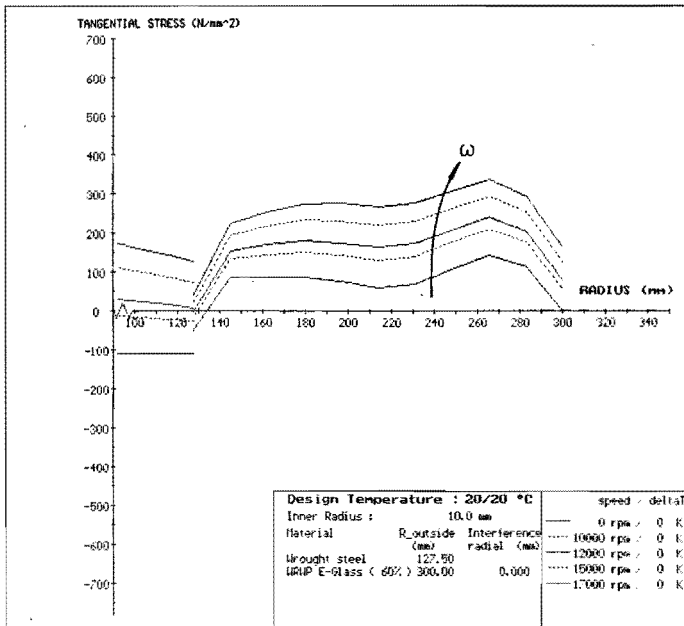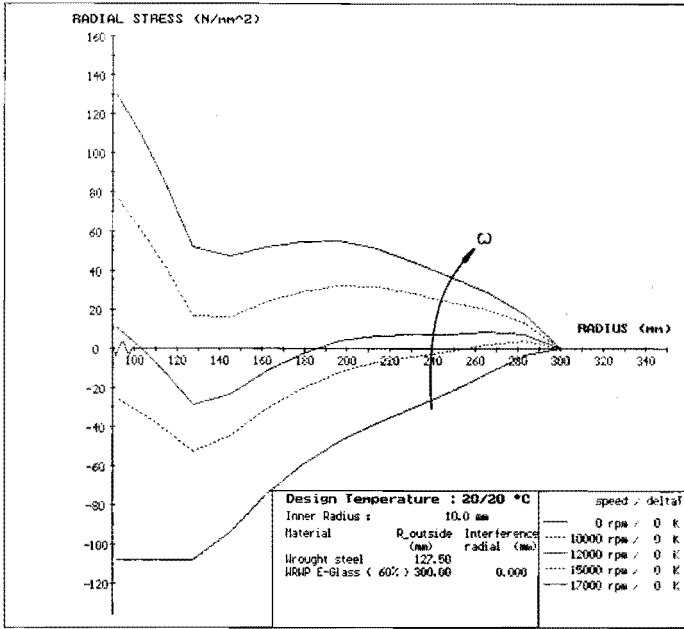
Fig. 8.10. Calculated stress distribution of E-glass epoxy WRWP flywheel on massive steel test spindle (inner radius of 10 mm assumed to accomodate boundary conditions in calculation model).

c) Test results
Several test flywheels have been wound using the WRWP winding machine. The first wheels were wound to investigate practical fabrication aspects: winding speed and impregnation, winding tension and fibre instability, effects of side plates on sideward resin flow. As soon as these aspects were under control the first flywheels for spin testing could be fabricated, see also Photo 8.1.
The spin testing was performed in a separate spin test facility. This is a vacuum containment in which the wheel is fixed to the drive shaft by a gimbal coupling. In this way the flywheel will spin overcritically, already for low speeds and the stresses caused by the spin testing are only due to centrifugal load and not because of dynamic vibrations.
The wheel is for these purposes attached to an auxiliary test spindle. This is a massive steel hub which is also used for balancing the wheel, by removing hub material. The first test flywheels were attached by winding them directly onto the test spindle. In a next stage they were attached by press fitting via a conical clamping sleeve.
The spin test facility with flywheel is shown on Photo 8.2.
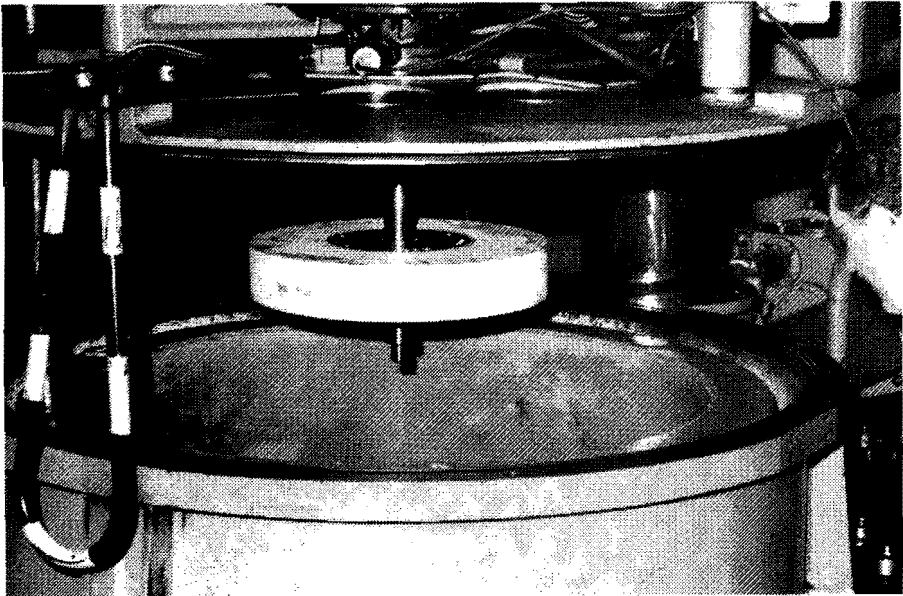
Photo 8.2. Flywheel testing.

The first tested flywheel, wound with pretension directly onto the test spindle, failed at about 10,000 rpm showing a benign failure behaviour, see Photo 8.3.
In a second test wheel it was observed, before spin testing, that the steel hub onto which the wheel was wound directly, could be removed sidewards with a considerably lower force than predicted.
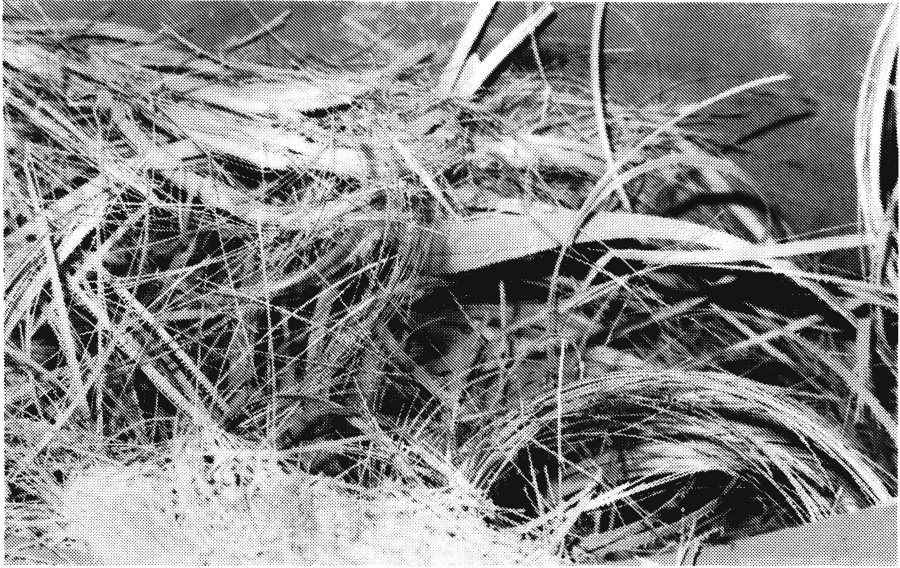
Photo 8.3. Flywheel failure of glass fibre WRWP wheel.

This can partly be explained by the presence of relatively large radial tensile stresses due to the warm curing process, see Fig.8.9. For the other part it can be concluded that:
- The pretensioning effects are not as calculated.
  This may be caused by incompleteness of the calculation model. The model calculates with properties of the cured material and does not take into account fabrication aspects such as: relaxation due to sideward resin flow during the winding process and resin shrinkage due to the curing process.
- The material properties may be less good than assumed.
  Especially the radial tensile strength is of major importance and can be strongly influenced during the fabrication process, e.g. by the quality of the impregnation and/or sideward resin flow.

The second test wheel, without steel hub, was therefore subjected to next further investigations [8.12]:
- Strain and displacement measurements for investigating the pretensioning effects.
  The radial change in strain as a function of the radius as well as the tangential strains and radial displacements at the inner radius were measured. This was done intermittently by dewinding the flywheel.
  Dewinding of the first 100 mm radius appeared not to influence the measured stresses and strains. In other words the winding of the last 100 mm radius has hardly influenced the radial stress distribution in the flywheel. The maximum radial strains were of the order 0.03% to 0.04% and were measured in the middle of the rim.
  The pretensioning effect is therefore considerably lower than calculated, probably because of stress relaxation due to sideward resin flow and resin shrinkage during the fabrication.

- Determining of material properties.
  The mass density, fibre content, impregnation and porosity, radial Young's modulus
  and radial tensile strength all have been determined as a function of the radius.
  The mass density and fibre content appeared to be about proportional with winding
  tension. The radial Young's modulus and radial tensile strength showed a large
  spread and were considerably lower than assumed. Radial Young's modulus:
  measured 5-10 GPa, assumed 13 GPa. Radial tensile strength: measured 4-7 MPa,
  assumed 40 MPa.
  From microscopic investigations it could be seen that the cotton weft fibre is the
  cause of the low radial strength. The cotton fibre is hardly or not impregnated and
  always initiates the rupture.

From the above, it can be concluded that, with respect to the calculations, both the
material properties and the resin flow during fabrication have been assumed too
optimistic. Moreover radial tensile stresses due to the curing process should be
avoided or minimized.

8.5.4. WRWP and press fitting

As the pretensioning does not give the desired stress distribution the WRWP principle
has also been investigated in conjunction with a press fit method. The press fit can be
realized by means of a conical clamping sleeve as illustrated in Fig. 8.3.
The third testwheel for the EMAFER preprototype consists therefore of a steel
clamping sleeve, with dimensions ϕ255 (mean inside cone diameter) x ϕ265 x 110
mm, on which a glass epoxy WRWP flywheel was wound with dimensions ϕ265 x
ϕ600 x 100 mm. After curing, the wheel was assembled with 0.5 mm radial press fit
with the test spindle. Fig. 8.11., page 103, shows the calculated stress distribution in
the wheel due to combined press fitting and centrifugal load. The pretensioning effects
of the WRWP process have been neglected. The material properties are according to
Table 8.1., page 94. When comparing Figs. 8.6. and 8.11., it can be seen that press
fitting is an effective method for the reduction of radial tensile stresses.
The flywheel has been spin tested up to 12,000 rpm without showing any sign of
failure. Referring to Fig. 8.11. and the measured radial tensile strength of 7 MPa, see
preceding paragraph, this means that press fitting alone is not sufficient for the
noticed reduction of the radial stress. This means in turn that the WRWP principle
has taken care of an additional reduction of the radial tensile stresses.
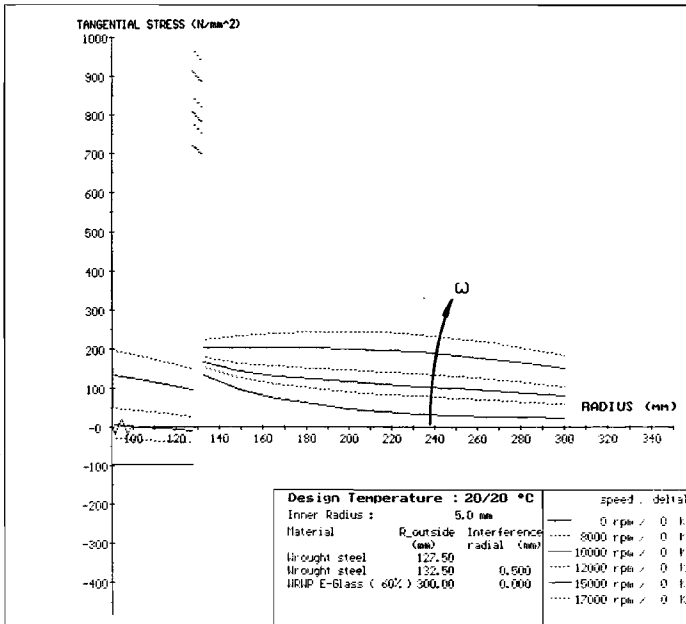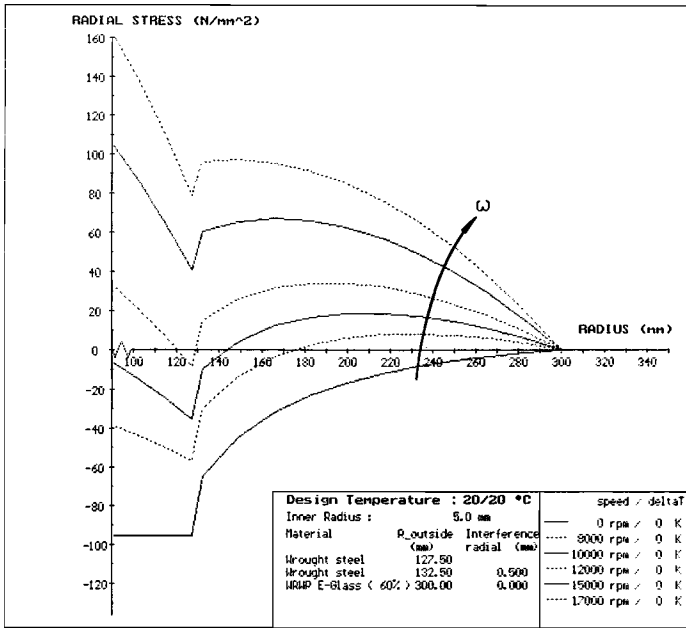
Fig. 8.11. Calculated stress distribution in E-glass epoxy WRWP flywheel assembled with 0.5 mm radial press fit with test spindle.

8.5.5. Conclusions on the WRWP flywheel

From the investigations above, it can be concluded that:
- The WRWP principle enables relatively short fabrication times and can be considered as a cost effective manufacturing method.
- The WRWP principle does not give the desired improvement of energy density. This is mainly due to the cotton weft fibre, the sideward resin flow during winding and the warm curing process.
- In conjunction with a press fit method the WRWP principle gets a better feasibility.
- Preventing the sideward resin flow and curing stresses, as well as replacing the cotton fibre weft by e.g. a glass-fibre weft, can make the WRWP principle more effective. In this respect impregnation after winding with a cold curing resin may be advantageous.

It is noted that materials with a high creep resistance must be used with the above technology as creep will reduce the pretensioning effects. The prestress load in the flywheel will then decrease until the material stresses are below the minimum creep level. This in turn will reduce the maximum achievable speed.

8.6. Development of the layered flywheel

The layered principle is a well known principle for the reduction of radial tensile stresses due to centrifugal load [8.1] and [8.4]. However, it does not offer a solution for a rigid flywheel attachment method. The radial displacement due to centrifugal load at the cylindrical connection interface will always be larger for the composite rim than for the metallic hub, see also section 7.5.
With the help of the insights and experiences gathered from the WRWP flywheel development, the layered principle is given full feasibility by combining it with the press fitting principle.

8.6.1. Construction and fabrication of the layered flywheel

The layered flywheel is composed of concentric annular elements of different materials. The specific Young's modulus of the material (Young's modulus in tangential direction with respect to mass density) increases from inner to outer radius, thus reducing the radial tensile stresses due to centrifugal load. Of course this goes at the expense of increased tangential stresses, see Fig. 8.12. The stress distribution can be optimized by varying the layer thicknesses and materials.
The flywheel attachment is provided by means of a conical clamping sleeve that allows for a strong press fitting of the flywheel onto the hub. This press fitting yields, combined with the layer principle, an additional reduction of radial tensile stresses, at the expense of tangential stresses, however, see Fig. 8.12.
Of course it is also possible to practice the press fit method at more interface radii in the flywheel, between or within the material layers (a kind of modified WRWP flywheel). In this way a further reduction of radial tensile stresses is possible. As will be shown later, it is even possible to obtain only radial compressive stresses over the full radius up to the maximum speed.
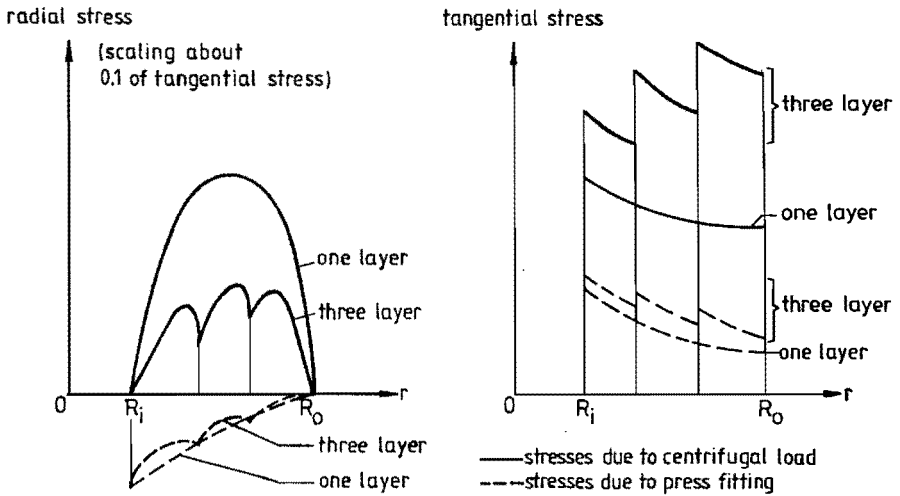
Fig. 8.12. Radial and tangential stresses in fibre composite flywheel due to centrifugal load and press fitting (excluding hub).

The press fitting has to be done by conical interfaces, see Fig. 8.13., as shrink fitting would require impractical temperatures to be effective, see also section 8.4.2. To prevent eventual sideward rupture of the composite at the interfaces, the press fit can be realized via metal clamping sleeves, see Fig. 8.13.
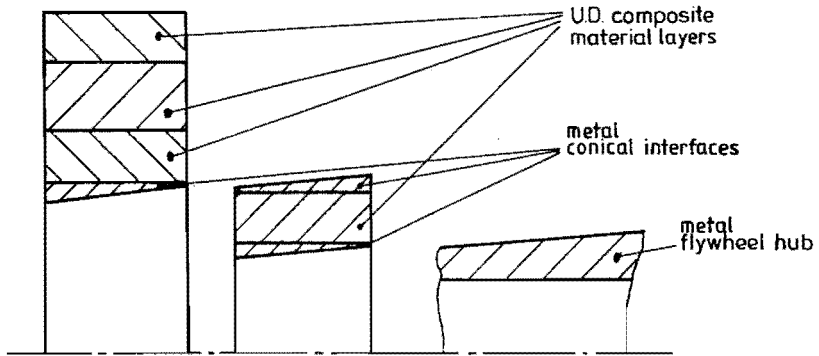
Fig. 8.13. Layered flywheel with plural press fit.

The layered flywheel can be fabricated by filament winding with one or more rovings. This can be done on conventional winding machinery, see Fig. 8.14.
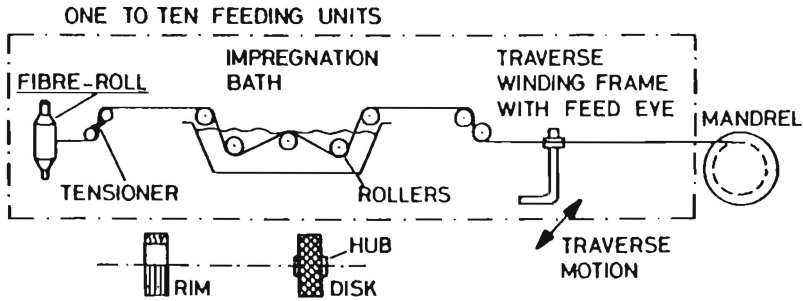
Fig. 8.14. Filament winding process [8.6].

The rovings are fed from a bobbin through a tensioner to the impregnation bath. The winding tension is, as contrasted with the WRWP fabrication, small and only serves to control the fibre content. From the impregnation bath the fibre continues through a feed eye to a mandrel where, between side plates, the flywheel is wound on. Transverse motion of the feed eye is necessary to wind the fibre with cross ply orientation for covering the flywheel width. As soon as the desired layer thickness has been reached another fibre material is glued to the winding surface and winding is continued. The flywheel is wound and cured intermittently to prevent fibre instability and resin flow. A cold curing epoxy resin is used for preventing thermal stresses, see also section 8.3. and Fig. 8.9. On Photo 8.4. the layered flywheel (from inner to outer radius respectively steel conical clamping sleeve, E-glass, aramid and high strength carbon epoxy layers), suited for the EMAFER preprototype can be seen (flywheel disc dimensions $\phi255$ x $\phi600$ x 100 mm).
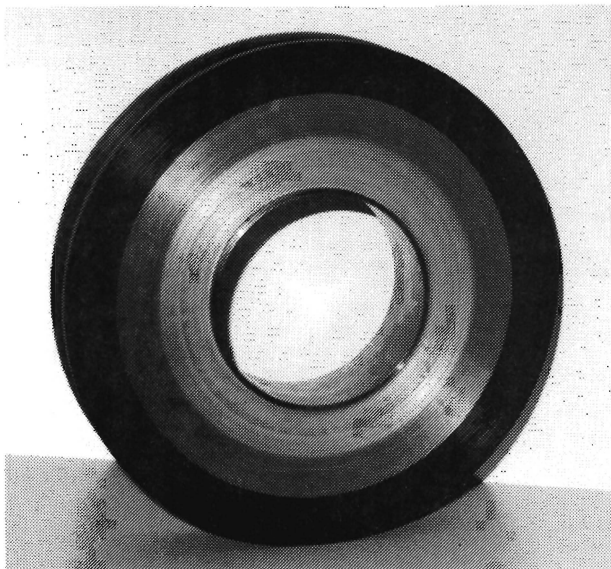
Photo 8.4. Layered flywheel for EMAFER preprototype.

8.6.2. Stress analysis of the layered flywheel

The stresses in this flywheel exist due to centrifugal load, press fitting and thermal effects. Assuming a plane stress state and constant material properties over each material layer, the stress distribution for each load condition can be determined in a similar way as for the WRWP flywheel, see section 8.5.2.

The only difference is that in the layered flywheel more layers have to be considered. This results in proportionally more differential equations and boundary conditions, which follow from the continuity demand of radial stresses and displacements at the layer interfaces. Superimposing the solutions of each load situation gives the resulting stress distribution due to the combined load situation.

The first orientating calculations were made by TNO-Delft [8.13] and [8.14]. Their model took only into account centrifugal load and thermal effects. Press fitting could be calculated in a rather restrictive way: only at the flywheel hub interface by simulating it as an internal pressure at the inner diameter of the composite rim. Therefore, a special computer program was developed [8.11], which takes into account all above load conditions for a number of material layers and press fit interface radii, which are free to choose. With the help of this model the layered flywheel has been optimized.

8.6.3. Theoretical and experimental investigations of the layered flywheel

a) Material selection

The material selection is based on the specific Young's modulus (E/ρ) on one hand and by the tangential fatigue strength on the other hand. From inner to outer radius, materials with increasing specific Young's modulus have to be used to meet the radial stress limit. The tangential fatigue strength determines the maximum allowable radius of the material according to the following equation (no radial stresses supposed):

$$\sigma_t \approx \rho \omega^2 r^2 \tag{8.10}$$

in which: σ_t = tangential stress
ρ = mass density
ω = rotational speed
r = radius

In Table 8.2. the material data of the materials considered, as used in the further calculations, have been listed as well as the specific Young's modulus and the maximum allowable radius for a rotational speed of 17,000 rpm.

From this table, it follows that it is possible to find material combinations that meet both restrictive demands of the layer construction principle: increasing specific Young's modulus with increasing flywheel radius without exceeding the tangential fatigue strength.

As resin a cold curing epoxy resin is chosen in order to prevent thermal stresses due to the curing process.

Table 8.2. Relevant data of considered materials for the construction of a layered flywheel (Suppliers information).

Materials	Uni-directional composites (60% fibre vol.)				Wrought metals	
Material data (at room temperature)	E-glass	HM-aramid	HS-carbon	HM-carbon	Steel 26NiCr MoV 145	Alum. 7075-T6
density (kg/m³)	2000	1360	1530	1570	7800	2800
Young's modulus						
longitudinal (GPa)	42	79.4	138	224	210	71.8
transversal (GPa)	10	5.5	8.5	10	210	71.8
Poisson's ratio	0.25	0.33	0.25	0.31	0.30	0.30
tensile strength						
longitudinal (MPa)	1100	1400	2000	1728	950	529
transversal (MPa)	35	27	50	40	950	529
compressive strength						
longitudinal (MPa)	800	270	1350	1150	950	529
transversal (MPa)	140	140	170	150	950	529
tensile fatigue strength [1]						
longitudinal (MPa)	220	700	1600	1380	550	173
transversal (MPa)	10	8	15	12	550	173
compressive fatigue strength [2]						
longitudinal (MPa)	160	130	1080	920	550	173
transversal (MPa)	56	56	68	60	550	173
expansioncoëfficient						
longitudinal (10⁻⁶K⁻¹)	7.9	-4	-0.5	-0.5	10	23
tranversal (10⁻⁶K⁻¹)	50	56	50	50	10	23
specific Young's modulus (MNm/kg)	21	58.4	90.2	142.7	26.9	25.6
allowable radius (m) [3]	0.186	0.402	0.574	0.527	0.149	0.140

1) for composites calculated from tensile strength:
   // using fatigue reduction factor for 10^7 cycles, according to [4.11];
   ⊥ using creep reduction factor (0.3) according to [4.6] and [4.7].
2) no data available for U.D. materials; // fatigue/strength ratio supposed similar as for tensile stresses.
   ⊥ using supposed creep reduction factor of 0.4.
3) at 17,000 rpm; for U.D. composites referring to longitudinal tensile fatigue strength.

b) Calculations

In first instance only the centrifugal load situation has been considered. These first orientating calculations have been done by TNO [8.13]. It appeared that the layered principle alone does not give sufficient reduction of radial tensile stresses and relies upon the bonding properties of the composite with the steel.

Therefore the layered principle has been considered further in conjunction with press fitting. This has, in first instance, been done with press fitting at the hub/flywheel interface. The press fitting is realized by means of a conical clamping sleeve between steel rotor and composite flywheel.

- Centrifugal load and press fitting.

The calculations for optimizing the layer thicknesses and press fits have, in first instance, been done by TNO [8.14]. The results have been validated with the newly developed program [8.11] as mentioned in section 8.6.2.

The material data for these calculations are as listed in Table 8.2. The considered dimensions, concerning the preprototype, are (axial dimensions not considered in calculations):
- steel rotor electrical machine   : ϕ 208 x ϕ 255 x 600 mm.
- flywheel disc, steel clamping sleeve : ϕ 255 x ϕ 265 x 110 mm.
  composite rim   : ϕ 265 x ϕ 600 x 100 mm.
The most advantageous radial stress distribution for the above flywheel appeared to be possible with next configuration:
- Material layers : E-glass ϕ 265 x ϕ 390 mm.
  HM-aramid ϕ 390 x ϕ 480 mm.
  HS-carbon ϕ 480 x ϕ 600 mm.
- Press fit   : 600 bar at inner radius composite corresponding with 0.7 mm radial press fit with rotor electrical machine.

The resulting radial and tangential stresses are presented in Fig. 8.15., page 110. From this figure, it can be concluded that it is possible to reduce the radial stresses in the composite material to levels within the fatigue limits, by combining the layered principle and the press fit principle. Moreover, there is no longer need for relying on the bonding between composite and steel. The steel clamping sleeve will, however, be submitted to intolarably high stresses. This will result in plastic deformation of the sleeve and finally fatigue rupture. This aspect is of minor importance for the restricted life testing of the preprototype. It will be dealt with later in the layered principle with double press fit, see section 8.6.4.

- Spin testing
The influence of the applied press fit depends also on the configuration of the inner flywheel hub. The radial stresses in case of a massive hub, as is the case for the spindle for separately spin testing of the flywheel, are illustrated in Fig. 8.16., page 111, for the same radial press fit (0.7 mm) as in case with the rotor of the electrical machine.
By comparing Figs. 8.15. and 8.16. it can be seen that the radial stress amplitudes in the composite material are larger in case of a massive flywheel hub than in case of a hollow flywheel hub. With respect to the maximum radial and tangential tensile stresses, the spin test conditions are about similar to the operational conditions in the machine.

- Thermal stresses
The layered flywheel will also seriously be submitted to thermal stresses. The thermal radial stresses for operating temperatures below (-45°) and above (+60°) the curing temperature (20°C) have been calculated for the above flywheel, using the expansion coëfficients as listed in Table 8.2. Centrifugal load and press fitting have not been considered in these calculations. The results are presented in Fig. 8.17., page 112. It can be seen from this figure that the thermal effect has a considerable influence on the radial stresses. For operating temperatures higher than the curing temperature this effect is advantageous as it causes radial compressive stresses in the flywheel. Care should be taken that, in conjunction with press fitting, the compressive strength is not exceeded at standstill. For operating temperatures below the curing temperature, the thermal effect causes radial tensile stresses. Care should be taken that the radial tensile strength will not be exceeded for the maximum speed condition.

Fig. 8.15. Calculated stress distribution in layered flywheel with (0.7 mm radial) press fit on rotor electrical machine EMAFER preprototype.
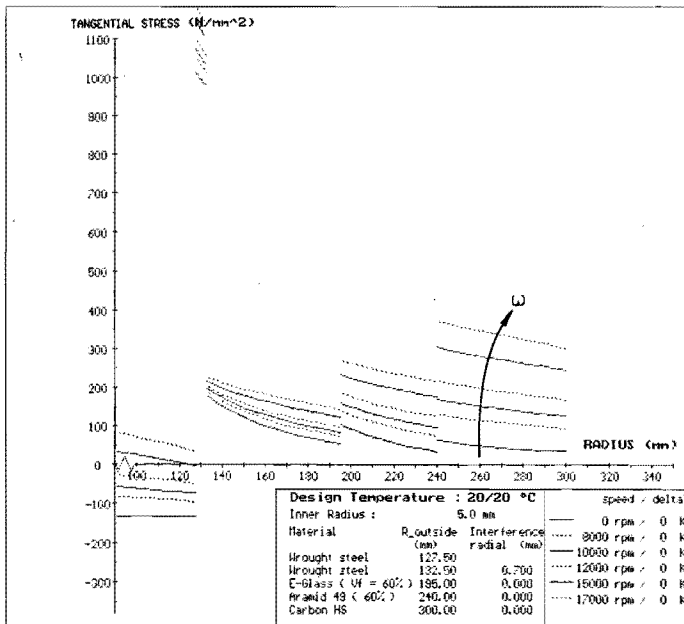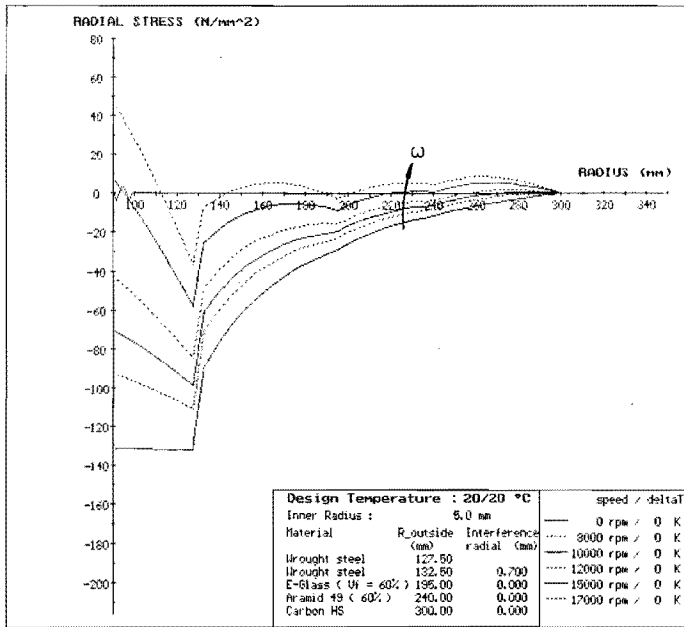
Fig. 8.16. Calculated stress distribution in layered flywheel with (0.7 mm radial) press fit on massive test spindle.
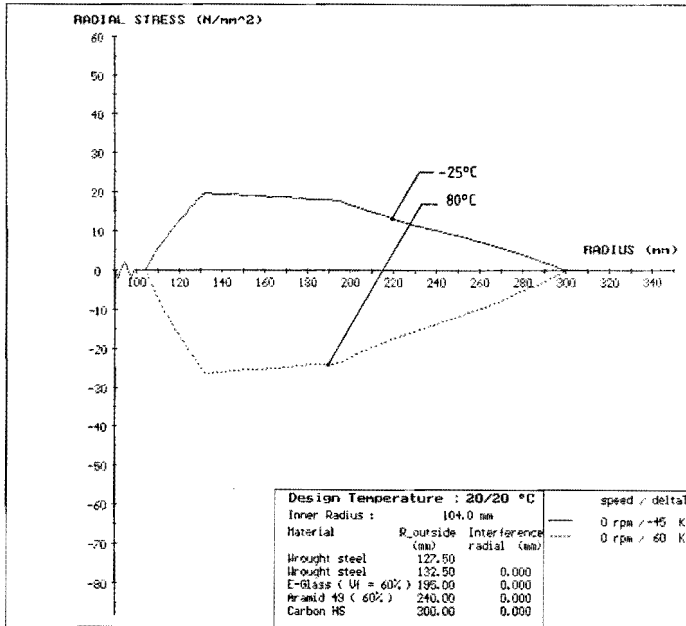
Fig. 8.17. Calculated thermal radial stresses for layered flywheel on rotor electrical machine EMAFER preprototype.

c) Test results

The first test flywheel with layered construction was wound between side plates, directly onto a conical clamping sleeve. The side plates define the width and the conical clamping sleeve can provide the press fit with the rotor of the electrical machine or the test spindle. The flywheel is built up by intermittently winding and curing. In this way resin flow and fibre instability are prevented and a well defined product with relatively high accuracy is possible. It is therefore not needed to process the cured wheel on a lathe for retouching the outer surface. The above test flywheel for the EMAFER preprototype is shown on Photo 8.4.

The spin testing has been done in the same way and in the same test facility as described in section 8.5.3. The wheel was assembled with a radial press fit of 0.7 mm on the massive test spindle. The wheel was spin tested up to 17,000 rpm without showing any sign of failure or defect. This confirms the calculations as presented in Fig. 8.16. Only a small deviation of the imbalance was measured after spin testing, probably due to assessment effects. The spin testing by means of the test facility was not further continued as long duration tests were foreseen using the preprototype assembly. Also in this assembly the flywheel had a radial press fit of 0.7 mm at the rotor/flywheel interface. In the assembly the flywheel could not be spin tested above 12,000 rpm due to a poor rotordynamic system behaviour.

The flywheel was speeded up to 10,000 rpm every day for a period of half a year. It was noticed that the vibration behaviour was reproducable as soon as the unit was at operating temperature. Therefore it can be concluded that up to 10,000 rpm no change of imbalance, due to centrifugal load, occurs, only due to thermal effects.

Then the flywheel was disassembled from the rotor of the electrical machine as the fixation of the rotor magnets had to be repaired and modified. When the flywheel was assembled again with the rotor, a circumferential crack in the aramid layer was noticed at a radius of 215 mm. From Figs. 8.15. to 8.17., representing all the load situations that occurred during testing, it can be seen that the maximum stress at the radius of the crack has not been higher than 5 Mpa. From this it may be concluded that the material properties of the aramid are less than assumed, possibly due to a fabrication failure with resin impregnation of the fibre.

In order to enable further testing with this wheel, the radial press fit was enlarged up to 0.95 mm. The associated calculated stresses, without thermal effects, are presented in Fig. 8.18., page 114. It can be concluded from this figure that radial tensile stresses at a radius of 215 mm will only occur for rotational speeds above 17,000 rpm. Despite of the crack in the aramid layer, testing could thus be continued.

The wheel was tested daily during half a year at 10,000 rpm, for studying the vibration behaviour. No signs of failure were noticed and no change of imbalance due to centrifugal load, only due to thermal effects. Finally the wheel was speeded up to 15,000 rpm during a short time. Due to the poor vacuum conditions and strong vibration levels, it was too risky for long duration tests at this speed. Again no signs of failure have been noticed, thus validating the above calculation results.

However, the steel clamping sleeve is subjected to plastic deformation (tangential stresses out of range of diagram), which will result in premature rupture. This problem can be solved by application of a double press fit in the wheel, see section 8.6.4.
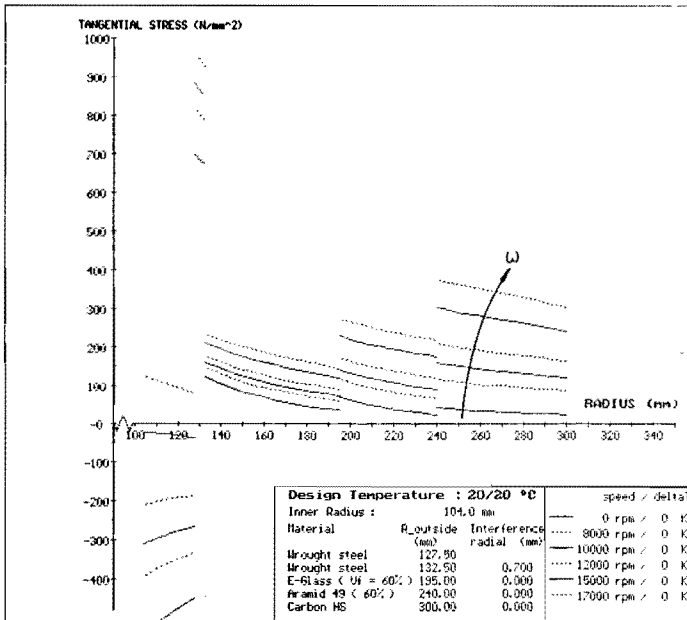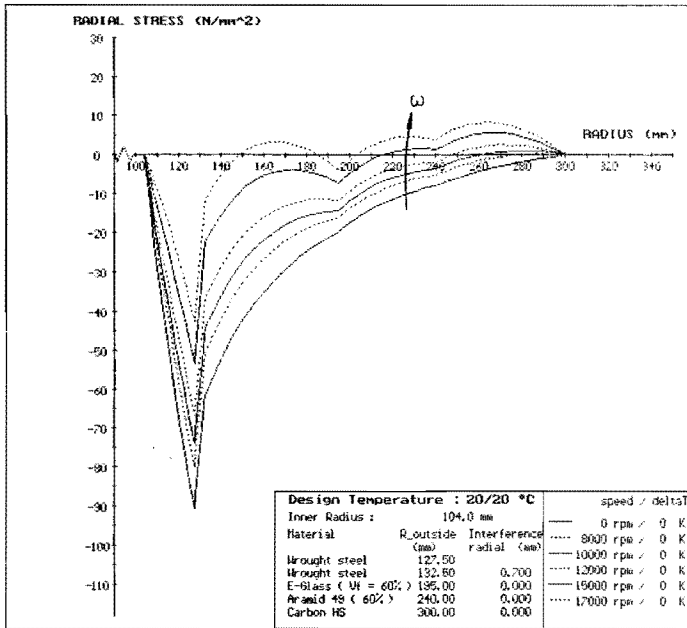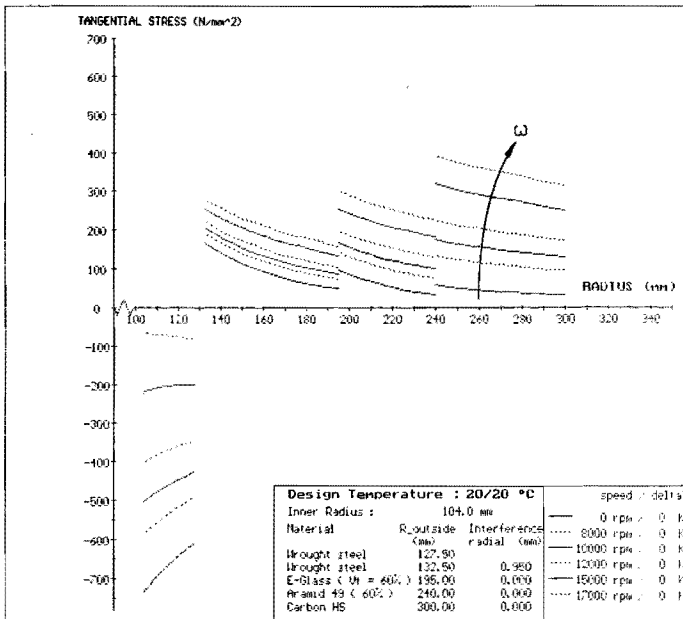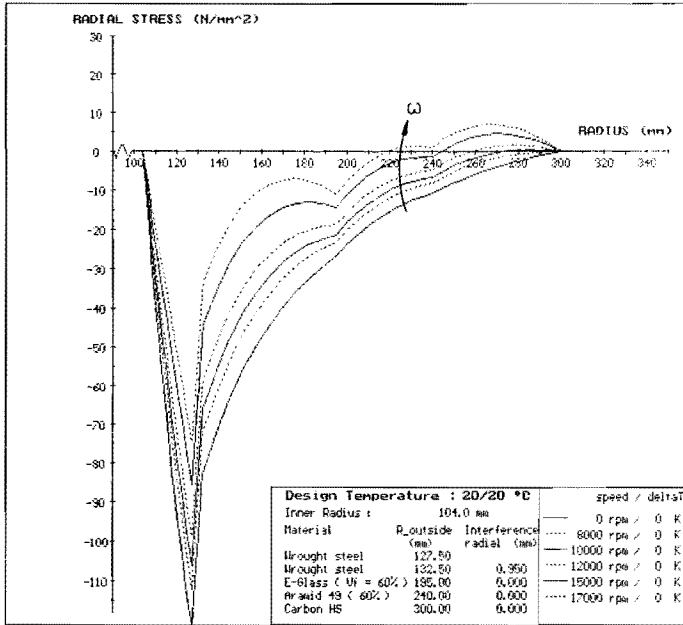
Fig. 8.18. Calculated stress distribution in layered flywheel with 0.95 mm radial press fit on rotor electrical machine EMAFER preprototype.

8.6.4. Layered principle with double press fit

From the preceding section, it follows that a flywheel attachment by press fitting, in conjuction with the layered principle, is an effective method for controlling the stress distribution in a thick rim flywheel. The method is limited by the allowable stresses of the inner material. By also press fitting at an interface radius in the flywheel, the effectiveness of the method can be improved. This has been investigated for the flywheel for the EMAFER prototype.

The flywheel for the EMAFER prototype differs from the flywheel for the EMAFER preprototype on following points:
- Operating speed range: 8,000 - 15,000 rpm.
  Determined by constructive and rotordynamic considerations.
- Diameter dimensions: ϕ 280 x ϕ 680 mm.
  Same circumferential speed and energy density as flywheel for preprototype; the width is unmodified 100 mm.
- Material layers: E-glass, HS carbon and HM carbon composite.
  Aramid epoxy is no longer used due to the negative experiences concerning radial tensile strength.

Within these boundary conditions, several alternatives with respect to layer thicknesses and location and size of press fits have been investigated [8.15]. A flywheel with radial compressive stresses up to the maximum speed appeared to be possible, even without exceeding the fatigue stresses (material data according to Table 8.2.). For practical reasons (number of parts, costs), the glass layer between the two press fit radii and all the clamping sleeves, see Fig. 8.13., were replaced by an aluminium layer (7075-T6). As the mass density of aluminium is higher than of glass composite (respectively 2.7 and 2 kg/dm^3), the energy density of this modified flywheel will be slightly lower, about 3%, than in case of a full composite flywheel. The stresses for the optimal flywheel configuration for the EMAFER prototype are given in Fig. 8.19., page 116. Only centrifugal load and press fit load have been considered here.

From these calculations it can be concluded that no radial tensile stresses occur up to about 16,000 rpm without exceeding the fatigue stresses, in radial as well as tangential direction.

Also thermal effects have been considered as these may influence the above stress distributions negatively. The stresses resulting from centrifugal load, press fits and thermal effects (-45° below and 60° above a supposed curing temperature of 20°C) are illustrated in Fig. 8.20., page 117.

It can be clearly seen from Fig. 8.20. that there are two worst case situations: maximum speed at temperatures below curing temperature and standstill at temperatures above curing temperature. For the flywheel at issue it appeared possible to bring the stresses for these situations below the radial tensile, respectively compressive strength.
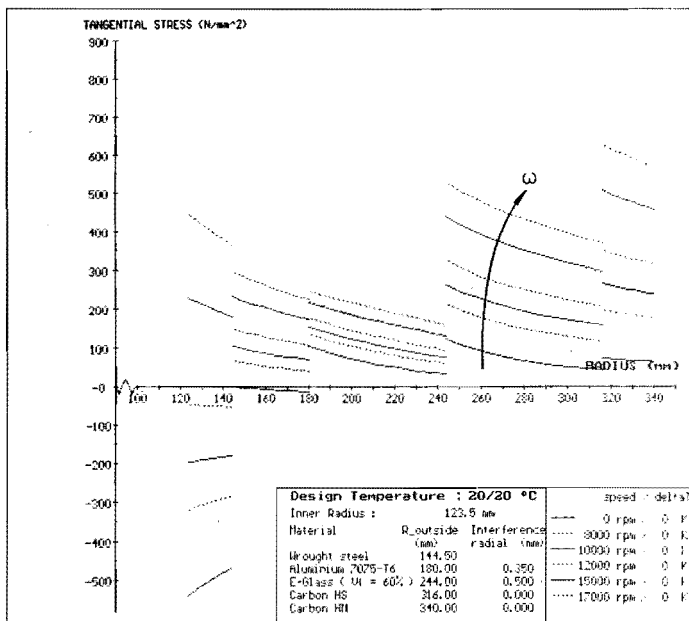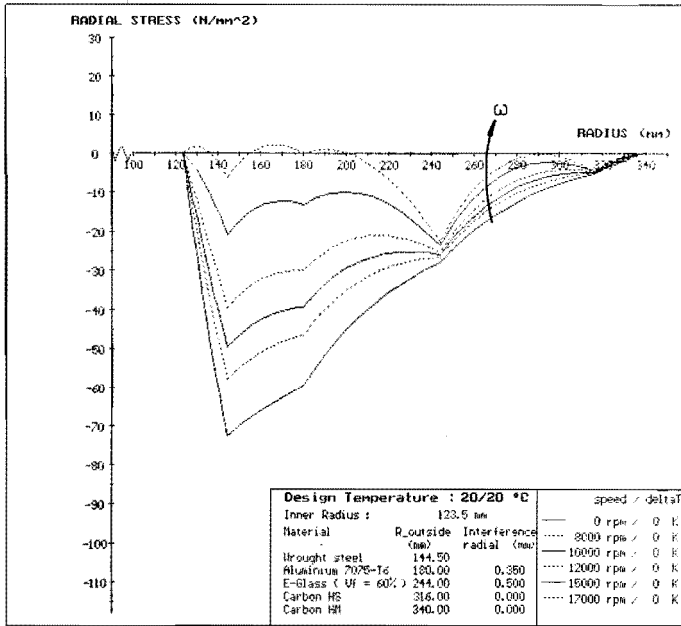
Fig. 8.19. Calculated stress distribution in layered flywheel with double press fit for EMAFER prototype.
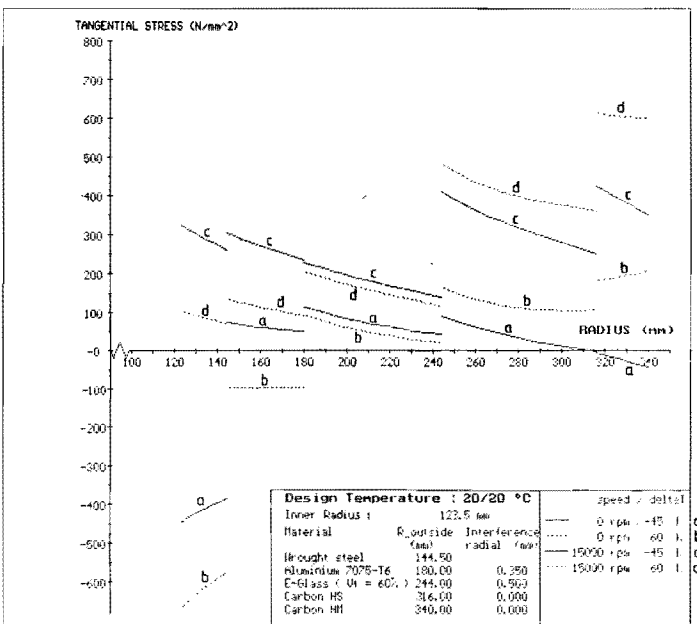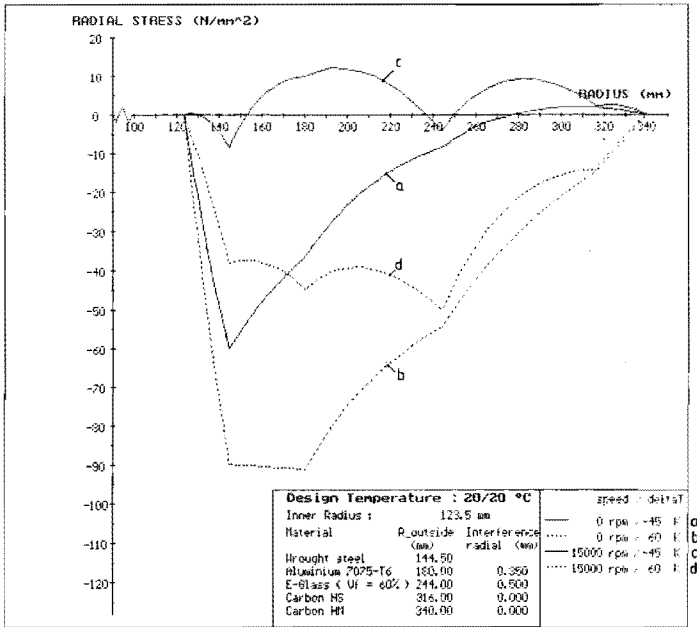
Fig. 8.20. Calculated stress distribution due to combined load situations in layered flywheel for EMAFER prototype.

8.6.5. Conclusions on the layered flywheel

From the above investigations into the layered flywheel, it can be concluded that:
-   The layered principle reduces the radial tensile stresses but is only feasible in conjunction with press fitting. In conjunction with a double press fit, a flywheel without radial tensile stresses is possible.
-   The test results confirm the theoretical considerations.
-   A reliable, fail safe thick rim flywheel is possible.
-   A well defined and reproducable fabrication process is possible. Due to the necessarily long fabrication times it is not so cost effective as the WRWP process.

Similar to the WRWP flywheel it is noted here that possible creep of the materials used may reduce the press fit effects. This can be minimized by a good creep resistance of the inner and outer materials, e.g. steel, respectively carbon epoxy.

8.7. Evaluation

Considering the results of the preceding investigations concerning the WRWP and layered flywheels, the following main conclusion can be drawn:

The layered principle with press fitting enables the most reliable composite thick rim flywheel with high energy density.

However, the fabrication method as followed in this investigation via filament winding, partial curing and finally assembling via press fitting, is not a cost effective method. The WRWP principle on the other hand offers a cost effective fabrication method but at the expense of reliability and energy density of the flywheel. Combining these two principles, layered construction with WRWP fabrication, could offer a cost effective and reproducable fabrication method for composite thick rim flywheels with high energy density.

Chapter 9

Vibration research

9.1. Introduction

The EMAFER flywheel energy storage system is a light weight and compact system related to its energy content and power capacity. Because of the weight and compactness demands, a high speed system with a composite flywheel is involved. The system operates a wide speed range, ratio max:min of about 2:1 and the composite flywheel is expected to suffer from imbalance change and material damping. These characteristics put special demands on the design concerning the rotordynamic behaviour. This has been studied extensively for the EMAFER concept and is reported underneath.

9.2. Objectives

Related to the vibration behaviour, the successful design of the EMAFER concept involves:
- Avoiding critical speeds in the operating speed range.
- Minimizing dynamic response at resonance, if critical speeds must be traversed.
- Minimizing vibration and dynamic loads transmitted to the machine structure, throughout the operating speed range.
- Avoiding rotordynamic instabilities.

Rotordynamic analysis can help to accomplish these objectives. Appendix III: "Vibrations in systems with rotating elements", comprises an explanatory consideration of the subjects concerned with rotordynamics as they have been investigated for the EMAFER concept. For an extensive explanation of rotordynamics, the reader is referred to some good books on this subject [9.1] to [9.3].
For the investigation of the vibration behaviour of the EMAFER concept a simulation model has been set up, which takes into account the influence of mass, stiffness and damping. The masses of the construction parts are greatly determined by their performance demands, whereas the stiffness and damping characteristics of some construction parts can be adjusted to meet the objectives as mentioned above.
The stiffness and damping effects have been investigated seperately by calculations with the simulation model and measurements of the preprototype system. With the help of these results a good rotordynamic design of the EMAFER prototype has been attained.

9.3. Rotordynamic model

A rotordynamic model is indispensable for analyzing and developing high speed rotor systems. It can help to: 1) avoid or to change critical speeds; 2) minimize vibrations and dynamic loads; 3) prevent rotordynamic instability. For these purposes the model has to take into account masses, moments of inertia, stiffness and damping characteristics of the construction parts and the coupling elements, gyroscopy and possible destabilizing effects. This requires a complex simulation model which is only possible with the help of an extensive Finite Element Method (FEM). The complexity is further enlarged when non-linear elements, such as "squeeze film dempers" (SFD's), are involved.

In the case that the natural frequencies of the several construction parts and assemblies of a system are clearly above the maximum rotor speed, these parts may be assumed as rigid body elements. The rotordynamic behaviour can be investigated then, using the more simpler Rigid Body Method (RBM).

The natural frequencies of construction parts and assemblies can be calculated without taking into account gyroscopy, damping and destabilizing forces. A relatively simple FEM can be used then for verifying the rigid body assumption, respectively determining the design modifications to meet this assumption.

For the EMAFER concept, and in general from a rotordynamics standpoint, a rigid body behaviour is preferred. Structural vibrations and fatigue loading of the main construction parts are minimized then, whereas vibrations between the main parts can effectively be taken care of by purpose designed coupling elements with proper stiffness and damping characteristics. The dynamic system behaviour of the EMAFER concept has been investigated with the help of the FEM and the RBM. The FEM for making the conditions for the rigid body behaviour and the RBM for investigating the gyroscopic, damping and possible destabilizing effects.

9.3.1. Finite Element Method (FEM)

Many problems in the field of dynamic system behaviour, e.g. analysis of natural frequencies can be tackled with linear numerical models. For these cases FEM analysis with the help of commercially available program packages that can be run on a PC, can be used. These programs are relatively simple, do not take into account gyroscopic effects, and consider a construction only in a two dimensional way.

From the system equations of motion, the program is able to calculate all kinds of output data, e.g. the natural frequencies with associated mode shapes (in mathematical terms respectively eigenvalues and eigenvectors), amplitudes and forces.

FEM model for EMAFER concept

The natural frequencies of the single construction parts as well as assemblies were calculated with the help of the FEM program package GIFTS [9.5]. The construction parts were modelled as beam elements and the coupling elements as spring elements. Damper elements were not taken into account as a moderate amount of damping does not influence strongly the natural frequencies. The construction is modelled in a two dimensional way in which only lateral vibrations are considered. In Fig. 9.1. the FEM model of the EMAFER preprototype is illustrated. The several construction parts are also indicated.
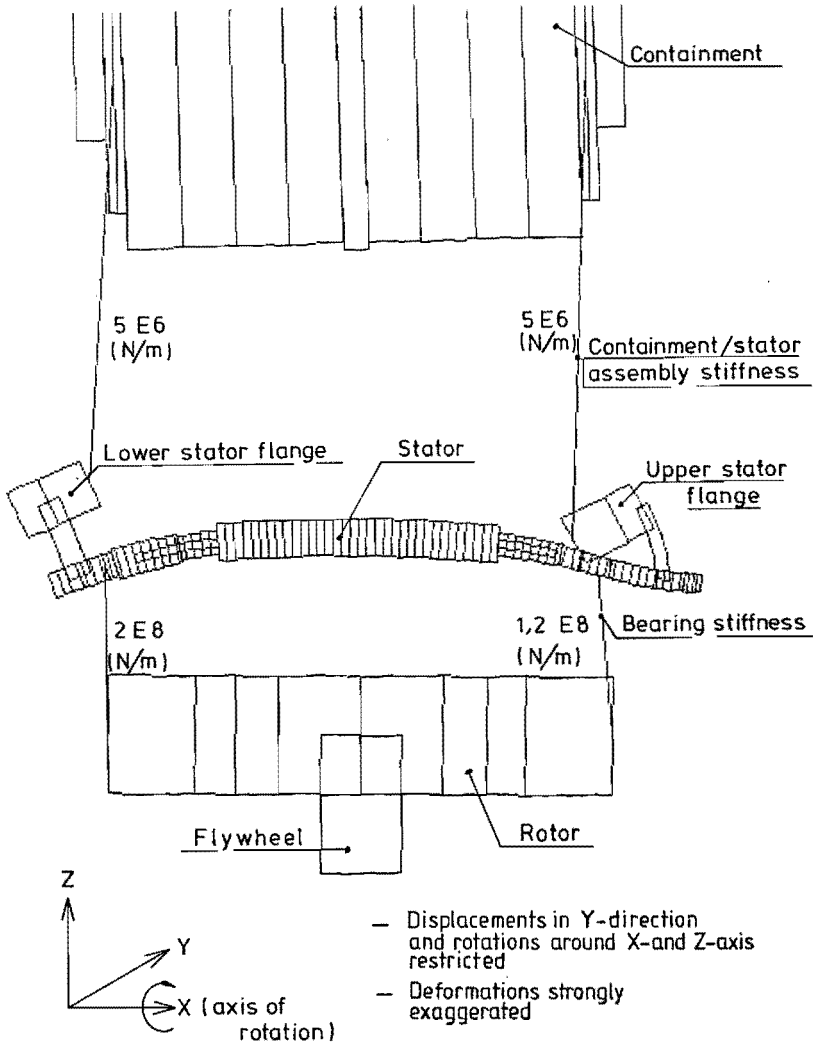
Fig. 9.1. FEM model for EMAFER preprototype.

Experimental analysis

The testing for natural frequencies and associated mode shapes can be done in a relatively simple way with the help of excitation over a certain frequency domain by a vibration generator (shaker excitation). Simultaneously the fundamental harmonics of the response vibration velocity are measured with the help of vibration velocity or acceleration transducers at several places on the system. For this purpose construction parts and assemblies are hung from the ceiling via long ropes (negligible horizontal stiffness) and excited and measured in a direction perpendicular to the axis of rotation and the ropes.

9.3.2. Rigid Body Method (RBM)

The RBM considers the construction parts and assemblies with an infinite stiffness and involves the determination of the total system behaviour while taking into account gyroscopic, damping and destabilizing effects.

The first RBM model of the EMAFER concept was meant for determining the stiffness and damping of the coupling elements in the EMAFER preprototype [9.6]. The rigid body elements, being rotor assembly, stator assembly and containment, were coupled via linearized spring and damper elements, all in symmetric and isotropic configurations. The later RBM model of the EMAFER concept [9.8], for determining the required stiffness and damping of the coupling elements in the EMAFER prototype, is more extended than the first one. It offers the possibility to consider all kinds of stiffness configurations, as well as to introduce SFD's as non-linear damping elements.

RBM model for EMAFER concept
This model consists of four rigid body elements, coupled via spring and damper elements, see Fig. 9.2. For each body element four degrees of freedom are considered, two translations in Y- and Z-directions plus two rotations around Y- and Z-axis. The spring elements between rotor and stator, representing the bearing supports, and between stator and containment can be considered as isotropic as well as anisotropic, being equal respectively different in orthogonal directions. The bearing support stiffnesses can moreover be considered in symmetric as well as asymmetric configurations, being equal respectively different at both ends of the machine.

For taking into account destabilizing internal damping, due to hysteris of the composite flywheel material, the rotor assembly can be subdivided into two rigid body elements coupled via a stiffness and a damping [9.8].

The equations of motion have been derived with the help of the conditions for equilibrium. The several body elements can be subjected to forces and moments due to acceleration, spring and damper elements, gyroscopy and excitation, e.g. imbalance. This results in a system of 16 second order differential equations. For the derivation of these equations, see [9.7] and [9.8].
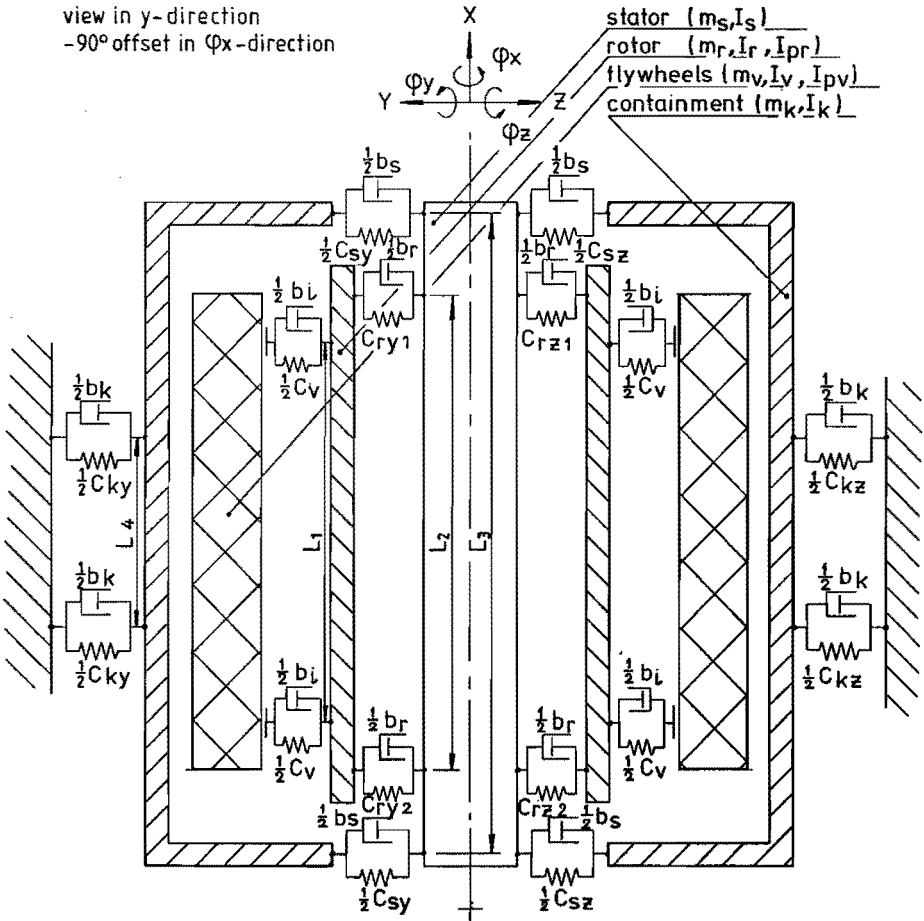
Fig. 9.2. RBM model for EMAFER concept.

a. Linear situation

For the linear situation and without excitation the total system equation of motion, written in matrix notation, is given by:

$$M.\frac{d^2r}{dt^2} + (G + B_e + B_i).\frac{dr}{dt} + (K - j.\Omega.B_i).\underline{r} = \underline{0} \qquad (9.1)$$

in which
$\qquad$ M $\;=\;$ the mass matrix
$\qquad$ G $\;=\;$ the gyroscopic matrix
$\qquad$ B_e $\;=\;$ the external damping matrix
$\qquad$ B_i $\;=\;$ the internal damping matrix
$\qquad$ K $\;=\;$ the stiffness matrix
$\qquad$ Ω $\;=\;$ the spin speed
$\qquad$ $\underline{r}$ $\;=\;$ the displacement vector

The time dependent character of the vibration amplitude can be found by substituting in eq. (9.1):

$$\underline{r} = \underline{a} \cdot e^{\lambda t} \tag{9.2}$$

In this way eq. (9.1) can be transformed into usual eigenvalue problem in which λ respresents the eigenvalues of the transformed system matrix. With the eigenvalues, the natural frequencies of the system are known as these are the imaginary parts of the eigenvalues. In the case of damping and/or destabilizing forces also the stable or unstable character of the associated vibration modes is known. This is represented by respectively a negative or a positive real part of the eigenvalues.

The effectiveness of the stiffness and damping values of the coupling elements is usually evaluated with the help of the imbalance transmissibility factor. This is the ratio of the flexible coupling force due to imbalance to the imbalance force itself. For designing of the coupling elements the absolute displacements have to be known and for these purposes the **displacement imbalance response** is therefore preferred above the imbalance transmissibility factor.

The displacements in the coupling elements, due to imbalance, can be calculated from the inhomogeneous system equation of motion:

$$M \cdot \frac{d^2 \underline{r}}{dt^2} + (G + B_e + B_i) \cdot \frac{d \underline{r}}{dt} + (K - j \cdot \Omega \cdot B_i) \cdot \underline{r} = \underline{F} \tag{9.3}$$

in which $\underline{F}$ is the imbalance excitation vector.

b. Non-linear situation

The above mathematical model of the EMAFER concept represents the linear situation. However, it is also suitable for the non-linear situation. This is possible by taking into account the non-linear behaviour of the concerning elements in the system equations of motion in an itterative way. By assuming a value of the eccentricity, studying the behaviour of the system, computing the resulting amplitudes and then repeating the calculations, the actual amplitudes can be calculated.

Computer model

For further calculation of the above mathematical model, a computer program has been written [9.8]. This program calculates from the design parameters (masses, moments of inertia, stiffness and damping values) for several spin speeds the eigenvalues, the imbalance transmissibility factor and the displacement imbalance response as required. A graphical procedure can draw from these results the following maps:
- The spin-whirl map: the graphical presentation of the natural frequencies of all vibration modes as a function of the spin speed.
- The stability map: the graphical presentation of the eigenvalues in their complex coordinates for various spin speeds.
- The transmissibility map: the graphical presentation of the ratio of the flexible coupling force to the imbalance force as a function of the spin speed.

- The displacement map, which is a variant on the transmissibility map: the graphical presentation of the displacements in the coupling elements due to imbalance as a function of the spin speed.

Experimental analysis

The experimental analysis of the system behaviour can be done by means of so called proximity probes at the coupling elements of the assemblies. By placing the proximity probes in orthogonal directions, the whirl orbits can be measured and so the imbalance response and the critical speeds.

Instability problems can be identified with the help of the **waterfall or cascade** plot [9.1] in which the results of spectrum analysis from a Fast Fourier Transform (FFT) unit are plotted at various spin speeds. An instability manifests itself by a subsynchronous, fixed (or only slightly changing) frequency vibration, increasing rapidly with increasing spin speed. In addition to identifying rotordynamic instabilities, these maps quickly indicate which components are related to rotational speed.

9.4. Stiffness effects

Proper stiffness characteristics of construction parts and coupling elements are required for prevention or reduction of structural vibrations below the maximum speed as well as avoiding critical speeds in the operational speed range. This has been investigated for the EMAFER prototype.

By first investigating the natural frequencies for the stationary system and in succession for the dynamic system, effective design modifications for the above purpose have been determined.

9.4.1. Natural frequencies of the stationary system (zero rotor speed)

In this analysis the rotary influence of rotating elements is not taken into account. This offers the possibility for considering the construction parts with a relatively simple FEM package. Also measurements can easiest be done at the stationary system. See also section 9.3.1.

The following analysis commences with the preprototype construction and predicts in succession the effects of the design modifications for the prototype construction.

Preprototype construction.

In the design phase the preprototype construction has been analyzed assuming the stator and rotor assembly as well as the containment as rigid body elements, see also section 9.3.2. This analysis is described in [9.6]. As the measurements on the realized system gave more and different natural frequencies from those calculated, the model was in doubt.

It was necessary to do a further investigation into the natural frequencies. Because of the complexity of the system this was done progressively with the help of theoretical and experimental investigations of the construction parts as well as of the total stationary system. An extensive report of these investigations is given in [9.5].

The natural frequencies and associated mode shapes of several assemblies have been calculated with the help of the FEM model for the EMAFER concept as discussed in section 9.3.1. This model calculates the natural frequencies and mode shapes from the geometrical dimensions plus material data (mass density and Young's modulus) of the construction parts and the stiffness characteristics of the coupling elements.

Most of these natural frequencies and mode shapes have also been measured for evaluation of the simulation model. This was done progressively: stator construction, stator construction with stator flanges (stator assembly), stator assembly with rotor, stator assembly with rotor and flywheel and finally the total assembly as illustrated in Fig. 9.1., section 9.3.1. This method was followed to get a good apprehension and insight into the influence of construction parts and assemblies on the vibration behaviour. Also parameters of the construction parts (e.g. the effective diameter for the stiffness of the lamination stack and the bearing stiffness) could be determined in this way. It is noted that the EMAFER preprototype has been constructed with relatively high bearing stiffness (about 2.0 E8 N/m per bearing) and a relatively weak (5.0 E6 N/m per side) stator/containment coupling. The bearing stiffness is determined by the preloaded angular contact ball bearings themselves as these are mounted directly on the shaft and not via flexible elements, see also section 7.8.

The weak stator/containment coupling was needed for practical reasons as a hard coupling gave misalignment of the bearings, which resulted among others in a malfunctioning of the preload system of the bearings and with this in bearing damage. The above investigations were done for frequencies up to about 1500 Hz (about 90,000 rpm) for which several natural frequencies and mode shapes were found. An overview of the most important calculated and measured results of the representative assemblies is given in Table 9.1.

Table 9.1. Natural frequencies and mode shapes of several assemblies of EMAFER preprototype, stationary case.

Assemblies with vibration mode shape* of EMAFER preprototype, see Fig. 9.3.	Natural frequencies (Hz)		Difference (%)
	calculated	measured	
1. Stator (effective stiffness diameter 85 mm)			
first bending mode	802	777	+ 3.2
second bending mode	1180	1215	- 2.9
2. Stator assembly (Stator and flanges)			
tilt mode upper stator flange	122	119	+ 2.5
first bending mode stator	211	225	- 6.2
second bending mode stator	374	317	+ 18.0
third bending mode stator	705	713	- 1.1
3. Stator assembly with rotor*			
tilt mode upper stator flange	121	125	- 3.2
first translation mode rotor/stator	202	200	+ 1.0
second translation mode rotor/stator	287	292	- 1.6
first tilt mode rotor/stator	370	405	- 8.7
second tilt mode rotor/stator	569	567	+ 0.4
4. Stator assembly with rotor and flywheel*			
tilt mode upper stator flange	121		
first translation mode rotor/stator	200	not	
second translation mode rotor/stator	258	measured	
first tilt mode rotor/stator	361		
second tilt mode rotor/stator	524		
5. Stator assembly with rotor and flywheel and containment*			
translation mode containm./stator	56	52	+ 7.6
tilt mode containm./stator	66	90	- 25.5
tilt mode upper stator flange	130	160	- 18.8
first translation mode rotor/stator	193	208	- 7.2
second translation mode rotor/stator	266	252	+ 5.5
first tilt mode rotor/stator	310	300	+ 3.3
second tilt mode rotor/stator	540	555	- 2.7

*Note: the first translation and tilt mode of rotor/stator involve mainly stator deflections (first and second bending mode of stator) whereas the second translation and tilt mode of rotor/stator (modified first and second bending mode, due to stator flanges) involve stator deflections as well as bearing deflections.

From these results, it follows that all the mode shapes found, involve bending of the stator. The stator itself has bending modes with relatively high natural frequencies, which are strongly reduced by adding the stator flanges. Compare situations 1 and 2 in Table 9.1.

By adding the rotor and flywheel via high stiffness bearings to the stator assembly, respectively situations 3 and 4, a translation and a tilt mode appear for natural frequencies within the operating speed range (8,500 - 17,000 rpm, corresponding with 142-283 Hz). The completion of the system with the containment, situation 5, introduces two additional rigid body modes, a translation and a tilt mode, of stator/containment. Because of the weak stator/containment coupling, these are at low natural frequencies.

It can be concluded that:
- The natural frequencies within the operating speed range are caused by the flywheel motor/generator unit. This is in turn mainly due to the combination of slender stator journals with relatively heavy stator flanges and relatively high bearing stiffness.
- The containment hardly influences the vibration behaviour within the operating speed range.

From these conclusions it follows that design modifications are necessary in order to avoid natural frequencies within the operating speed range. These design modifications concern stator assembly and bearing support construction.

Concerning the stator assembly, there are two principal solutions for modifying the construction: reducing the stiffness characteristics in order to shift the natural frequencies caused by the stator assembly to below the operating speed range, or enlarging the stiffness characteristics in order to shift the natural frequencies caused by the stator assembly to above the operating speed range. The second solution is preferred because it will result in a more robust construction part, ensuring a better loading capability, e.g. with respect to torque loading and shock loading in case of a failure. Further this part will be no longer subjected then to dynamic fatigue loading due to structural vibrations.

The stiffness of the ball bearings is relatively high, of the order of 2.0 E8 N/m, and can only considerably be reduced by the bearing support construction. With the option of enlarged stiffness of the stator assembly, the bearing support is from a rotordynamics point of view preferred to be more flexible than the stator as well as the rotor. A low support stiffness reduces the dynamic loads transmitted through the bearings, thus prolonging bearing life, and allows for an effective damping at the bearing location. These design modifications, enlarged stator stiffness and reduced bearing stiffness, have been investigated as to their effects on the natural frequencies for implementation in the prototype construction.

Prototype construction
With respect to the vibration behaviour, the main differences in the prototype construction compared to the preprototype construction are:
- Enlarged energy storage capacity by enlarged flywheel height: 400 mm instead of 100 mm.
- Increased stator stiffness.
- Weak bearing supports.
- Modified operating speed range: 8,000-15,000 rpm.

The stator/containment coupling is again relatively weak (1.0 E6 N/m per side). A stiff stator/containment coupling would have the same effect as a stiffly coupled rotor, namely structural vibrations of the stator within the operating speed range. In the prototype all three main parts (stator, rotor, containment) are weakly coupled, thus ensuring "compliance" of the parts and reducing dynamic loads and minimizing structural vibrations.

With the help of the FEM model, based on a preliminary design of the prototype [9.9], the effect of the above design modifications on the natural frequencies has been predicted [9.7]. The effective stiffness diameter of the lamination stack was assumed 100 mm, whereas the bearing support stiffness was 2.5 E7 N/m per side and the stator/containment stiffness 1.0 E6 N/m per side. The influence of the containment appeared to be negligible on the natural frequencies of translation and tilt.

In an attempt to enlarge the range between the natural frequencies of translation and tilt, the influence of different support stiffnesses for each bearing has been investigated. It appeared that this method is effective as can be seen in Table 9.2. The range between the natural frequencies of translation and tilt increases in this example by about 50%. However, this range is still not wide enough to cover sufficiently the total operating speed range. One of the natural frequencies of translation or tilt, depending on the bearing support stiffness, will still be within or near the operating speed range.

Table 9.2. Natural frequencies rotor/stator of EMAFER prototype, stationary system, with respect to bearing support stiffness.

Support stiffness (N/m)		Natural frequencies rotor/stator			
Upper bearing	Lower bearing	Translation mode		Tilt mode	
		(Hz)	(rpm)	(Hz)	(rpm)
2.5 E7	2.5 E7	118	7,080	232	13,920
1.0 E7	5.0 E7	93	5,580	258	15,480

9.4.2. Natural frequencies for the dynamic system (non-zero rotor speed)

The natural frequencies of the EMAFER prototype have been further investigated taking into account gyroscopy in combination with different configurations for bearing support stiffnesses: symmetric and asymmetric, i.e. equal or unequal at both ends, as well as isotropic and anisotropic, i.e. equal or unequal in orthogonal directions. As only the natural frequencies in or near the operational speed range are considered here, the influence of the containment can be neglected, see also section 9.4.1. The rotor assembly is, because of the rigid flywheel attachment, for these purposes considered as one rigid body element. These simplifications allow for a more explicit analysis of the above influences on the natural frequencies of the flywheel motor/generator unit. The RBM model for the EMAFER concept can be reduced then to two rigid body elements, being the stator and the rotor assembly, coupled via four spring elements, see also Fig. 9.2.

The system is further considered as a free system, not coupled to the earth, where only the natural frequencies of stator and rotor assembly with respect to each other are of interest. As the model has two elements with each four degrees of freedom, there will thus be eight non-zero natural frequencies to be considered, four associated with cylindrical modes and four with conical modes.

These natural frequencies are represented in the spin-whirl map. As contracted with the example of this map in Appendix III, section III.2., in the further considerations all natural frequencies have been represented in the first quadrant of this map. In this way the forward (FW) and backward whirling (BW) speeds associated with gyroscopy, can be easily recognized by respectively with rotor speed inclining and declining curves.

In this way, the influence of the bearing support stiffness configuration has been studied. On the basis of the most suitable configurations, the critical speeds of the complete prototype system have been determined in succession.

Bearing support stiffness configurations
Four different bearing support configurations have been studied:

a. Symmetric isotropic bearing stiffnesses
This is the most simple situation in which all four stiffnesses between rotor and stator are equal. For this situation the course of the natural frequencies is represented in Fig. 9.3.
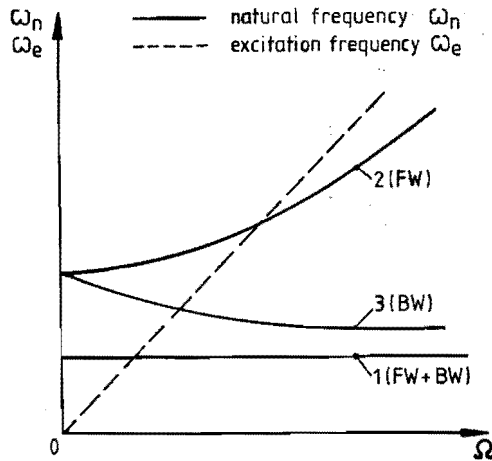
Fig. 9.3. Spin-whirl map of EMAFER flywheel motor/generator unit with symmetric isotropic bearing stiffnesses.

From this figure it can clearly be seen that line 1 and curves 2 and 3 concern the natural frequencies for respectively a cylindrical mode and a conical mode. The natural frequencies associated with the cylindrical mode are in this case independent of spin speed as no gyroscopy is involved.

There are four natural frequencies found which can be associated with the cylindrical mode: for each orthogonal direction a conjugate pair. For isotropic stiffnesses these frequencies are equal for the two orthogonal directions. When plotting these in the first quadrant, all four can be represented by one horizontal line 1.

The natural frequencies associated with the conical mode depend on the spin speed, curves 2 and 3 in Fig. 9.3. Four solutions are found, two conjugate pairs. When plotting these in the first quadrant, the curves 2 and 3 are found, curve 2 having the sloping asymptote $\omega = \Omega.Ip/Ieq$, see also Appendix III, section III.2.

When referring to the most prevalent excitation, namely imbalance, represented in Fig. 9.3. by the $\omega_e = \Omega$ line, it can be concluded that for the considered system and speed range a maximum of two critical speeds can occur. Excitations with backward components, also represented by the $\omega_e = \Omega$ line in Fig. 9.3., e.g. harmonically varying excitation with fixed position, should be avoided as they can excite additional backward natural frequencies, which results in a smaller speed range between two neighbouring critical speeds.

b. Asymmetric isotropic bearing stiffnesses
For this situation, with different stiffnesses at both rotor/stator ends and equal stiffnesses in orthogonal directions, the course of the natural frequencies of the flywheel motor/generator unit is represented in Fig. 9.4.
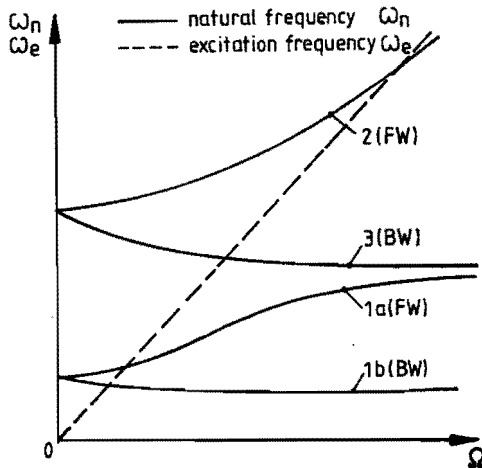
Fig. 9.4. Spin-whirl map of EMAFER flywheel motor/generator unit with asymmetric isotropic bearing stiffnesses.

Comparing Figs. 9.3. and 9.4., it can be seen that the most significant effects of asymmetric, compared to symmetric, bearing stiffnesses are:
- The natural frequencies of the cylindrical mode being dependent on spin speed. Forward whirling speeds (curve 1a) and backward whirling speeds (curve 1b) can be distinguished for the cylindrical mode.
- Enlarging of the speed range between the two neighbouring critical speeds of the cylindrical and conical modes.

c. Symmetric anisotropic bearing stiffnesses

In this case the stiffnesses at both rotor/stator ends are equal whereas the stiffnesses in orthogonal directions are different. The course of the natural frequencies of the flywheel motor/generator unit for this situation is represented in Fig. 9.5.
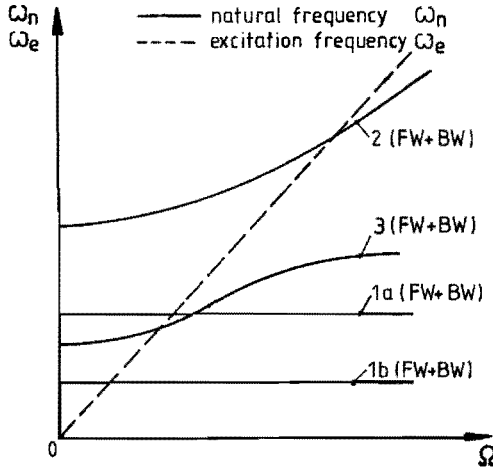
Fig. 9.5. Spin-whirl map of EMAFER flywheel motor/generator unit with symmetric anisotropic bearing stiffnesses.

Comparing Fig. 9.3. and 9.5., it can be seen that anisotropic, compared to isotropic bearing stiffness, results in:
- An additional natural frequency curve for the cylindrical mode. In Fig. 9.5. curves 1a and 1b represent the natural frequency curves for the cylindrical modes.
- Moving away from each other the natural frequency curves for the conical modes. In Fig. 9.5., curves 2 and 3 represent the natural frequency curves for the conical modes. It is not possible any more to distinguish which curves represent the frequencies, which will be excited by either forward or backward excitations. Anisotropy will namely force any response into an elliptical response with forward and backward components for the excitation.

Anisotropic, compared to isotropic bearing stiffness, will thus cause the double number of critical speeds. From the point of view of minimizing the number of critical speeds, anisotropy in bearing stiffness should be avoided therefore.

d. Asymmetric anisotropic bearing stiffnesses

This situation, for which all four bearing stiffnesses are different, is not extensively considered, as the effects for imbalance excitation can be predicted from the preceding situations:
- Similar to the situation with asymmetric isotropic bearing stiffnesses, the speed range between two neighbouring critical speeds of the cylindrical and conical modes will be enlarged compared to the situation with symmetrical bearing stiffnesses.

- Similar to the situation with symmetric, anisotropic bearing stiffnesses, a maximum of four critical speeds will be found: two for the cylindrical mode and two for the conical mode.

From the above considered bearing stiffnes configurations, it can be concluded that asymmetry, compared to symmetry, enlarges the speed range between two neighbouring critical speeds whereas anisotropy, compared to isotropy, decreases this speed range by causing additional critical speeds.

Critical speeds of EMAFER prototype

The critical speeds of the EMAFER prototype can be found from the spin-whirl map of the complete system, see also Appendix III, section III.2. The spin-whirl map has been determined for the design parameters as they apply for the EMAFER prototype according to the final design [9.10]. The operating speed range of this design is 8,000 - 15,000 rpm. The design parameters as used in the calculations are listed in Table 9.3. The total mass of the prototype system is not as low as required. This is mainly due to the stage of the development. In this stage the safety function of the containment is probably overdone and the stator assembly has some additional parts for test purposes.

For calculating the spin-whirl map, damping is not taken into account as this only slightly influences the critical speeds. The coupling stiffnesses between rotor, stator, containment and earth are the realized stiffness values, which are comparable with those found from the considerations in section 9.4. The flywheel/rotor coupling stiffness has been calculated from the lowest measured natural frequency of a prototype flywheel disc.

Table 9.3. Design parameters of EMAFER prototype, see also Fig. 9.2.

Construction assemblies	Masses (kg)	Moments of inertia		Coupling stiffness in orthogonal radial directions (N/m)	Distance between couplings (m)
		polar (kgm²)	equatorial (kgm²)		
Containment (earth)	290		24	2.0 E6	0.20 (L4)
Stator (containment)	160		6.30	2.0 E6	0.75 (L3)
Rotor (stator)	114	1.70	4.40	upper 7.0 E6 lower 6.0 E7	0.61 (L2)
Flywheel (rotor)	220	13.70	10.70	1.0 E9	0.40 (L1)

* in parentheses: via indicated stiffness coupled part.

The spin-whirl map as calculated from the parameters in Table 9.3. is displayed in Fig. 9.8. From this map, it can be seen that, at least as long as backward excitations are prevented, the EMAFER prototype has an operating speed range free of critical speeds.

This is possible thanks to the asymmetric bearing support stiffnesses and the gyroscopic effect by which the natural frequency of especially the conical mode rotor/stator is considerably raised, see also Fig. 9.6.

In total there are eight critical speeds in the system, preconceived there are no backward excitations. Besides the first critical speed of the flywheel motor/generator unit at about 5,000 rpm, there are also four lower critical speeds between 500 and 2,500 rpm. These are due to the weak couplings of the total system to the earth and of the flywheel motor/generator unit to the containment.

The second critical speed of the flywheel motor/generator unit is at about 28,000 rpm and is clearly above the operating speed range. There are still two higher critical speeds. These are due to the rigid flywheel/rotor attachment.

In this way all critical speeds are clearly below and above the operating speed range, thus allowing for a good vibration behaviour in the operating speed range.

Natural frequency curves

1. tilt flywheel/rotor
2. translation flywheel/rotor
3. tilt rotor/stator
4. translation rotor/stator
5. tilt containment/stator
6. translation containment/stator
7. tilt containment/earth
8. translation containment/earth
a = Forward whirling modes
b = Backward whirling modes
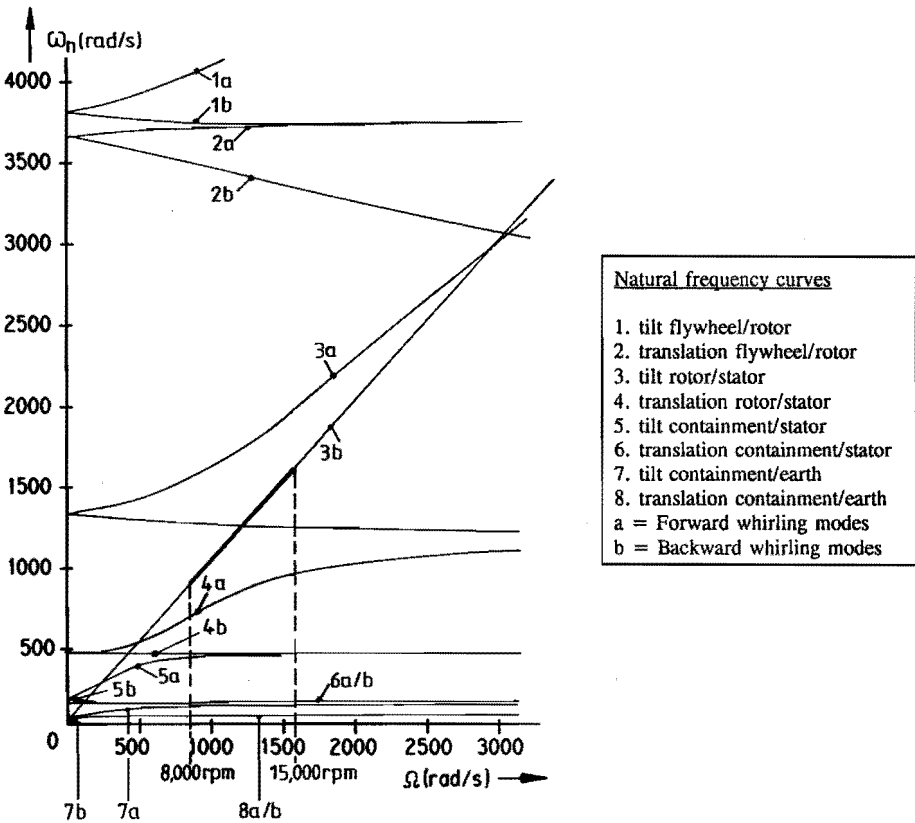
Remark: the forward and backward natural frequency curves of modes 6 as well as mode 7 coincide as these modes are almost purely translational.

Fig. 9.6. Spin-whirl map of EMAFER prototype.

9.5 Damping effects

Proper damping characteristics of the coupling elements are required to attenuate resonant vibrations and to suppress rotordynamic instability. This has been investigated for the EMAFER prototype with the help of the RBM model as discussed in section 9.3.2. In the first instance coupling elements with ideal linear viscous damping have been assumed for investigating the damping requirements of the construction. In succession the total system behaviour has been calculated taking into account the non-linear behaviour of the required SFD's.

9.5.1. Damping parameters

For the EMAFER prototype, elastomeric dampers and SFD's have been considered. Both are non-linear elements. However, for investigating the damping requirements of the construction, a linearized approach is very helpful. The damping values as used in this approach are listed in Table 9.4. It is noted that it is very difficult to determine accurately the damping values. Fortunately the vibration behaviour has no strong sensitivity with respect to the damping values as followed from the investigations into the damping effects [9.8].

For the elastomeric coupling elements the damping value is assumed to be 5% of the critical value of damping, following measurements of [8.8]. For a complex system this value can be determined with the help of the lowest natural frequency. The critical value of damping given in eq. (III.4) section III.3., is therefore written as:

$$B_{crit} = 2\sqrt{cm} = 2\sqrt{\frac{c}{m} \cdot m} = 2\omega_n \cdot m = 2\frac{c}{\omega_n} \qquad (9.4)$$

in which B_{crit} = the critical damping, c = the effective stiffness, m = the effective mass and ω_n = the natural frequency which can be allocated to the mass-spring system in question.

SFD's can have considerably higher damping values than elastomeric dampers, but it is uncommon to express these as a percentage of the critical damping. In the linear approach a high, as obtainable for SFD's, and constant damping value is assumed.

The damping value of the flywheel material is, following the measurements at the flywheel of the EMAFER preprototype, maximum 1% of the critical value of damping [9.6].

Damping in the rotor assembly, which can in the case at issue be due to material damping and damping in fit interfaces, has a destabilizing effect, see also Appendix III, section III.3. All rotor damping is further supposed to be concentrated in the flywheel material for which an enlarged damping value is assumed, being 5% of the critical value of damping. Together with no damping at the bearing supports, thus a worst case situation with respect to the stability behaviour of the system will be considered.

Table 9.4. Damping values EMAFER prototype for linearized consideration, see also Fig. 9.2.

Coupling element	Natural frequency (Hz)	Damping value (total) (Ns/m)	
		elastomeric	SFD
Earth/containment	7	4,500	--
Containment/stator	20	1,600	10,000
Stator/rotor (bearing supports)	78	0	10,000
Rotor/flywheel	592	26,800	--

For the design of the SFD's, and for considering their rotordynamic effects, the non-linear behaviour of the SFD's has been taken into account. This has been done with the help of [9.4] where the damper forces are derived for non-sealed short and long SFD's, both cavitated and uncavitated.

Cavitation is undesirable from a rotordynamics standpoint as it can introduce non-linear jump phenoma [9.1]. As shown in [9.4], the damper forces of an uncavitated SFD will be composed of a tangential component caused by viscous effects and a radial component caused by fluid inertia effects. The tangential component has a damping capability, whereas the radial component has a dynamic stiffness effect. However, in this case the radial fluid inertia forces are negligible compared to the rotor inertia forces and are therefore not further considered.

In the EMAFER prototype, the short sealed SFD is preferred as this type is very advantageous with respect to the prevention of cavitation, the required oil flow rates and its compactness. The forces of the short sealed SFD can be described with the help of the formulas for a short non-sealed damper by multiplying these forces with a factor 4, to take sealing into account [9.11]. For the short sealed and uncavitated SFD, the tangential damping force is described then by:

$$F_t = \frac{2\pi\mu R L^3 \dot{\psi} \epsilon}{C_r \left(1 - \epsilon^2\right)^{3/2}} \tag{9.5}$$

Where
- F_t = tangential damper force (positive when applied as force opposite to circumferential orbit velocity)
- μ = dynamic viscosity of the fluid
- R = journal radius
- L = damper length
- C_r = radial clearance
- ϵ = eccentricity ratio = e/C_r, where e = journal eccentricity
- $\dot{\psi}$ = angular whirl velocity

This damping force is strongly non-linear related to journal eccentricity for eccentricity ratios larger then 0.4 [9.4]. The non-linear behaviour of the elastomeric elements will be of minor importance for the total system behaviour, due to their considerably lower damping capability with respect to the SFD's. They have therefore been taken into account as linear elements with damping values as listed in Table 9.4.

9.5.2. Damping requirements

For investigating the damping requirements of the system, linear viscous damping is assumed as this, with respect to non-linear damping, considerably facilitates the calculations without affecting the conclusions concerning damping requirements. The damping effects are expressed in terms of suppressing rotordynamic instability and attenuation of resonant vibration, respectively via the stability and the displacement maps. Therefore four damping configurations, as listed in Table 9.5., have been investigated [9.8]. For the design parameters, see Tables 9.3. and 9.4.

Table 9.5. Damping configurations for EMAFER prototype.

Configuration* Coupling element	1	2	3	4
Earth/containment	elastomeric	elastomeric	elastomeric	elastomeric
Containment/stator	elastomeric	SFD	elastomeric	SFD
Stator/rotor	no damping	no damping	SFD	SFD
Rotor/flywheel	elastomeric	elastomeric	elastomeric	elastomeric

* For numeric damping values, see Table 9.4. and eq. (9.5) for non-linear SFD's.

Stability map
The stability map represents the course of the eigenvalues with varying spin speeds. As each eigenvalue is associated with a particular mode, it can be seen directly from this map which mode for what rotor speed tends to instability. This is illustrated for the extreme damping configurations 1 and 4 in above table, respectively in Figs. 9.7. and 9.8. The stability line, see also Appendix III, section III.3., represents a logaritmic decrement of about 0.06, corresponding with a damping ratio of 1%. This value is generally assumed to assure sufficient rotordynamic stability.
It can be concluded from Figs. 9.7. and 9.8. that:
- With only elastomeric damping elements and no bearing support damping, the rotor/stator modes will practically become unstable, see Fig. 9.7.
- SFD's at the containment/stator couplings as well as at the bearing supports considerably improve the stability behaviour of all modes, no modes tend to instability anymore, see Fig. 9.8.
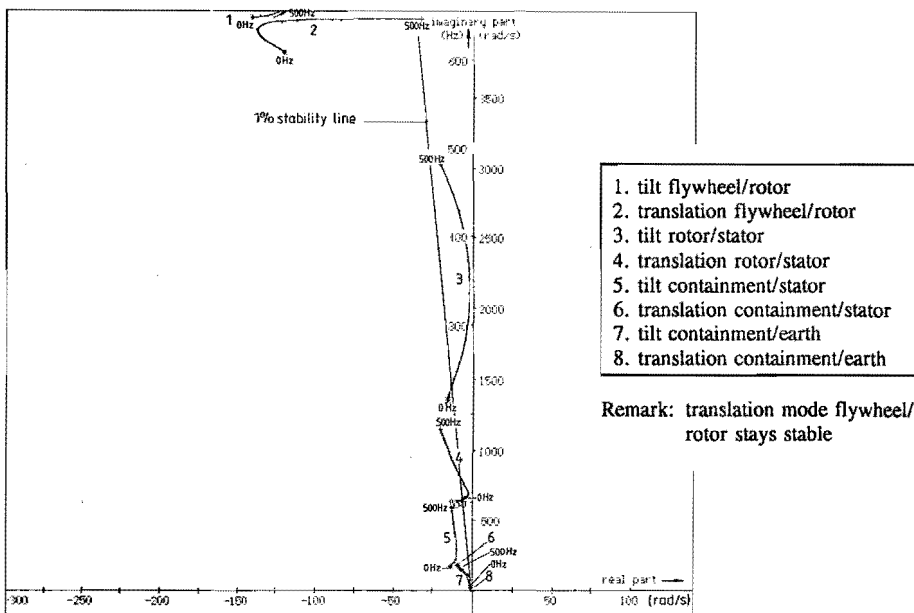
Fig. 9.7. Stability map EMAFER prototype for damping configuration 1 (see Table 9.5.).
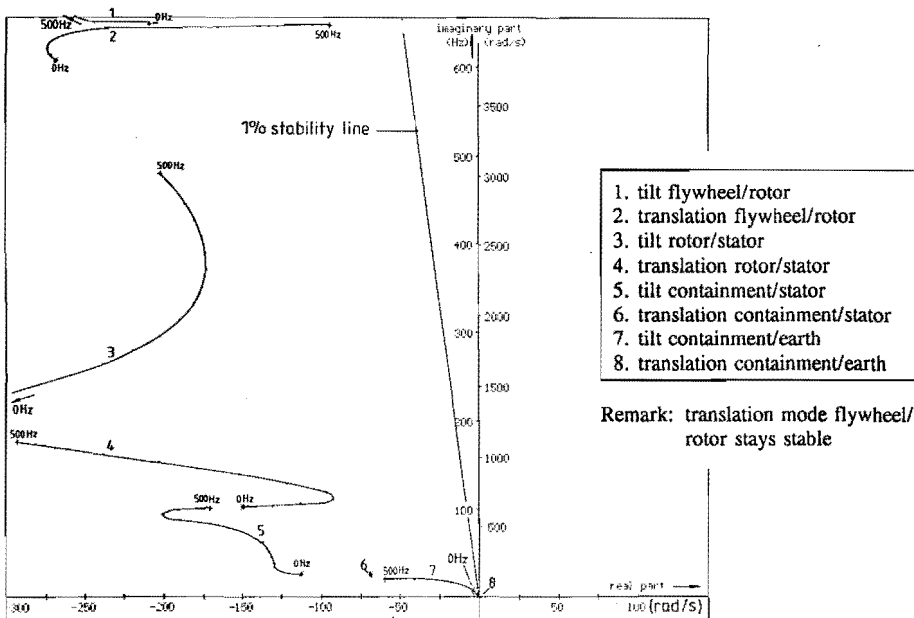
Fig. 9.8. Stability map EMAFER prototype for damping configuration 4 (see Table 9.5.), linearized consideration.

From a constructive point of view, SFD's are undesirable at the bearing supports as damping oil has to be supplied and drained. This interferes with the minimum oil quantity lubrication of the bearings. From a stability point of view, at least SFD's at the stator/containment couplings are required therefore.

Displacement map

The attenuation of resonant vibrations can be shown via the displacement map, which gives the displacements in the coupling elements, due to imbalance excitation, as a function of the spin speed. The displacements at the bearing supports are shown as these are the most representative for evaluating the vibration behaviour. The displacement curves for the low and high stiffness bearing support are represented seperately for an imbalance, which is combined of static and dynamic imbalance. The maximum imbalance is assumed to be 130 grcm static and 3900 grcm² dynamic. This agrees with a balancing quality, which is one grade less as required for aircraft turbines [9.12].

The effect of SFD's at the stator/containment couplings can be seen by comparing Figs. 9.9. and 9.10., representing the displacements at the bearing supports for respectively damping configuration 1 and 2 in Table 9.5. It can be seen that SFD's at the stator/containment couplings considerably attenuate resonant imbalance response.

From the above linearized damping considerations it can be concluded that with no damping at the bearing supports, strong damping elements, such as SFD's, at the stator/containment couplings are required.
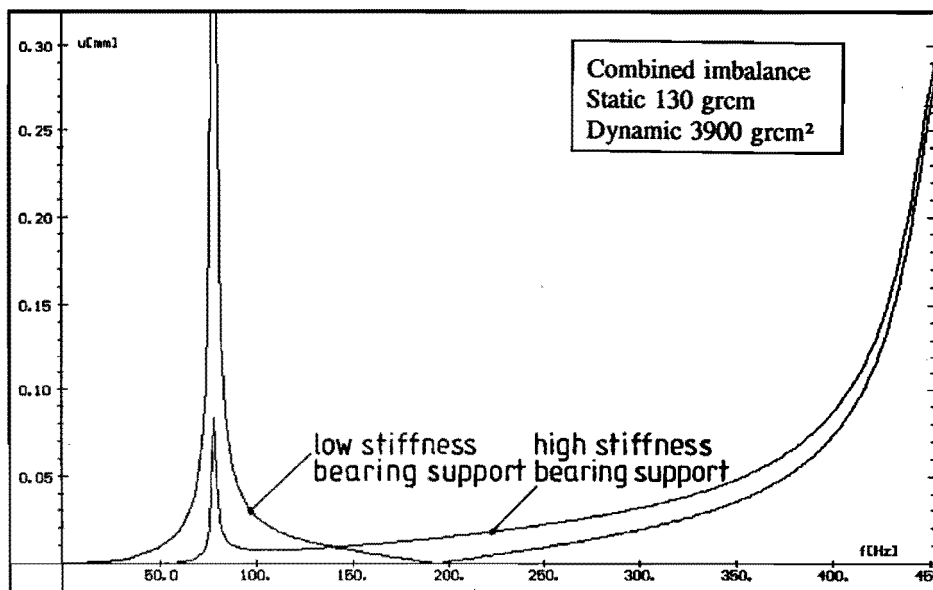
Fig. 9.9. Displacement map bearing supports EMAFER prototype for damping configuration 1 (see Table 9.5).

Combined imbalance
Static 130 grcm
Dynamic 3900 grcm²

low stiffness
bearing support

high stiffness
bearing support
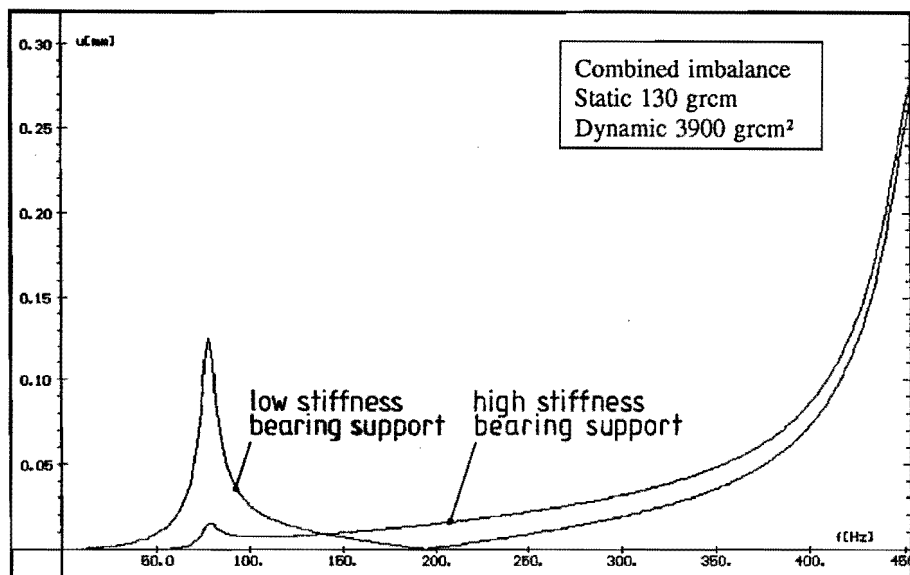
Fig. 9.10. Displacement map bearing supports EMAFER prototype for damping con-
figuration 2 (see Table 9.5.), linearized consideration.

9.5.3. Damping with squeeze film dampers (SFD's)

The strong damping requirements in the EMAFER concept can be provided via
SFD's. The rotordynamic effects, with taking into account the non-linear behaviour,
have been investigated via the stability and displacement maps of the EMAFER
prototype. From a rotordynamics standpoint, SFD's at the bearing supports are
preferred, whereas from a constructive standpoint, SFD's at the stator/containment
couplings are preferred, see also section 9.5.2. Both configurations, 2 and 3 in Table
9.5., have been considered next.
The design parameters of the SFD's as used in these considerations have been derived
from practical considerations and the linear displacement maps. They are listed in
Table 9.6. As end seals are used, no cavitation is supposed.

Table 9.6. Design parameters of SFD's in EMAFER prototype.

		SFD Bearing support	SFD Stator/containment
Damping medium		lubrication oil	cooling oil
Dynamic viscocity μ	(NS/m²)	5.0 E-3	5.0 E-3
Damper radius R	(m)	80 E-3	183 E-3
Damper width L	(m)	30 E-3	28 E-3
Clearance C_r	(m)	0.2 E-3	0.4 E-3

Stability map

The stability map of the EMAFER prototype for damping configuration 2, see Table 9.5., is shown in Fig. 9.11. By comparing Figs. 9.7. and 9.11., it can be seen that the SFD's at the stator/containment couplings particularly improve the stability of the stator/containment modes. The stability of the rotor/stator modes are less strong influenced and still tend to instability at higher rotor speeds. SFD's at the stator/containment coupling only are likely unsufficient for preventing rotordynamic instability. SFD's at the bearing supports will certainly be more effective in this respect.
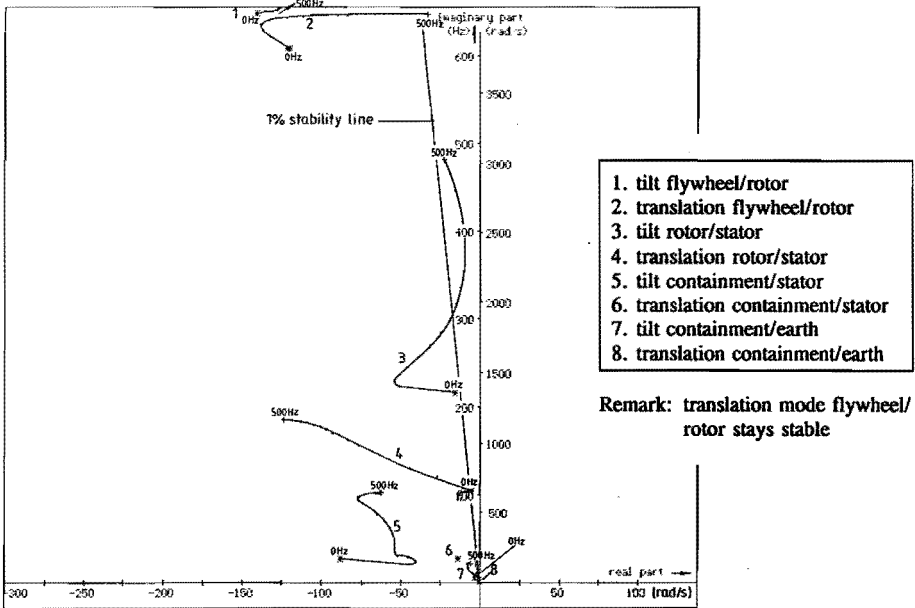
Fig. 9.11. Stability map EMAFER prototype for damping configuration 2 (see Table 9.5.) with non- linear, uncavitated SFD's.

Displacement map

The displacement map, associated with the above stability map, is shown in Fig. 9.12. In this case of asymmetric bearing support stiffnesses, each bearing support has its own displacement curve, representing the displacements due to combined static and dynamic imbalance. The maximum imbalance is assumed to be 130 grcm static and 3900 grcm² dynamic.

The maximum damping of the stator/containment SFD appears to be about 4,000 Ns/m per damper. This is lower than assumed in the linear damping considerations, compare Figs. 9.10. and 9.12, and is sufficient to prevent excessive vibrations during passing the first critical speed of the flywheel motor/generator unit.

The displacement map for damping configuration 3, see Table 9.5., is shown in Fig. 9.13. This results in a far better attenuation of the resonant vibrations, compared to SFD's at the stator/containment coupling. This can be explained by the location of the SFD's, direct at the bearing supports, as well as the considerably higher damping values that are obtained by these dampers, maximum 18,000 Ns/m per damper.
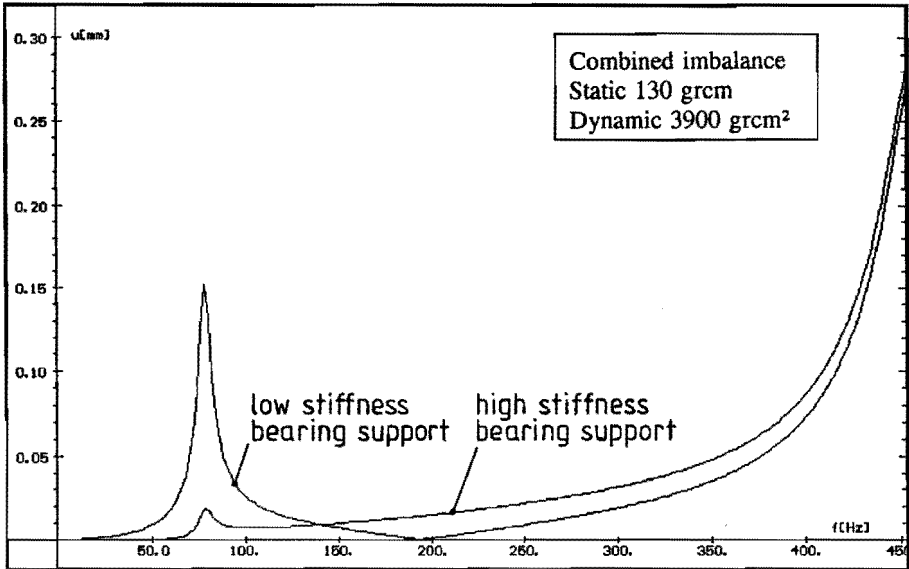
Fig. 9.12. Displacement map bearing supports EMAFER prototype for damping configuration 2 (see Table 9.5.) with non-linear, uncavitated SFD's.
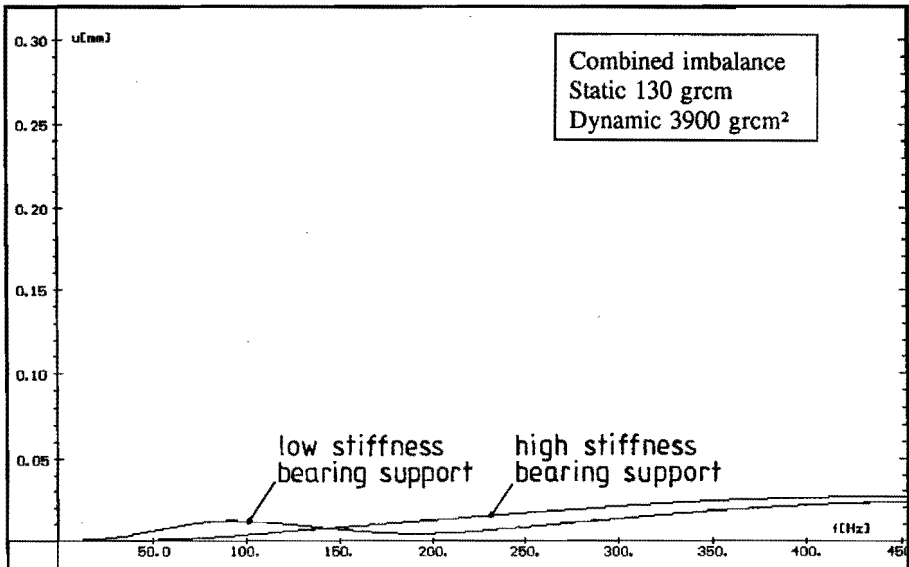
Fig. 9.13. Displacement map bearing supports EMAFER prototype for damping configuration 3 (see Table 9.5.) with non-linear, uncavitated SFD's.

9.6. Conclusions

The preceding vibration research is undispensable in achieving a good rotordynamic design of the EMAFER concept. With the help of the simulation model, the following objectives have been accomplished:
- An operating speed range free of critical speeds and negligible structural vibrations below the maximum speed. The operating speed range is located between the first and second critical speed of the flywheel motor/generator unit.
- A good reduction of the whirl amplitudes when traversing the first critical speed.
- Prevention of rotordynamic instability.
- The application of SFD's as beneficial non-linear damping elements.

Therefore the EMAFER concept must be composed of rigid main assemblies for rotor, stator and containment, coupled to each other via relatively weak coupling elements with proper damping characteristics. For this reason the coupling elements of the EMAFER prototype have been constructed as steel spring elements combined with elastomeric damping elements and optional SFD's. The construction offers options to modify the stiffness and damping characteristics of the coupling elements in a relatively easy way. Thus the objectives mentioned above can be evaluated experimentally.

Chapter 10

Evaluation

10.1. Introduction

The results of the preceding investigations into the mechanical aspects of the EMAFER concept have been implemented in the prototype construction. By realizing and testing the prototype, the investigation results with respect to the flywheel development and vibration research have been evaluated.

10.2. Prototype

The prototype, as a successor to the preprototype, differs mainly from the last one regarding constructive measures concerning flywheel construction, safety and vibration behaviour. See also section 7.8. The prototype has been designed with stringent specifications as required for application in large vehicles such as commuter trains and city buses. The system is, as well, suitable for uninterruptable power supply (UPS) systems, see also chapter 3.

The main specifications of the prototype system (excluding electronics) are:
- Energy storage capacity   : 4 kWh effective
- Power capacity   : 300 kW continuous
- Total mass   : 780 kg.
- Main dimensions   : ϕ 1 m x 0.8 m
- Operating speed range   : 8,000 - 15,000 rpm
- Turnaround efficiency   : 92%
- Service life   : 10^7 charge/discharge cycles

The final design has been worked out in composition drawings [9.10]. In this design the mass of the system is not as low as desired (600 kg). This is mainly due to the stage of the development. The containment and stator assembly are not yet weight optimized because of safety requirements and test purposes.

The most important construction parts are described underneath.

Flywheel
The flywheel of the EMAFER prototype consists of four thick rim modules of the layered type with double press fit. In this way no dangerous radial tensile stresses occur up to the maximum speed, see also section 8.6.4. Thus an intrinsically fail safe flywheel is achieved. The main specifications are:
- Dimensions: ϕ 290 x ϕ 680 x 100 mm.
- Materials, from inner to outer radius: Aluminium 7075-T6, E-glass epoxy, HS-carbon epoxy and HM-carbon composite.
- Operating speed range: 8,000-15,000 rpm.
- Flywheel/electrical machine attachment: via press fit.

Electrical machine

The mechanical design of the electrical machine differs mainly from the preprototype construction by the greatly improved stiffness characteristics of the stator. For this purpose the stator journals are relatively thick and short while the sheetings of the lamination stack are glued to each other. All other construction principles, e.g. for rotor and cooling system, are identical to these of the preprototype, see also section 7.8.

In electromagnetic respect, the prototype differs from the preprototype by the sheetings for the lamination stack which are very thin (0.2 mm) for reducing the electrical iron losses as much as possible. Further the rotor has high grade permanent magnets (Neodynium-Iron-Boron) for increasing the power density.

Bearing system

The bearing system is based on high precision angular contact ball bearings in combination with squirrel cage elements and squeeze film dampers, see also chapter 7, Fig. 7.7. In this way the stiffness and damping requirements, which follow from the rotordynamic considerations, see chapter 9, can be met.

The bearing construction is designed in such a way that, in spite of the outer rotating rotor, the bearing has a rotating innerrace and a static outerrace. Thus the allowable speed limit of the bearing can be satisfied.

Containment

The containment is designed to provide a vacuum environment for the flywheel motor/generator unit and with special attention for the safety function. Penetration of the containment structure by flywheel fragments is prevented by minimizing the initial rotor clearance to 10 mm, in combination with an aluminium liner thickness of 20 mm and a bare overwrap thickness of 40 mm. The aluminium liner has an integrated steel tube for cooling purposes.

The containment structure is supported and enclosed by a steel cage, which provides additional strength in the axial direction. This cage limits also the tangential reactions to the surroundings in case the rotor is locked. The cage enables a defined, torque limited, rotation of the whole containment in the cage.

The cage is coupled to the surroundings via a cardanic suspension. In this way torque transmission is possible while bearing forces due to gyroscopic effects can be minimized.

Coupling flywheel motor/generator unit with containment

The flywheel motor/generator unit is constructed as a self supporting package complete with transducers and is mounted as a unit in the containment. Special attention has been paid to the coupling of this unit, via the stator, with the containment. This coupling transmits the torque from the stator to the containment while providing stiffness and damping characteristics as required from rotordynamic demands. The stiffness characteristics are defined by steel brackets whereas elastomeric ring elements with optional squeeze film dampers take care of the damping requirements.

The EMAFER prototype and a flywheel disc are shown in respectively Photos 10.1. and 10.2. Photo 10.1. shows the EMAFER prototype with the top cover removed, so that the upper part of the flywheel motor/generator unit is visible. The containment is supported and enclosed by a steel cage. The cardanic suspension is not shown here. Photo 10.2. shows on the foreground one of the four flywheel discs as used in the EMAFER prototype. The flywheel is balanced by adding correction weights on the aluminium hub.
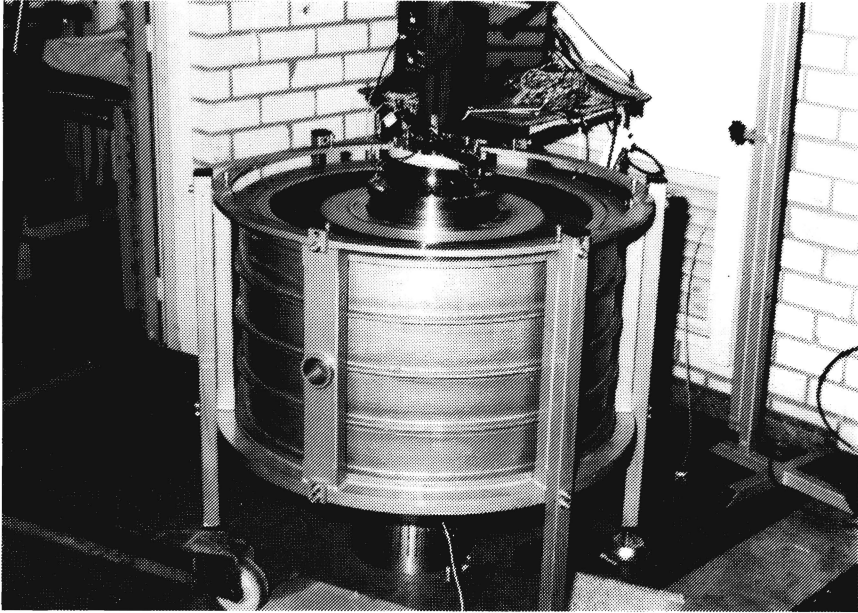
Photo 10.1. EMAFER prototype.
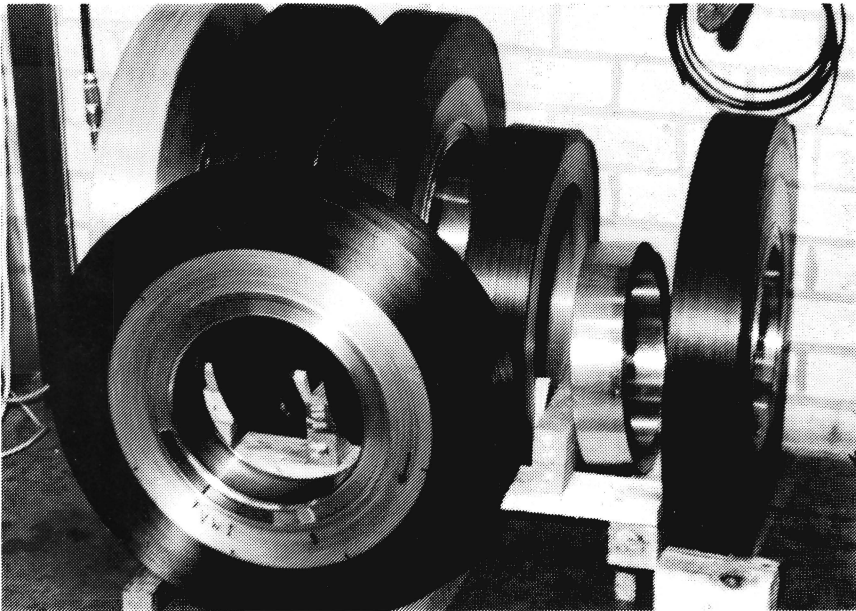
Photo 10.2. Layered disc flywheel of EMAFER prototype.

10.3. Flywheel evaluation

The layered flywheel with double press fit, as used in the EMAFER prototype, is a very promising concept, see also section 8.6.4. However, when designing the prototype no practical experience existed with this concept. For this reason the concept was submitted to tests concerning manufacturing method and spin behaviour.

10.3.1. Manufacturing method

The manufacturing method of the layered flywheel as proposed for the prototype, has two new aspects compared to the layered flywheel of the preprototype, namely the winding and assembling method. Both aspects have been tested with the help of a full E-glass epoxy rim with the same dimensions as the layered prototype wheels.

a) Winding method
Intermittently winding and curing as done for the layered flywheel of the preprototype is very expensive. Therefore winding and curing of the total rim thickness (160 mm) at one go has been considered.
The winding of the total rim thickness was done at one go with more rovings at a time and using a high accuracy mandrell with side flanges. The rovings were impregnated with a cold curing epoxy resin. Curing was done on the mandrell at ambient temperature. For improving the mechanical properties of the epoxy at high operational temperatures, the rim was "post cured" at high temperature (about 80°C).
The thus manufactured E-glass epoxy flywheel showed excellent and smooth disc surfaces without any signs of fibre instability or cracks.

b) Assembling method
A conical metallic hub is inserted directly into the composite rim. In this way a high press fit can be achieved. The inserting was done with the help of some auxilliary tools for a good support of the composite rim. While inserting the conical hub, the interface surfaces were lubricated via a high pressure pump. By using a proper lubrication medium, the assembling forces are minimized.
With this method a high and good defined press fit could be obtained without any observable damage of the composite rim.

10.3.2. Spin testing

For checking the flywheels and for evaluating the simulation model, all the flywheels have been separately spin tested. The flywheel was for this purpose attached with a special test spindle having the same centrifugal growth characteristic as the rotor of the electrical machine. This test spindle serves for individual balancing of the flywheels as well.
The first test wheel was the E-glass epoxy flywheel. For testing the principle of radial tensile stress reduction, the size of the press fits used is less important. Due to the large tolerances in interface radii, this wheel was therefore assembled with lower radial press fit pressures than required for the layered flywheel, see Figs. 10.1. and 8.19.

Following the stress calculations of this wheel, including thermal effects as present during testing, see Fig. 10.1., a maximum rotational speed of 10,000 rpm should be possible. This corresponds to a maximum radial tensile stress of nearly 30 MPa. However, delamination was noticed already at 9,000 rpm, corresponding to a maximum radial tensile stress of 20 MPa. This can be due to a poor radial tensile strength of the E-glass epoxy. The tangential (hoop) stresses in the E-glass epoxy are at a maximum of 300 MPa and thus far below the ultimate tensile strength (1100 MPa) of the material.

The layered flywheels for the EMAFER prototype were initially designed with the assumption of a 20°C curing temperature and no post cure. For preventing premature delamination, because of additional thermal tensile stresses caused by the post cure, the design was modified. This was done by enlarging the radial press fit between the aluminium hub and composite rim from 0.5 mm to 0.6 mm. The stress distribution for this modified flywheel design, including thermal effects, is illustrated in Fig. 10.2. The main difference with the original concept can be seen by comparing Figs. 8.20 and 10.2. It appears that the modified concept compared to the original concept, has higher radial tensile stresses in the carbon epoxy (curves a and c), while the tangential stresses are about the same for both concepts. However, with this modification the flywheels are suitable for the EMAFER prototype, be it for a more limited temperature range. During spin testing at about 10°C, speeds up to 17,000 rpm can be reached as can be seen from curve e in Fig. 10.2.

The layered flywheels with above modification have been successfully tested up to 17,000 rpm at about 10°C. No signs of delamination or failure were observed. This is an important confirmation of the flywheel concept and the simulation model.

Flywheels with triple press fit can be used for further compensating the radial tensile stresses due to the curing process. Also compressive stresses in the E-glass epoxy at standstill can then be smaller. Orienting calculations have shown that this principle enables circumferential speeds up to 800 m/s or 22,500 rpm for a design diameter of 680 mm.
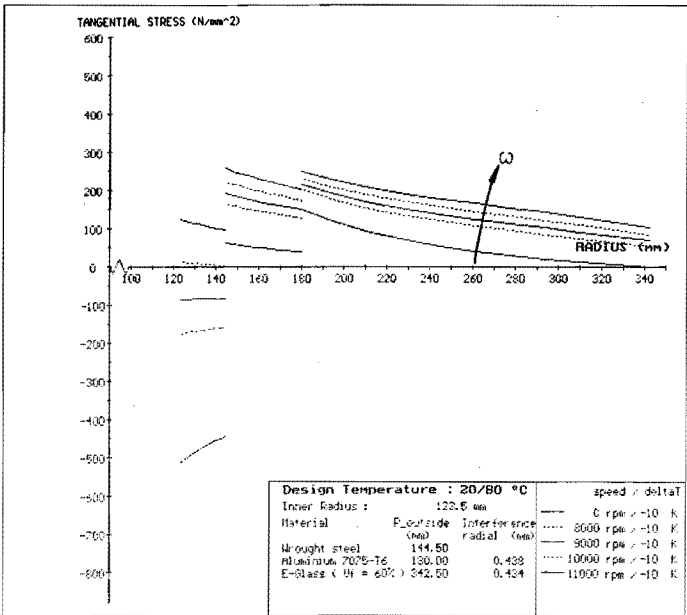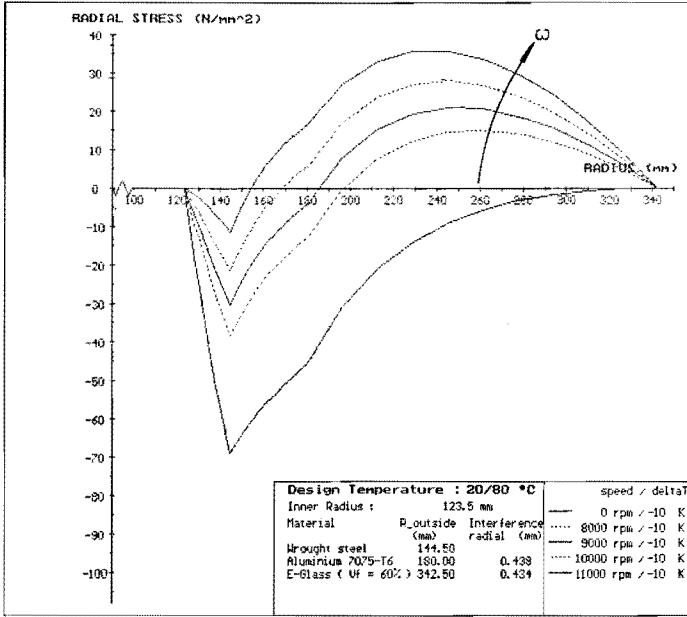
Fig. 10.1.   Calculated stress distribution in E-glass epoxy test flywheel.
(For explanation subscriptions, see Fig.8.6., chapter 8).
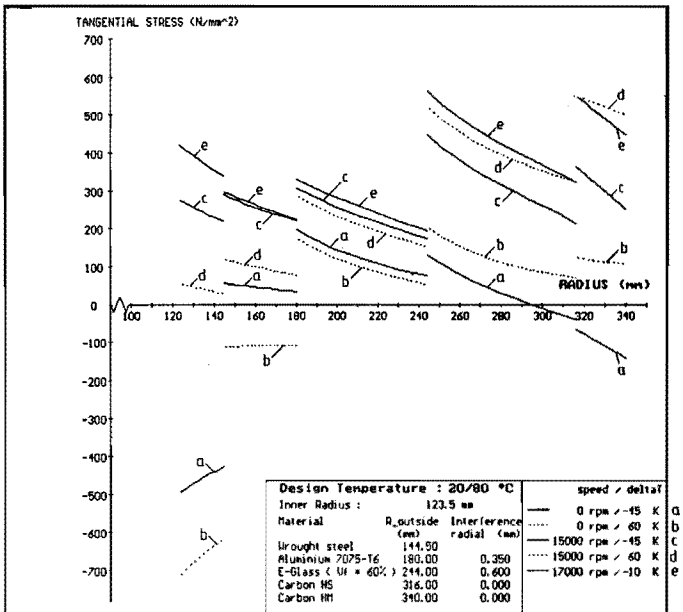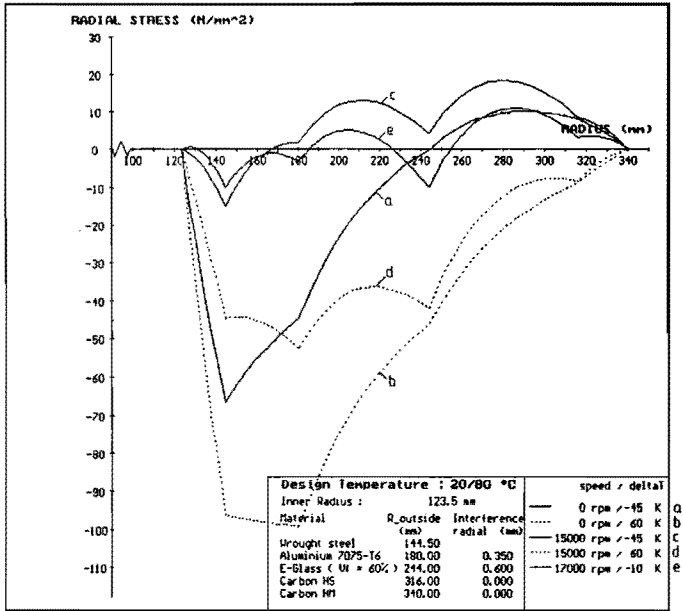
Fig. 10.2. Calculated stress distribution in modified layered flywheel for EMAFER prototype.

10.4. Evaluation of the vibration behaviour

For the considered speeds, the EMAFER prototype consists of the rigid main assemblies of rotor, stator and containment. These main assemblies are coupled to each other via specially designed coupling elements with proper stiffness and damping characteristics. As followed from the vibration research in chapter 9, a favourable rotordynamic behaviour is achieved in this way. The system has an operating speed range free of critical speeds, a good suppression of resonant whirl amplitudes and no rotordynamic instability. See also sections 9.4. and 9.5.

The vibration behaviour has been evaluated by comparing the theoretical and measured results. The measurements were started with determining the natural frequencies of the stationary system, followed by measurements on the dynamic system for determining imbalance, critical speeds, vibration amplitudes and possible instability phenomena.

10.4.1. Measurements on the stationary system

The measurements on the stationary system have been restricted to the measurement of the natural frequencies of a flywheel disc and of the flywheel motor/generator unit. The natural frequencies of these parts are of vital interest as they determine the eventual critical speeds in the operating speed range. The natural frequencies of the flywheel moreover indicate the speeds above which instability effects may be expected due to material damping of the flywheel.

For determining the natural frequencies of the flywheel disc, the disc assembled with the inner aluminium hub, was freely hung and excited over a frequency domain from 100 Hz (6,000 rpm) to 1500 Hz (90,000 rpm) by a vibration generator. Simultaneously the fundamental harmonics of the response vibration velocity were measured. The natural frequencies manifested by high velocity amplitudes as can be seen in Fig. 10.3. From this figure, it follows that the lowest natural frequency occurs at about 48,000 rpm. This is clearly above the operating speed range and the flywheel disc may be considered as a rigid body element with no destabilizing effects, preconceived that the structural stiffness is not considerably lowered at high spin speeds.

When measuring the natural frequencies of the flywheel motor/generator unit as a stationary system, the influence of gyroscopy is not taken into account, see also Appendix III, section III.2. However, the method offers a good evaluation of the functioning of the bearing support construction. Similarly as in case of the flywheel disc, the flywheel motor/generator unit was freely hung and excited by a vibration generator up to about 500 Hz (30,000 rpm). The fundamental harmonics of the vibration amplitude were measured with the help of a proximity probe at a bearing support. The results are shown in Fig. 10.4. The first natural frequency of the flywheel motor/generator unit is at about 9,000 rpm and the second at about 17,000 rpm.

The theoretical natural frequencies of the flywheel motor/generator unit are those associated with respectively the translation and the tilt of rotor/stator, however, without gyroscopic influences since it concerns the stationary system. From Fig. 9.6. in chapter 9, it follows that the theoretical natural frequencies of the concerning rotor/stator modes for spin speed zero are respectively 67 Hz (about 4,000 rpm) and 222 Hz (about 13,000 rpm). These values clearly differ from those measured. This large difference must be due to differences in the realized and theoretical bearing support stiffnesses.
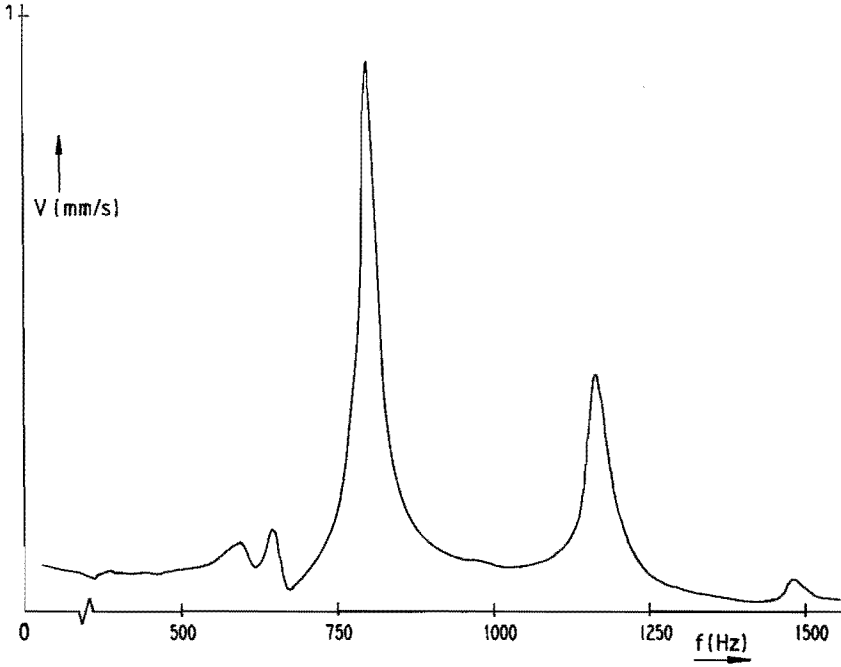
Fig. 10.3. Vibration velocity response to shaker excitation of the stationary flywheel disc of the EMAFER prototype.
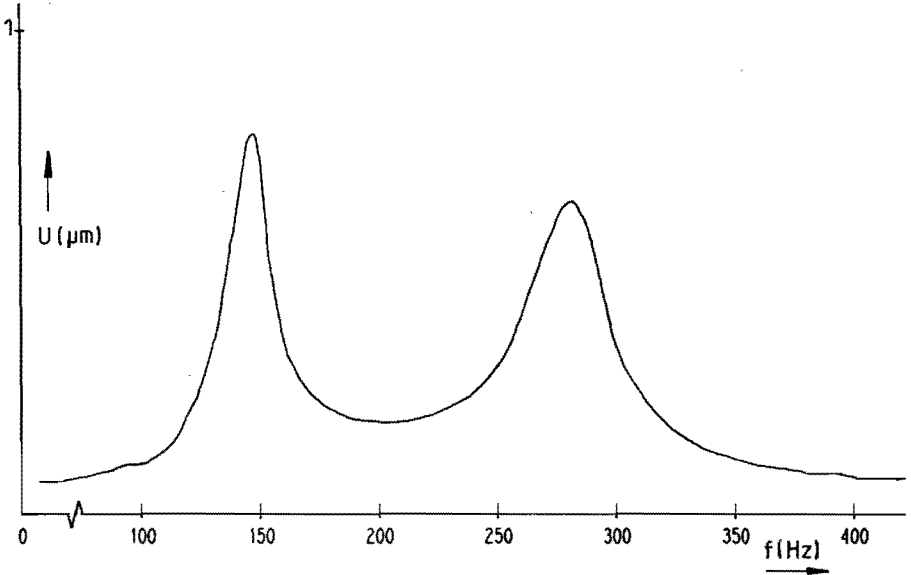
Fig. 10.4. Vibration amplitude response at the bearing support to shaker excitation of the stationary flywheel motor/generator unit.

Measurements for directly determining the radial bearing support stiffness showed that the radial stiffness of the lower bearing support was close to the design value. However the stiffness of the upper bearing support clearly differed from the design value by showing a very large hysterisis loop, due to friction in these parts. The upper bearing support had to be redesigned and replaced by an improved type with a proper stiffness characteristic showing no hysteresis [10.1].

10.4.2. Measurements on the dynamic system

The complete arrangement of measuring equipment for monitoring the vibration signals is shown in Photo 10.3. This arrangement includes the temperature monitoring of the bearings, the stator windings and the cooling oil systems for stator and containment as well.

Photo 10.3. Arrangement measuring equipment for EMAFER prototype.
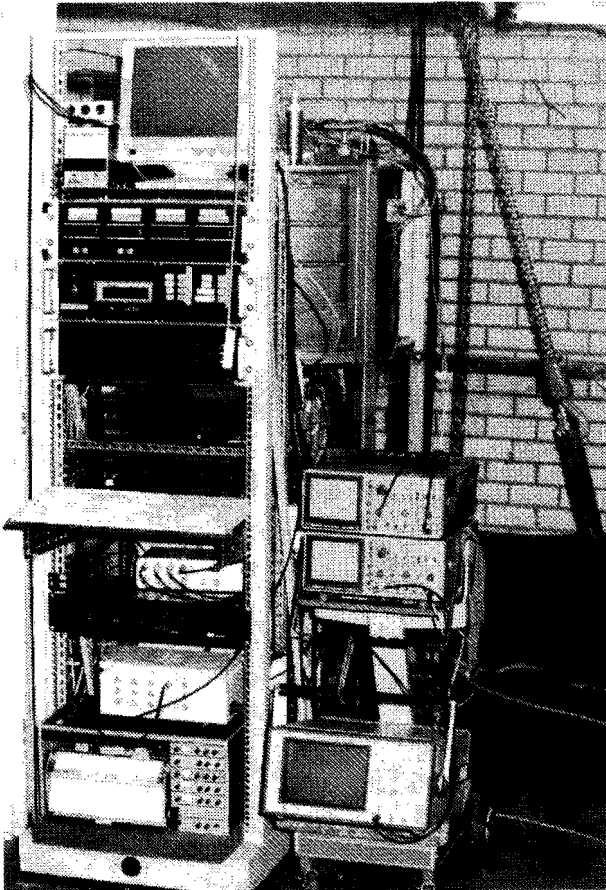
The EMAFER prototype has extensively been tested at critical speeds, resonant vibration amplitudes and possible instability phenomena. The prototype is well equipped for these measurements as the main assemblies of rotor, stator and containment all have proximity probes at the coupling elements. The amplitudes between the main assemblies can so be measured with both high accuracy and high frequency. The proximity probes are mounted in orthogonal radial directions so that the whirl orbits can also be displayed. With a keyphasor the rotor speed and the rotational position of the rotor relative to the stator are measured. From these signals the imbalance response and the resonance frequencies can be determined. With the help of a Fast Fourier Transformation (FFT) all the rotor speed related vibration components can be indentified as well as possible instability problems.

The first measurements on the dynamic system concerned the balancing of the flywheel motor/generator unit, not mounted in the containment but freely hung at a cable. In this way the functioning of this unit could be tested for low speeds and possible disturbing influences of the containment or support structure on the balancing could be avoided. The balancing was done at a low speed of about 1,500 rpm. The smallest correction weight at each bearing location was 2 gr. At a balancing radius of 13 cm, this agrees with a maximum imbalance of about 50 grcm static and 1600 grcm^2 dynamic, which is clearly smaller than the assumed imbalance in the calculations.

After balancing, the speed could be raised up to 3,000 rpm and the unit ran very smoothly at this speed with an orbit radius of not more than 2 μm. Higher speeds than 3,000 rpm were intolerable because of safety aspects and too high windage losses with respect to the temperature of the unit, which had no operational cooling system during these tests.

After assembling the unit with the containment for a complete system, the speed could be raised. The unit still had the malfunctioning upper bearing support at this time and the speed was not raised further than 8,000 rpm due to strongly increasing vibration amplitudes. There was a real danger for total system loss when passing the first critical speed, which was according to the natural frequency measurements on the stationary system at about 9,000 rpm. The system behaviour was unpredictable at this critical speed due to the undefined radial stiffness of the upper bearing support.

While raising the speed up to 8,000 rpm some resonances were noticed in the range below 3,000 rpm. These can be allocated to modes of the total system, which is weakly coupled to the earth and to modes of the containment with respect to the weakly coupled stator. These resonance frequencies could be passed with small vibration amplitudes, in the order of 20 μm at the stator/containment couplings. Damping was then only due to the elastomeric elements and eventual friction in the couplings.

To be able to raise the speed further than 8,000 rpm, the malfunctioning upper bearing support was replaced by an improved type showing a radial stiffness with considerably less hysteresis than the first one [10.1]. The first critical speed appeared now at about 5,000 rpm. This speed was passed without any problem with a maximum vibration amplitude at the lowest stiffness bearing support of about 25 μm. This was reached without having any squeeze film damper (SFD) active in the system. The elastomeric elements and eventual friction at the several couplings evidently give sufficient damping to attenuate effectively resonant vibrations.

The following limiting factor for speed appeared to be the bearing temperature of the lower bearing. The speed could be raised no further than 12,000 rpm. For this reason the SFD at the lower bearing support was used for cooling purposes. This appeared to give sufficient cooling capacity for raising the speed up to the maximum target speed of 15,000 rpm. This speed was reached then with a vibration amplitude increasing to a maximum of 25 μm at the low stiffness bearing support, which is very acceptable. The measured vibration behaviour, with one SFD active at the high stiffness bearing support, is illustrated via the waterfall or cascade plot in Figs. 10.5A and 10.5B for respectively the low stiffness and the high stiffness bearing support. These vibration spectra have been measured while the machine was freely coasting down to eliminate possible influences of electromechanical forces of the electrical machine. This has been done for speeds down to the first critical of the rotor/stator assembly, as at lower speeds the vibrations at the bearing supports were negligible.

A forced response can be seen clearly at running speed and at twice the running speed. Some small response can also be seen at fractional running speed. The response at the running speed is imbalance response, which shows clearly the first critical at about 5,000 rpm. The forced response with fixed amplitude at twice the running speed may be due to misalignment of rotor and stator or magnetic anisotropy. It is not harmful for the functioning. The other noticed vibration levels at fractional rotor speed can be due to small imperfections in the ball bearings and have negligible influences on the vibration behaviour of the machine.

With respect to stability behaviour, it can be seen from the waterfall diagram that there are no fixed or nearly fixed frequency components in the diagram which increase rapidly with increasing spin speed. This indicates that destabilizing forces are not present in the construction. The construction of the rotor assembly with strong press fits and the high structural stiffness of the flywheel discs have proven to be sufficiently effective for preventing rotordynamic instability.

Summarizing, the measured vibration behaviour of the prototype system is very satisfying. There are no critical speeds in the operating speed range, the vibration levels are very acceptable and there are no rotordynamic instabilities. In other words the system as tested has proper stiffness and damping characteristics.
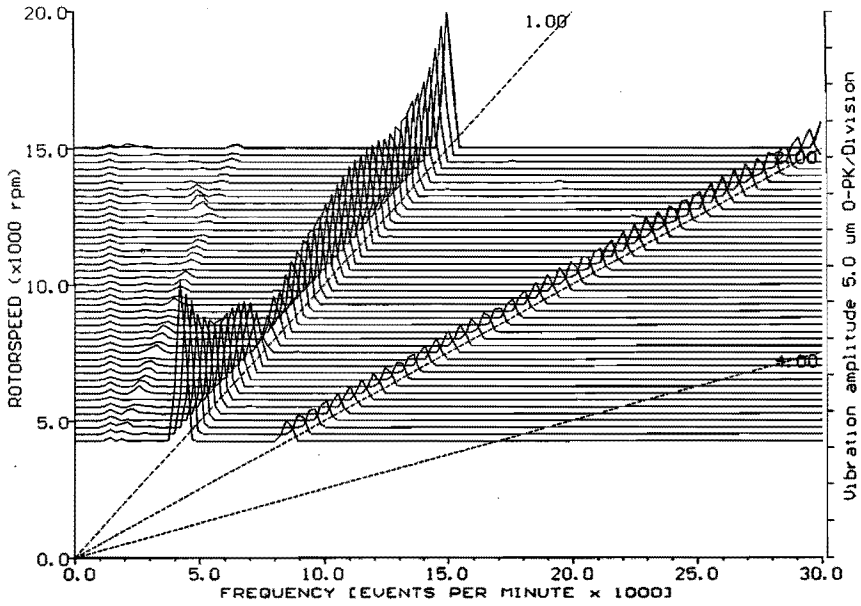
A. Low stiffness bearing support.
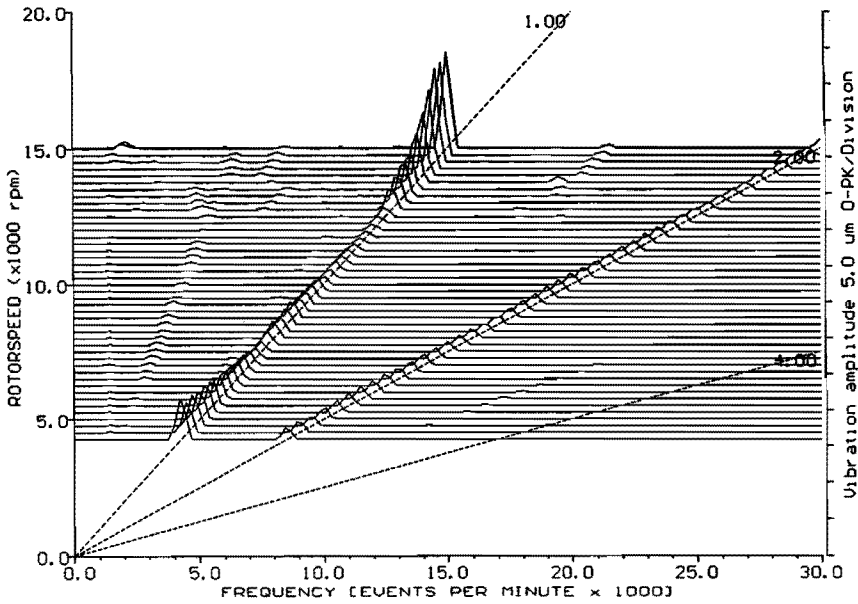
B. High stiffness bearing support.

Fig. 10.5. Waterfall diagram measured at the bearing supports of the EMAFER prototype.

10.4.3. Comparison of calculated and measured vibration behaviour

This comparison was done with respect to the critical speeds and the vibration amplitudes. In this way the stiffness and damping influences in the simulation model can be evaluated.

Critical speeds
The calculated critical speeds can be found from the spin-whirl map as represented in Fig. 9.6., chapter 9. The measured critical speeds can be found from Figs. 10.5A. and 10.5B. From Fig.9.6. it follows that the lower critical speeds all occur below 2,500 rpm and are in fact the resonance frequencies of the total system with respect to the earth and of the containment with respect to the flywheel motor/generator unit. These frequencies have also been noticed during the testing of the dynamic system. They are of minor interest as they are clearly below the operating speed range and could be passed without any difficulty.
A more important critical speed is the first one of the flywheel motor/generator unit, which is according to the spin-whirl map of Fig. 9.6. at about 4,700 rpm and according to the waterfall plot in Figs. 10.5A. and 10.5B. at about 5,000 rpm. The second critical speed of the flywheel motor/generator unit is according to Fig. 9.6. at about 28,000 rpm and so clearly above the operating speed range. During testing there was indeed no second critical speed of the flywheel motor/generator unit observed.
It can be concluded from this comparison that there is a good similarity between calculated and measured critical speeds, or in other words the simulation model predicts stiffness effects in a reliable way.

Vibration amplitudes
The comparison between calculated and measured vibration amplitudes only has a qualitative character as the real damping values in the construction are difficult to determine accurately. For the calculated vibration amplitudes refer to chapter 9, Figs. 9.9., 9.10. and 9.13. The measured results can be seen from Figs. 10.5A. and 10.5B. When comparing the calculated and measured results, it can be concluded that:
- The course of vibration amplitude with rotor speed is similar for both calculated and measured amplitudes. The vibration amplitudes have a maximum at the first critical speed of the flywheel motor/generator unit and show a change of its vibration mode at the low stiffness bearing support. This follows, besides from the zero value of the amplitude, also from the phase angle of the signals. The phase data are, however, not shown as they have not been considered further in this condensed survey. The change of cylindrical to conical mode of the rotor/stator is thus indicated. In the measurements this change of vibration mode is already at about 8,000 rpm and in the calculations at about 12,000 rpm. This can be declared by the magnitude of static and dynamic imbalance. In the calculations the static imbalance dominates whereas in the measurements the dynamic imbalance dominates.
- The calculated and measured vibration levels show a comparable behaviour at the first critical speed for both bearing supports. For the maximum speed the calculated vibration levels of the low stiffness bearing support are smaller than of the high stiffness bearing supports, whereas the opposite phenomenon has been noticed during testing. This last effect is again due to the difference in theoretical and real magnitude of static and dynamic imbalance.

- The measured vibration levels (Figs. 10.5A. and 10.5B.) are roughly in between the vibration levels as calculated for pure elastomeric damping (Fig. 9.9.) and for SFD's at the bearing supports (Fig. 9.13.). The real damping in the coupling elements is therefore of a proper magnitude, already with only one SFD active at the high stiffness bearing support.
- Rotordynamic instability is observed neither in the calculations nor in the measurements.

It therefore follows that the simulation model predicts the effects of damping influences in a proper way.

10.5. Conclusions

The realized EMAFER prototype system is mainly based on the results of the flywheel development and the vibration research. From the preceding evaluation results, it can be concluded that, with respect to the:

- Flywheel
The layered flywheel with double press fit is a feasible and reliable concept for a high speed flywheel system. The concept allows for a well defined fabrication method and has a predictable behaviour.

- Vibration behaviour
The concept for a good vibration behaviour, by means of rigid main assemblies and coupling elements with proper stiffness and damping characteristics, has been proved both predictable and effective.

With the above results the technical feasibility of the EMAFER concept has been demonstrated. Potentially such flywheel systems, when properly applied, could ultimately become a significant contribution to reduce the World's energy consumption.

APPENDICES

Appendix I

Specifications for a future gyrobus

I.1. Introduction

With the threatening problems of fossil energy shortage and air pollution, particularly in urban areas, the future city bus should have an energy efficient, clean and silent propulsion system while retaining the flexibility of the current diesel-fuelled city bus. The gyrobus, a fully flywheel driven city bus with brake energy recuperation, offers these options. The feasibility of this bus type has already been demonstrated in the early 1950's by the Oerlikon gyrobus [2.14]. See also section 2.4.1. However, for the present and the future city traffic the performance of the Oerlikon gyrobus must be strongly improved. The basic specifications of the future gyrobus, as far as they concern the drive system, are given below.

I.2. Basic specifications

The following basic specifications are meant for establishing the performance demands of the drive system. Therefore the bus has to be considered in conjunction with the bus route and the driving cycles.

a) Bus
The gyrobus is a fully flywheel driven city bus. The flywheel supplies the propulsion energy and is charged by brake energy recovery and by the electrical supply at the bus stops. See Fig. I.1.
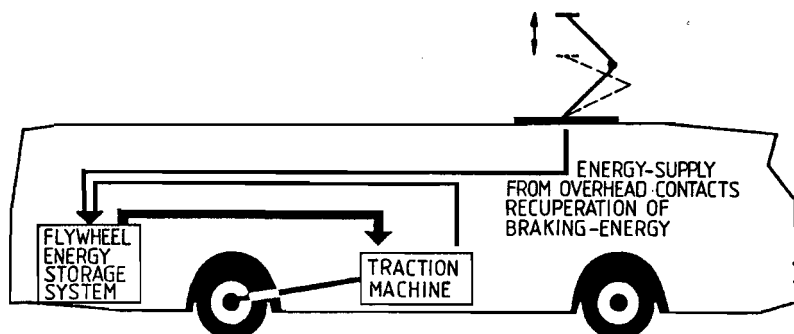
Fig. I.1. Scheme of gyrobus.

The performance of this bus has been defined so, that it can participate as a full value vehicle in the present and the future city traffic and is in every way competitive with current city buses (diesel and trolley). This leads to the following specifications [3.2]:

- Mass   : 12.5 tons excluding passengers;
  17.5 tons including 80 passengers;
  1,000 kg rotating inertia equivalent.
- Speed   : max. 70 km/h.
- Acceleration   : fully loaded, on horizontal plane,
  0 -18 km/h: constant acceleration 1.2 m/s^2;
  18-50 km/h: constant acceleration power 120 kW;
  50-70 km/h: acceleration power inversely proportional with velocity.
- Deceleration   : fully loaded, on horizontal plane,
  electrical brake : 70-50 km/h: constant braking power 294 kW;
  50-5 km/h: constant deceleration 1.3 m/s^2.
  friction brake   : for all velocities up to 4.5 m/s^2.
- Rolling resistance : 1.5% of the total weight.
- Airdrag   : 1400 N at 70 km/h.

b) Bus route and driving cycles
The bus route and driving cycles are not standardized but relate to urban circumstances as they occur in the typical European cities. This gives the following characteristics:
- Horizontal plane
- Bus stops   : every 300 m to 600 m.
- Stop time   : 15 s. and 20 s. for respectively 300 m and 600 m cycle.
- Recharging facilities : electrical (750 V DC) by means of overhead contacts at the bus stops;
  charging time: 10 s. for 300 m cycle; 17 s. for 600 m cycle.

The driving cycle is schematically represented in Fig. I.2.
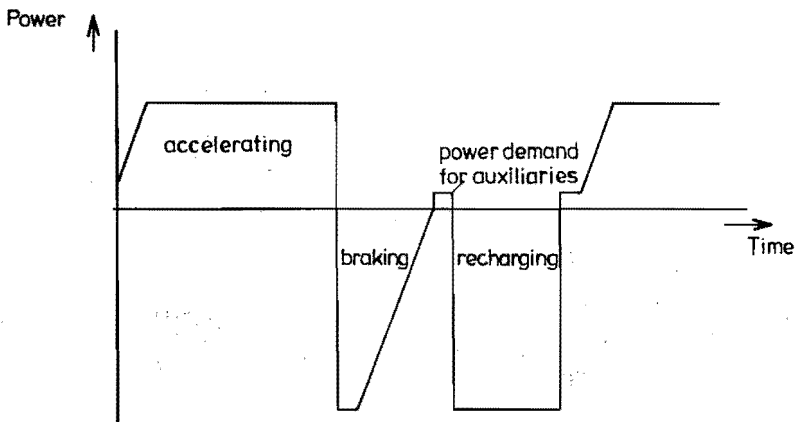
Fig. I.2. Driving cycle of city bus.

I.3. Power and velocity profiles

The power and velocity profiles define the course of the power, respectively velocity as a function of the time. They are needed for the energy evaluation and power rating of the system. They have been determined for a fully loaded bus with the above basic specifications.

The highest demands upon the propulsion system are made when the acceleration phase is directly followed by the braking phase (no constant velocity phase, see also Fig. I.2.).

Fig. I.3. (next page) gives the propulsion power, respectively Fig. I.4. the braking power as a function of the time at the driving wheels and at the flywheel (constant efficiency assumed) for the 300 m as well as for the 600 m driving cycle.

It can be seen, that the braking power can be considerably high and is representative for the power rating of the system. The associated velocity profiles are given in Fig. I.5. It can be seen, that the maximum speed of 70 km/h will not be reached within these driving cycles.
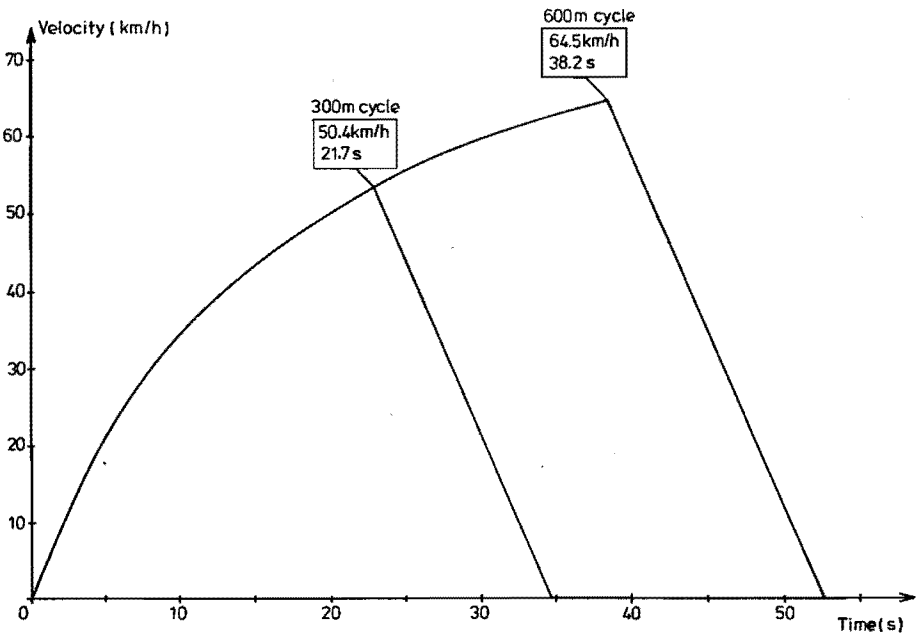
Fig. I.5. Velocity profiles for 300 m and 600 m city bus driving cycle.
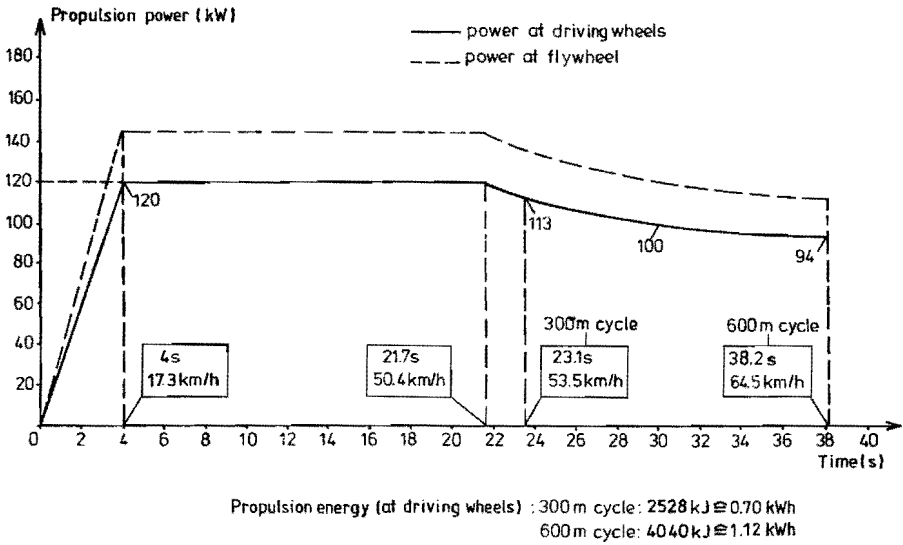
Fig. I.3. Propulsion power profile for 300 m and 600 m city bus driving cycle.
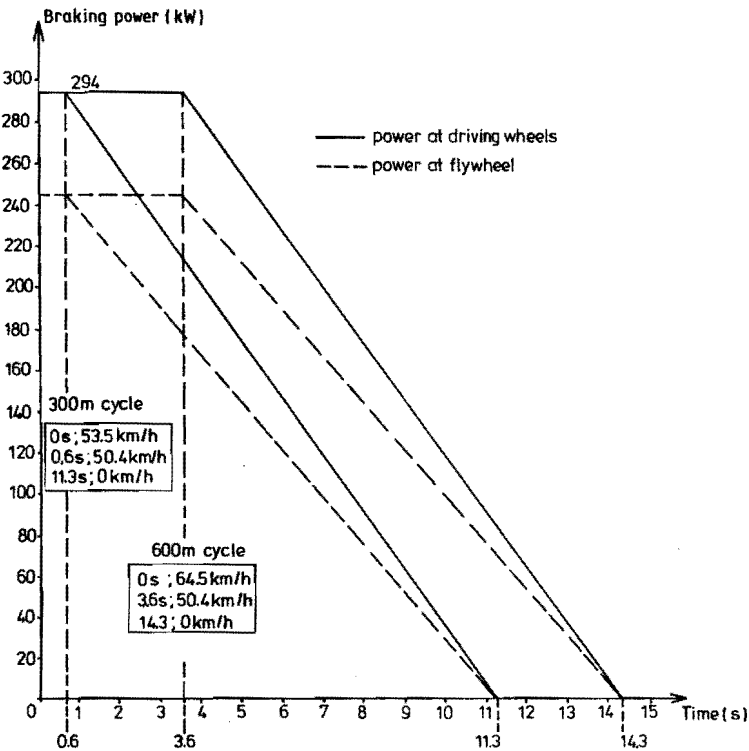
Fig. I.4. Braking power profile for 300 m and 600 m city bus driving cycle.

Appendix II

A synopsis on power split continuously variable transmissions (PS-CVT)

II.1. Introduction

The power-split continuously variable transmission (PS-CVT) transmits mechanical power, partially by a fixed ratio path and partially by a continuously variable ratio bypass. The fixed ratio path is usually a straight mechanical gear drive, whereas the variable ratio bypass can be of the mechanical, electrical or hydrostatic type. Splitting and adding of power is taken care of by a planetary drive of which the fixed ratio part is usually a part of. An electrical or hydrostatic CVT also offers the possibility for a PS-CVT design without involvement of any gear drive.
The goal of a PS-CVT is to improve certain characteristics of the pure CVT, e.g. efficiency, speed ratio range, power density, torque and power rating. For the PS-CVT's with planetary gear drive, these aspects are known from literature, [II.1] and [II.2]. This synopsis aims for an overview of all basic PS-CVT types, with and without gear drive and with the accent on the influence of these types on transmission efficiency.

II.2. PS-CVT with gear drive

In this consideration the variable ratio bypass consists of a conical sheaves variator (CSV). The results apply as well for electrical as for hydrostatic CVT's as variable ratio bypasses.

a) Basic configurations
The gear drives in the PS-CVT's are simple planetary drives of which the most common designs are illustrated in Fig.II.1.

a	b	c	d	e	f
$i_0 < -1$	$i_0 < 0$	$i_0 = -1$	$i_0 > 0$	$i_0 > 0$	$i_0 > 1$
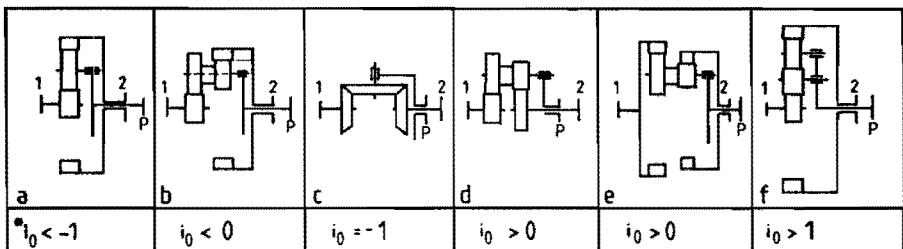
* $i_0 = n_1/n_2$ with $n_p = 0$; n_{index} = rotation speed of respective shaft

Fig.II.1. Most common designs of planetary gear drives [II.3].

As can be seen from Fig.II.1., the planetary gear drive consists of a three shaft gear transmission of which one shaft, indicated with index p, is connected with the planet wheels. Coupling of a planetary drive with a CSV to a PS-CVT is possible in three basically different configurations as illustrated in Fig.II.2.

Configuration A^*

CSV (transmission ratio i_{CSV})

coupling gears (transmission ratio i_T)

planetary gear drive (transmission ratio i_0)

$$i_{PS-CVT} = \frac{i_{CSV} - i_T (1 - i_0)}{i_0}$$

1) $$\left|P_{CSV}/P_{out}\right| = \frac{1}{\eta_{CSV}} \cdot \left|\frac{1}{1 + \frac{i_T}{i_{CSV}} (i_0 - 1)}\right|$$

2) $$\left|P_{CSV}/P_{out}\right| = \left|\frac{1}{\eta_{CSV} + \frac{i_T}{i_{CSV}} (i_0 - 1)}\right|$$

$$i_{CSV} = \frac{n_1}{n_{in}} \; ; \; i_T = \frac{n_p}{n_{in}}$$

Configuration B^*

$$i_{PS-CVT} = \frac{(i_0 - 1) i_{CSV} + i_T}{i_0}$$

1) $$\left|P_{CSV}/P_{out}\right| = \frac{1}{\eta_{CSV}} \cdot \left|\frac{1}{1 + \frac{i_T}{i_{CSV} (i_0 - 1)}}\right|$$

2) $$\left|P_{CSV}/P_{out}\right| = \left|\frac{1}{\eta_{CSV} + \frac{i_T}{i_{CSV} (i_0 - 1)}}\right|$$

$$i_{CSV} = \frac{n_p}{n_{in}} \; ; \; i_T = \frac{n_1}{n_{in}}$$

Configuration C^*

$$i_{PS-CVT} = \frac{i_{CSV} - i_T \cdot i_0}{1 - i_0}$$

1) $$\left|P_{CSV}/P_{out}\right| = \frac{1}{\eta_{CSV}} \cdot \left|\frac{1}{1 - \frac{i_T \cdot i_0}{i_{CSV}}}\right|$$

2) $$\left|P_{CSV}/P_{out}\right| = \left|\frac{1}{\eta_{CSV} - \frac{i_T \cdot i_0}{i_{CSV}}}\right|$$

$$i_{CSV} = \frac{n_1}{n_{in}} \; ; \; i_T = \frac{n_2}{n_{in}}$$

* in all configurations: $i_{PS-CVT} = \dfrac{n_{out}}{n_{in}}$; $i_0 = \dfrac{n_1}{n_2}$ with $n_p = 0$;

P_{CSV} = input power CSV; P_{out} = output power PS-CVT

planetary drive can be any of the designs of Fig.II.1.

1) for in/out shaft configurations as defined; 2) for in/out shaft configurations changed.

Fig.II.2. Basic configurations of PS-CVT with planetary gear drive.

The planet wheels can be coupled with:
- a shaft of the CSV, being an external shaft of the PS-CVT: configuration A, Fig.II.2.
- a shaft of the CSV, being no external shaft of the PS-CVT: configuration B, Fig.II.2.
- an external shaft of the PS-CVT, being no CSV-Shaft: configuration C, Fig. II.2.

The external shaft can be an input or an output shaft (bi-directional CVT). Changing indices 1 and 2 gives another three configurations, which are, however, basically the same as illustrated in Fig.II.2.

b) Transmission ratio, power flow ratio and efficiencies

The overall transmission ratio of the PS-CVT (i_{PS-CVT}) and the ratio of power transmitted by the CSV to the output power of the PS-CVT (P_{CSV}/P_{out}) can be calculated with the help of the following basic formulas for speed ratio and torque ratio of a planetary drive [II.3]. See also Fig.II.1.

$$i_o = \frac{n_1}{n_2} \quad \text{under condition} \quad n_p = 0 \tag{II.1}$$

$$n_1 - n_2 . i_o - n_p .(1 - i_o) = 0 \tag{II.2}$$

$$T_1 + T_2 + T_p = 0 \tag{II.3}$$

and under condition of 100% transmission efficiency

$$\frac{T_2}{T_1} = -i_o \; ; \quad \frac{T_p}{T_1} = i_o - 1 \; ; \quad \frac{T_p}{T_2} = \frac{1}{i_o} - 1 \tag{II.4}$$

In these formulas n_{index} = rotation speed of respective shaft
T_{index} = torque in respective shaft.

For each of the 3 basic configurations of the PS-CVT, the transmission ratio and the power flow ratio have been calculated as a function of the transmission ratios of the CSV (i_{CSV}), of the planetary gear drive (i_o) and of the coupling gears (i_T). Transmission losses are only considered in the CSV (constant efficiency η_{csv} assumed), since the gear losses are assumed to be negligible compared to the CSV losses. The results are represented in Fig.II.2. The power flow ratios have been expressed as an absolute value as the transmission efficiency is related to this value. The actual power flow direction in the CSV is not important in this respect, see also formula (II.8). Changing input and output shaft, slightly influences the power flow ratios as also indicated in Fig. II.2.
The overall efficiency of the PS-CVT is calculated from the power flow ratios as follows:

$$P_{in} = P_{out} + P_{loss} \tag{II.5}$$

$$P_{loss} = (1 - \eta_{csv})|P_{csv}| \tag{II.6}$$

$$\eta_{PS\text{-}CVT} = \frac{P_{out}}{P_{in}} \tag{II.7}$$

Combining (II.5) to (II.7) gives:

$$\eta_{PS\text{-}CVT} = \frac{1}{1 + (1 - \eta_{CSV}) \left|\dfrac{P_{csv}}{P_{out}}\right|} \tag{II.8}$$

In these formulas
$$
\begin{aligned}
P_{loss} &= \text{loss power in CSV} \\
P_{csv} &= \text{input power CSV} \\
P_{in} &= \text{input power PS-CVT} \\
P_{out} &= \text{output power PS-CVT} \\
\eta_{csv} &= \text{transmission efficiency CSV} \\
\eta_{ps\text{-}cvt} &= \text{transmission efficiency PS-CVT}
\end{aligned}
$$

Taking into account gear losses, the derivation will get more complicated. The gear losses in the planetary gear drive depend on the configuration and the power flow direction [II.3]. In combination with the CSV they depend moreover on the transmission ratio of the CSV. These second order effects are not further considered here.

With the help of the above formulas, the PS-CVT has been further analyzed with respect to speed ratio range, power flows and efficiencies. Therefore the PS-CVT with increased and with decreased speed ratio range,compared to the pure CVT, have been distinguished.

c) Increased speed ratio range
Enlarging of the speed ratio range of the PS-CVT, compared to the pure CSV, means:

$$R_{PS\text{-}CVT} = \frac{i_{PS\text{-}CVT,max}}{i_{PS\text{-}CVT,min}} > \frac{i_{CSV,max}}{i_{CSV,min}} = R_{CSV} \tag{II.9}$$

in which formula all i's are assumed positive.
By substituting the transmission ratio of the PS-CVT, see Fig.II.2., in eq. (II.9), the condition for the range of gear transmission ratios i_o for enlarging the speed ratio range of the pure CVT can be found. For a chosen or a given i_o and $R_{ps\text{-}cvt}$, the transmission ratio i_T can in turn be calculated from the above equations. With i_o and i_T known, the power flow ratios for the PS-CVT can be calculated with the help of the $|P_{csv}/P_{out}|$ ratio as indicated in Fig.II.2.

Fig.II.3., page 170, represents the conditions for i_o an i_T as well as the courses of overall transmission ratio and power flow ratio as a function of the transmission ratio of the CSV. Input and output shaft configurations are as defined in Fig. II.2.

It can be seen that for an increased speed ratio range, the power transmitted by the CSV is always larger than the output power of the PS-CVT. In other words there is a "circulating power".

The consequence on the efficiency of the PS-CVT can be calculated with the help of eq. (II.8). The course of this efficiency, as a function of the CSV transmission ratio, is as well displayed in Fig.II.3. It can be seen that in particular for the lower transmission ratios of the PS-CVT, the transmission efficiency is very low due to the "circulating power".

It is noted that for increasing the speed ratio range, there are in case of configuration A and C, more conditions for i_o an i_T possible than listed. However, this is beyond the scope of this synopsis and does not affect the here illustrated influence of the PS-CVT principle on the transmission efficiency.

d) Decreased speed ratio range

In a similar way as described for the increased speed ratio range, the gear transmission ratios (i_o and i_T) and power flow ratios for a decreased speed ratio range can be derived from:

$$R_{PS-CVT} = \frac{i_{PS-CVT,max}}{i_{PS-CVT,min}} < \frac{i_{CSV,max}}{i_{CSV,min}} = R_{CSV} \qquad (II.10)$$

in which all i's are assumed positive.

Fig.II.4., page 171, represents the thus derived characteristics of the PS-CVT with decreased speed ratio range. It can be seen that the power transmitted by the CSV is always smaller than the output power of the PS-CVT. This influences the overall efficiency of the PS-CVT in a positive way.

The efficiency of the PS-CVT is calculated with the help of eq. (II.8). Fig.II.4. represents also the course of this efficiency as a function of the CSV transmission ratio. Input and output shaft configurations are as defined in Fig. II.2. It can be seen from Fig. II.4., that the efficiency is improved compared to the pure CSV.

Also here, it is noted that for decreasing the speed ratio range, there are for all configurations more conditions for i_o and i_T possible than listed. However, this is beyond the scope of this synopsis and does not affect the here illustrated influence of the PS-CVT principle on the transmission efficiency.

$$R_{PS-CVT} > R_{CSV}$$

Legend:
i_{PS-CVT} ———
$\left|P_{CSV}/P_{out}\right|$ ▬▬
η_{PS-CVT} ‑‑‑‑

Axis labels: $\left|P_{CSV}/P_{out}\right|$; $C = \left|P_{CSV}/P_{out}\right|_{i_{CSV}=i_T}$; $1/\eta_{CSV}$; 1; η_{CSV}; $i_{PS-CVT,max.}$; $i_{PS-CVT,min}$; $\pi/4$; 0; b; i_T; $i_{CSV(-)}$; i_{CSVmin}; $i_{CSV max.}$; i_{CSV} for $i_{PS-CVT}=0$; a; i_{PS-CVT} for $i_{CSV}=0$

	config. A *	config. B *	config. C *
i_0	$> 0 \ \wedge \ < 1$	< 0	$> 0 \ \wedge \ < 1$
i_T	$\dfrac{R_{PS-CVT} \cdot i_{CSV,min} - i_{CSV,max}}{(1-i_0)(R_{PS-CVT}-1)}$	$\dfrac{(i_0-1)(i_{CSV,max} - i_{CSV,min} \cdot R_{PS-CVT})}{R_{PS-CVT}-1}$	$\dfrac{R_{PS-CVT} \cdot i_{CSV,min} - i_{CSV,max}}{i_0(R_{PS-CVT}-1)}$
a	$-i_T \cdot \left(\dfrac{1-i_0}{i_0}\right)$	$\dfrac{i_T}{i_0}$	$-i_T \cdot \dfrac{i_0}{1-i_0}$
b	$i_T \cdot (1-i_0)$	$\dfrac{i_T}{1-i_0}$	$i_T \cdot i_0$
c	$\dfrac{1}{\eta_{CSV}} \cdot \dfrac{1}{i_0}$	$\dfrac{1}{\eta_{CSV}} \cdot \dfrac{i_0-1}{i_0}$	$\dfrac{1}{\eta_{CSV}} \cdot \dfrac{1}{1-i_0}$

* Configurations illustrated in Fig.II.2.

Fig.II.3. Characteristics of a PS-CVT with increased speed ratio range.

Fig.II.4. Characteristics of a PS-CVT with decreased speed ratio range.

The table in the figure:

	config. A *	config. B *	config. C *
i_0	> 1	> 1	< 0
i_T	$\dfrac{R_{PS\text{-}CVT} \cdot i_{CSV,min} - i_{CSV,max}}{(1 - i_0)\,(R_{PS\text{-}CVT} - 1)}$	$\dfrac{(i_0 - 1)\,(i_{CSV,max} - i_{CSV,min} \cdot R_{PS\text{-}CVT})}{R_{PS\text{-}CVT} - 1}$	$\dfrac{R_{PS\text{-}CVT} \cdot i_{CSV,min} - i_{CSV,max}}{i_0\,(R_{PS\text{-}CVT} - 1)}$
a	$-i_T \cdot \left(\dfrac{1 - i_0}{i_0}\right)$	$\dfrac{i_T}{i_0}$	$-i_T \cdot \dfrac{i_0}{1 - i_0}$
c	$\dfrac{1}{\eta_{CSV}} \cdot \dfrac{1}{i_0}$	$\dfrac{1}{\eta_{CSV}} \cdot \dfrac{i_0 - 1}{i_0}$	$\dfrac{1}{\eta_{CSV}} \cdot \dfrac{1}{1 - i_0}$

* Configurations illustrated in Fig.II.2.

It can be concluded from the above, that power-splitting with the help of a gear drive enables modifying of the speed ratio range and the efficiency. However, increasing of the speed ratio range goes at cost of the efficiency and vice versa.

II.3. PS-CVT without gear drive

Besides the power-split principle with the help of a planetary drive, the electrical as well as the hydrostatic CVT offer a relatively simple power-split principle, which does not involve the use of a gear drive.

a) Basic configurations

The electrical as well as the hydrostatic CVT offer the possibility to allow the casing (or the stator) of one of the two machines of the CVT to rotate. This is further illustrated on the basis of an electrical CVT.

Two basic configurations are possible, depending on the parts of the two machines that are directly, mechanically coupled.

- Rotor-stator coupled PS-CVT, see Fig.II.5A. The stator which is allowed to rotate, is directly coupled with the rotor of the other electrical machine (mechanical path), whereas the rotating "stator" is electrically coupled with the other machine via slip rings (electrical path). The rotors of both machines are, as usually, the external shafts of the CVT.
- Rotor-rotor coupled PS-CVT, see Fig.II.5B. The rotors of both machines are directly coupled (mechanical path), whereas the rotating stator is electrically coupled with the other machine via slip rings (electrical path). The coupled rotors and the rotating "stator" are the external shafts now.
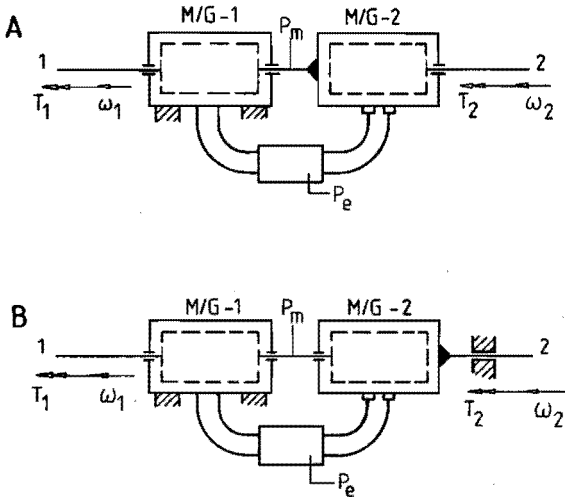
Fig.II.5. PS-electrical CVT without gear drive.

It can be seen that all power is transmitted mechanically when the transmission ratio is equal to unity (M/G-2 acts as a blocked coupling then). As soon as electrical power transmission is involved, all other transmission ratios from zero to one (shaft 1 as input and shaft 2 as output shaft) are possible. Thus an infinite speed ratio range without "circulating power" is possible.

Assuming that the mechanical transmission efficiency is better than the electrical efficiency, this results in an improved efficiency of this PS-CVT type compared to the purely electrical CVT while maintaining the infinite speed ratio range. This can be derived as follows.

Starting from Fig.II.5A and II.5B with shaft 2 as input and shaft 1 as output shaft, this transmission is a retarding CVT.

The mechanical losses in the transmission are assumed as a mechanical torque loss between the machines, whereas the electrical losses are assumed as conversion losses in the converter between the machines. The following expressions apply then for this transmission:

$$i_{PS-CVT} = \frac{\omega_1}{\omega_2} \quad ; \quad 0 \le i_{PS-CVT} \le 1 \tag{II.11}$$

$$\eta_{PS-CVT} = \frac{P_{out}}{P_{in}} = \frac{P_1}{P_2} \quad ; \quad \eta_e = \frac{P_{e1}}{P_{e2}} \quad ; \quad \eta_m = \frac{P_{m1}}{P_{m2}} \tag{II.12}$$

$$P_{in} = P_{m2} + P_{e2} \quad ; \quad P_{out} = P_{m1} + P_{e1} \tag{II.13}$$

$$P_{m1} = T_{m1} \cdot \omega_1 \quad ; \quad P_{m2} = T_{m2} \cdot \omega_1 = T_{e2} \cdot \omega_1 \tag{II.14}$$

$$P_{e1} = T_{e1} \cdot \omega_1 \quad ; \quad P_{e2} = T_{e2} \cdot (\omega_2 - \omega_1) \tag{II.15}$$

The new symbols used here are:

η_e, η_m = transmission efficiency of mechanical, respectively electrical path.

$P_{m1,2}$ = mechanically transmitted power via shaft 1, respectively 2.

$T_{m1,2}$ = mechanically transmitted torque via shaft 1, respectively 2.

$T_{e1,2}$ = electrically transmitted torque via shaft 1, respectively 2.

The transmission efficiency of the PS-CVT can be found by substituting the expressions of (II.12) in eq. (II.5), from which it follows:

$$P_{in} = \eta_{PS-CVT} \cdot P_{in} + (1 - \eta_e) \cdot P_{e2} + (1 - \eta_m) \cdot P_{m2} \tag{II.16}$$

Dividing by P_{in} gives:

$$1 = \eta_{PS-CVT} + (1 - \eta_e) \cdot \frac{P_{e2}}{P_{in}} + (1 - \eta_m) \cdot \frac{P_{m2}}{P_{in}} \tag{II.17}$$

From (II.11) and (II.13) to (II.15), it follows:

$$\frac{P_{m2}}{P_{in}} = i_{PS-CVT} \quad \text{and} \quad \frac{P_{e2}}{P_{in}} = 1 - i_{PS-CVT} \tag{II.18}$$

Substituting (II.18) in (II.17) gives:

$$\eta_{PS-CVT} = \eta_e + i_{PS-CVT} \cdot (\eta_m - \eta_e) \tag{II.19}$$

With $\eta_m > \eta_e$ and $0 \le i_{ps-cvt} \le 1$, it follows from eq. (II.19) that the above type of PS-CVT has an increased efficiency compared to the purely electrical CVT and tends to the mechanical transmission efficiency for increasing transmission ratio.

II.4. Conclusions

From the above considerations it is obvious that the speed ratio range as well as the efficiency of a pure CVT can be modified by the power-split principle. The way in which these characteristics influence each other depends on the kind of power-split principle:
- Power-splitting with gear drive.
  Increasing of the speed ratio range goes at cost of the efficiency and vice versa.
- Power-splitting without gear drive.
  This type of PS-CVT is restricted to the electrical and hydrostatic CVT's. It enables combining of a wide speed ratio range with increasing of the efficiency of the pure CVT. Power-splitting for hydrostatic and electrical CVT's is therefore preferred without gear drive above with gear drive.

Besides the above important characteristics of the PS-CVT, the principle may also include other advantages compared to the pure CVT, such as higher torque and power rating and smaller weight and volume. For a lot of applications the PS-CVT can thus be a very attractive transmission, offering many possibilities.

Appendix III

Vibrations in systems with rotating elements

III.1. Introduction

This condensed survey comprises an explanatory consideration of the subjects concerned with rotordynamics as they have been investigated for the EMAFER concept.
Vibrations in a system are characterized by a frequency and an amplitude. Systems with rotating elements will have a number of discrete natural frequencies of lateral vibrations.

III.2. Natural frequencies

The natural frequencies of a system are the frequencies at which the vibration amplitude of the system is a maximum, when the system is excited with this frequency. The natural frequencies are also indicated as resonance frequencies. Each natural frequency will have an associated mode shape, being the positions of the construction parts relative to each other and/or the deformations of the construction parts themselves, at the instant of maximum strain during the vibration. The natural frequencies, as well as the associated mode shapes, are determined by the distribution of mass and stiffness along the construction parts as well as by the stiffness of the coupling elements.
When in a system with rotating elements, the rotational speed coincides with one of the natural frequencies of the system, this natural frequency generally will be excited by the rotating element, e.g. by imbalance. This speed is indicated as a critical speed of the rotating element. At the critical speed the rotor whirls about its bearing center line in a mode shape, associated with the particular natural frequency. These whirling mode shapes are indicated as whirl modes.

Critical speeds
The natural frequencies of a rotor system will be influenced by the rotational speed when the rotor has polar and equatorial moments of inertia that cannot be neglected. This phenomenom is called gyroscopy and has to be taken into account when determining the critical speeds of a rotor system.
A rotating element has an angular momentum which is characterized by a magnitude and a position. It can be expressed in vector notation as:

$$\underline{L} = I.\underline{\Omega} \tag{III.1}$$

in which
$\underline{L}$ = angular momentum vector
I = moment of inertia matrix
$\underline{\Omega}$ = rotational speed vector

The gyroscopy manifests itself in a rotating element as a moment of reaction, the gyroscopic moment, acting on the rotating shaft when the position of the angular momentum is changed, e.g. by rotor imbalance. This gyroscopic moment is proportional to the angular momentum and angular velocity of positional change. Its direction is perpendicular to the angular momentum and the direction of positional change.
In vector notation:

$$\underline{M}_G = \underline{L} \times \underline{\dot{\varphi}} \qquad \qquad (III.2)$$

in which
$\underline{M}_G$ = gyroscopic moment vector
$\underline{L}$ = angular momentum vector
$\underline{\varphi}$ = angular velocity vector of positional change of rotation axis.

From (III.2) it follows that the gyroscopic moment will also be involved in a rotor tilting by e.g. dynamic imbalance. Then the gyroscopy manifests itself as a coupling stiffness of the rotor with the earth, influenced by spin speed. As a consequence the natural frequencies of the rotor will vary with spin speed.
The graphical presentation of the natural (whirl) frequencies as function of the rotor (spin) speed is called the **spin-whirl map**. For the "Laval rotor" (stiff disc on a massless shaft with isotropic stiffness) as considered in literature [9.2] for these effects, the spin-whirl map is illustrated in Fig. III.1.
In this diagram positive and negative natural frequencies are plotted against shaft rotational frequency. The associated whirl modes all involve tilting of the rotor as all natural frequency curves change with spin speed. The actual directions here are immaterial. What is important, is the direction of the rotation of the whirl motions and the rotation of the shaft: the first and third quadrant as well as the second and fourth one are identical.
Considering the first and fourth quadrant, the positive natural frequencies are indicated as the forward whirl speeds, i.e. the speeds of the whirl motions in which the mode shape of the rotor rotates in the direction of the spin speed. The negative natural frequencies give the **backward whirl speeds**, in which the directions of the spin and whirl motions are opposite to each other. The forward whirl speeds will be excited by rotorwise rotating (forward) excitation, whereas the backward whirl speeds will be excited by counter rotating (backward) excitations.
Imbalance is a specific example of forward rotating and rotor speed coupled excitation. Backward rotating excitation occurs usually in conjunction with forward rotating excitation in for instance harmonically varying excitation that does not change position or non-circular excitation, e.g. in case of anisotropic support stiffness.
The resonance frequencies of a system can be found by the intersections of the excitation frequency curves, which may be a function of the rotational frequency Ω, with the natural frequency curves. The intersections of the natural frequency curves with the $\omega_c = \Omega$ line, the imbalance excitation line, give the critical speeds.
Finally it is noted that the natural frequency curves in Fig. III.1. have three horizontal asymptotes and one sloping asymptote, which is of special interest.

$$\omega_n = \Omega \cdot \frac{I_p}{I_{eq}} \tag{III.3}$$

in wich
I_p = polar moment of inertia
I_{eq} = equatorial moment of inertia

From Fig. III.1., it is clear that for thin single disc rotors ($H < < R$ and $I_p \approx 2I_{eq}$), there is only one critical speed since the sloping asymptote has a slope I_p/I_{eq} of about 2. For thick single disc rotors ($I_p/I_{eq} < 1$), there is a second critical speed. Rotors for which $I_p = I_{eq}$ should be guarded against. The sloping asymptote will near the imbalance excitation line then, see Fig. III.1. This means that for all higher spin speeds "near resonance operation" will occur.
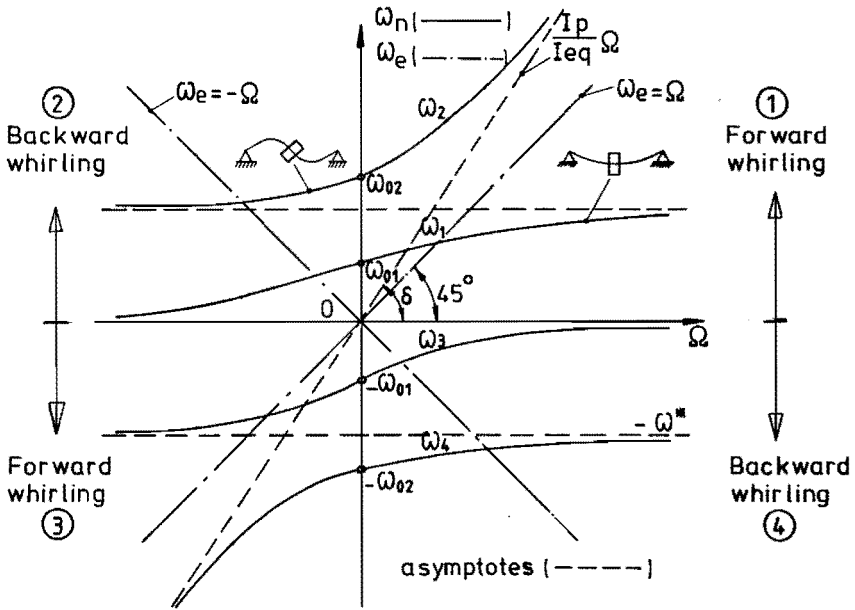
Fig. III.1. Spin-whirl map for stiff disc, asymmetrically fixed on a massless isotropic elastic shaft [9.2].

Whirl modes
The whirl modes or whirling mode shapes of a rotor system can be distinguished into **rigid body modes** and **bending modes**. These modes involve respectively no bending and bending of construction parts of the rotor system. This depends strongly on the support stiffnesses in relation to the stiffnesses of the construction parts. This is illustrated for a uniform shaft, for which the first three modes change with increasing bearing support stiffness as shown in Fig. III.2.

For zero rotor speed the first and second mode are indicated respectively as "translation mode" and "tilt mode". For a rotating element the translation mode will trace a cylinder and the tilt mode will trace two cones. These modes are called respectively "cylindrical" and "conical" whirl modes. A special terminology for the third order mode shapes is not used.
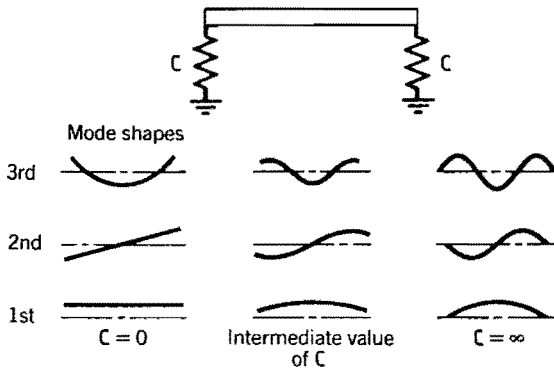
Fig. III.2. Effect of bearing support stiffness on the whirl modes for a uniform shaft [9.1].

III.3. Vibration amplitudes

The maximum vibration amplitudes of a system are strongly determined by the damping characteristics of the system. A rotor system can have several different sources of damping with associated different effects. With respect to these effects, the most important characteristic of damping is whether the damping is associated with the rotating parts or with the stationary parts. Damping associated with stationary parts will always have a stabilizing effect, whereas damping associated with rotating parts will have, for supercritical conditions, a destabilizing effect.

Stable motions
The stable motions cover the majority of rotordynamic problems, involving synchronous whirl, i.e. response to imbalance. For these situations stationary damping has the following effects:
- Modification, only slightly, of critical speeds.
- Attenuation of vibration amplitudes and with this the transmitted loads while traversing critical speeds. The minimum value of damping at which the whirl amplitudes are smaller than the excitation amplitudes, is designated as critical damping.

It has the value:

$$B_{crit} = 2\sqrt{c\ m} \tag{III.4}$$

in which B_{crit} is the critical value of damping, c is the effective stiffness and m the effective mass associated with the considered vibration.

It has become common practice to quantify the damping in terms of a percentage of the critical damping. Thus the dimensionless "damping ratio" ξ is b/B_{crit} and the "percent damping" is 100 ξ. Here b is the damping coefficient and B_{crit} the critical damping of the considered system.

For damping values smaller than the critical damping ($\xi < 1$), the logaritmic decrement δ_{ln}, which indicates the rate of "dying down" of free vibrations, is defined as:

$$\delta_{ln} = \ln \frac{\text{vibration amplitude}(t)}{\text{vibration amplitude}(t+p)} = 2\pi\xi \tag{III.5}$$

where p represents one vibration period.

- For supercritical operation bearing support damping increases the dynamic load transmitted through the bearing. Too much damping can "lock up" the supports. The ratio flexible support bearing force to rigid support bearing force is indicated as the **transmissibility** and is an important dimensionless factor for evaluating the effectiveness of bearing support stiffness and damping.

Unstable motions

The unstable or self-excited motions cover the remaining minority of rotordynamic problems, involving nonsynchronous rotor whirling at one of the natural frequencies of the rotor, below or above the running speed. This whirling motion becomes unstable, typically when a certain speed, called the **treshold speed of instability**, is reached. This is referred to as rotordynamic instability and can severely damage or even destroy the equipment.

A considerable degree of understanding concerning unstable motions has been developed by assuming that rotordynamic instability is produced by forces which are tangential to the rotor whirl orbit, acting in the same direction as the instantaneous whirl motion and linearly proportional to the whirl orbit. A dynamic instability is in mathematical terms defined then as a solution to the linear differential equation of motion characterized by a complex eigenvalue with a positive real part. The graphical presentation of the (complex) eigenvalues is indicated as the **stability map** of the system, from which it can be concluded whether the system involves whirl motions, which can become unstable, see Fig.III.3.

The system is theoretically stable when all eigenvalues are left of the imaginary axis. In praxis a safety margin, represented by a stability criterion is used. This stability criterion, by which the amount of stability can be guaranteed, is expressed via the logaritmic decrement:

$$\delta_{ln} = 2\pi\xi = 2\pi\frac{\text{real part}}{\text{imaginary part}} \tag{III.6}$$

The stability criterion is represented by the stability line in Fig. III.3.
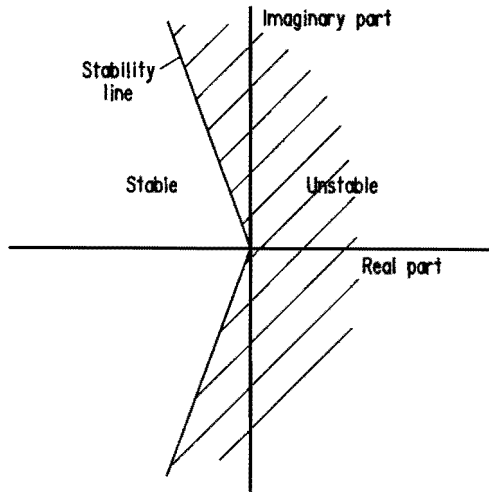
Fig.III.3. Stability map: graphical presentation of eigenvalues.

For "curing" instability, there are a number of design measures which address directly to the destabilizing mechanisms. For instance, the magnitude of the destabilizing forces, caused by internal rotor damping, can be reduced by minimizing the number of separate rotor elements, by avoiding of slipping in fit interfaces and by using rotor material with as low as possible material damping or hysteresis (e.g. no elastomeric rotor elements). Besides internal rotor damping as destabilizing mechanism, a number of others have been identified or hypothesized to explain incidents of rotordynamic instability. For these known or hypothetical sources, together with the design measures to avoid or eliminate instability, see [7.3].

Besides the design measures, which address directly the destabilizing mechanisms, there are two more approaches, which are very general and apply to all systems.

- Introduction of additional external damping to raise the instability onset speed above the operational speed range. The installation of "squeeze film dampers" (SFD's) at the bearing supports, represents the most common approach for adding more external damping to an unstable rotor bearing system.

  It is, however, noted that these dampers must be designed with considerable care. They have the potential for either significantly improving or degrading response and stability characteristics of a rotor. For a more comprehensive explanation of SFD's and their effects on rotordynamics, see [9.4].

- Maximize the value of the critical speed of the rotor so that the treshold speed of instability will be higher.

  However, this approach is generally very challenging since it involves stiffening the system without significantly increasing its active mass. Moreover, locating of critical speeds in the operating speed range should be avoided.

References

[1.1]   Thoolen, F. (1990).
        Energy and Emission Reduction by Energy Storage.
        Proceedings of the Florence World Energy Research Symposium.
        Firenze, Italy, 28 May - 1 June 1990.

[1.2]   British Petroleum (1993).
        BP Statistical Review of World Energy.
        BP Government & Public Affairs Department,
        Britannic House, Moor Lane, London EC2Y9BU.

[1.3]   Langeweg, F., Ed. (1989).
        Zorgen voor morgen: nationale milieuverkenning 1985-2010,
        by order of Rijksinstituut voor Volksgezondheid en Milieuhygiëne.
        Samson H.D. Tjeenk Willink, Alphen a/d Rijn, The Netherlands.

[1.4]   Elenco N.V. (1989).
        Elenco N.V. develops and Manufactures Fuel Cells.
        Information Bulletin, Dessel, Belgium, April 1989.

[1.5]   Krekel, N, Berdowski, P. and Dieren, A. van (1987).
        Duurzame energie een toekomstverkenning.
        Krekel van der Woerd Wouterse B.V., Management Consultants,
        Rotterdam, the Netherlands, October 1987.
        (By order of NOVEM, Utrecht, The Netherlands).

[1.6]   Dutch Ministery of Economic Affairs (1988).
        Opslag van elektriciteit in Nederland. Haalbaar en aanvaardbaar?
        Eindrapport van de commissie opslag elektriciteit Directoraat-Generaal voor
        Energie, The Hague, The Netherlands, May 1988.

[1.7]   Korkmaz, F. (1980).
        Voraussetzungen für einen Erfolg versprechendem Einsatz von Fahrzeug
        Antrieben mit Bremsenergie-Rückgewinnung.
        ATZ Automobiltechnische Zeitschrift 82 (1980) 4, pp 221-226.

[1.8]   Beachley, N. and Frank, A. (1981).
        Practical Considerations for Energy Storage Motor Vehicles.
        SAE paper 819417.

[1.9]   Nikolaus, H. (1984).
        Hydrostatische Stadtbus-Antriebe mit neuartiger Abschalttechnik.
        Konstruktion 36 (1984) H.5, S. 161-166.

[1.10] CBS (1986).
        Emissies door wegverkeer 1978 - 1984.
        Publicatie nr. C 23 CBS (Centraal Bureau voor de Statistiek), Voorburg/Heer-
        len, The Netherlands.

[1.11] Spreng, D. (1988).
        Wieviel Energie braucht die Energie?
        Originalausgabe: Net Energy Analysis, Praeger N.Y. 1988.

[2.1]   Biermann, J., Schraut R. (1983).
        Schwungradspeicher als Antriebselement für Schienenfahrzeuge.
        ETR (32) 01.02.1983, pp 99 - 105.

[2.2]   Kapellen, D., Jamzadeh, F., Wang, S. and Frank A. (1984).
        Analysis of Energy-Storage Concepts for Refuse Collection Trucks.
        SAE paper 840056.
[2.3]   Graaf, R. van der (1987).
        An IC-Engine Flywheel Hybrid Drive for Road Vehicles.
        EAEC conferences, Strassburg, June 1987.
[2.4]   Frank, A. (1983).
        Flywheel-Engine Hybrid Power Source. Investigation for Forklift Trucks, final
        report. College of Engineering Propulsion Energy Management Group.
        University of Wisconsin - Madison.
[2.5]   Dann, R. (1973).
        The revolution in Flywheels.
        Machine Design, May 17, 1973.
[2.6]   Nikolaus, H. (1985).
        Hydrostatische Getriebe mit Energiespeicherung.
        Oelhydraulik und Pneumatik no. 4, 1985.
[2.7]   Dongen, L. van (1983).
        Energetical Optimization of Propulsion Systems for Electric Vehicles, chapter 6.
        Dissertation, Eindhoven University of Technology, The Netherlands.
[2.8]   Tromp, J. (1980).
        Regeneratieve remsystemen bij stadsbussen.
        De Ingenieur, nr. 28/29, 10 juli 1980, pp 7-9.
[2.9]   Cuypers, M. (1980).
        Numerical Evaluation of the Torque Capacities of Mechanical Drives,
        especially for Continuously Variable Transmissions.
        ASME publication 80-C2/Det-120.
[2.10] Weh, H. (1982).
        Hochausgenutzte elektrische Maschinen mit Permanenterregung.
        ETZ Archiv Bd.4 (1982) H.7, pp 219-224.
[2.11] Weh, H., Wahlen, H., Gumbrecht, R. and Brauchmann, W. (1982).
        Vehicle Traction Motor fed by Transistor Inverter.
        Motorcon September 1982 proceedings, pp 50-60.
[2.12] Thoolen, F. (1989).
        Overview of realized regenerative energy storage systems for vehicular
        applications.
        Internal report C.C.M., Nuenen, The Netherlands.
[2.13] Genta, G. (1985).
        Kinetic Energy Storage.
        Theory and practice of advanced flywheel systems, chapter 1.
        Butterworths, London.
[2.14] Dünner, E. (1957).
        Gyrovoertuigen, speciaal wat betreft hun elektrische uitrusting.
        De Ingenieur, JRG 69/NR6/8FEB 1957, pp V.15-V.22.
[2.15] New York Subway tries out flywheel energy storage.
        Railway Gazette International, January 1975, pp 23-24.
[2.16] Evans, P., Karlsson, A. (1981).
        The Volvo city bus. I Mech E 1981, C157/81.

[2.17]   Bartsch, H., Helling, J. and Schreck, H. (1977).
         Hybridantrieb für Kraftfahrzeuge mit vorwiegend instationärer Betriebsweise.
         VDI-Z 119 (1977) Nr. 3 - Februar, pp 141-146.
[2.18]   Zanten, M. van (1979).
         Onderzoek aan vliegwielsystemen voor energie-opslag.
         De Ingenieur, JRG 91/NR4/25JAN 1979, pp 62-68.
[2.19]   Bader, C. (1979).
         Elektrische und hybride Antriebe für Nutzfahrzeuge.
         ATZ Automobiltechnische Zeitschrift 81 (1979) 6, pp 283-289.
[2.20]   Drewitz, H. (1982).
         Antriebssysteme mit Bremsenergierückgewinnung für Stadtbusse.
         Referat 8.2.1982, RAI Amsterdam.
[2.21]   Kinetisch electrische aandrijving van autobus.
         Aandrijftechniek, 17 maart 1980, pp 120-121.
[2.22]   Renner - Smith, S. (1980).
         Battery saving flywheel gives electric car freeway zip.
         Popular Science, October 1980.
[2.23]   Olmsted, D. (1984).
         Development of Flywheel Energy Propulsion System for Transit Buses.
         Garrett Airesearch Manufacturing Company, report nr. 82-19511, Rev.2,
         May 24, 1984.
[2.24]   Kinetic Energy Storage System (1985).
         BP publication of the BP Research Centre, Chertsey Road, Sunbury on Thames,
         Middlesex TW 16, 7.LN, England.
[2.25]   Gilmore, D., Bullock, K. (1982).
         An on Road Evaluation of a 1500 kg Multi Purpose Hybrid Vehicle with
         Threemodal Energy Storage.
         Proceedings 19th International FISISTA Congress, Melbourne 1982.
         Paper 82053.
[2.26]   Heidelberg, G. and Reiner, G. (1988).
         The Magneto Dynamic Storage Unit - test results of an electrical flywheel
         storage system in a local public transport bus with a diesel electrical drive.
         IECEC 1988, paper 889230, pp 75-80.
[2.27]   Heidelberg, G. and Reiner G. (1988).
         The Magneto Dynamic Storage Unit - a flywheel storage system for peak
         levelling, voltage and frequency regulation in island networks.
         IECEC 1988, paper 889145, pp 43-46.
[2.28]   Martini, S. (1984).
         The M.A.N. Hydrobus, a Drive Concept with Hydrostatic Brake Energy
         Recovery.
         Symposium on advanced and hybrid vehicles, Glasgow, September 1984.
[2.29]   Volvo Cumulo: Technical description.
         Volvo Flygmotor AB, Sweden, z.j.
[2.30]   Hybride voertuig op basis van de Alfa Romeo 33.
         Press Release Alfa Romeo Nederland, 1987.
[2.31]   VW Golf mit Diesel/Elektro Hybridantrieb.
         VW Dokumentation 1989.

[2.32]   Winkelman, J. and Frank, A. (1973).
         Computer Simulation of the University of Wisconsin Hybrid Electric Vehicle
         Concept. Society of Automotive Engineers, paper 730511.
         Automobile Engineering Meeting Detroit, Mich. May 14-18, 1973.

[3.1]   Hurwitch, J. Carpenter, C. (1991).
         Technology and application options for future battery power regulation.
         IEEE Transactions on Energy Conversion, Vol.6, No.1, March 1991.
[3.2]   Hoogerwaard, A., Bockel, O. van (1982).
         Perspectief van een openbaar stadsvervoer met elektrisch aangedreven bussen,
         die zijn uitgerust met een vliegwielsysteem.
         Report made by Holec Machines and System Group, Ridderkerk and F.D.O.
         Technical Advisors, Amsterdam, The Netherlands.
         By order of the Dutch Management Office for Energy and Environment
         (NOVEM), Utrecht, The Netherlands.
[3.3]   Hoogerwaard, A. (1982).
         Studie naar de haalbaarheid van vliegwielen in stoptrein materieel voor de opslag
         en hergebruik van remenergie.
         Report made by Holec Machines and System Group, Ridderkerk, The Netherlands
         By order of the Netherlands Railways, section St.& O., Utrecht, The Netherlands.
[3.4]   Thoolen, F. (1985).
         Vermogensbepaling vliegwielmachine t.b.v. het EMAFER-projekt.
         Internal notice C.C.M., Nuenen, The Netherlands, December 1985.

[4.1]   Genta, G. (1985).
         Kinetic Energy Storage.
         Theory and practice of advanced flywheel systems, chapter 3.
         Butterworths, London.
[4.2]   Lawson, L. (1971).
         Design and Testing of High Energy Density Flywheels for Application to
         Flywheel/Heat Engine Hybrid Vehicle Drive.
         IECEC 1971, paper 719150, pp 1142-1150.
[4.3]   Ledbetter, H. (1982).
         Physical Properties Data Compilations Relevant to Energy Storage.
         Mechanical properties Data on Alloys for Use in Flywheels.
         Fracture and Deformation Division, National Bureau of Standards,
         Boulder, Colorado 80303. Issued January 1982.
[4.4]   Emmens, W., Ratelaar, S. (1976).
         Energie-opslag in vliegwielen.
         De Ingenieur/JRG 88/NR 47/18 Nov 1976, pp 943-947.
[4.5]   Inspection protocol of 26 CrNiMoV 14 5, by order of CCM, Nuenen,
         the Netherlands. Saar Stahl GmbH, Völkingen, Germany, 28 Feb 1987;
         Vermoeiingsonderzoek Materiaal (26 NiCrMoV14 5) Vliegwielmachine.
         Rapport CTO/3/10.676/135, 2 juli 1987.
         Centrum voor Technisch Onderzoek, Concordiastraat 67, 3551 EM Utrecht,
         The Netherlands.
[4.6]   Toland, R. (1978).
         Current Status of Composite Flywheel Development.
         Sampe 23, May 1978, pp 856-876.

[4.7] Chiao, T. (1980).
Fiber Composite Materials Development for Flywheel Applications.
Lawrence Livermore Laboratory Report, Contract No. W-7405-ENG.

[4.8] Dyneema, Vof (1991).
Brochure Dyneema SK 60: Properties and Applications.
DSM High Performance Fibers B.V., Eisterweg 3, 6422 PN Heerlen, the Netherlands.

[4.9] Nijhof, A. (1983).
Specifieke mechanische eigenschappen van vezelversterkte kunststoffen.
College diktaat T.U. Delft, afd. Werktuigbouwkunde, vakgroep vezeltechniek, 1983-1984, 2e druk.

[4.10] Courtaulds Grafil (1989)
Technical data sheet for grafil continuous carbon fibres.
Courtaulds Grafil Ltd, P.O. Box 16, Coventry CV 65 AE, England.

[4.11] Rijn, L. van (1985).
Literatuuronderzoek over het vermoeiingsgedrag van kunststof vezels.
Aanvulling op TNO-rapport 371/'84 by order of C.C.M., Nuenen,
The Netherlands.

[4.12] Widmer, J., Asper, H., Riesen, H., Thoolen, F. (1986).
Dynamic Stability of Rotors on Selfcentering Hubs.
IECEC 1986, paper 869195, pp 885-889.

[4.13] Hagg, A., Sankey, G. (1974).
The Containment of Disc Burst Fragments by Cylindrical Shells.
Journal of Engineering for Power/ April 1974, pp 114/123.

[4.14] Coppa, A. (1981).
Design and fabrication of containment rings for use in tests of six prototype flywheel rotors.
General Electric Company, Energy systems program department.
Report prepared for Lawrence Livermore Laboratory, subcontract 6624409, February 1981.

[4.15] Sapowith, A., Handy, W. (1982).
A composite flywheel burst containment study.
Prepared for Lawrence Livermore National Laboratory,
University of California, Livermore, California 94550.
Document no. AVSD-0350-81-RR.

[5.1] Van Doorne's Transmissie B.V. (1992).
Company profile and product range.
Brochure of VDT, Dr. Hub van Doorneweg 120, Tilburg, The Netherlands, May 1992.

[5.2] Frank, A, Beachley, N., Harter, R., Dietrich, A, and Lau, K. (1977).
Continuously-Variable Transmission Concepts Suitable for Flywheel Hybrid Automobiles.
IECEC 1977, paper 779005, pp 26-33.

[5.3] Schlösser, W. (1975).
Aandrijftechniek, hoofdstuk 27: Shunt-stroom overbrengingen.
College dictaat "Aandrijftechniek". T.U. Eindhoven (April 1975).

[5.4] Roodenhuis, G. (1964).
       Elektrodynamische overbrenging tussen een aandrijvende en een aangedreven as.
       Octrooiraad Nederland. Octrooi no. 108945, 18 juni 1964.
[5.5] Genta, G. (1985).
       Kinetic Energy Storage.
       Theory and practice of advanced flywheel systems, chapter 6, section 6.4.
       Butterworths, London.
[5.6] Genta, G. (1985).
       Kinetic Energy Storage.
       Theory and practice of advanced flywheel systems, chapter 4, section 4.3.
       Butterworths, London.
[5.7] Rooij, J. van (1991).
       Private correspondence with ir. J.H.M. van Rooij, Autodivisie Volvo Car B.V.,
       Advance Car Technology Transmission, Helmond, The Netherlands,
       October 1990.
[5.8] Schlösser, W. (1992).
       Private correspondence with prof.dr.ir. W.M.J. Schlösser, Helmond,
       The Netherlands.
[5.9] Asper, H. (1985).
       Sinewave synthesis for high efficiency DC-AC conversion.
       IECEC 1985, pp 1696-1701.
[5.10] Ketelaars, G. (1993).
       The combustion engine EMAFER hybride bus.
       System design of a flow floor flywheel hybrid city bus.
       M.Sc. Thesis, Eindhoven University of Technology, The Netherlands.

[6.1] Thoolen, F., Vaessen, L., Hoorn, R. van der (1983).
       Conceptstudie gyrobus-aandrijving. Internal notices CCM, Nuenen,
       The Netherlands. Reportnr. 125.01.03 and 125.01.04, October 1983.
[6.2] Canders, W. (1982).
       Zur Berechnung von Schwungradenergiespeichern aus Faserverbundwerkstoff mit
       elektrischem Energiewandler, Kapitel 3.
       Dissertation, Technical University Braunschweig, Germany.
[6.3] Nieuwe Akkutechnieken
       Elektuur 56, januari 1989.
[6.4] ABB-Hochenergiebatterie für Elektro Fahrzeuge und Spitzenlastdeckung.
       Druckschrift Nr. DHB 1340 88D.

[7.1] Meer, R. van der (1987).
       EMAFER machine ontwerp.
       Internal report C.C.M., Nuenen, The Netherlands.
[7.2] Offringa, L. (1991).
       Electronic power converter for a flywheel unit with a synchronous electrical
       permanent magnet machine.
       Dissertation Eindhoven University of Technology Eindhoven, The Netherlands.
[7.3] Ehrich, F., Childs, D. (1984).
       Self-excited vibration in high performance turbo machinery.
       Mechanical Engineering, May 1984, pp. 66-79.

[7.4]   Satchwell, D., Towgood, D., (1980).
        High energy density composite flywheel.
        AiResearch Manufacturing Company, Report no. SAND 79-7019.

[7.5]   Mc Michael, C. et al (1992).
        Practical adaptation in bulk superconducting magnetic bearing applications.
        Appl. Phys. lett. 60 (15), 13 April 1992.

[7.6]   Neale, M. (editor; 1973).
        Tribology Handbook.
        Butterworths, London.

[7.7]   Holmes, R. (1989).
        Private correspondence with prof. R. Holmes, University of Southampton,
        Highfield, Department of Mechanical Engineering, Southampton, 5 June 1989.

[7.8]   GMN catalogue 1261, (1989).
        Spindelkugellager, GMN, Georg Müller Nürnberg AG, Nürnberg, Germany.

[7.9]   SKF Catalogue 3700 E (1987).
        Precision bearings. SKF Kugellagerfabriken GmbH, Schweinfurt, Germany.

[7.10] Steele, R. (1981).
        Composite flywheel balance experience.
        IECEC 1981, paper 819413.

[7.11] Eisenhaure, D., Downer, D. (1981).
        Aerodynamic heating and windage loss characteristics of flywheel rotors.
        Reportnr. R-1472, June 1981. The Charles Stark Draper Laboratory, Inc.,
        Cambridge, Massachusetts 02139.

[7.12] Genta, G. (1985).
        Kinetic Energy Storage.
        Theory and practice of advanced flywheel systems, chapter 4.
        Butterworths, London.

[7.13] Coppa, A. (1982).
        Energy storage flywheel housing design concept development.
        Lawrence Livermore Laboratory report nr. UCRL-15448.

[7.14] Wutz, Adam, Walcher.
        Theorie und Praxis der Vacuumtechnik.

[7.15] Clarke, R. (1973).
        Rotor disk burst characteristic data analysis.
        Reportno. S&N 73-1,
        Boeing Commercial Airplane co.

[7.16] Korten, J. (1991).
        Constructie van de vliegwielcontainer voor het EMAFER projekt.
        Internal report C.C.M., Nuenen, The Netherlands.

[7.17] Janssen, W., Mohede, R. (1987).
        EMAFER preprototype, composition drawings; cross section, upper view, and
        side view; all numbered 14603.0017.
        C.C.M., Nuenen, The Netherlands.

[8.1]   Genta, G. (1985).
        Kinetec Energy Storage.
        Theory and practice of advanced flywheel systems, chapter 3.
        Butterworths, London.

[8.2]   Canders, R. (1982).
        Zur Berechnung von Schwungradenergiespeichern aus Faserverbandwerkstoff mit
        elektrischem Energiewandler, kapitel 2.
        Dissertation Technische Universität Braunschweig.

[8.3]   Bessonov, A.P., Ochan, M. (1987).
        Composite Flywheel Optimization.
        Mechanical Engineering Research Institute USSR Academy of Sciences, Griboe-
        dor Street 4, 101000 Moscow-Centre, 1987.

[8.4]   Vemura, F., Lyana, H., Fukunaga, Y. (19..).
        Rotational strength and optimal design of a hybrid filament wound disc.
        Composite structure, editor Marshall, J.

[8.5]   Flanagan, R. (1986).
        Design, manufacture and test results for four high energy density fibre
        composite rotors.IECEC 1986, paper 869202.

[8.6]   Knight jr, C., Pollard, R. (1977).
        Prestressed Thick Flywheel Rims.
        Flywheel Technology Symposium, San Francisco, Oct. 1977, pp.183-192.

[8.7]   Widmer, J., Asper, H. (1985).
        Woven Ribbon Composite Flywheel with Selfcentering Hub.
        IECEC 1985, paper 859319.

[8.8]   Widmer, J., Asper, H. (1986).
        New results on Woven Ribbon Wound Flywheels.
        IECEC 1986, paper 869194.

[8.9]   Post, R., Post, S. (1973).
        Flywheels. Advances in material and mechanical design make it possible to use
        giant flywheels for the storage of energy in electric power systems and smaller
        ones for the propulsion of automobiles, trucks and buses.
        Scientific American, December 1973, volume 229, nr. 6.

[8.10] Widmer, J. (1985-1987).
        Correspondence with J. Widmer, Swiss Federal Institute of Technology,
        Zürich. Several calculation results WRWP flywheel during period December
        1985 to August 1987.

[8.11] Houppermans, W. (1988).
        Optimalisering van composiet vliegwielen.
        M.Sc.Thesis, Eindhoven University of Technology, The Netherlands.
        WFW report 88.052, August 1988.

[8.12] Hart 't, W., Boogers, J. (1988).
        Onderzoek C.C.M. vliegwiel, rapport NLR TR 88051 L.
        National Aerospace Laboratory NLR, Amsterdam, The Netherlands, April 1988.

[8.13] Rijn, L. van (1984).
        Composiet vliegwiel voor een gyrobus (vooronderzoek).
        KRI-TNO-rapport 371/'84 (3 Oct.'84) by order of CCM., Nuenen,
        The Netherlands.

[8.14] Rijn, L. van (1987).
        Calculation results for layered flywheel with press fit at hub/flywheel interface,
        (in Dutch). KRI-TNO-report 265/'87 (19 Febr.'87) by order CCM., Nuenen,
        The Netherlands.

[8.15] Lommen, W., Thoolen, F. (1991).
Optimization layer construction flywheel with double press fit for EMAFER prototype.
Internal report, CCM, Nuenen, The Netherlands, February 1991.

[9.1] Vance, J.M. (1987).
Rotordynamics of Turbomachinery.
A Wiley-Interscience publication, 1987.

[9.2] Gasch, R., Pfützner, H. (1975).
Rotordynamik, Eine Einführung, Kapitel 8.
Springer Verlag 1975.

[9.3] Flügge, W. (1962).
Handbook of Engineering Mechanics, chapter 58.
McGraw Hill Book Company, Inc. 1962.

[9.4] Thoolen, F. (1990).
A synopsis on Squeeze Film Dampers.
Internal notice C.C.M., Nuenen, The Netherlands, November 1990.

[9.5] Schoofs, P. (1990).
Trillingsanalyse van een hoogtoerige vliegwielmachine.
Stageverslag Hogeschool Eindhoven, afdeling Werktuigbouwkunde.

[9.6] Hamilton, L. (1987).
Optimalisatie m.b.t. rotordynamica en lagerflensontwerp bij een snel draaiende rotor. Afstudeerrapport WFW - 87.071
Vakgroep Fundamentele Werktuigkunde, Faculteit der Werktuigbouwkunde, Technische Universiteit Eindhoven, november 1987.

[9.7] Lommen, W. (1990).
Trillingsanalyse vliegwielaggregaat.
Afstudeerverslag Hogeschool Eindhoven, afdeling Werktuigbouwkunde, mei 1990.

[9.8] Lommen, W. (1990).
Uitbreiding van het EMAFER model.
Internal C.C.M. report, Nuenen, The Netherlands, November 1990.

[9.9] Schoofs, P. (1990).
EMAFER prototype, composition drawing preliminary design, designalt. 1, drawing nr. 146.01.0001, dated April 1990.
C.C.M., Nuenen, The Netherlands.

[9.10] Mohede, R. (1991).
EMAFER prototype, composition drawing final design, drawing nr. 250.010000.
C.C.M., Nuenen, The Netherlands.

[9.11] Holmes, R. (1991).
Private correspondence with prof. R. Holmes, University of Southampton, Highfield, Department of Mechanical Engineering, Southampton, 29 January 1991.

[9.12] ISO 1940 (1973).
Balance quality of rotating rigid bodies.

[10.1] Michels, J. (1992).
Constructie-alternatieven voor lagerpositionering (in Dutch).
Internal report, CCM, Nuenen, The Netherlands, October 1992.

[II.1]   Dubbel (1981).
         Taschenbuch für den Maschinenbau, Kapitel 9.9.
         ISBN 3-540-09422-9,14. Auflage, Springer Verlag.
[II.2]   Polder, J. (1969).
         A network theory for variable epicyclic gear trains.
         Dissertation T.H. Eindhoven, The Netherlands.
[II.3]   Müller, W. (1976).
         Einheitliche Berechnung von Planetengetrieben.
         Eine Anleitung zum praktischen Gebrauch. Teil I: Berechnung einfacher
         Planetengetriebe.
         Antriebstechnik 15 (1976) Nr. 1.

List of symbols

a	acceleration	(ms^{-2})
	amplitude	(m)
a_{abs}	absolute mean value of acceleration	(ms^{-2})
b	damping coefficient	(Nsm^{-1})
b_{index}	damping coefficient of respective part	(Nsm^{-1})
B_e	external damping matrix	(Nsm^{-1})
B_i	internal damping matrix	(Nsm^{-1})
B_{crit}	critical value of damping	(Nsm^{-1})
c	stiffness value	(Nm^{-1})
c_{index}	stiffness of respective part	(Nm^{-1})
C	maximum constant stress	(Nm^{-2})
C_r	radial clearance	(m)
e	journal eccentricity	(m)
e_m	energy per unit mass (mass energy density)	(Jkg^{-1})
e_v	energy per unit volume (volume energy density)	(Jm^{-3})
E	Young's modulus	(Nm^{-2})
E_r, E_t	Young's modulus for respectively radial and tangential orthotropic directions	(Nm^{-2})
E_k	kinetic energy	(J)
E_{keff}	effective kinetic energy	(J)
E_{flwh}	energy at the flywheel	(J)
E_{wh}	energy at the driving wheels	(J)
ERF	energy reduction factor	$(-)$
F	imbalance force, pretension force	(N)
F_t	tangential damper force	(N)
G	gyroscopic matrix	(Nsm^{-1})
h	axial rim height, local axial flywheel height	(m)
h_c	axial flywheel height at centre	(m)
h_o	axial flywheel height at outer radius	(m)
i	transmission ratio (ratio output to input shaft speed)	$(-)$
i_o	transmission ratio of planetary drive	$(-)$
i_t	transmission ratio of coupling gear drive	$(-)$
i_{csv}	transmission ratio of conical sheaves variator	$(-)$
i_{cvt}	transmission ratio of continuously variable transmission	$(-)$
i_{ps-cvt}	transmission ratio of power split transmission	$(-)$
I	moment of inertia	(kgm^2)
I_p	polar moment of inertia	(kgm^2)
I_{eq}	equatorial moment of inertia	(kgm^2)
K	stiffness matrix	(Nm^{-1})
	shape factor	$(-)$
K_{max}	maximum value of shape factor	$(-)$
L	angular momentum	(kgm^2s^{-1})
	length	(m)
m	mass	(kg)

M	mass matrix	(kg)
M_G	gyroscopic moment	(Nm)
n	rotational shaft speed	(s^{-1})
n_{index}	rotational speed of respective shaft	(s^{-1})
p	vibration period	(s)
P	power	(W)
P_e	electrically transmitted power	(W)
P_m	mechanically transmitted power	(W)
P_{csv}	power transmitted via Conical Sheaves Variator	(W)
P_{flwh}	power at the flywheel	(W)
P_{in}	input power	(W)
P_{loss}	loss power	(W)
P_{MVB}	power transmitted via Metal-V-Belt transmission	(W)
P_{out}	output power	(W)
P_{slip}	power related to slip losses in the transmission	(W)
P_{wh}	power at the driving wheels	(W)
$P_{wh,ac}$	acceleration power at the driving wheels	(W)
$P_{wh,dec}$	deceleration power at the driving wheels	(W)
r	radial displacement	(m)
	vibration amplitude	(m)
	local flywheel radius	(m)
r_i	inner flywheel radius	(m)
r_o	outer flywheel radius	(m)
R	journal radius	(m)
	speed ratio range of transmission	(-)
R_{index}	speed ratio range of respective transmission	(-)
S	ratio between tangential and radial ultimate strength	(-)
t	time	(s)
t_{ac}	acceleration time	(s)
t_{dec}	deceleration time	(s)
t_{off}, t_{slip}	time during which ratio of rotational speeds of flywheel and driving wheels are out of speed ratio range of transmission, respectively during deceleration and acceleration	(s)
T	torque	(Nm)
T_e	electrically transmitted torque	(Nm)
T_m	mechanically transmitted torque	(Nm)
U	radial displacement	(m)
v	velocity, speed	(ms^{-1})
v_c	circumferential speed	(ms^{-1})
v_m	mean velocity	(ms^{-1})
V	material volume	(m^3)
α_r, α_t	thermal expansion coefficient for respectively radial and tangential orthotropic directions	(K^{-1})
ß	ratio inner to outer radius of flywheel	(-)
δ	ratio between radial and tangential thermal expansion coefficient	(-)
δ_m	inner system damping coefficient	(Nsm^{-1})
δ_o	outer system damping coefficient	(Nsm^{-1})

δ_{ln}	logaritmic decrement	(-)
Δt	time difference	(s)
ϵ	ratio journal eccentricity to journal radius	(-)
ϵ_r	radial strain	(-)
ϵ_t	tangential strain	(-)
η	power transmission efficiency	(-)
η_e	efficiency of electrical transmission	(-)
η_{csv}	transmission efficiency Conical Sheaves Variator	(-)
η_{cvt}	transmission efficiency Continuously Variable Transmission	(-)
η_{diff}	transmission efficiency gear differential	(-)
η_{flwb}	transmission efficiency of flywheel package	(-)
η_m	efficiency of mechanical transmission	(-)
η_{MVB}	efficiency of Metal-V-Belt transmission	(-)
η_{ps-cvt}	transmission efficiency of power-split CVT	(-)
η_{T1}	transmission efficiency of gear drive	(-)
η_{tr}	overall transmission efficiency	(-)
$\eta_{tr,ac}, \eta_{tr,dec}$	overall efficiency of total transmission between flywheel and driving wheels, respectively during acceleration and deceleration	(-)
Θ	temperature difference	(K)
λ	eigen value	(s^{-1})
μ	dynamic viscosity of fluid	(Nsm^{-2})
	square root of ratio tangential to radial Young's modulus	(-)
ν	Poisson's ratio	(-)
ν_{tr}, ν_{rt}	Poisson's ratio for respectively radial and tangential orthotropic directions	(-)
ξ	damping ratio	(-)
ρ	mass density	(kgm^{-3})
σ	material stress	(Nm^{-2})
σ_a	allowable material stress	(Nm^{-2})
σ_r	radial stress	(Nm^{-2})
σ_t	tangential or hoop stress	(Nm^{-2})
σ_u	ultimate material strength	(Nm^{-2})
σ_{ur}, σ_{ut}	ultimate material strength in respectively radial and tangential orthotropic directions	(Nm^{-2})
$\dot{\varphi}$	angular velocity of positional change of rotation axis	(rads^{-1})
χ	ratio of local to outer radius of flywheel	(-)
$\dot{\psi}$	angular whirl velocity	(rads^{-1})
ω	angular speed	(rads^{-1})
ω_{max}	maximum angular speed	(rads^{-1})
ω_{min}	minimum angular speed	(rads^{-1})
ω_c	characteristic angular frequency	(rads^{-1})
ω_e	excitation frequency	(rads^{-1})
ω_n	natural frequency	(rads^{-1})
Ω	rotational frequency	(rads^{-1})
	spin speed	(rads^{-1})

Curriculum Vitae

Franciscus Johan Marie Thoolen was born on May 29th, 1953 in Echt, The Netherlands. He attended the Bisschoppelijk College in Sittard where he gained his HBS-B certificate in 1971. Also in 1971, he started his study of mechanical engineering at the Eindhoven University of Technology, where he graduated with distinction as a Master of Science in 1976.

Soon thereafter he was employed by the Centre for Construction and Mechatronics (CCM), Nuenen, The Netherlands. With CCM, he has since been involved with the actual implementation of innovative technical developments. The latter cover a very wide range of industrial sectors ranging from consumer products and food industries to automotive, off-shore and transport industries.

As a senior project manager he has been working full-time since 1986 on the development of the high speed flywheel energy storage system EMAFER. Besides heading the multidisciplinary "EMAFER team", he is actually involved in all the work concerning the mechanical aspects of this project. In this context he also wrote this thesis on the development of a high speed flywheel energy storage system.

Acknowledgements

As a contribution towards the solution of the threatening fossil energy shortage and environmental pollution an advanced high speed flywheel energy storage system, designated as EMAFER[1], has been developed. This work was initiated by NS[2] by means of a research and development order. This order was for the greater part funded by NOVEM[3] and performed by my employer CCM[4].
I want to thank the organizations mentioned above for enabling me to use the results of this work for my thesis. In this context I am very grateful to Ir. F. Oudendal, late head of the department Studie & Onderzoek of NS and Dr.Ir. L. van Dongen, contact for the EMAFER project at NS. Further to mention are: Ir. L. Boreel, C. Douma, Ing. B. van Spanje and Ir. J. van Meel, successive contacts for the EMAFER project at NOVEM.
I especially want to thank Ir. J. Kummeling, director of CCM, for his stimulating advices and his understanding and support in overcoming difficult periods during this work.

Furthermore, I want to thank all persons who have contributed to achieving the results as described in this thesis. These are of course all those who are or were involved in the EMAFER project. However, because of their large number, they are not all named here. I would like to mention some key figures of the "EMAFER team": Jan Engelen, Wilbert Lommen, Rob van der Meer, Lodewijk Offringa and Eugenio Smits. Without this interdisciplinary team of highly skilled colleagues, it would not have been possible to achieve the status as realized in the EMAFER prototype system. I thank all of them for their cooperation, contributions and the pleasant work climate.
A special word of thanks is due to Wilbert Lommen for his direct assistance to me in all the work concerning the mechanical aspects of the EMAFER system.
I also want to thank all my other colleagues at CCM for their contributions, constructive remarks and the pleasant work climate.

Then I want to thank all persons who were directly connected to my thesis. These are primarily all the members of my committee who were willing to review my work.
I would like to mention the following people in particular: Prof.Dr.Ir. M. Schouten, as first promotor, for the many stimulating discussions and reviews; Prof. A. Frank, as second promotor, for his critical review; Prof.Ir. J. Schot for his very close involvement in this project and for his conscientious review; Prof.Dr.Ir. W. Schlösser for his many constructive criticisms and Dr. H. Asper for his refreshing remarks and for making me part of his experiences with "flywheel colleagues" from all over the world.
Further a word of thanks to: Carmen Beekmans for her enormous devotion and tireless efforts and accuracy in typing this work; Roy Mohede for making the numerous figures and Harry Clerx for making the photos in this publication.

Last, but certainly not least, a sincere thank you goes to my wife Anneke and our children Jean-Pierre, François and Lilian. I want to thank them for their understanding, patience and encouragements, which were indispensable for making this thesis.

[1] EMAFER : Electro Mechanical Accumulator for Energy Reuse.
[2] NS   : Nederlandse Spoorwegen (Netherlands Railways).
[3] NOVEM   : Nederlandse Maatschappij voor Energie en Milieu, Utrecht, The Netherlands.
[4] CCM   : Centre for Construction and Mechatronics, Nuenen, The Netherlands.

STELLINGEN

behorende bij het proefschrift

DEVELOPMENT

of an advanced high speed

FLYWHEEL

ENERGY STORAGE SYSTEM

van

F.J.M. Thoolen

Eindhoven, 7 december 1993

1. De inzet van regeneratieve energie-opslagsystemen zal het verbruik van fossiele energie sterk verminderen en daarmee positieve gevolgen met betrekking tot het leefmilieu bewerkstelligen.

    Dit proefschrift, hoofdstuk 1.

2. Het vliegwiel is zowel het meest originele als het meest inspirerende middel voor energie-opslag.

    Dit proefschrift, hoofdstuk 2.

3. De eigenschappen van een regeneratief energie-opslagsysteem worden bepaald door de mate van integratie van opslag-, transmissie- en regelcomponent, waarbij de onderlinge afstemming belangrijker is dan de individuele optimalisatie van deze componenten.

    Dit proefschrift, hoofdstuk 6.

4. Het vliegwiel met een gelaagde opbouw van concentrische ringelementen uit kunststof met vezelversterking, tezamen met een naafverbinding met perspassing, vormt het meest betrouwbare vliegwielconcept met een hoge energiedichtheid.

    Dit proefschrift, hoofdstuk 8.

5. De conclusie van R. Post en S. Post waarbij wordt gesteld dat de optimale constructie voor een vliegwiel van kunststof met vezelversterking bestaat uit concentrische ringen van dit materiaal, welke met elkaar zijn verbonden door elastische tussenlagen, is onjuist omdat deze conclusie alleen betrekking heeft op een optimale materiaalbenutting, terwijl het belang van een goed trillingsgedrag onvoldoende wordt onderkend.

    Post, R.F., and Post, S.F., Scientific American, 229 (Dec. 1973), 17.
    Post, R.F., Kenneth Fowler, T. and Post, S.F., Proceedings of the IEEE, vol. 81, No.3, March 1993.

6. Blijkens recente octrooiaanvragen wordt het (vlieg)wiel nog steeds opnieuw uitgevonden.

    Eigen ervaring, 1990 - 1993.

7. Indien men zich als betrokkene zelf in een probleem verdiept kan men voorkomen dat een geconsulteerde specialist onnodig meer en andere problemen zal genereren en kan men bereiken dat hij zich beter richt op het vraagstuk waarvoor men hem benaderde.

Eigen ervaring, 1985 - 1993.

8. Met betrekking tot de milieuproblematiek is het verontrustend te moeten vaststellen dat op economische gronden een compleet ontmoedigingsbeleid wordt gevoerd waar het betreft het repareren van gebruiksgoederen en een waar stimuleringsbeleid voor het vervangen van gebruiksgoederen, zelfs als deze nog functioneren.

9. Forse verhogingen van de energieprijs hebben op de korte termijn een energiebesparend effect, matige verhogingen zijn alleen goed voor het dekken van het financieringstekort van de overheid.

10. Om tot een betere ontwikkeling van de aanleg van studenten te komen, verdient het aanbeveling minstens de oorspronkelijke breedte van het eindexamen V.W.O. te herstellen.

11. Praktische en financiële beperkingen bij een onderzoek kunnen door hun improvisatieverhogend effect ook zeer effectief zijn.

Eigen ervaring, 1985 - 1993.

12. Aan de stelligheid, respectievelijk hardheid van uitspraken kan men veelal ontlenen of deze een wetenschappelijke dan wel een commerciële achtergrond hebben.